University of Glasgow

Investigation on the Aerodynamic Performance of Cycloidal Rotors with Active Leading-Edge Morphing

Liam Ferrier

Submitted in fulfilment of the requirements for the
Degree of Doctor of Philosophy

Aerospace Sciences Research Division
School of Engineering
College of Science and Engineering
University of Glasgow

August 2020

"A pessimist sees the difficulty in every opportunity; an optimist sees the opportunity in every difficulty."

– Winston Churchill (1874 – 1965)

ABSTRACT

A cycloidal rotor is a novel form of propulsion system which has a geometrical design differing completely from the conventional screw propeller. The blades of a cycloidal rotor rotate about the horizontal axis of rotation. A key advantage of this rotor system is the instantaneous control of the net thrust vector, meaning that the thrust can be adjusted to any desired direction, perpendicular to the rotor's horizontal axis of rotation. Few investigations have been conducted to assess the negative impact dynamic stall has on the cycloidal rotor's performance characteristics. Dynamic stall is a complex phenomenon associated with unsteady aerofoil pitching motion that generates large hysteresis effects on the blade's aerodynamic characteristics during the pitch cycle.

In this study, an investigation is conducted to assess the effect of active leading-edge morphing on alleviating the negative impact dynamic stall has on the aerofoil aerodynamic characteristics as well as the cycloidal rotor performance characteristics. Computational studies are performed for a large-scale cycloidal rotor and for a single pitch-oscillating symmetric aerofoil operating at a large Reynolds number, Re > 1,000,000. Dynamic stall wind tunnel testing of a single NACA0015 aerofoil with an active leading-edge flap is also conducted to validate the effects of leading-edge morphing from the single pitch-oscillating aerofoil's CFD model.

The main findings from this study showed that applying active leading-edge morphing resulted in significant improvements of both the single aerofoil's aerodynamic characteristics and the cycloidal rotor's performance characteristics. The results from the CFD for the single pitch-oscillating aerofoil showed that the negative effects of dynamic stall were alleviated when applying active leading-edge morphing. The results from the cycloidal rotor CFD simulations showed that the effects of dynamic stall were alleviated which led to a reduction in the level of blade-wake interference. This led to a significant improvement in the cycloidal rotor performance characteristics, such as a 4-blade cycloidal rotor with active leading-edge morphing applied producing less power dissipation in comparison to a rigid 2-blade cycloidal rotor. The main findings from the experimental analysis showed that active leading-edge morphing reduced negative effects of dynamic stall such as the level of aerodynamic hysteresis, as well as improving the aerodynamic efficiency.

CONTENTS

LIST OF FIGURES

LIST OF TABLES

PREFACE

This thesis presents work carried out by the author in the Aerospace Sciences Research Division at the University of Glasgow during the period from October 2015 to February 2019, supervised by Dr Marco Vezza and Dr Hossein Zare-Behtash. The work was supported by a University of Glasgow College of Science and Engineering EPSRC scholarship, Grant Number 00227099.

ACKNOWLEDGEMENTS

I would sincerely like to thank both my supervisors, Dr. Marco Vezza and Dr. Hossein Zare-Behtash for providing me with the opportunity to pursue research in the field of computational and experimental aerodynamics. I am very grateful for their invaluable advice, guidance, and technical support they provided to me over the duration of the project.

I would also sincerely like to thank all of the technical support staff who were instrumental in the experimental design process, particularly Mr Alistair Macfarlane, Mr John McCulloch, Mr Neil Owen, and Mr Bruce Robertson.

I would like to give a special thanks to David Pickles and Pavlos Artemi for their invaluable support, assistance, and good banter during wind tunnel testing. The frequent lunch trips and moral support definitely helped when working in the cold winter months. I would also like to thank Dr. Richard Green for his technical support and guidance during the wind tunnel testing.

Special thanks goes to my Fiancée Megan who has provided me with constant support, encouragement and has always been there for me since starting University as a under-graduate. A special mention is also made to my pet cat Blue who kept me amused with his mischief antics during the writing up period. Finally, I would also like to thank all my family and friends who have supported me throughout the years.

AUTHOR'S DECLARATION

"I declare that, except where explicit reference is made to the contribution of others, that this dissertation is the result of my own work and has not been submitted for any other degree at the University of Glasgow or any other institution."

Printed Name: Liam Ferrier

Date: 22/08/2020

NOMENCLATURE & ABBREVIATIONS

UNITS

All units of measurement throughout this thesis conform to the *Système Internationale*, with deviations from this rule noted where appropriate.

NOTATION

This section describes the general form of notation for properties such as scalars, vectors and matrices and their derivatives.

TIME DERIVATIVES

$\dot{x}$	first derivative of x with respect to time
$\ddot{x}$	second derivative of x with respect to time
$x^{(n)}$	nth derivative of x with respect to time

SCALARS, VECTORS AND MATRICES

x	scalar
x_i	ith element of vector f
$f(x)$	function of scalar x
L_f	Lie derivative in the direction of f

SYMBOLS

The following symbols are used throughout this thesis. Where a symbol is used only briefly, it is defined at the appropriate point in the text.

LATIN

A	Rotor disk area

$A_{testsection}$	Wind tunnel test section cross-sectional area
AR	Aspect Ratio
b	Span
c	Aerofoil chord
C_{aero}	General aerodynamic force or moment coefficient
Ca	Axial force coefficient
Cd	Drag coefficient
Cl	Lift coefficient
Cm	Moment coefficient
Cn	Normal force coefficient
Cp	Pressure coefficient
C_P	Power coefficient
C_T	Thrust coefficient
D	Rotor diameter
$D_{endplate}$	End plate diameter
$D_{endplate}/c$	End plate diameter sizing ratio
DL	Disk-loading
F_x	Rotor side force
F_y	Rotor vertical force
FD_{amp}	Leading-edge fixed droop amplitude
G	Grid density
h	Wind tunnel test section width
H_{ground}	Vertical distance from ground
i	Blade current azimuthal position
I	Turbulence intensity
k	Reduced frequency
L_{scale}	Turbulent length scale
Ma	Mach number

M_{flap}	Leading-edge flap mass
M	Moment
MT	Leading-edge morphing method
n	Total number of blades
P_{total}	Total pressure
p	Static pressure
P	Aerodynamic power
P_{rotor}	Total aerodynamic power
PL	Power-loading
q	Dynamic pressure
R	Rotor radius
R^2	Coefficient of determination
R_{ac_y}	Leading-edge flap moment arm length
Re	Reynolds Number
T	Period
t	Time
T_{res}	Rotor resultant thrust vector
T_{static}	Static temperature
U_∞	Free-stream velocity
V_t	Rotor tangential velocity
Vol_{model}	Aerofoil model volume
x	x-coordinate
X_{amp}	Thrust rod displacement
x_{morph}/c	Morphing axis origin
y	y-coordinate
y^+	Wall y plus

GREEK

α	Incidence angle

α_{amp}	Cyclic amplitude
α_M	Mean incidence angle
β_{max}	Leading-edge morphing amplitude
Δt	Time-step
Δt^*	Non-dimensional time-step
ΔC_{aero}	Delta force or moment coefficient
ϵ	Total blockage effect
ϵ_{sb}	Solid blockage factor
ϵ_{wb}	Wake blockage correction
μ	Dynamic viscosity
Ω	Rotor rotational velocity
ω_z	Vorticity
ω_z^*	Non-dimensional vorticity
ϕ	Direction of resultant thrust vector
ψ	Blade azimuthal position
ψ_0	Initial blade azimuth angle
ψ_{act}	Morphing initial actuation azimuthal position
ψ_i	Blade initial azimuthal position
σ	Rotor solidity
θ	Blade pitch angle
θ_{max}	Maximum blade pitch amplitude

SUBSCRIPTS

ac	Actuator
av	Average
end	End value
inc	Increment
l	Lower
LE	Leading-edge

max	Maximum
min	Minimum
qc	quarter chord
ref	Reference
res	Resultant
rotor	rotor
stagnation	Stagnation value
start	Start
t	Tangential
total	Total value
u	Upper
un	Uncorrected

ABBREVIATIONS

ANN	Artificial Neural Network
BTV	Blade Tip Vortices
BVI	Blade Vortex Interaction
CFD	Computational Fluid Dynamics
CROP	Cycloidal Rotor Optimised for Propulsion
DAQ	Data Acquisition System
DARPA	Defence Advanced Research Projects Agency
DBD	Dielectric Barrier Discharge
DNS	Direct Numerical Simulation
FEA	Finite Element Analysis
FM	Figure of Merit
GG	Green-Gauss
GUI	Graphical User Interface
HAWT	Horizontal Axis Wind Turbine
HSUI	Hydraulic System User Interface

LES	Large Eddy Simulation
LEV	Leading-Edge Vortex
LSQ	Least Squares
MAV	Micro Air Vehicle
NACA	National Advisory Committee for Aeronautics
PIV	Particle Image Velocimetry
RANS	Renolds-Averaged Navier Stokes
SA	Spalart-Allmaras
SIMP	Solid Isotropic Material with Penalization
SST	Shear-Stress Transport
STA	Servotube Actuator
TEV	Trailing-Edge Vortex
TVB	Total Variation Bounded
UAV	Unmanned Air Vehicle
URANS	Unsteady Reynolds-Averaged Navier-Stokes
UVLM	Unsteady Vortex Lattice Method
VAWT	Vertical Axis Wind Turbine
VDLE	Variable Droop Leading-Edge
VTOL	Vertical Take-Off and Landing

CHAPTER 1

INTRODUCTION

1.1 LITERATURE REVIEW

1.1.1 INVESTIGATING THE PERFORMANCE OF CYCLOIDAL ROTORS

1.1.1.1. INTRODUCTION TO CYCLOIDAL ROTORS

A cycloidal rotor is a novel form of propulsion system which can be adapted to various forms of transport such as air and marine vehicles, with a geometrical design differing completely from the conventional screw propeller. A visualisation of a conventional manufactured cycloidal rotor system is shown in Fig. 1.1. The blades of a cycloidal rotor rotate about the horizontal axis of rotation. A key advantage of the cycloidal rotor is that all spanwise blade sections operate under similar aerodynamic conditions (similar flow velocities, Reynolds numbers, and incidence angles), which allows the blades to be more easily optimised in order to achieve the optimal aerodynamic efficiency [1, 2]. This also results in a uniform force distribution along the blade's spanwise direction which means that the rotor can operate at lower tip speeds. Another key advantage of using this rotor system is the near instant control of the net thrust vector, meaning that the thrust can be adjusted to any desired direction perpendicular to the rotor's horizontal axis of rotation. This provides the vehicle with 360° control capability to allow for a wide range of possible manoeuvres, for example, achieving Vertical Take-Off and Landing (VTOL) successfully. Controlling the direction of the net thrust vector generated by the rotor can be achieved, either by varying the pitch or phase angle of the individual blades of the rotor.

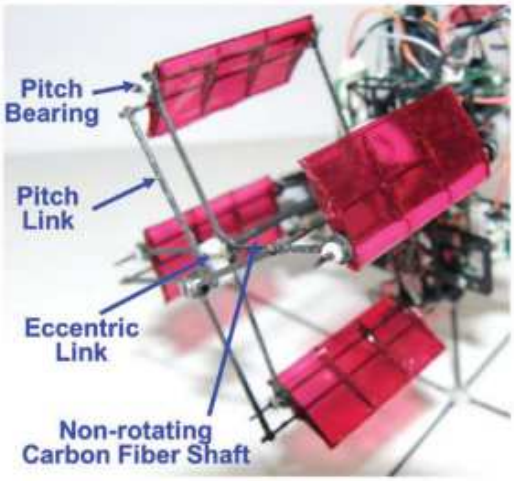

FIGURE 1.1: Illustration of a pitch-linkage system to provide pitch control for a meso-scale cycloidal rotor [2].

The pitch angle of each blade is controlled via a pitch-linkage which connects all of the blades to a control ring. A schematic of a four-bar linkage system which is used to provide pitch control is visualised in Fig. 1.2. The control ring is positioned eccentrically (as visualised by the symbol, e, in Fig. 1.2) to the rotor shaft, and is a controlling mechanism which can actively vary the resultant thrust vector to its desired direction [3]. The blade will achieve its maximum pitch angle at the upper and lower points of the rotor azimuthal positions if the control ring is positioned below the rotor shaft which is effective in generating blade lift and thrust [4]. A change in the control ring position also results in an near instant change in the magnitude and direction of the net thrust vector, which allows for the cycloidal rotor to achieve very good manoeuvrability capability [5]. McNabb [6] developed a theoretical model of a cycloidal propeller for various models of blade sinusoidal pitch scheduling. A four-bar linkage system theoretical model was developed to characterise the blade's realistic pitching motion. The four-bar linkage system was used as the control mechanism for the cycloidal propeller to control the individual blades. By moving a single common point to each of the four-bar linkages, the magnitude and direction of the blade's incidence angle profile could be controlled, as illustrated previously by the schematic diagram in Fig. 1.2.

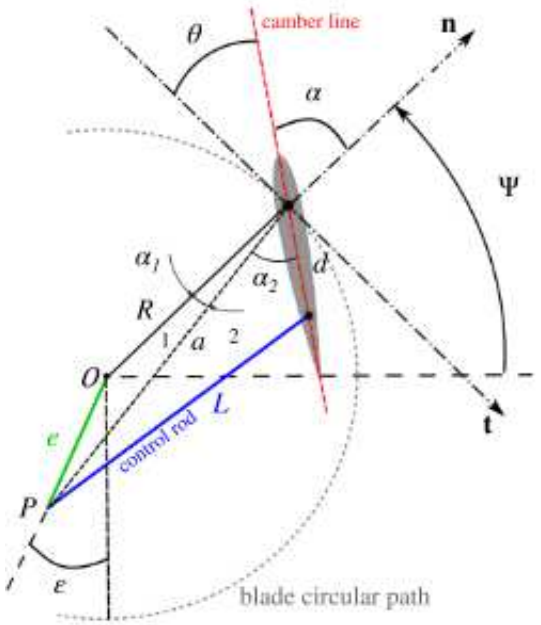

FIGURE 1.2: Schematic of a four-bar linkage system used to provide pitch control [7].

PREVIOUS INVESTIGATIONS ON CYCLOIDAL ROTOR PERFORMANCE

The idea for this novel rotor system originated in the early 1920s and was claimed to be invented by Professor F. K. Kirsten [8] from the University of Washington. The rotor was initially termed the "Kirsten-Boeing Propeller". Kirsten conducted wind-tunnel experiments on a large cycloidal propeller that comprised of 24 blades with a propeller diameter of 15 ft as shown in Fig. 1.3. The Kirsten-Boeing propeller was powered using a Wright aircraft engine rated at 400 hp, positioned at the left side of the propeller. The power generated by the engine produced a rotor rotational speed of 225 rpm and a thrust coefficient of 0.2 were recorded using a load balance suspended between the propeller and a fixed point.

FIGURE 1.3: Kirsten-Boeing Propeller, positioned on a test stand [8].

Throughout the 1930s, further research was conducted at the National Advisory Committee for Aeronautics (NACA) to further develop and understand the aerodynamics and operation of cycloidal rotors. Strandgren [9] developed analytical models to illustrate how the lift and propulsive forces generated by cycloidal rotors were obtained and served as an outline of the general principles and elementary theory of paddle wheels. In his study, he claimed that the vehicle's angle of attack could be changed instantaneously without modifying the orientation of the aircraft, which remained fixed. Wheatley [10] developed a simplified aerodynamic model for assessing the cycloidal rotor performance and for design purposes. Using assumptions such as constant induced velocity acting across the rotor cylinder and neglecting blade interference effects introduced errors in the aerodynamic results obtained. In 1934, Wheatley [11] conducted wind tunnel experiments for an 8 ft diameter, 4 bladed, cyclogyro rotor and verified that the cyclogyro would be able to ascend vertically, fly horizontally and glide without power (auto rotation).

In the late 1960s, an extensive review relating to the preliminary design concepts for cycloidal rotor powered vehicles as well as a detailed discussion about the kinematics of cycloidal motion was produced by the U. S. Army Aviation Materiel Laboratories [12]. An example of a cycloidal rotor configuration concept to act as a torque balance air vehicle is shown in Fig. 1.4. The pair of rotors shown rotate in opposite directions to cancel out the net vehicle torque to improve the stability and efficiency for this specific aircraft configuration. The paper also defined the cycloid curve as the path followed by the longitudinal axis of any single, cyclogyro rotor blade operating in forward flight.

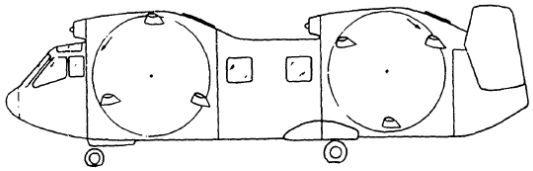

FIGURE 1.4: Cyclogyro rotor anti torque design concept [12].

Figure 1.5 visualises the comparison of rotor performance between cycloidal rotors and other rotorcraft propulsion systems at different scales [13]. The rotor performance between the rotorcraft systems are compared by assessing the Power Loading (PL) and Disk Loading (DL) performance curves. The Power Loading (PL) is the ratio of the rotor resultant thrust to the rotor power absorption (T_{res}/P), with units, N/kW. The disk-loading (DL) is the ratio of the rotor resultant thrust to the rotor disk area (T_{res}/A), with the units, N/m^2. Figure 1.5 demonstrates that cycloidal rotors can generate large levels of thrust however the Figure of Merit (FM), which is used to determine the overall aerodynamic performance, is lower than for conventional micro-rotor configurations. This is due to conventional micro-rotor systems commonly using cambered blade sections which improves the rotor performance characteristics, however cycloidal rotors can not utilise cambered blade sections as it has to operate at both positive and negative incidence angles [13].

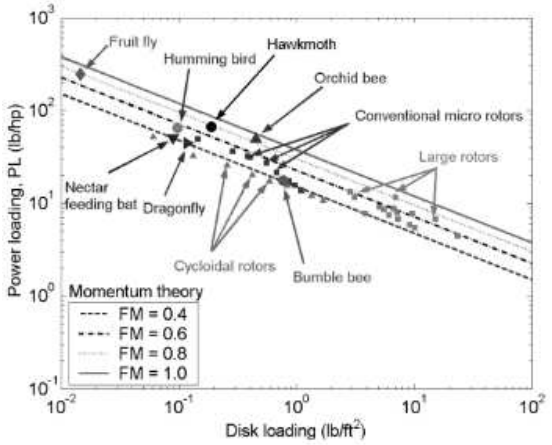

FIGURE 1.5: Rotor performance comparison between cycloidal rotors and other conventional rotorcraft systems [13].

Extensive computational and experimental research has been conducted on cycloidal propulsion systems which have been applied to Vertical Axis Wind Turbine (VAWT) applications [14–19]. VAWTs are different to Horizontal Axis Wind Turbines (HAWT) as the VAWT's rotating axis is perpendicular to the wind direction. VAWTs are not as efficient as HAWTs, but can operate effectively in highly unsteady and turbulent flows, can operate successfully regardless of the flow direction, and require less maintenance [16, 20–22]. An illustration of various VAWT configuration types are shown in Fig. 1.6. The Savonius turbine generates torque by a combination of the drag and internal forces and uses a complex blade design [23]. The Darrieus wind turbine is the most common and effective of the VAWT configurations, and its assembly normally contains three or four aerofoils to generate lift [16]. The Wollongong turbine, as visualised in Fig. 1.6b, is a new VAWT configuration which has four straight blades with their axes parallel to the main rotor axis. The blades are simple flat plates, and the blade's pitch motion is controlled via a transmission chain of bevel gears which allows for the blades to be rotated about their mid-chord axis by 180° for each full revolution of the main rotor [16]. The main advantages of the Wollongong turbine over the Savonius wind turbine is that the Wollongong wind turbine has good self-starting performance and generates higher torque. The Wollongong turbine can generate a mean total static torque coefficient of 1.09, meaning that the turbine can start well in any rotor azimuth position. The Savonius rotor can generate a mean total static torque coefficient of 0.16, meaning that its self starting capability is poorer in comparison to the Wollongong wind turbine configuration.

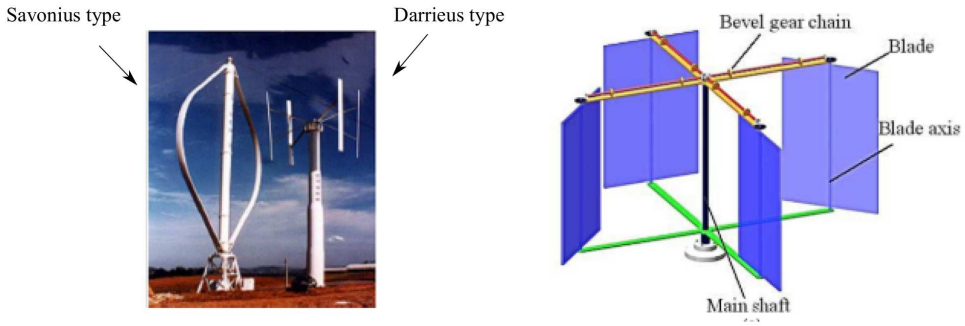

(A) Savonius and Darrieus type VAWTs [14] (B) Wollongong type VAWT [16]

FIGURE 1.6: Visualisation of various VAWT type configurations.

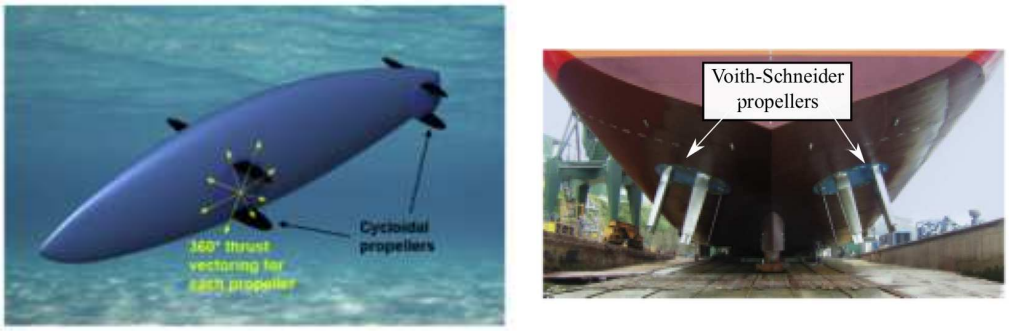

(A) Underwater vehicle [28] (B) Voith-Schneider propeller [28]

FIGURE 1.7: Visualisation of various marine vehicle applications for cycloidal rotors.

Marine type vehicles are another form of transport which cycloidal rotor propulsion systems can be applied to and have already demonstrated to be effective in operation [24–28]. The near instantaneous control of the net thrust vector means that there is no requirement for a rudder to provide yaw control. Cycloidal rotor systems such as the Voith-Schneider propeller have successfully demonstrated this extra level of control authority [24]. A visualisation of the Voith-Schneider propeller as well as an underwater cycloidal rotor vehicle concept is shown in Fig. 1.7.

Dimensionless parameters are introduced to assess the aerodynamic performance characteristics of cycloidal rotors from previous studies which include: the Thrust Coefficient, C_T and the Power Coefficient, C_P. The thrust and power coefficients are defined as:

$$C_T = \frac{T_{res}}{0.5\rho V_t^2 A} \tag{1.1}$$

$$C_P = \frac{P}{0.5\rho V_t^3 A} \tag{1.2}$$

where T_{res} is the rotor resultant thrust with units, N, P is the rotor total aerodynamic power with units, W, ρ is the air density in kg/m^3, V_t is the rotor tangential velocity in m/s, and A is the rotor disk area in metres.

Research and development of cycloidal rotor propulsion systems for aerospace applications were abandoned for approximately three decades due to interest in popularity of using jet engines to power conventional aircraft. However in 1998, Bosch Aerospace Inc [29] developed and tested a prototype Curtate cycloidal propeller for Unmanned Air Vehicles (UAVs). Finite-wing theory was applied to perform a theoretical assessment of the steady aerodynamics of the cycloidal rotor. They discovered that the number of blades that can be incorporated into the design should be as high as aerodynamically possible to maximise the active blade air time (maximise dynamic pressure acting over the blades). It was verified through computer modelling that with four or more blades, the rotor system improved stability and became less

erratic. The prototype rotor design included a chord to rotor radius ratio (c/R) and aspect ratio (AR) of 0.5 and 4 respectively. Six blades were included in the design which was calculated to be the minimum number of blades required to produce smooth and continuous thrust without excessive turbulence and inter-blade flow interference effects. At a rotor rotation speed of 650 rpm, the thrust coefficient and power coefficient were calculated to be 0.994, and 0.253 respectively.

Yun et al [30] investigated applying cycloidal propeller systems to small scale cyclocopters using NACA 0012 symmetric aerofoils. An analytical analysis was conducted using momentum and blade element theory to characterise the cycloidal rotor's aerodynamic performance by assessing the effect of varying the rotor radius and the total number of blades. Next a Computational Fluid Dynamics (CFD) analysis was performed using a moving mesh approach to simulate the rotor rotation and pitching motion of the blade, using a k-ε, low Reynolds turbulence model and was shown to validate well with the analytical results. Finally an experimental study was conducted to assess the hover state of the cycloidal rotor for a sinusoidal, low-pitch system. The main results from the study showed that a reduction in c/R from 0.375 to 0.3 resulted in an increase in C_T by approximately 16.4 %. Moreover, an increase in the total number of blades from two to six also led to an increase in C_T by approximately 61 %.

Research has also been conducted to assess whether varying the blade's geometry would have an effect on optimising the aerodynamic and power loading efficiency of cycloidal rotors. Yu, Bin, & Beng [31] developed an Unsteady Vortex Lattice Method (UVLM) to assess the changes in aerodynamic performance whilst varying cycloidal rotor design parameters including the blade taper ratio, aspect ratio and the addition of winglets. Six NACA 0012 aerofoils were used with a c/R of 0.417 and AR of 6.4. The rotational speed range varied from 250 to 1000 rpm. The results demonstrated that the blade's taper ratio does not effect the power loading efficiency, therefore having a high taper ratio would result in overall rotor weight savings and reduce the root blade bending moment. Increasing the aspect ratio led to an increase in the power loading efficiency at a constant disk-loading. The results also showed that adding winglets to the blades reduced the power loading efficiency of the cycloidal rotor as well as increasing the overall weight and blade root bending moment.

In 2008, Hwang, & Kim [32] assessed the changes in the aerodynamic performance of a cycloidal rotor using the commercial CFD package STAR-CD. The cycloidal rotor configuration was scaled for a small quadrotor with a blade pitch amplitude of 25° and rotor rotational speed of 1200 rpm. The results from the unsteady, two-dimensional CFD simulations illustrated that power loading efficiency improved by approximately 17% when the blade pivot point transitioned from 60% to 25% along the aerofoil chord line. A change in the blade pivot point results in a change to the virtual camber of the blade, which leads to an alteration of the blade's aerodynamic characteristics. The effect of virtual camber on cycloidal rotor performance will be discussed later in this

section.

Hwang et al [33] continued research in this field by developing a cyclocopter using four rotors, with elliptic blade planforms and a swash plate to improve the rotor performance and control mechanism respectively. This air vehicle was designed using CFD and Finite Element Analysis (FEA) methods as well as experimental tests to measure the vehicle's thrust and required power. The designed cyclocopter with four rotors, each containing four elliptic blades is shown in Fig. 1.8. A single rotor has a chord to rotor radius value, c/R = 0.42, and blade aspect ratio value, AR = 4.762, and can generate C_T and C_P values of 0.43 and 0.12 respectively when operating at 1,200 rpm. An elliptic blade planform was chosen to minimise the induced drag which led to a reduction in the cycloidal rotor power requirements, based on Prandtl's classical lifting line theory [34]. During the flight test, it was observed that the cyclocopter was successfully able to sustain hover flight mode.

FIGURE 1.8: Designed cyclocopter with a total of 16 elliptic blades [32].

In recent years, interest has grown in a new form of aerospace vehicle called a Micro Air Vehicle (MAV) due to their small scale, low cost for fabrication and the numerous potential applications in both civil and military sectors. MAVs operate in low Reynolds number regimes, where laminar flow mainly dominates the flight regime. Unsteady effects arising from the vehicle's flight mechanics and environmental issues such as wind gusts have a significant effect on control stability issues of MAVs. Due to this problem, the University of Maryland has studied extensively on the feasibility of employing cycloidal rotors as the propulsion system on MAVs.

The first cycloidal rotor prototype fabricated at the University of Maryland was designed and built by Belloli and Sirohi [35]. In 2005, Parsons [36] investigated a small scale cycloidal rotor to determine its feasibility as a propulsion system for MAVs. An analytical model was developed to assess the rotor performance characteristics as well as the flowfield around the cycloidal rotor, which was based on momentum theory. An experimental study was conducted to validate the analytical model for unsteady cases where the mechanism used for achieving the blade pitch motion was passive.

Extensive research has been carried out by Benedict et al [1, 13, 37–40] to further understand the aerodynamic and performance characteristics of cycloidal rotors, applied to MAVs. Benedict began focussing on optimising the performance of a micro-scale, cyclocopter through experimental Particle Image Velocimetry (PIV) studies [13]. For the PIV procedure, a recursive technique called a deformation-grid correlation algorithm was applied to the images as this was said to be more accurate for measuring the high-velocity gradients found inside the rotor wake flow. This study highlighted how the resultant thrust was obtained along with the angle made by the resultant thrust vector, as well as visualising the flow field characteristics across the rotor domain. An illustration of the time-averaged velocity measurements recorded from the PIV analysis for a 4-blade cycloidal rotor domain is shown in Fig. 1.9. The PIV flowfield highlights key flow features such as: re-circulation inside the cycloidal rotor domain and skewness of the downwash flow.

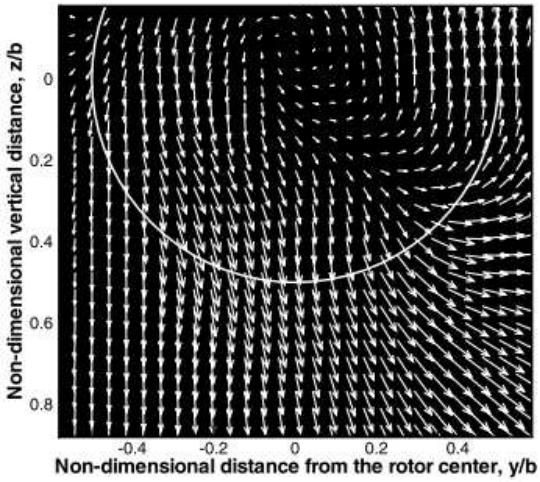

FIGURE 1.9: Time-averaged velocity PIV flowfield measurements for a 4-bladed cycloidal rotor [13].

Benedict, Jarugumilli, & Chopra [38] later conducted systematic performance measurements on a manufactured MAV cyclocopter to understand the function of the rotor geometry and blade pitching kinematics on the performance characteristics whilst in hover flight mode. The rotor parameters varied in this analysis included the rotor radius, span, chord and the blade planform whilst the aerofoil section remained fixed as NACA 0015. The total number of blades were also fixed at 4-blades. A key finding taken from this study was that trapezoidal blade planforms with moderate taper ratios improved on the cycloidal rotor's power loading efficiency in comparison to rectangular blades at higher disk loading. Experimental and computational studies were then focussed on the forward flight state to further improve on the fundamental understanding of the physics behind the lift and thrust production of the cycloidal rotor [39].

Recently, Benedict et al [40] presented a detailed design procedure and control system implementation of a quad cyclocopter in an axi-symmetric plus-shaped configuration. The vehicle was designed so that the magnitude and direction of the net thrust vector could be varied either by the rotor rotational speed or through thrust vectoring capability. A visualisation of the quad cyclocopter along with other cyclocopter configurations manufactured by Benedict et al. is shown in Fig. 1.10.

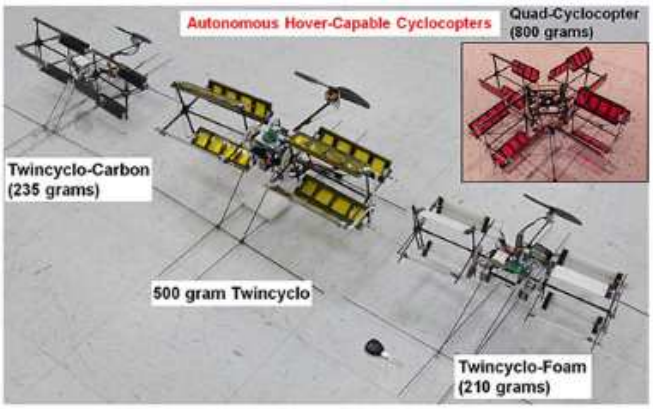

FIGURE 1.10: Manufactured quad cyclocopter, prototype, MAV [40].

Meso-scale UAVs are another vehicle application that cycloidal rotors can be adapted to which are defined by the Defence Advanced Research Projects Agency (DARPA) as between nano-scale (< 20 g) and micro-scale (100 g) in terms of weight and vehicle dimension. A visualisation of manufactured and flight tested meso-scale cycloidal rotor vehicles is shown in Fig. 1.11. There have been previous experimental and computational studies performed to assess the performance characteristics of meso-scale cycloidal rotors [2, 41–43]. Shrestha et al. [2] designed and tested a meso-scale twin-cyclocopter which consisted of two optimised cycloidal rotors and a horizontal tail rotor, as visualised in Fig. 1.11a. The horizontal tail rotor acted as an anti-torque capability to counter-act the pitching moment generated by the two cycloidal rotors spinning in the same direction. The cycloidal rotor dynamics posed an issue of gyroscopic coupling and inherent instability which was caused by a net angular momentum from the twin cycloidal rotors spinning in the same direction. The manufactured 60 g meso scale twin-cyclocopter was able to achieve stable, sustained hover successfully with an incorporated autopilot control system.

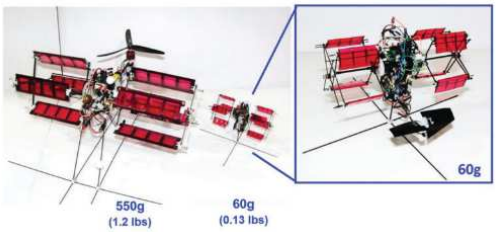

(A) 60g twin-cyclocopter [2]

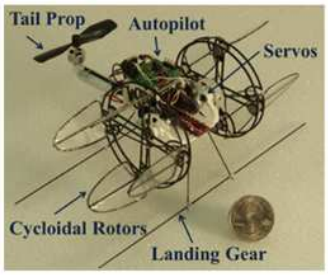

(B) 29g twin-cyclocopter with cantilevered blades [41]

FIGURE 1.11: Visualisation of various manufactured meso-scale cycloidal rotors.

Runco, Himmelberg, & Benedict [41] conducted performance and flowfield measurements on a 29 g meso-scale cycloidal rotor which was designed to operate at an ultralow Reynolds number of approximately 11,000. The design of the meso-scale cycloidal rotor was significantly different to previous models as the rotor utilised cantilevered blades which consisted of flat-plate aerofoil and a low aspect ratio elliptical blade planform. A visualisation of this 29 g meso-scale twin-cyclocopter vehicle is shown in Fig. 1.11b. The PIV flowfield measurements showed that for this specific configuration, the cycloidal rotor is highly three-dimensional and unsteady.

The wide range of aerospace applications of cycloidal rotors has been further demonstrated by other researchers such as Xisto et al [44, 46–48]. Most numerical analysis studies on cycloidal rotors have been applied to MAV scale models however Xisto et al [44] performed an unsteady, two-dimensional CFD analysis on a larger scale cycloidal rotor, which could potentially be applied to vehicles such as light-weight aircraft. Xisto [44] assessed changes in geometrical parameters to observe the changes in the PL efficiency against DL. The parameters assessed in this computational study included the variation of the symmetric aerofoil profile thickness and the total number of blades. The results obtained from the CFD simulations were validated against experimental data taken from the IAT21 L3 Cycloidal Rotor configuration [45]. It was concluded that there was an increase in C_T as well as a decrease in C_P when the aerofoil profile increased from NACA0006 to NACA0018 across the rotor rotational velocity range (200 to 800 rpm). This is due to a reduction in the re-circulation zone size when the blade operates at the rotor upper half for the larger aerofoil thickness profile. Figure 1.12 visualises the relative velocity streamlines for the four NACA 4-series aerofoils assessed which illustrates a reduction in the re-circulation zone for an increase in the aerofoil thickness profile [44]. When increasing the total number of blades from two to six, there is an increase in C_T however there is also an increase in C_P as a result of an increase in the level of blade-wake interference.

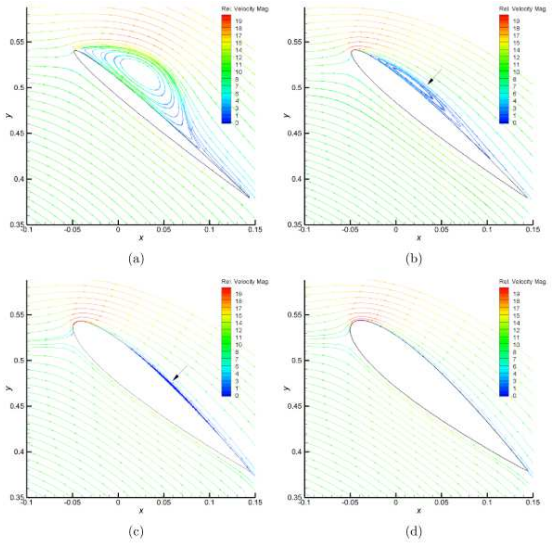

FIGURE 1.12: Relative velocity streamlines which visualise a reduction in the recirculation zone for an increase in aerofoil thickness [44]. a) NACA0006; b) NACA0010; c) NACA0015; d) NACA0018.

Xisto et al [46] also conducted the first study, in which plasma actuators were modelled to assess the changes in deep dynamic stall conditions, experienced by cycloidal rotors. In this study, a CFD analysis of a cycloidal rotor with single and multi-Dielectric Barrier Discharge (DBD) plasma actuators for active flow control was performed. The design parameters for the cycloidal rotor were taken from the IAT21 D-DALUS concept as shown in Fig. 1.13. The results from the unsteady, two dimensional CFD simulations showed that using multi-DBDs could be superior than using a single DBD plasma actuator for delaying dynamic stall and obtaining a faster reattachment of the flow across the blade.

FIGURE 1.13: IAT21 D-Dalus UAV concept [46].

Both studies conducted by Xisto, relating to varying the geometry parameters of the cycloidal rotors as well as applying plasma actuators to assess the aerodynamic performance characteristics, formed a part of the extensive Cycloidal Rotor Optimised for Propulsion (CROP) project, led by Pascoa [47]. The CROP report, published in 2015, outlined in significant detail the numerical and experimental research conducted on cycloidal rotor propulsion for a wide range of potential applications.

Schwaiger, & Wills [48] presented experimental test results for D-Dalus concepts with an example being the L3. The 6-blade L3 cycloidal rotor has a blade span to rotor radius (b/R) equivalent to 2. The calculated C_T and C_P based on a rotor rotational velocity of 1,000 rpm were 0.704 and 0.393 respectively. This model is based on a four rotor cyclogyro propulsion system which is integrated onto an aerodynamic winged body. A key application for this type of aerospace vehicle is a lightweight VTOL passenger aircraft.

EVALUATION OF PERFORMANCE PARAMETERS ON CYCLOIDAL ROTOR PERFORMANCE

There have been numerous computational and experimental studies that have investigated important characteristics of a cycloidal rotor system including: the virtual camber effect, optimising the cycloidal blade's aerofoil geometric profile, ground effect on cycloidal rotor performance, three dimensional effects of cycloidal rotor performance, and the effect of asymmetric pitching kinematics on the cycloidal rotor performance. Details of the previous studies on the various cycloidal rotor characteristics is discussed next.

The virtual camber effect is related to the effect of flow curvature experienced by a cycloidal rotor blade as it performs a trajectory profile with an orbital motion. The orbital motion experienced by the cycloidal rotor blade exposes the aerofoil to a curvilinear flow which results in the aerofoil's performance behaviour altering in comparison to the same aerofoil's performance in a rectilinear flow [49]. A visualisation of the virtual camber effect is shown in Fig. 1.14.

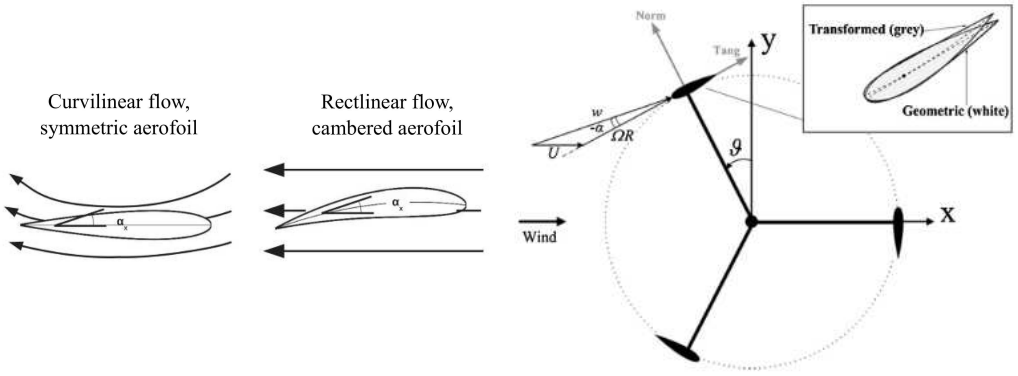

(A) Differences between curvilinear and rectilinear flow [50]

(B) Differences between virtual camber geometry and rigid geometry [51]

FIGURE 1.14: Visualisation of the virtual camber effect generated by cycloidal rotors.

There have been previous studies investigating the effect that virtual camber has on the blade performance for both cycloidal rotors and VAWTs [50–52]. Rainbird et al [51] investigated the effects of virtual camber for VAWT applications using experimental, computational, and analytical methods. Wind tunnel testing was performed for three different aerofoil geometries: a NACA0018 symmetric aerofoil and two cambered aerofoils which represented the virtual camber of the NACA0018 aerofoil at two different c/R ratios. The flow of the wind tunnel represented rectilinear flow conditions. An unsteady CFD analysis was also performed for the three aerofoil geometries assessed and was simulated in a curvilinear flow which had a rotor motion profile applied similar to a typical Darrieus VAWT motion profile. The results showed that a lower c/R value of 0.114 produced similar C_P values between the symmetric NACA0018 and transformed aerofoils across the rotor rotational velocity range assessed. An increase in c/R from 0.114 to 0.25 resulted in an increase in the level of C_P absorbed by the cambered aerofoil at the rotor upper half in comparison to the symmetric NACA0018 aerofoil which highlighted the significance of the virtual camber effect.

Jain, & Abhishek [50] developed an analytical method to model the effects of virtual camber, which determined the shape of an effective camber aerofoil in a rectilinear flow from a symmetric aerofoil exposed in a curvilinear flow. Corrections were applied to the lift, drag, and moment coefficient to take into account the effect of virtual camber, and the aerodynamic forces were derived using thin aerofoil theory. There was a better agreement in C_P between the analytical and experimental results when applying the virtual camber correction to the aerodynamic coefficients. There was an under-prediction C_P when the virtual camber correction was not applied to the aerodynamic coefficients.

Zhang, Hu, & Wang [52] investigated the effect that variation of the aerofoil camber has on the performance of cycloidal rotors at MAV scale. Both experimental and computational studies were performed on 11 different aerofoils: five cambered aerofoils, a single symmetric aerofoil, and five inverse camber aerofoils. The results showed that cycloidal rotor blades with large positive camber produced the lowest hovering efficiency, however both the symmetric aerofoil and the low inverse camber aerofoils achieved the highest hovering efficiency. The large positive camber aerofoils were also shown to increase the intensity of the blade vortex interaction (BVI) at the lower half of the cycloidal rotor in comparison to both the symmetric and low inverse camber aerofoils. The authors also suggested that deformable camber could be introduced to improve the aerofoil performance at different rotor azimuth angles.

Tang et al [53] applied an optimisation design method to optimize the geometry of a NACA0012 aerofoil profile in order in improve on cycloidal performance characteristics such as the Figure of Merit (FM) which relates C_T to C_P. The optimization technique was applied for a cycloidal rotor operating in hover conditions at a single rotor rotational speed of 1200 rpm. A class-function/shape-function transformation

parametrisation method was used to define the aerofoil geometric profile with different parameters such as: the leading-edge radius, the aerofoil maximum thickness, the aerofoil boat-tail angle, and the trailing-edge thickness. Sample points in the design space were selected using the Latin hypercube design methodology. The sample data aerodynamic performance characteristics of the cycloidal propeller were obtained using RANS CFD with a sliding-mesh technique. The sample data was then applied to a surrogate model which was based on the kringing model, therefore reducing the computational costs from running further CFD simulations. The FM was assigned as the objective function and a genetic algorithm method was utilised to determine the optimised aerofoil in the design space. The results from the study showed that the maximum thickness of the optimised aerofoil was larger in comparison to the baseline NACA0015 aerofoil. The optimised aerofoil also had a small amount of positive camber applied (about 0.5 %) which indicates that a positive camber aerofoil may lead to better cycloidal rotor performance in comparison to using symmetrical aerofoil profiles. The optimised aerofoil was able to achieve an increase in the FM by approximately 18 % in comparison to the baseline aerofoil at the designed rotational speed. Moreover, the level of reduction in C_P increased for an increase in the rotor rotational velocity.

Habibnia, & Pascoa [4] performed a numerical study investigating the ground effect for an operational six bladed cycloidal rotor in take-off and landing phases. The downwash flow produced by the cycloidal rotor sheds as it leaves the bottom half of the rotor and this large volume of flow can have a significant effect on the cycloidal rotor UAV's operational functionality, especially near ground level [4, 54]. Two-dimensional CFD modelling was performed using the RANS equations with $k-\omega$ SST turbulence modelling as it better represents the flow characteristics of blade interactions and ground effects [55]. Various parametric conditions were assessed including: vertical distance from the ground, maximum pitching amplitude, and the rotor rotational velocity, in order to gain a better understanding of the downwash flow impact. The effect of the vertical distance from the ground, H_{ground}, on the cycloidal rotor performance was assessed through the dimensionless parameter, H_{ground}/R. The range of H_{ground}/R values assessed were 6.25 to 37.5. The CFD results showed that the most efficient operational conditions for the cycloidal rotor at close-ground attitude is at a pitch amplitude of 30 degrees and a rotor rotational velocity of 200 rpm. The results also showed that the vertical distance of the cycloidal rotor vehicle significantly effects the efficiency of the rotor producing thrust. Across the rotor rotational velocity range at 40 degrees pitch amplitude, the lowest H_{ground}/R value of 6.25 generated the largest levels of C_T in comparison to the largest H_{ground}/R value of 37.5.

The flow characteristics of cycloidal rotors are inherently three-dimensional, especially when end plates are not applied to the rotor design. It has previously been demonstrated that two-dimensional experimental and computational modelling can predict the time-averaged cycloidal rotor performance characteristics well, however the effects of the blade tip vortices (BTV) are neglected [5, 56]. Hu, Zhang, & Wang [5]

conducted a computational study of a MAV scale cycloidal rotor to understand the effects of the three-dimensional flow modelling of a cycloidal rotor. The operational range of the Reynolds number was between 20,000 to 80,000, and the $k-\omega$ SST turbulence model was used with a low Reynolds number correction applied. Four different structured mesh configurations were assessed: two-dimensional, 2.5 dimensional with periodic boundary conditions applied at the end faces, three-dimensional of a half bladed rotor, and three-dimensional of the full rotor. The sliding mesh technique was utilised to model the pitching motion of the blades as well as the rotor motion. The key findings from the study showed that although the time-averaged results between the two-dimensional and three-dimensional mesh configurations were similar, the flow structure mechanisms were different. The two-dimensional simulations with large pitching amplitudes showed the production of leading-edge and trailing-edge vortices due to dynamic stall which leads to parallel blade-wake interactions and the fluctuation of aerodynamic forces at the lower right quarter of the rotor region. The flow structure for the three-dimensional simulations is also dominated by dynamic stall and blade-wake interference, however dynamic stall along the span was smoother, meaning that the parallel blade-vortex interactions were weaker. It was also shown that no aerodynamic fluctuations were observed at the lower right quarter of the rotor domain; the fluctuations were present for the two-dimensional simulations. The three-dimensional model also predicts the side-force better than the two-dimensional model as the three-dimensional model captures spanwise blade wake interactions which induces cross flow in the lower half of the rotor domain. This effect is neglected when performing two-dimensional simulations.

Dekterev et al [57] also performed a three-dimensional computational study to investigate the effects that open and closed end plates have on the cycloidal rotor performance characteristics as well as the flowfield structure. A comparison between two-dimensional and three-dimensional computational modelling was made using a URANS solver with the $k-\omega$ turbulence model. The results from the study showed similar cycloidal rotor performance characteristics were obtained between the three-dimensional and two-dimensional computational models for the closed end disk configuration. The addition of the closed end plates for the rotor resulted in a downwash flow with a more developed core structure where the flow spread is contained within the size of the rotor domain in both the span and diameter. The cycloidal rotor with open end disks (no end faces) led to a considerable amount of air suction at the blade tips, resulting in a much wider lateral flow spread. This resulted in large differences in the cycloidal rotor performance and flowfield characteristics between the two-dimensional and three-dimensional computational models. Three-dimensional computational modelling is expensive, therefore two-dimensional computational modelling to assess the cycloidal rotor performance characteristics is sufficient based on the assumption that closed end disks are included in the cycloidal rotor model design.

It has been previously shown that symmetric pitching kinematics may not lead to efficient aerodynamic performance of the cycloidal rotor, especially in forward flight as

it can lead to blade dynamic stall which results in an increase in power consumption as well as exert significant loads on the pitch control mechanism [1]. Asymmetric pitching kinematics is where a constant, mean blade pitch amplitude is applied to the pitching schedule so that the blade achieves larger pitch angles at one half of the rotor region, and lower pitch angles at the opposite half. Recent computational and experimental studies have been performed to assess the effect that asymmetric pitching kinematics has on the cycloidal rotor performance in both forward flight and hover conditions [1, 42].

Benedict, Jarugumilli, & Chopra [1] applied time-averaged performance measurements and flowfield visualisation techniques to assess the performance of asymmetric pitching kinematics for a MAV-scale cycloidal rotor in forward flight. The rotor advance ratio was varied which is defined as the ratio between the free-stream velocity to the rotor rotational (tangential) velocity. The results from the study showed that for low to moderate advance ratios, there was a significant reduction in the power absorption whilst maintaining similar rotor propulsive thrust values. A drawback from applying asymmetric pitching kinematics was that there was also a reduction in the rotor lift production compared to applying a symmetric pitching schedule. The flowfield visualisations showed that dynamic stall was produced by the upstream blade due to the implementation of highly asymmetric pitching kinematics. This resulted in the downstream blade interacting with a more significant unsteady flow environment in comparison to the symmetric pitching schedule. The azimuthal position at the which the blade-wake interaction occurred changed based on the setting used for the mean blade pitch amplitude.

Walther et al [42] also investigated the effects that symmetric and asymmetric pitching kinematics have on the aerodynamic performance of cycloidal rotors at a ultralow Reynolds number range (Re = 18,000). A combination of experimental force/flowfield measurements and computational studies were performed. For the computational method, a structured overset mesh was utilised and used the Spalart-Allmaras turbulence model for closure of the compressible URANS equations. For the experimental method, PIV was used to perform high-resolution flowfield measurements around the blades of a cycloidal rotor which were submerged in a water tank. The results from the study showed that the blade lift reduced in the upper half of the rotor due to negative virtual camber, and increased in the lower half of the rotor due to positive virtual camber. Applying asymmetric pitching kinematics so that larger pitch angles are achieved in the upper half and lower pitch angles in the lower half counteracted the rotor lift asymmetry and improved rotor efficiency due to producing a more uniform lift distribution. The authors also stated that this was the first study where the instantaneous blade forces were measured and compared against the predicted computational blade instantaneous forces. The two-dimensional computational model which was developed correlated well against the experimental measured results for both the force and flowfield characteristics.

Finally, few investigations have been conducted to assess the negative impact that dynamic stall has on the aerodynamic and power loading efficiency of cycloidal rotors [58]. Various passive and active methods that can be implemented to mitigate the negative effects of dynamic stall and could potentially be implemented in a cycloidal rotor system are discussed in the next section.

1.1.2 ALLEVIATING THE NEGATIVE EFFECTS OF DYNAMIC STALL USING PASSIVE AND ACTIVE FLOW CONTROL

INTRODUCTION TO DYNAMIC STALL

The majority of research performed on cycloidal rotor's performance has not assessed how to mitigate dynamic stall, which can have a detrimental effect on rotor performance. Dynamic stall is a complex phenomenon associated with unsteady aerofoil pitching motion and produces large hysteresis effects on the aerofoil's aerodynamic parameters during the pitch cycle. Dynamic stall occurs at larger incidence angles for a pitch oscillating aerofoil in comparison to the static aerofoil stall which results in a larger loss of lift during the stall process, with associated increases in drag and negative pitching moment [59–61]. Dynamic stall occurs on the helicopter's retreating blade at high advance ratios, resulting in fatigue and structural vibration issues [62–64]. The problems of retreating blade stall for helicopter rotor blades are not as severe for cycloidal rotors, implying that the rotor can operate at larger levels of forward flight speed [46]. However, the significant unsteady pitching nature of the cycloidal rotor blades still make it susceptible to dynamic stall.

The dynamic stall process for pitch oscillating aerofoils has been investigated extensively over the last few decades and is briefly described here. An illustration of the dynamic stall process and its effect on the normal force and pitching moment coefficient is shown in Fig. 1.15 [60]. Initial signs of flow separation appear on the aerofoil's aft upper surface and travel upstream towards the leading-edge during the upstroke phase of the pitch cycle. Near the end of the upstroke, the reversed flow (adverse pressure gradient) reaches the leading-edge resulting in the formation of a strong leading-edge vortex (LEV). Shortly afterwards, the LEV convects across the aerofoil's upper surface towards the trailing-edge, resulting in a positive contribution to dynamic lift past the static stall angle. When the LEV reaches the trailing-edge, strong suction is developed on the lower surface of the trailing-edge. This leads to the formation of a strong counter-rotating trailing-edge vortex (TEV) which triggers the separation of the LEV, and the initiation of the severe moment stall. This is followed by the beginning of the lift stall and significant flow separation. The flow remains separated for the majority of the pitch down-stroke until flow reattachment occurs before the start of the upstroke [65]. For a further detailed description of the dynamic stall process for helicopter rotors, the reader is referred to the work of Leishman [66].

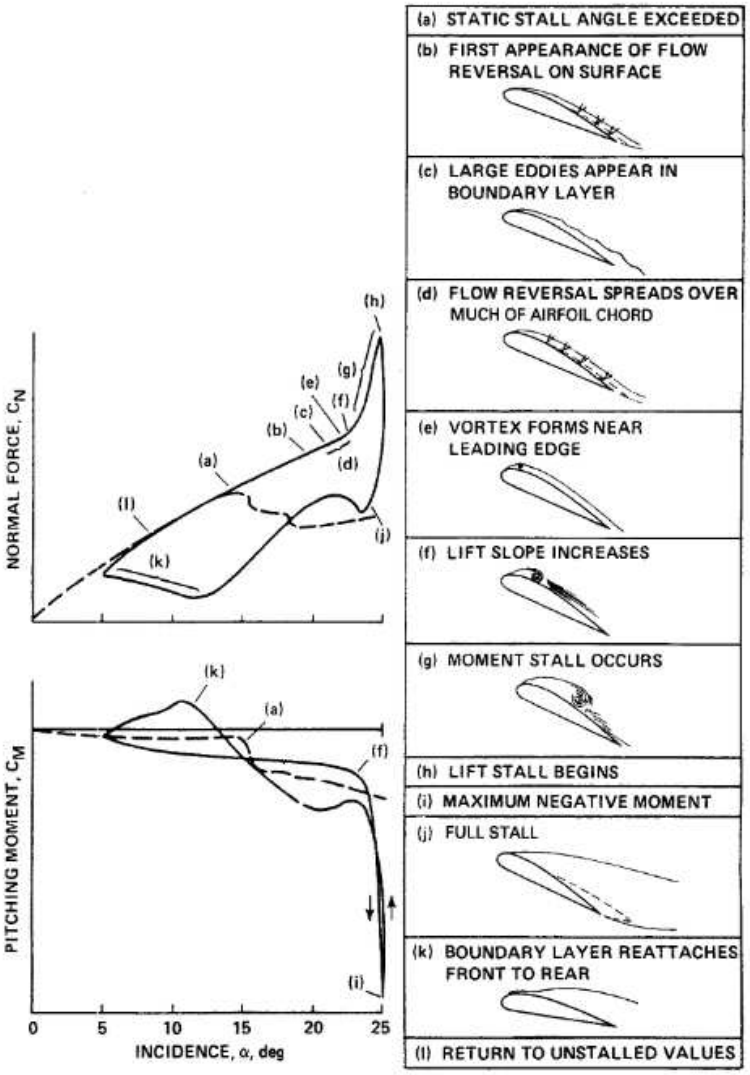

FIGURE 1.15: Dynamic stall process for a symmetric NACA aerofoil at a low compressibility Mach number range [60].

The key flow mechanism responsible for dynamic stall is the formation, convection, and separation of the LEV, which results in significant flow separation and excessive nose-down pitching moments. If the LEV could be suppressed or delayed, then the dynamic stall effect can be mitigated with a reduction in flow separation and associated improvement in the aerodynamic performance. Previous numerical and experimental research has investigated various passive and active techniques applied to oscillating aerofoils to control dynamic stall.

PASSIVE CONTROL METHODS FOR DYNAMIC STALL ALLEVIATION

Passive control methods have previously been assessed to control dynamic stall due to their simplicity to implement and proven effectiveness in mitigating the adverse effects of dynamic stall. Choudhry, Arjomandi, & Kelso [67] assessed three different passive control devices experimentally on an oscillating NACA 0021 aerofoil with operational conditions similar to wind turbine applications. The three passive control methods tested to improve the post-stall aerodynamic characteristics included vortex generators, an elevated wire concept and a circular cavity. All passive control devices were assessed individually and applied on the aerofoil's upper surface, near the leading-edge. The vortex generators yielded the most benefits in terms of less abrupt lift decay after separation and fewer post-stall lift oscillations. The circular cavity was the least effective control method as the cavity displayed no aid in flow reattachment due to its operation in the separated region during the downstroke phase of the pitch cycle. It should be noted that implementing passive control devices such as vortex generators can lead to a reduction in the lift curve slope as the incidence angle increases in the attached flow region [67]. This results in a reduction of the lift-to-drag ratio for the passive control aerofoil in comparison to the clean surface aerofoil.

ACTIVE CONTROL METHODS FOR DYNAMIC STALL ALLEVIATION

Active flow control methods are better suited in helicopter and cycloidal rotor applications to suppress the adverse effects of dynamic stall, as they only need to be actuated during specific phases of the pitch cycle. This would mean that the baseline aerofoil design can be used in the rotor advancing side and the active flow control applied at the rotor retreating side where dynamic stall occurs. Numerous active flow control methods have previously been investigated on oscillating aerofoils including back-flow flaps [68], active blowing techniques [69], plasma actuators [46, 70], trailing-edge flaps [71–73], and varying leading-edge droop [74–76], to determine their influence on dynamic stall control.

Gardner, Richter, & Rosemann [69] numerically investigated the effect of blowing air jets as fluidic control devices on suppressing dynamic stall. Three different jet configurations were assessed including inclined/skewed jets, tangential slot blowing jets, and vertical blowing jets, which were applied on the aerofoil upper surface, near the leading-edge. The aim of the vertical porthole configuration for the blowing jets

was to stabilise the LEV and provide an anchor point for the trailing-edge separation, limiting its travel upstream. The results demonstrated that the vertical jet configuration was the most effective case with significant reductions in the pitching moment peak of 85%, drag peak reduction of 78% and a reduction in cycle-averaged drag of 42%. The main issue with active blowing is the practicality of implementing this device in realistic operation due to the requirement constraints and heavy actuator systems required.

Another novel active flow control technique that is currently being investigated to alleviate dynamic stall effects on oscillating aerofoils is Dielectric Barrier Discharge (DBD) plasma actuators. DBD-plasma actuators control the flow by adding momentum to the fluid by means of generating an ionic wind next to the control surface [46]. Advantages of using DBD-plasma actuators include: lack of moving parts, fast response times, easy integration, and reduction in complexity.

Post, & Corke [70] conducted experiments on plasma actuators integrated into an oscillating NACA0015 aerofoil to assess its effect on improving the post-stall lift characteristics. A single actuator was used and bonded directly to the surface of the aerofoil at $x/c = 0$. The plasma actuator was orientated to produce a velocity component in the mean free-stream direction over the aerofoil's suction surface and generated a maximum velocity in the order of 2 to 3 m/s. The closed-loop control actuator achieved the greatest improvement in the lift pitch cycle, with the highest mean lift produced and elimination of the sharp lift stall that is commonly associated with dynamic stall.

Active trailing-edge flaps applied to oscillating aerofoils have also been extensively researched to alter the TEV characteristics which are highly influential on the peak negative moment and negative aerodynamic damping. Feszty, Gillies, & Vezza [71] utilised a discrete vortex numerical method on an oscillating NACA0012 aerofoil with an active trailing-edge flap accounting for 16% of the chord with the aerofoil oscillating under deep stall conditions. Only the pulsed actuated, upward (positive) flap deflections, reduced the negative aerodynamic damping and the level of reduction increased with an increase in upward flap deflection. Green, Gillies, & Wang [72] complemented the work performed by Feszty [71] by experimentally investigating the effect that the active trailing-edge flap had on alleviating the negative aerodynamic damping. Surface mounted pressure transducers were used to obtain the pressure forces and moment coefficients. The results from the experiments showed that the negative aerodynamic damping, with the peak negative moment coefficient, were significantly reduced and could be considered negligible when the flap was actuated. Gerantakos, & Lee [73] also experimentally investigated the level of dynamic stall control that could be achieved on a oscillating NACA0015 aerofoil with pre-scheduled trailing-edge flap control. PIV and surface pressure measurement techniques were used to gain an understanding of the flow control mechanisms during the dynamic stall process. It was shown that when an upward flap deflection is applied, there

is a reduction in the negative peak moment due to the increased suction pressure generated on the flap's lower surface. The downward flap deflection increased the maximum lift coefficient due to flap-induced camber effects, however this led to an increase in the peak negative moment coefficient.

Although trailing-edge flaps have been shown to mitigate the impact of dynamic stall on oscillating aerofoils after the formation of the LEV, active camber change could be applied at the leading-edge to suppress the full formation of the LEV. Chandrasekhara, Martin, & Tung [74] experimentally investigated the effect that fixed droop and variable droop leading-edges had on dynamic stall control under compressible flow conditions. A VR-12 aerofoil was used as the test model, with a chord and span of 15.2 cm and 25 cm respectively. The leading-edge droop section covered 25% of the chord. The results from the Variable Droop Leading-Edge (VDLE) aerofoil were shown to decrease the peak suction pressure coefficient from -7.92 to -3.46, relative to the 0 deg droop case. This resulted in a flatter pressure distribution which suggests that high lift is still being produced during the downstroke phase of the cycle. It was also shown that the VDLE aerofoil delayed the onset of dynamic stall and achieved large reductions in the drag and moment coefficients, ranging from 50% to 75%. Martin et al [75] applied a numerical code based on the approximate factorisation implicit methodology with deforming grid capability to evaluate the effect that VDLE aerofoils have on alleviating dynamic stall. For a free-stream Mach number of 0.3, the reduction in Cl_{max}, Cd_{max}, and Cm_{min} were 11%, 72%, and 68% respectively, when the VDLE nose section was deflected. It was highlighted that having a sharp transition on the hinge line at the leading-edge upper surface could result in a significant modification of the boundary layer which could lead to dynamic stall. Bain et al [76] included modelling of the wind tunnel wall effects in the numerical analysis, which was shown to improve on the accuracy of the aerodynamic results, in contrast to modelling the onset flow as uniform free-stream conditions. The CFD results were shown to under-predict the peak magnitude in lift, however the model was able to accurately simulate the delay of the dynamic stall onset.

INTRODUCTION TO MORPHING

More recently, morphing structures such as compliant mechanisms have been investigated to alleviate dynamic stall on rotorcraft and is the main focus of this study. Morphing structures can also be utilized to improve the aerodynamic characteristics of fixed wing aircraft throughout the entire mission envelope. Compliant mechanisms are single-piece, flexible structures that exhibit joint-less functionality and are designed to generate the desired motions upon application of external forces [77]. The surfaces of compliant structures provide a smooth aerodynamic contour that is free of steps and discontinuities normally linked with traditional joints [78, 79]. The design process for compliant mechanisms takes the following parameters into account: shape morphing requirements, the power required to achieve the target deflection, actuator packaging issues, durability, and dynamic performance. This presents many

challenges when designing an adaptive control surface for a rotorcraft blade due to the limited space available, weight constraints, and centrifugal loads exerted on the structure periodically.

Kota et al [78] assessed various compliant mechanism devices to efficiently morph fixed wing aircraft to improve on the aerodynamic performance throughout the mission envelope. Three different compliant mechanisms were evaluated including a variable leading-edge flap, a variable trailing-edge flap, and high frequency vortex generators with compliant motion amplifiers. The primary goal of the compliant leading-edge flap is to maintain structural integrity under extreme aerodynamic loading without any penalties in weight and aerodynamic performance. A structural optimisation algorithm was used to generate the design of the compliant structure which possesses maximum stiffness relative to the external loads and minimum stiffness relative to the intended deformation. It was shown that the compliant leading-edge flap maintained structural integrity while achieving a weight reduction; in contrast to the conventional leading-edge flap. Xinxing et al [80] designed and tested a compliant leading-edge flap for UAV applications. The Solid Isotropic Material with Penalization (SIMP) method was used for the topology optimisation. It was verified through benchtop experimental testing that the compliant leading-edge flap with a symmetric laminated plate had the capability of achieving the desired shape change when compared to the topology optimisation analysis. More recently, Vasista et al [81] designed and tested a compliant morphing nose droop wing tip which was scaled for a regional aircraft. The morphing droop-nose device comprised of a fiberglass composite skin and was supported by a topology optimised superelastic nickel titanium and aluminium internal compliant mechanism.

Preliminary investigations have been performed to assess the compliant mechanism's effectiveness for rotorcraft applications, where high inertial and centrifugal loading are present. Kota et al [77] designed and tested an active compliant leading-edge structure with the aim of maintaining an optimal profile through the entire rotor azimuth. This would generate added benefits, such as delaying blade stall, improving on the forward speed, manoeuvrability, and the rotor payload capacity. The manufactured leading-edge flap could be actuated at rates up to and exceeding 6 Hz. Only benchmark testing was performed to measure the shape displacement of the leading-edge compliant structure at 0, 5, and 10 deg flap positions. The measured points were shown to validate well against the finite element analysis of the topology optimised, compliant leading-edge flap. No static or dynamic wind tunnel testing was performed to validate the predicted aerodynamic efficiency enhancement.

1.2 RESEARCH MOTIVATION

Cycloidal rotors are a novel form of propulsion system which have a geometrical design differing completely from the conventional screw propeller as the blades rotate about the horizontal axis of rotation. Key advantages of the cycloidal rotor include

360 degree control capability through variation of the net thrust vector as well as the individual blades operating under similar flow conditions across the blade span. The pitching motion of the cycloidal rotor blades however make it susceptible to dynamic stall which can lead to a significant level of blade-wake interference and loss in rotor performance. There have been few investigations conducted which have assessed the negative impact that dynamic stall has on the aerodynamic and rotor performance efficiency for a cycloidal rotor. The main aim of this study is to investigate whether dynamic stall alleviation for a cycloidal rotor can be achieved through applying active leading-edge morphing to the individual cycloidal rotor blades at the rotor region where dynamic stall occurs. The main research questions proposed for this study include:

- Does applying active leading-edge morphing to the cycloidal rotor blades at the region where blade-wake interference effects are significant have a positive effect on the cycloidal rotor's performance characteristics in comparison to a rigid blade rotor?
- Is it more beneficial to apply active leading-edge morphing to a cycloidal rotor to achieve dynamic stall alleviation in comparison to applying a simpler leading-edge fixed droop (fixed camber) solution?
- Can the effects of leading-edge morphing and leading-edge fixed droop on aerodynamic performance for a single pitch-oscillating aerofoil which are predicted by CFD also be accurately represented in an equivalent experimental leading-edge flap wind tunnel model?
- Is there a correlation in the performance benefits gained from applying leading-edge morphing to either a single pitch-oscillating or single cycloidal rotor orbiting blade?

1.3 RESEARCH OBJECTIVES

To date, there has currently not been any literature available which has assessed the performance of active camber blades on cycloidal rotor performance. The current study investigates the effect of active leading-edge morphing of cycloidal rotor blades on the rotor performance and flowfield characteristics for large-scale air vehicle applications. The main objectives of this study include:

- Investigate the effect that active leading-edge morphing of a single pitch oscillating cycloidal blade has on mitigating the adverse effects of dynamic stall at a large Reynolds number range, $Re \approx 1{,}000{,}000$.
- Perform experimental wind tunnel testing of a single pitch oscillating blade with an active leading-edge morphing flap in order to validate the effects of active leading-edge morphing on alleviating the adverse effects of dynamic stall at the large Reynolds number range, $Re \approx 1{,}000{,}000$.

- Perform a computational parametric study to investigate the effects that active leading-edge morphing of cycloidal rotor blades have on the cycloidal rotor performance and flowfield characteristics for large-scale vehicle applications under hover conditions.

Computational methods such as CFD modelling and experimental methods such as dynamic stall wind tunnel testing have been utilised to perform the analysis of the proposed research objectives.

1.4 THESIS OVERVIEW

The thesis is divided into the following sections:

Chapter 1 presents the current state of the art on cycloidal rotor performance research and dynamic stall control methods.

Chapter 2 provides a description of the computational methodology used to develop the CFD models for both a single pitch oscillating aerofoil and the cycloidal rotor CFD model.

Chapter 3 presents the findings for the CFD analysis of a single pitch oscillating aerofoil with active leading-edge morphing. A description of the mesh and physic settings used is provided. A parametric study is conducted to assess various parameters associated to leading-edge morphing with aim to characterising their effect on reducing the negative impact of dynamic stall.

Chapter 4 provides a description of the experimental methodology used to develop the dynamic stall aerofoil model with an active leading-edge flap. Details of the experimental techniques and the apparatus used is provided.

Chapter 5 presents the results from the experimental analysis for the dynamic stall aerofoil model with an active leading-edge flap at a Reynolds number, $Re \approx 1{,}000{,}000$. Both static and dynamic motion cases are assessed.

Chapter 6 presents the findings for the CFD analysis of a cycloidal rotor model with active leading-edge morphing applied. A two-dimensional, parametric study is performed to characterise the different parameters associated to leading-edge morphing and to determine it's effect on the cycloidal rotor performance and flowfield characteristics.

Chapter 7 presents the general conclusions from all research conducted in this study and recommendations for future work ideas are presented.

Appendix A presents the bill of materials for the CAD Model design discussed in Chapter 4.

Appendix B presents a derivation process of the force and moment coefficients in relation to surface pressure measurements.

Appendix C presents the pressure transducer positioning list for the leading-edge flap aerofoil model discussed in Chapter 4.

Appendix D presents the measurement uncertainty analysis for the instrumentation described in Chapter 4.

Appendix E presents the list of publications produced for the duration of this study.

CHAPTER 2

COMPUTATIONAL METHODOLOGY

2.1 INTRODUCTION

Modelling the effects of dynamic stall and the operational motion of a cycloidal rotor is difficult due to the presence of significant unsteady and complex flow features. The main flow feature characteristics of dynamic stall include the formation and convection of an LEV which separates, followed by the initiation of a secondary stall vortex before flow re-attachment occurs. Dynamic stall flow features are also present when modelling the transient motion of cycloidal rotors, however other complex flow features are also produced such as the virtual camber effect, and blade-wake interference.

Wind tunnel testing is a common method of investigating the effects of dynamic stall as well as the performance of small-scale cycloidal rotors through quantitative methods and qualitative methods. Wind tunnel testing however is an expensive approach due to the large manufacturing and operational costs. It can also limit the number of design iterations which can be assessed.

Computational Fluid Dynamics (CFD) is a numerical tool which solves the partial differential equations governing the flow physics for external and internal type flows [82]. CFD can be used to model the complex flow features of dynamic stall and cycloidal rotor operation, which is achieved through solving of the Navier-Stokes equations. The three main forms of the Navier-Stokes equations include the conservation of mass, momentum, and energy. The governing equations are discretised which allows for finding approximate solutions to the set of partial differential equations using computational methods. Transient motion effects such as the pitching motion of an aerofoil and the cycloidal rotor blade operational motion can be achieved using the overset mesh method. The overset mesh technique allows for simulating the rigid body motion of various bodies in a flow-domain through rigid body displacements of the mesh surface. Morphing effects can also be modelled in CFD which applies

deformation to the mesh surface of interest. In this chapter, a description of the numerical method used to model the effects of dynamic stall, morphing, and the cycloidal rotor operational motion is presented. The commercial CFD software package, STAR-CCM+ 12.04.010-R8, was used to conduct all CFD analysis presented in this study.

2.2 GRID STRUCTURE METHODOLOGY

The CFD grid is one of the most important factors to consider as it is used to discretize the computational domain, which the physical flow solver uses to produce a numerical solution. A finite volume method is used for this study which subdivides the solution domain into a finite number of cell-centred control volumes [83]. The flow domain is replaced with a discrete number of elements, where the governing equations which describe the flow-field behaviour are solved at each individual cell. This means the quality of the CFD grid and the time it takes to complete the simulation depends on the grid resolution at the regions of interest where complex flow physics occur. Different types of grids can be implemented as well as the types of grid refinements which are applied to increase the number of cells in the regions of interest, such as near the aerofoil wall surface boundary.

The two types of grids commonly used in the CFD analysis for various applications include structured and unstructured grids. The structured grid provides a robust and efficient method of producing a high quality grid for simple and complex grid construction problems [83]. In STAR-CCM+, directed meshing is a method for generating high quality swept meshes on CAD geometries. Directed meshing is effective in providing a structured mesh in the axial direction that is flow-aligned, resulting in better accuracy within the flow solvers [83]. Previous computational studies have adopted a structured grid approach to model dynamic stall, coupled with a dynamic mesh to represent the pitching motion [84, 85].

A type of unstructured grid method in STAR-CCM+ uses polyhedral elements which are efficient when applied to complex geometries due to easy adaptability whilst ensuring sufficient grid quality. The geometry can be represented by an unstructured grid as the cells are distributed efficiently throughout the computational domain and provides robust grid refinements at the regions of interest such as the aerofoil surface. It is common in computational aerofoil studies to adopt a hybrid mesh approach which utilises an unstructured grid for the core flow domain and a orthogonal prism layer mesher which grows normal to the direction of the aerofoil surface [7, 86].

The structured grid is better suited in problems where the axial flow direction is dominant (e.g. modelling the flow inside a channel or wind tunnel). The grid elements are arranged and constructed based on the main direction of the flow. The unstructured grid which uses polyhedral cells is better suited for cases that involves complex geometries with multiple blended parts and surfaces. It should be noted however that the polyhedral elements are dependent on the quality of the starting

surface triangulation, which means that a bad representation of the geometry surface would result in the generation of a poor quality surface/volume mesh. The structured grid is not directly dependent on the surface quality and is therefore is more likely to produce a sufficient quality mesh for most CFD problems [83].

The prism layer mesh is part of the hybrid mesh and is used to generate prismatic cells next to wall surfaces or boundaries such as the aerofoil surface. As well as achieving an increase in the near wall mesh resolution, the prism layer mesh allows high aspect-ratio cells to be used, therefore providing better cross-stream resolution without incurring an excessive stream-wise resolution. The use of the prism layer mesh also results in the reduction in numerical diffusion near the wall which significantly improves the accuracy as a result. [83].

There are multiple ways that the prism layer mesher can be controlled using the built-in mesh feature in STAR-CCM+. A wall thickness distribution method was implemented as this method constructs a structured prism layer mesh from the aerofoil surface based on the total thickness of the prism layers, the total number of prism layers, and the cell height of the initial prism layer from the boundary surface. The size of the prism layer's total thickness should be selected so that it models the boundary layer which develops across the aerofoil surface. Depending upon the Reynolds number, the boundary layer requires in excess of 10-20 prism layers in the cross-stream direction in order to accurately represent the turbulent flow profiles [83]. Setting the cell height size of the initial prism layer results in control of resolving the viscous sublayer more accurately, which leads to control of the resultant non-dimensional distance value, y^+. This allows for setting the viscous sublayer directly (low $y^+ = 1$), or for coarser meshes, a wall function can be applied which results in high y^+ values > 30 [83].

The non-dimensional wall parameter, y^+, is an important factor describing how many cells should be positioned within the boundary layer [87]. Wall functions which are used in the turbulence models are valid for a specific range of y^+. It is recommended that the first cell height should not be too large that it falls outside of the log-layer when applying wall functions [87]. In order to effectively model the boundary layer characteristics without applying wall functions, the non-dimensional wall parameter should be set to approximately, $y^+ <= 1$, to resolve the laminar sub-layer region [88]. Previous computational dynamic stall studies have fixed the first prism-layer row cell height to ensure that the calculated $y^+ < 1$ was achieved [46, 84, 86, 89]. The initial prism layer cell height has also been fixed for previous computational cycloidal rotor studies which aim to achieve the desired y^+ values below 1 [7, 44, 88].

When performing dynamic stall or cycloidal rotor studies, an alternative grid method is deployed which allows for transient motion to be applied through moving grids. Different types of grids which can incorporate transient motion include dynamic meshes, sliding interface meshes, and overset meshes. A dynamic mesh is defined as a change in the relative distance between grid points by either squeezing and stretching of cells in time to adjust to the unsteady motion of a wall boundary such as an aerofoil surface [85]. The dynamic mesh is a popular mesh method for performing computational dynamic stall studies of pitching aerofoils [84, 85]. For the sliding-interface mesh technique, the grid is split into two zones which are the rotating and stationary zones [88]. The rotating zone contains a wall boundary such as an aerofoil and the stationary zone represents the flowfield domain. Both zones are connected via a sliding-interface boundary condition. The sliding-interface mesh technique is commonly used in previous cycloidal rotor computational studies for representing the transient motion of the rotor [7, 44, 86, 88]. A visualisation of a dynamic mesh and a sliding-interface mesh is shown in Fig. 2.1.

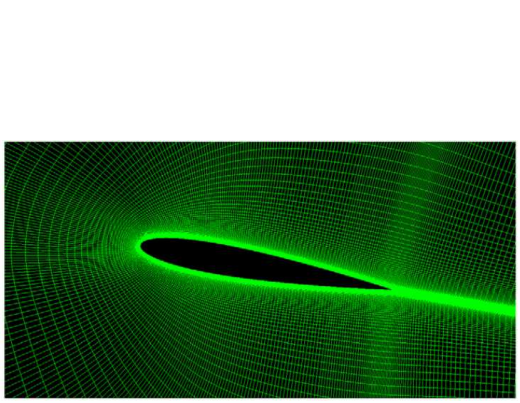

(A) Dynamic mesh [84]

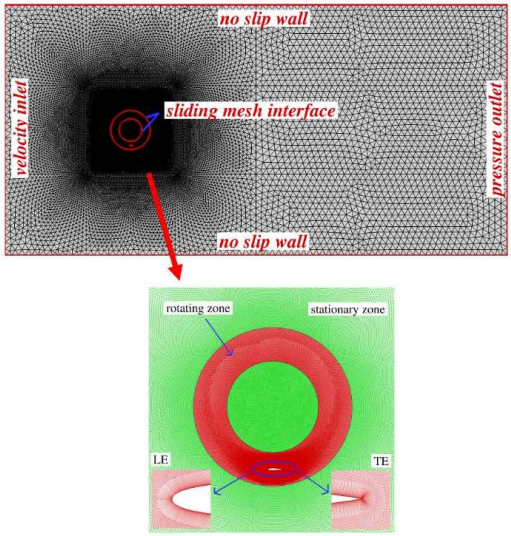

(B) Sliding-interface mesh [88]

FIGURE 2.1: Visualisation of various mesh types which can represent transient motion applications.

The overset mesh, otherwise known as a "Chimera" or overlapping mesh, is implemented in this study using STAR-CCM+, which discretises the computational domain with several different meshes that overlap each other in an arbitrary manner. They are most useful in problems involving multiple moving bodies, as well as optimisation and parametric studies [83]. A key advantage of using overset meshes is that the overset mesh does not require any modifications to the mesh if a body is rotated or translated to a new position, which offers greater flexibility over the standard meshing techniques. This is beneficial in parametric studies which involve rotating an aerofoil surface at different incidence angles which can be easily achieved using an overset mesh; a standard mesh would need further modifications in order to represent the physical geometry change. The implementation of the overset mesh also allows to simulate complex body motions, such as bodies that are close together, or have large, multiple motions applied.

When implementing the overset mesh technique, the flow domain grid is split into two types of mesh: a stationary background mesh which represents the flowfield domain, and an overset mesh which contains a single body such as an aerofoil. Multiple overset meshes can be used to represent applications such as cycloidal rotor computational simulations. The overset mesh is created using an overset mesh boundary, which is the outer boundary of the overset region that transfers information between the overset mesh and background mesh through interpolation.

In an overset mesh, cells for both the background and overset grids are split into active, inactive, or acceptor cells [83]. The discretized governing equations are solved for the cells which are active. For inactive cells, no equations are solved; cells will only become active at certain points if the overset motion has motion applied [83]. The function of the acceptor cells is to separate active and inactive cells in the background region and are attached to the overset boundary in the overset region. Acceptor cells are also used to couple solutions on the two overlapping grids. Variable values at donor cells of one mesh express variable values at acceptor cells in the other mesh through interpolation. The donor cells are the active cells from the other mesh that are closest to the nearest acceptor cell.

A linear interpolation method was selected for the overset mesh which dictates the set of donor cells that are chosen as well as the number of active cells in the donor region around the acceptor cell centroid. The linear interpolation method uses shape functions spanning a triangle for two-dimensional simulations which is defined by centroids of the donor cells. This interpolation option is the most computationally expensive within the CFD solver STAR-CCM+, however it results in a robust and accurate result. A successful coupling of the overset interface between both the background and overset region results in a "hole" being cut in the background mesh. This process is defined as the hole-cutting process. After initialising the overset interface which executes the hole-cutting process, the status of the over mesh cells are determined, i.e. it is determined which cells are active or inactive.

Compared to a standard static mesh, the overset mesh method is not conservative which results in an interpolation error at the overset mesh interface leading to a mass imbalance [83]. It is therefore recommended to have a sufficient number of cells across the overlapping zone which contains at least to 4-5 layers in both the background and overset meshes. To reduce the discretisation error, the cell sizes for both the background and overset regions should be of similar magnitude in size. The coarser of the two coupled meshes determines the level of error in the interpolation. Moreover, for transient motion simulations, it is recommended that the overset region displacement within one time-step meets the following condition: when the 2nd order implicit time integration scheme is selected for time integration, the maximum movement is half the smallest cell size in the overlapping zone [83]. The 2nd order implicit scheme requires two time-steps to compute the rate of change term.

There are built-in field functions in STAR-CCM+ which can assess the constructed overset mesh, including: the overset cell status, and the overset error status. The overset cell status function highlights the status of each cell in the background and overset regions during the duration of the simulation. A visualisation of the overset cell status for the generated overset mesh models for the single aerofoil dynamic CFD model (Chapter 3) and the cycloidal rotor model (Chapter 6) is presented in Fig. 2.2.

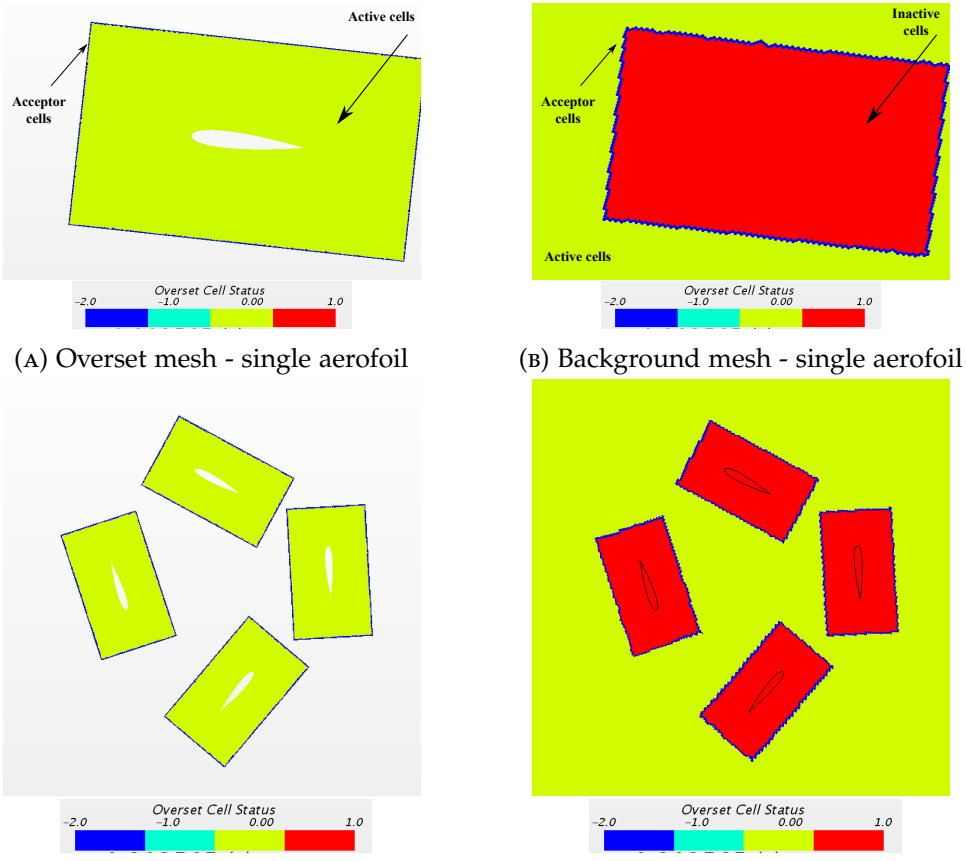

(A) Overset mesh - single aerofoil

(B) Background mesh - single aerofoil

(C) Overset mesh - cycloidal rotor

(D) Background mesh - cycloidal rotor

FIGURE 2.2: Visualisation of the overset cell status for both the single aerofoil CFD model and the cycloidal rotor CFD model.

2.3 GOVERNING EQUATIONS

Continuum mechanics is modelled in STAR-CCM+ which studies the behaviour of continua in response to mechanical forces. The fundamental laws that govern the mechanics of fluids and solids are the conservation of mass, linear momentum, angular momentum, and energy. The conservation of mass through a control volume is defined by the continuity equation as:

$$\frac{d\rho}{dt} + \frac{d}{dx_j}(\rho U_j) = 0 \tag{2.1}$$

where ρ is the density, t is the time, x_j is the j^{th} component of the position vector, and U_j is the j^{th} component of the velocity vector.

The linear momentum rate of change is equivalent to the resulting force acting on the continuum and is expressed as follows:

$$\frac{d}{dt}(\rho U_i) + \frac{d}{dx_j}(\rho U_i U_i) = -\frac{dp}{dx_i} + \frac{d\tau_{ji}}{dx_j} \tag{2.2}$$

where p is the pressure and τ_{ji} is the viscous stress tensor. The conservation of angular momentum requires that the stress tensor is symmetric. The viscous stress tensor is defined as:

$$\tau_{ij} = 2\mu S_{ij} \tag{2.3}$$

where μ is the dynamic viscosity, and S_{ij} is the mean strain-rate tensor. The mean strain-rate tensor is defined as:

$$S_{ij} = \frac{1}{2}\left(\frac{dU_i}{dx_j} + \frac{dU_i}{dx_i}\right) - \frac{1}{3}\frac{dU_k}{dX_k}\delta_{ij} \tag{2.4}$$

where δ_{ij} is the kronecker delta.

Using the first law of thermodynamics when applied to the control volume, the conservation of energy can be written as:

$$\frac{d}{dt}[\rho(e + \frac{1}{2}U_i U_i)] + \frac{d}{dx_j}[\rho U_j(h + \frac{1}{2}U_i U_i)] = \frac{d}{dx_j}(U_i \tau_{ij}) - \frac{dq_j}{dx_j} \tag{2.5}$$

where $h = e + \frac{p}{\rho}$ is the specific enthalpy and q_j is the heat flux.

The heat flux, q_j, is flow of heat per unit area and is defined as:

$$q_j = -\lambda\frac{dT}{dx_j} = -C_p\frac{\mu}{Pr}\frac{dT}{dx_j} \tag{2.6}$$

λ represents the thermal conductivity, T is the temperature, and Pr is the Prandtl number. Pr is a dimensionless quantity, which is defined as the ratio of momentum diffusivity to thermal diffusivity.

A Newtonian fluid is the simplest mathematical model to describe the viscous characteristics of liquids and gases such as water and air [83]. The Sutherland's law is commonly used for approximating the viscosity of gas which is dependent on temperature and is defined as:

$$\mu = \mu_{ref} \left(\frac{T}{T_{ref}} \right)^{3/2} \left[\frac{T_{ref} + T_s}{T + T_s} \right] \tag{2.7}$$

where μ_{ref} is the reference dynamic viscosity, T_{ref} is the reference static temperature, and T_s is the Sutherland temperature ($T_s = 110.4K$).

Boundary conditions are applied to complete the mathematical model, and enable the flow to enter or to leave the flowfield domain [83]. The main types of boundary conditions that are implemented in this study include: a velocity inlet, pressure outlet, wall, and symmetry plane. The velocity inlet allows for applying uniform or non-uniform free-stream velocity settings as well a flow direction which is either specified normal to the boundary surface, as individual angle components, or directly as flow direction angles. The pressure outlet boundary is a flow outlet boundary where the velocity at the boundary is extrapolated (velocity at the boundary is equal to the internal velocity). The wall boundary condition represents an impermeable surface that confines the fluid or solid regions such as an aerofoil surface. The no-slip condition can be applied to the wall surface when modelling viscous effects, which results in the fluid sticking to the wall and therefore has the same velocity as the wall surface. This means that for stationary flow, the velocity at the wall is at zero, however when motion is applied to the wall (e.g. pitching aerofoil), the fluid velocity at the wall matches the velocity of the moving surface. The symmetry plane boundary condition represents the imaginary plane of the simulation where the shear stress is set to zero.

Modelling the viscous flow effects at the wall boundary allows for the development of a boundary layer over the wall's surface which grows from the start of the wall surface. Due to the no-slip condition, the boundary layer at the wall surface has zero velocity and grows upto approximately 99% of the free-stream velocity, U_∞. There are two main types of boundary layer flow: a laminar flow where the airflow passes over the aerofoil surface smoothly in a stream-lined manner, and a transition to turbulent flow which results in fluctuation motions that are superimposed on the average flow velocity [90]. A laminar boundary layer generates less drag however is more susceptible to flow separation, whereas a turbulent boundary can delay flow separation from the surface. This is due to the formation of a laminar separation bubble for the clean configuration aerofoil case which allowed for the free transition

development, which was not present for the forced transition case.

Due to the different types of boundary layer flows that can be produced, it is important to determine what factors control the transition from laminar to turbulent boundary layer flow which can affect the flow separation characteristics. The transition point to turbulent flow from laminar flow moves forward with an increase in either the flow velocity or air density [90]. The transition point moves backwards for an increase in the air viscosity. The transition point to turbulent boundary layer flow is also dependent on the length of the wall surface (e.g. aerofoil chord) as increasing the chord will result in an increase in the length of region of favourable pressure gradient [90]. The Reynolds number, Re, is a dimensionless quantity which is defined as a ratio of inertial forces to viscous forces and is useful for characterising the type of boundary layer flow developed on an aerofoil surface. The Reynolds number is expressed as:

$$Re = \frac{\rho U_\infty c}{\mu} \tag{2.8}$$

where U_∞ is the free-stream velocity and c is the aerofoil chord.

The Reynolds number is used for obtaining similar flow characteristics between a wind tunnel model and full scale (known as dynamic similarity), which is required as it would not be feasible to test a full-scale wing in a wind tunnel [90]. When operating at low Reynolds numbers, the air flow over a wing's suction surface is mainly of a laminar boundary layer type, which would generate performance issues if adverse pressure gradients developed in this region. This is because the slight presence of adverse pressure gradients within a laminar boundary layer result in flow separation [91]. A significant level of laminar flow over a wing's surface is developed when operating at ($70,000 \leq Re \leq 200,000$), and the production of the laminar separation bubble can lead to performance issues as a result of flow separation [92]. The transition point moves forward for an increase in Re [90]. Richter et al [93] conducted two-dimensional CFD modelling of dynamic stall for various Reynold numbers cases above 1,000,000. The model was validated against three different experimental test cases with varying Mach number and Reynolds numbers under deep dynamic stall conditions. The Reynolds number for all of the test cases were above 1,000,000, therefore no transition strips were required to force transition of the boundary layer at the leading-edge. The CFD turbulence models used were also fully turbulent and did not require any forced transitional modelling. A comparison was made between transitional and fully turbulent CFD modelling and it was shown that there was only small changes in the transition location with an increase in incidence angle at a Reynolds number of 1,200,000.

A comparison was made between transitional and fully turbulent CFD modelling and it was shown that there was only small changes in the transition location with an increase in incidence angle at a Reynolds number of 1,200,000.

The equations of state are constitutive relations that describe the relationship between the density and the internal energy to pressure and temperature [83]. For modelling incompressible flow conditions, the constant density model is used where local change of density with respect to time in eq. (1.1-1.3) is set to zero. Compressible flow conditions can be modelled using the ideal gas law which expresses density as a function of temperature and pressure, and is defined as:

$$P = \rho R_{gas} T \tag{2.9}$$

where R_{gas} is the specific gas constant with a value of 287.1 $J/kg - K$.

The Mach number, Ma, is a non-dimensional quantity which is used to determine whether the flow conditions are incompressible or compressible and is defined as:

$$Ma = \frac{U_\infty}{a_{sonic}} \tag{2.10}$$

where a_{sonic} is the sonic velocity. The sonic velocity is defined as:

$$a_{sonic} = \sqrt{\gamma R_{gas} T} \tag{2.11}$$

Compressible flow conditions are present when the free-stream Mach number achieved is $Ma \geq 0.3$ and incompressible flow conditions can be assumed below 0.3. Many dynamic stall and cycloidal rotor CFD studies have been modelled using incompressible flow conditions when operating at a free-stream Mach number $Ma \leq 0.3$ [71, 94]. As the incidence angle increases, the flow acceleration which occurs at the leading-edge's suction surface is approximately four to five times greater than the free-stream value [60]. This means that generating high lift at a free-stream Mach number of Ma = 0.2, which would be considered as incompressible flow conditions, can result in induced sonic velocity locally on an aerofoil when pitched to high angles of attack. This also means that there may be local regions in the flow domain which are compressible (near the aerofoil suction) even though the free-stream Mach number is below 0.3. This effect has been discussed in previous dynamic stall studies [95–97].

2.4 NUMERICAL METHOD

For the numerical method, STAR-CCM+ uses a finite volume method which subdivides the solution domain into a finite number of cell-centered control volumes [83]. Discrete versions of the integral form of the conservation (governing) equations are applied to each control volume and the finite volume method transforms the mathematical model into a system of algebraic equations. This transformation also involves discretising the governing equations in both space and time. The resulting linear equations are then solved with an algebraic multi-grid solver.

All conservation equations can be expressed in terms of a generic transport equation. Through integration of the general transport equation over a control volume **V**, and by applying Gauss's divergence theorem, the discretised form of the transport equation can be obtained:

$$\frac{d}{dt}(\rho\phi V)_0 + \Sigma_f[\rho\phi(\mathbf{v}\cdot\mathbf{a})]_f = \Sigma(\Gamma\nabla\phi\cdot\mathbf{a})_f + (S_\phi V)_0 \tag{2.12}$$

where ϕ is the general transport quantity, a is the surface area vector of cell face, f, Γ is the diffusion coefficient, and S_ϕ is the source term.

The four main terms in the general transport equation as shown in eq. (2.12) from left to right are: the transient term, convective flux term, diffusive flux term, and the source term. The transient term relates to the time rate change of ϕ inside the control volume. The convective flux is defined as the net rate decrease of ϕ across the volume boundaries due to convection. The diffusive flux corresponds to the net rate of decrease of ϕ across the volume boundaries due to numerical diffusion. The source term expresses the generation/destruction of ϕ inside the control volume.

When performing transient simulations, time is the extra dimension on top of the spatial dimensions. Numerical procedures require that this extra dimension is discretised as well as the spatial discretisation which means the total time interval is subdivided into time-step increments. An implicit, unsteady, second-order temporal scheme discretisation of the unsteady term was chosen which uses the solution at the current time level, the next time-step, as well as solutions from the previous two time-steps and is expressed as:

$$\frac{d}{dt}(\rho\phi V)_0 = \frac{\{(a^2-1)[(\rho\phi V)_0^{n+1} - (\rho\phi V)_0^n] + [(\rho\phi V)_0^{n-1} - (\rho\phi V)_0^n]\}}{\alpha(\alpha-1)\Delta t^{n+1}} \tag{2.13}$$

where

$$\alpha = 1 + \frac{\Delta t^{n+1}}{\Delta t^n} \tag{2.14}$$

$$\Delta t^{n+1} = t^{n+1} - t^n \tag{2.15}$$

$$\Delta t^n = t^n - t^{n-1} \tag{2.16}$$

Note, on the initial time-step of a second-order temporal simulation, first order discretisation is applied since only two time levels are available at this point.

The values at a cell face centre are not known and are approximated through discretisation interpolation schemes linked to the convective flux and diffusive flux.

The approach in which ϕ is calculated can have a pronounced effect on the stability and accuracy of the numerical scheme [83]. A second-order upwind scheme was adopted to discretise the convective flux term which is defined as:

$$(\phi\rho\mathbf{v}\cdot\mathbf{a})_f = (\dot{m}\phi)_f = \dot{m}_f\phi_f \tag{2.17}$$

where $\dot{m}_f$ is the mass flow rate at the face.

$$(\dot{m}\phi)_f = \begin{cases} \dot{m}_f\phi_{f,0}\, for\, \dot{m}_f \geq 0 \\ \dot{m}_f\phi_{f,1}\, for\, \dot{m}_f \leq 0 \end{cases} \tag{2.18}$$

$$\begin{aligned} \phi_{f,0} &= \phi_0 + s_0\cdot(\nabla\phi)_{r,0} \\ \phi_{f,1} &= \phi_1 + s_1\cdot(\nabla\phi)_{r,1} \end{aligned} \tag{2.19}$$

where:

$$\begin{aligned} s_0 &= x_f - x_0 \\ s_1 &= x_f - x_1 \end{aligned} \tag{2.20}$$

with $\phi_{f,n}$ for n = 0 and n = 1, linearly interpolated from the cell values on either side of the cell face as:

$$\phi_{f,n} = \phi_n + (x_f - x_n)\cdot(\nabla\phi)_{r,n} \tag{2.21}$$

Variable gradients are also required to be calculated at the cell centres and at the cell-face midpoints for: construction of variable values at the cell faces; secondary gradients calculation for diffusion terms; pressure gradients calculation for pressure-velocity coupling; and strain rate and rotation-rate calculations for the turbulence models [83]. The main steps required for computing gradients in STAR-CCM+ include: computing the unlimited reconstruction gradients, limiting the reconstruction gradients, and computing the cell gradients from the limited reconstruction gradients. The Hybrid Gauss-Least Squares method was implemented for computing the gradient values which was derived as follows:

$$(\nabla\phi)_r^u = \sum_f(\phi_n - \phi_0)\omega_f^0 \tag{2.22}$$

$$\omega_f^0 = \beta_{blend}\omega_f^{LSQ} + (1-\beta_{blend})\omega_f^{GG} \tag{2.23}$$

where β_{blend} represents a blending factor which is used to determine the method to be used in computing the gradient. The Least Squares (LSQ) method is used when

$\beta_{blend} = 1$ and the Green-Gauss (GG) method is used when $\beta_{blend} = 0$. The superscript, u, is the unlimited value, ω_f^{LSQ} and ω_f^{GG} are the computed methods for the LSQ and GG method respectively.

The main issue with reconstructing face values from the unlimited reconstruction gradients is that the reconstructed face values can fall outside the range of cell values found in the neighbouring cells (connected through faces). The maximum and minimum bounds therefore have to be determined in order to set a limit for the reconstruction gradients. A scale factor, α_{scale}, is used to limit the reconstruction gradients and is defined as:

$$(\nabla\phi)_{r,n} = \alpha_{scale}(\nabla\phi)_{r,n}^{u} \tag{2.24}$$

with $\alpha_{scale} = min(\alpha_f)$ and α_f is defined as the Venkatakrishnan gradient limiter which is expressed as:

$$\alpha_f = \frac{2r_f + 1}{r_f(2r_f + 1) + 1} \tag{2.25}$$

$$\Delta_f = (x_{f,n} - x_n) \cdot (\nabla\phi)_{r,n}^{u} \tag{2.26}$$

$$\Delta_{max} = \phi_0^{max} - \phi_0 \tag{2.27}$$

$$\Delta_{min} = \phi_0^{min} - \phi_0 \tag{2.28}$$

If the limitations set for the reconstructed gradients are significantly limited, then convergences can be affected by either slowing or stalling [83]. This problem exists most often with the gradients of near-constant fields, or when the limiter cycles between 0 and 1 without settling on a convergence value. To prevent this issue, a Total Variation Bounded (TVB) gradient limiter can be applied which is derived as:

$$\delta = \psi \cdot max(\delta_{max} - \delta_{min}) \tag{2.29}$$

where δ is the additional difference that TVB allows for varying the reconstructed values, $(\Delta_{max} - \Delta_{min})$ is the largest difference between the local maximum and the local minimum anywhere in the flow simulation and ψ can vary between 0 and 1.

In STAR-CCM+, it is possible to model the motion of multiple rigid bodies in six degrees of freedom within the fluid system [83]. The mesh displacement method was implemented at the overset mesh to model both the motion for the single pitching aerofoil motion as well as the motion of a cycloidal rotor under common operational

conditions. This method can also be used to simulate morphing which results in a deforming mesh. A rotation motion is used to rotate the mesh vertices of a region around a specified axis. For a single pitch aerofoil, the specified axis is set at the aerofoil's pitch axis. For a cycloidal rotor rotational motion, the specified axis is set at the rotor centre. A rotation rate is required and can be set as a constant (e.g. cycloidal rotor rotation rate) or specified as a function of time (e.g. aerofoil sinusoidal pitch oscillation). Superposing additional rigid rotations can also be utilised in STAR-CCM+ which allows for simulating the cycloidal rotor rotational motion as well as the superimposed cycloidal blade pitch oscillation motion. A local coordinate system is required for the superimposed cycloidal blade pitch oscillation motion which is positioned at the blade's pitch axis. The rigid body motion is only applied to the overset regions and is not applied to the background region which remains stationary.

The morphing motion in STAR-CCM+ redistributes the mesh vertices in response to the movement of control points. The mesh morphing utilises control points and their associated displacements to produce an interpolation field throughout the region which can be used to displace the actual vertices of the mesh [83]. Control points can be specified using vertices that lie on mesh boundaries, and can also be specified using points that are read from a table.

The "morpher incremental displacement" is the main morpher boundary condition used in this study. This morpher boundary condition allows for setting an incremental linear displacement as well as a coupled rigid body motion. The incremental linear displacement method allows for deforming the mesh of the wall surface by reading from a table containing control points at each time-step. The control points are based on the target coordinates which are expressed as:

$$\mathbf{X}_{target} = \mathbf{X}_{current} + \mathbf{X}_{inc} \tag{2.30}$$

where $\mathbf{X}_{target}$ is the target coordinate vector, $\mathbf{X}_{current}$ is the current coordinate vector, and $\mathbf{X}_{inc}$ is the incremental displacement vector calculated at each time-step.

The rigid boundary motion option allows for combining the incremental linear displacement morphing motion with a rigid motion. This allows for applying a pitching motion to the overset mesh region to account for a sinusoidal oscillation as well as applying mesh deformation to the wall surface from the incremental linear displacement model (e.g. deforming the leading-edge section of the aerofoil surface). An illustration of applying mesh deformation to the leading-edge morphing section of the NACA0015 aerofoil is shown in Fig. 2.3a. The position of the morphing axis origin, x_{morph}/c (highlighted by the circle marker), is set to a point along the x-direction which controls the amount of the aerofoil surface that has leading-edge morphing applied. $\vec{R_{LE}}$ is the morphing displacement vector which the maximum leading-edge deflection angle, β_{max}, is applied to. Fixed points are set on the aerofoil surface at x-positions $\geq x_{morph}/c$ to restrict the aerofoil deformation to the leading-edge section

only. Morphing boundary conditions are only applied to the overset mesh regions as the background region which represents the flowfield domain remains fixed.

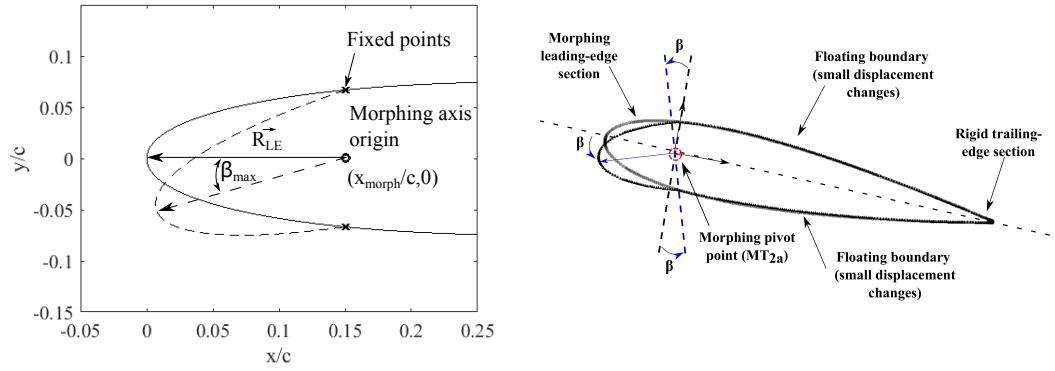

(A) Rigid boundary motion with incremental displacement mesh deformation

(B) Coupled rigid body morphing with floating boundary mesh deformation

FIGURE 2.3: Visualisation of two mesh deformation (morphing) methods used in this CFD study.

An alternative morphing method can be applied to deform the surface mesh without the need for a control point list. This reduces the computational time and also reduces the possibility of generating negative cell volumes due to stretching of long prismatic cells [83]. The alternative morphing method consists of an extra superimposed rotational rigid body motion which is applied at the leading-edge surface and has a local coordinate system (set as a morphing pivot point). The incremental linear displacement option is not used since a control point list is not required. A floating morphing boundary condition is required to be set to the remainder of the aerofoil surface which does not require mesh deformation. The floating morphing boundary condition allows for vertices on the wall surface boundary to move according to the interpolation of the displacement vector field. The mesh vertices on the boundary are not constrained therefore the vertices move in response to the interpolation field created by the morphing displacement. An illustration of the mesh displacement at the floating boundary region as a result of the leading-edge morphing section mesh deformation is shown in Fig. 2.3b. There is a small change in the node displacements at the floating boundary when adapting to the leading-edge morphing deformation, however the change is less than 0.1 % when compared against the rigid aerofoil section. The rigid trailing-edge section has no mesh deformation applied and only has rigid motion (aerofoil pitching motion) applied.

Various mesh controls were applied to ensure that the flow simulation remained stable with the applied mesh deformation as well as the superimposed rigid body rotational motions. An automatic thinning algorithm is implemented which uses an estimated deformation of the mesh to reduce (or thin-out) the number of control vertices. This can lead to a reduction in the calculation time required. A linear fitter option was also implemented which extracts a linear transformation of the prescribed

motion and uses this transformation to move vertices. This option is required for simulations which involve mesh deformation superimposed on a rigid body motion as the target coordinate vector is updated based on the rigid body displacement. Finally a morpher tolerance of 10^{-9} was set to ensure acceptable accuracy in morphing was achieved. This is due to the possibility of the morphing mesh containing extremely long and thin prism layer cells and was set to avoid the possibility of generating negative cell volumes during morphing execution.

2.5 TURBULENCE MODELLING

The majority of fluid flows are characterised by irregular fluctuating flow quantities which are usually at such small scales and high frequencies that resolving them both spatially and temporally results in excessive computational costs [83]. Turbulence models allow different approaches in modelling the small-fluctuating flow structures at a reduction in the computational cost required. Turbulence models are considered as an approximate representation of the physical phenomena of turbulence.

There are three main approaches for solving turbulent flows which include: Direct Numerical Simulation (DNS), Large Eddy Simulation (LES), and Reynolds-Averaged Navier Stokes (RANS). DNS is the most computationally expensive method as it solves the full unsteady Navier-Stokes equations for all turbulence scales and is restricted for flow simulation studies of simple geometries and low Reynolds number. DNS is therefore not practical when assessing dynamic stall conditions on a single aerofoil as well as a multi-blade cycloidal rotor study. Filtered Navier-Stokes equations are solved using the LES approach for the motion scales that are the order of the grid size and implements a turbulence model for the smaller sub-grid scale motions. The LES method is more cost effective computationally in comparison to the DNS approach. The LES approach has been applied to a dynamic stall study which had the aim of providing a reliable prediction of dynamic loads on wind turbines [85]. The author concluded that LES was capable of simulating highly separated flows under deep dynamic stall conditions within the transitional Reynolds number range. Significant computational resources were required to perform the simulations however, which can limit the number of test cases that can be performed in comparison to using the more computationally efficient RANS approach. Moreover, DNS and LES require three-dimensional models to perform the CFD computations. RANS is therefore a more suitable approach for this study as it allows for performing an detailed parametric CFD study using two-dimensional CFD models.

The RANS equations are an approximation of the Navier-Stokes equation and are obtained by a time-averaging process. The RANS turbulence models provide closure relations for the Reynolds-average Navier-Stokes equations that govern the transport of the mean flow quantities. The RANS equations are obtained by decomposing each

solution variable, ϕ, into its mean and fluctuating component as follows:

$$\phi = \overline{\phi} + \phi' \tag{2.31}$$

where $\overline{\phi}$ is the mean component and ϕ' is the fluctuating component.

The mean mass and momentum transport equations are derived as follows:

$$\frac{\delta \rho}{\delta t} + \nabla \cdot (\rho \overline{\mathbf{v}}) = 0 \tag{2.32}$$

$$\frac{\delta}{\delta t}(\rho \overline{\mathbf{v}}) + \nabla \cdot (\rho \overline{\mathbf{v}} \bigotimes \overline{\mathbf{v}}) = -\nabla \cdot \overline{P}\mathbf{I} + \nabla \cdot (\mathbf{T} + \mathbf{T}_t) + \mathbf{f}_b \tag{2.33}$$

where $\overline{\mathbf{v}}$ and $\overline{P}$ are the mean velocity and pressure respectively, $\mathbf{I}$ is the identity tensor, $\mathbf{T}$ is the viscous stress tensor, and $\mathbf{f}_b$ is the resultant of the body forces (e.g. gravity and centrifugal forces).

An additional term now appears in the momentum transport equation in eq. (1.32), which is known as the Reynolds stress tensor, and is defined as:

$$\mathbf{T}_t = -\rho \begin{bmatrix} \overline{u'u'} & \overline{u'v'} & \overline{u'w'} \\ \overline{u'v'} & \overline{v'v'} & \overline{v'w'} \\ \overline{u'w'} & \overline{v'w'} & \overline{w'w'} \end{bmatrix} \tag{2.34}$$

The main objective is therefore to model $\mathbf{T}_t$ in terms of the mean flow quantities, and therefore provide closure of the govern equations. Two basic approaches are used in STAR-CCM+: eddy viscosity models and the Reynolds stress transport models. The eddy viscosity models are used in this study due to the majority of previous dynamic stall and cycloidal rotor CFD studies implementing this approach.

Eddy viscosity models which are available in STAR-CCM+ are used to solve additional transport equations for scalar quantities that enable the turbulent viscosity, μ_t to be derived. Eddy viscosity models are based on the analogy between the molecular diffusion process and turbulent motion [83]. The most common eddy viscosity models implemented in both dynamic stall and cycloidal rotor CFD studies are the one-equation Spalart-Allmaras model and the $k - \omega$ model.

The Spalart-Allmaras (SA) one-equation turbulence model solves the transport equation for the modified diffusivity, in order to determine the turbulent eddy viscosity [83]. The SA turbulence model is suitable for flow conditions such as attached boundary layers as well as flows with mild separation, such as flow past a wing [98]. The SA model will yield the best results if these flow conditions are satisfied. Wilcox [99] concluded that the SA turbulence model is less suited for flows involving complex recirculation and body forces (e.g. buoyancy) and that two-equation models such as

the $k-\epsilon$ and $k-\omega$ turbulence models should be used instead.

The $k-\epsilon$, two-equation turbulence model solves transport equations for the turbulence kinetic energy, k, and the turbulent dissipation rate, ϵ, in order to determine the turbulent eddy viscosity. It achieves a good compromise between robustness, computational cost, and accuracy, but it is difficult to integrate through the viscous sublayer [83].

The $k-\omega$ turbulence model is a two-equation model that solves transport equations for the turbulent kinetic energy, k, and the specific dissipation rate, ω, in order to determine the turbulent eddy viscosity. The specific dissipation rate, ω is defined as the dissipation rate per unit turbulent kinetic energy ($\omega \approx \epsilon/k$). Wilcox [99] stated that the advantage of using the $k-\omega$ model over the $k-\epsilon$ model is that performance is improved for the boundary layer under adverse pressure gradients. Another key advantage is that the $k-\omega$ model can be applied throughout the boundary layer region, including the viscous sublayer region, without further requirements for modifications. A disadvantage of the $k-\omega$ model over the $k-\epsilon$ model is that the boundary layer computations are sensitive to ω values in the free-stream [83]. This problem does not exist when using the $k-\epsilon$ turbulence model.

Menter [100] addressed the issue of sensitivity to free-stream conditions for the $k-\omega$ turbulence model by recognising that the ϵ transport equations from the standard $k-\epsilon$ model could be transformed into an ω transport equation by variable substitution. This approach results in blending the $k-\epsilon$ model in the far-field with the $k-\omega$ model near the wall (viscous sublayer region). Menter [100] also introduced a modification to the linear constitutive equation and named the model containing the modifications as the $k-\omega$ SST (Shear-Stress Transport) model. The $k-\omega$ SST model has been frequently implemented in dynamic stall studies and has shown to achieve good qualitative agreements with experimental data in regions such as the formation of the primary LEV. The $k-\omega$ SST model has also been effective in previous cycloidal rotor studies as it achieved similar performance curve trends when compared against experimental results.

The SA model has previously been implemented in cycloidal rotor studies and has shown to provide a better match against experimental results in comparison to a two-equation model such as $k-\omega$ SST [7]. When compared against experimental results, the SA model was shown to over-predict rotor thrust as well as under-predict rotor power consumption, although similar performance curve trends were captured [7, 44]. Richter et al [93] conducted a comparison study of different grid types (structured/unstructured) as well as different turbulence models with the aim of improving the two-dimensional predictions of dynamic stall for a single aerofoil. It was shown that computations were significantly sensitive to the numerical discretisation and that only the $k-\omega$ SST model was able to achieve reasonable grid convergence; the SA model could not achieve this. It was also demonstrated that the SA turbulence model achieved good qualitative predictions of the primary dynamic stall event (LEV

formation), however suffered when predicting the secondary stall events. The $k-\omega$ SST model however achieved a good qualitative prediction for both the primary and secondary stall events, however was unable to predict the re-attachment phase during the pitch downstroke.

The $k-\omega$ SST turbulence model will therefore be implemented when performing CFD modelling of dynamic stall and cycloidal rotor motion, both with active leading-edge morphing deformation applied. The mean transport equations for the turbulent kinetic energy, k, and the specific dissipation rate, ω, are derived as:

$$\frac{\delta}{\delta t}(\rho k) + \nabla \cdot (\rho k \overline{\mathbf{v}}) = \nabla \cdot [(\mu + \sigma_k \mu_t)\nabla k] + P_k - \rho * f_{\beta^*}(\omega k - \omega_0 0) + S_k \tag{2.35}$$

$$\frac{\delta}{\delta t}(\rho \omega) + \nabla \cdot (\rho \omega \overline{\mathbf{v}}) = \nabla \cdot [(\mu + \sigma_\omega \mu_t)\nabla \omega] + P_\omega - \rho * f_{\beta^*}(\omega^2 - \omega_0^2) + S_\omega \tag{2.36}$$

where σ_k and σ_ω are the model coefficients, P_k and P_ω are the production terms, f_{β^*} is the free-shear modification factor, f_β is the vortex-stretching modification factor, S_k and S_ω are the user-specified source terms, and k_0 and ω_0 are the ambient turbulence values that counteract turbulence decay [101].

2.6 CONCLUSIONS

There are many complex flow features associated with dynamic stall and the operation of cycloidal rotors due to the presence of significant unsteady and complex flow characteristics such as blade-wake interference. Computational fluid dynamics modelling can be used to simulate the effects of dynamic stall for a pitch oscillating aerofoil as well a simulating the transient motion of a cycloidal rotor.

A description of the CFD method used in this study was presented in this Chapter. The Navier-Stokes governing equations are solved using a discretised unstructured grid. A hybrid mesh is selected which is a combination of a polyhedral core mesh and a structured prism layer mesh on the aerofoil surface. A structured prism layer mesh is used to model the boundary layer effectively as well as adequately resolving the viscous sublayer region without the use of wall functions. Rigid body rotations are implemented in the CFD model using the built-in motion method which is applied to the overset mesh region containing the aerofoil. The built-in morphing method is also implemented in the CFD model which allows for applying deformation to the mesh surface, either using a specified control points list or through a superimposed rotational motion. The flow is modelled as compressible as it is expected that local compressibility effects will be present at the aerofoil's suction surface when operating under dynamic stall conditions. A comparison of different turbulence eddy viscosity models is provided and the $k-\omega$ SST model was deemed to be the most suitable

model to use due to the results obtained from previous dynamic stall and cycloidal rotor computational studies.

CHAPTER 3

CFD ANALYSIS - ACTIVE LEADING-EDGE MORPHING OF A SINGLE PITCH OSCILLATING AEROFOIL

3.1 INTRODUCTION

A two-dimensional, unsteady CFD analysis is performed for an active leading-edge morphing NACA0015 aerofoil, pitching under deep dynamic stall conditions. Various input parameters from the CFD model developed in Chapter 2 such as the geometry, surface and volume mesh strategy are used as a reference for performing the dynamic motion mesh sensitivity analysis. The main objective of this study is to assess the effect that active leading-edge morphing has on alleviating the adverse effects of dynamic stall such as the significant loss in lift as well as the large increase in the drag rise and negative pitching moment. The results obtained from this CFD study are used as a reference for design of the experimental wind tunnel model for a NACA0015 aerofoil with an active leading-edge flap as discussed in Chapter 4.

This CFD analysis consists of a detailed parametric study which contains various sections. A description of the mesh construction method is provided as well as the CFD input settings used to set up the flow physics. Before performing the parametric study, a grid independence and temporal independence study is conducted to determine the adequate grid and time-step settings. The results from the grid and temporal independence study are compared against experimental wind tunnel results for a NACA0015 aerofoil model, pitching under deep dynamic stall conditions.

For the parametric study, multiple parameters are assessed to obtain detailed information relating to the effect that leading-edge morphing has on the dynamic stall control characteristics. First, the leading-edge morphing amplitude is varied over a range of angles and compared against the aerodynamic performance results produced by a rigid NACA0015 aerofoil. A comparison is then made against active leading-edge morphing and leading-edge fixed droop for a single leading-edge morphing amplitude to compare the differences in dynamic stall alleviation. Next, a study

into increasing the proportion of aerofoil chord which has leading-edge morphing applied is assessed. Moreover, an evaluation of different morphing strategies is also investigated to determine the change in dynamic stall control characteristics. Finally, the effect of varying the reduced frequency is evaluated to determine the effect of leading-edge morphing on the pitching flow unsteadiness characteristics.

3.2 MODEL DESCRIPTION

A description of the input conditions used for setting up the CFD model to simulate a two-dimensional, unsteady pitching aerofoil with active leading-edge morphing deformation is provided here.

3.2.1 Geometry

The geometry implemented in this CFD model such as the aerofoil, overset boundary, and the flowfield domain is the same as the geometry used in the CFD model discussion in Chapter 2. An illustration of the coordinate axis system defined for this study is shown in Fig. 3.1. The lift force, L, is defined positive in the positive y-direction and the drag force, D, is defined positive in the positive x-direction. The aerofoil pitching moment, M, has the origin located at the quarter chord (denoted as M_{qc}), and is defined positive in the clock-wise direction. The aerofoil incidence angle, α, represents the angle between the aerofoil's chord-line and the free-stream velocity, U_∞, and is defined positive in the clock-wise direction. There is another coordinate axis system shown in Fig. 3.1 which is positioned ahead of the aerofoil pitch axis coordinate system which represents the leading-edge morphing axis system. The leading-edge morphing axis system is used for applying deformation of the aerofoil leading-edge and this axis system is fixed to the region of the leading-edge flap. This results in the morphing axis system rotating relative to the pitch axis coordinate system. A more detailed description on setting up the leading-edge morphing model is provided in Section 3.2.4.

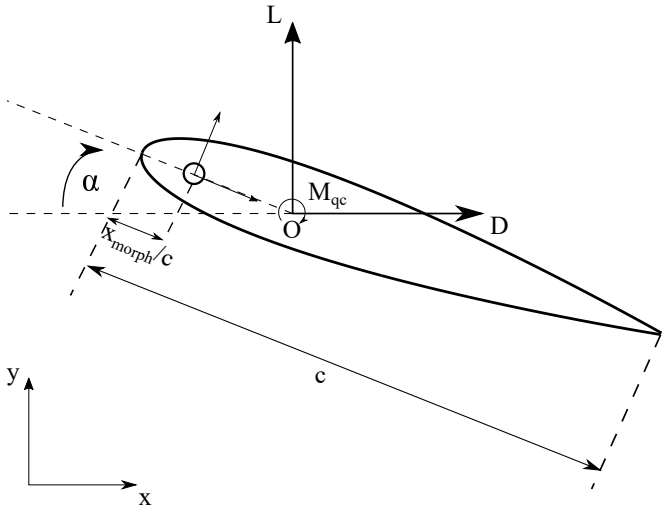

Figure 3.1: Illustration of the single aerofoil pitch axis coordinate axis system and leading-edge morphing axis system.

3.2.2 Mesh

A two-dimensional hybrid mesh was constructed, consisting of an unstructured polygonal mesher and a structured prism layer mesher applied at the aerofoil surface, which is used to effectively model the boundary layer characteristics. A cartesian rectangular grid was applied to both the flowfield (background) and overset boundary domain as shown in Fig. 3.2. The background boundary was extended 40 chord lengths downstream to ensure that the appropriate boundary conditions were satisfied [86]. Simulating dynamic stall on a pitch oscillating aerofoil was achieved using the overset mesh technique, commonly known as a chimera mesh. A detailed description of the setup procedure for generating an overset grid is provided in Chapter 2. The overset mesh technique allows for transient motion to be applied, for example, sinusoidal oscillations to a solid boundary such as an aerofoil.

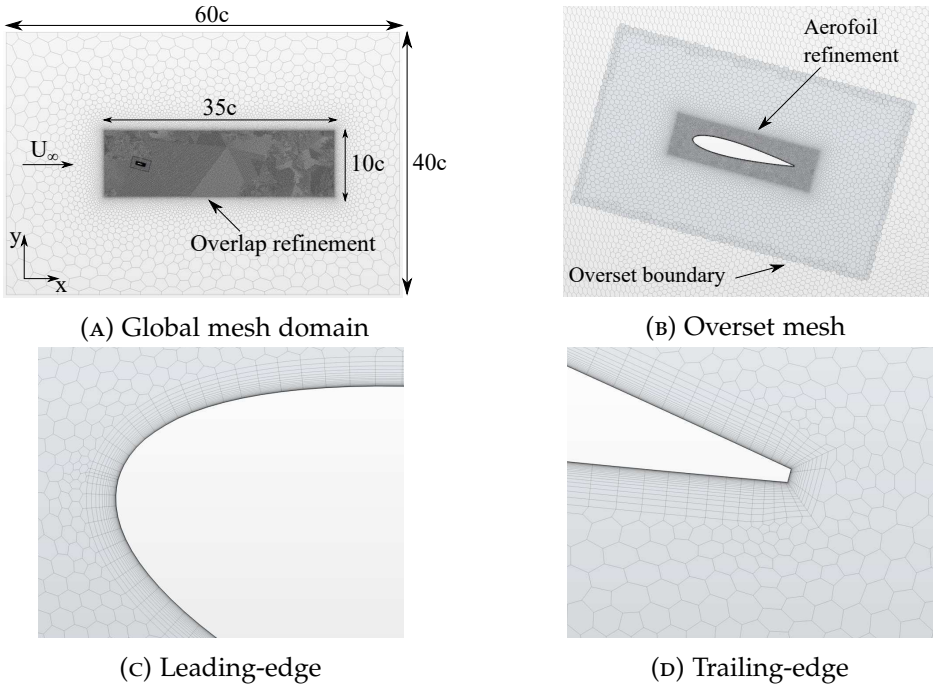

(A) Global mesh domain

(B) Overset mesh

(C) Leading-edge

(D) Trailing-edge

FIGURE 3.2: Global mesh domain and overset mesh visualisation. Grid, G_3, used as the example.

A single volumetric refinement control was applied to the background and overset meshes in order to increase the density of cells near the wall boundary where complex flow features such as the boundary layer/wake features are produced. For the overset mesh, curve refinement controls were also applied to increase the number of nodes representing the leading-edge and trailing-edge curvature at the aerofoil surface. A prism-layer mesher was applied to grow structured cells from the aerofoil surface in order to effectively model the boundary layer characteristics. A wall thickness prism layer distribution method was used for generating the prism-layer mesh which requires specifying the near-wall prism layer cell height. This allows for fixing the wall y+ value when performing the grid independence study which involves a variation in grid density. The near wall prism layer height was set to 0.0000075c to achieve an effective wall $y+$ value ≤ 1 and the total number of prism layers used was set to 30. The prism layer total height was set to 0.01 c which has been used as an approximation for capturing the full growth of the boundary layer from the leading-edge. The cell surface growth rate for both the background and overset mesh was set to 1.2.

A base size was set for both the background and overset meshes which was the parameter used to vary the grid density. All of the volumetric, surface, and curve refinement controls varied relatively to the change in the base size value. The base size values for the background and overset meshes for grid, G_3, were set to 0.08 m and 0.016 m respectively. The volumetric refinement control for the background mesh was set to 25% smaller than the base size.

For the overset mesh, the base size was set 20% smaller than the background refinement region to ensure that there were enough cells that overlap which is required

for sufficient interpolation of the overset boundary to the fixed background boundary [83]. To increase the grid density at the aerofoil surface as well as the core mesh near the aerofoil boundary, a volume and surface refinement was applied, which was set at 10% of the overset mesh's base size. A further surface refinement was applied at the aerofoil's leading-edge and trailing-edge surface to increase the curvature resolution, with the target surface size set to 3% of the overset mesh's base size.

3.2.3 Flow physics and solver

Unsteady Reynolds-Averaged Navier-Stokes (URANS) equations are solved with air modelled as an ideal, compressible gas. The dynamic viscosity, μ, was set to $1.821 \times 10^{-5}\ Pa - s$, based on the the operational conditions measured from experimental data [102]. Default settings were used for the Turbulent Prandtl number, with the value set to 0.9. A pressure-energy based coupled solver was applied using second order spatial discretisation, and gradients were calculated using the default Hybrid Gauss-LSQ method. Free-stream flow conditions were achieved by applying the following boundary conditions to the background domain: uniform velocity inlet at the left surface, pressure outlet at the right surface, and symmetry plane conditions at the top and bottom surfaces. For the uniform velocity inlet conditions, the direction is set to positive in the positive x-direction, as defined in Fig. 3.1. The free-stream uniform velocity set at the inlet boundary is also used for the initial flow conditions. For the pressure outlet conditions, the backflow specification's direction is extrapolated. All flow computations are fully turbulent and the $k - \omega$ SST model was used for turbulence closure of the URANS equations. The turbulence effects were characterised by the turbulence intensity, I, and turbulent length scale, L_{scale}, set as 0.02 and 2 % of the chord respectively [46, 102].

The temporal resolution was set to 2nd order and all of the computations were performed for 10 pitch cycles. The phase-averaged and individual cycles for the aerodynamic force and moment coefficient results (9 pitch cycles) is shown in Fig. 3.3. It is evident that there is a close match between the phase-averaged aerodynamic coefficients against their individual cycle counterparts. There are small differences in aerodynamic coefficients individual cycles at the dynamic stall region during the pitch downstroke. Figure 3.4 shows the average convergence results for the aerodynamic coefficients as a function of time. The difference in all of the aerodynamic coefficients assessed when comparing cycle-to-cycle is less than 1 % from the 5th cycle onwards. Due to this result, the aerodynamic coefficients for all cases presented in this CFD study are phase-averaged from the 5th cycle onwards.

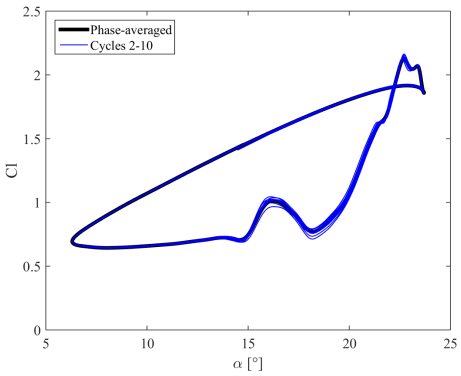

(a) Lift coefficient

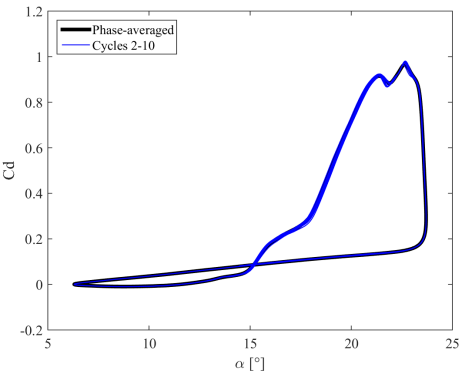

(b) Drag coefficient

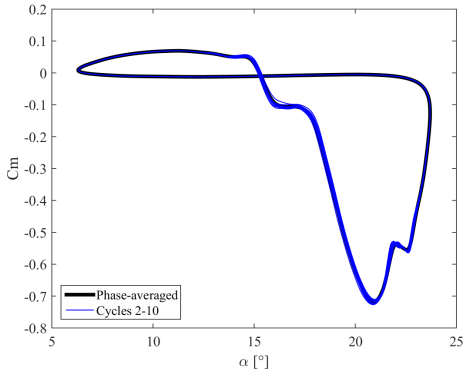

(c) Drag coefficient

Figure 3.3: Comparison between the phase-averaged and individual cycle (2 to 10) results for the aerodynamic force and moment coefficients. Operational conditions: Re = 1.48×10^6, $k = 0.153$, $\alpha_M = 15°$, $\alpha_{amp} = 8.7°$.

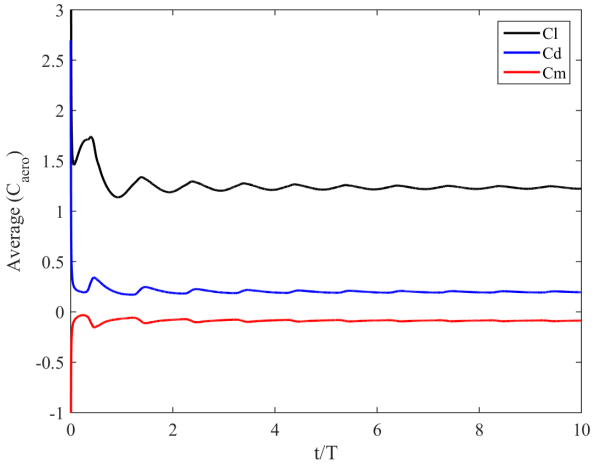

Figure 3.4: Average aerodynamic force and moment coefficient convergence results as a function of time.

The Courant number was set to 50, to improve on the convergence acceleration at each time-step without causing the simulation's residuals to diverge. The under-relaxation factors for the $k-\omega$ turbulence and turbulent viscosity parameters were set at the default values of 0.9.

3.2.4 Motion and morphing settings

Rigid rotational motion was applied to the overset mesh in order to simulate the pitch-oscillation motion of the aerofoil, using STAR-CCM+'s built in capability. The aerofoil's pitch origin is located at the quarter chord as shown in Fig. 3.1, and is defined positive in the clock-wise direction. The pitch axis origin remains fixed to the global coordinate system, however the leading-edge morphing axis coordinate system is fixed to the aerofoil, therefore this axis system will rotate relative to the pitch axis position.

Morphing of the aerofoil's leading-edge is performed directly within STAR-CCM+, which uses a multi-quadric radial splines morphing method to interpolate the displaced wall boundary surfaces [83]. The morphing motion redistributes mesh vertices in response to the movement of a set of control points. Each control point has an associated distance vector that specifies the linear displacement of the point within a single time-step.

Figure 3.5 illustrates the morphing coordinate system implemented in this study. The position of the morphing axis origin, x_{morph}/c (highlighted by the circle marker), is set to a point along the x-direction which controls the amount of the aerofoil surface that has leading-edge morphing applied. $\vec{R_{LE}}$ is the morphing displacement vector which the maximum leading-edge deflection angle, β_{max}, is applied to. Fixed points are set on the aerofoil surface at x-positions $\geq x_{morph}/c$ to restrict the aerofoil deformation to the leading-edge section only. For aerofoil surface points with x-positions $\leq x_{morph}/c$, a linear distribution method is applied to determine the rotational displacement of the control points.

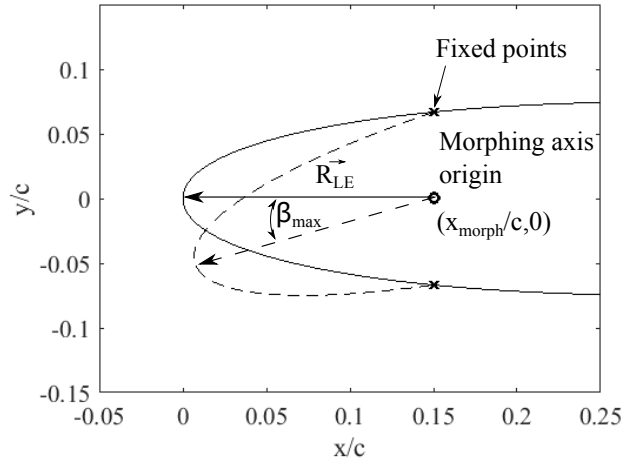

Figure 3.5: Leading-edge morphing coordinate system. Example is shown for a 15 % chord leading-edge morphing section.

The leading-edge droop deformation is applied to the vector $\vec{R_{LE}}$ at each time-step, with its components represented as:

$$\begin{aligned} R_{LE_x}(t) &= -R_{LE}cos\beta(t) \\ R_{LE_y}(t) &= R_{LE}sin\beta(t) \end{aligned} \tag{3.1}$$

The panel length displacements, (x_p, y_p), which represent the surface points of the aerofoil with leading-edge morphing applied at each time-step are determined using the following expressions:

$$\begin{aligned} x_p(t,i) &= x(i) + R_{LE_x}(t)\left[\frac{x(i) - x_{morph}}{x(LE) - x_{morph}}\right] \\ y_p(t,i) &= y(i) + R_{LE_y}(t)\left[\frac{x(i) - x_{morph}}{x(LE) - x_{morph}}\right] \end{aligned} \tag{3.2}$$

where i represents the current coordinate of the control point relative to the morphing axis origin's position, and $x(LE)$ is the single point coordinate at the aerofoil's leading-edge. Finally the control point displacements at each time-step due to the morphing of the leading-edge can be determined as follows:

$$\begin{aligned} x_{displacement}(t) &= x_p(t + \Delta t) - x_p(t) \\ y_{displacement}(t) &= y_p(t + \Delta t) - y_p(t) \end{aligned} \tag{3.3}$$

where Δt represents the time-step.

The control point displacements at each time-step are imported into STAR-CCM+ and applied to the aerofoil wall boundary. The motion profile of the control points displacements are coupled to the main rigid-body motion of the pitch oscillation

profile schedule.

3.2.5 Monitorables and convergence

The main monitorables recorded in this study include the aerofoil aerodynamic force and moment coefficients, residuals, the maximum local velocity magnitude, the maximum wall y^+ and the static pressure coefficient, C_p. Only the pressure component of the force and moment coefficients is considered as the experimental results were obtained by taking surface pressure measurements (the shear component of the force and moment coefficients were not measured). The maximum local velocity magnitude, V_{mag}, was recorded as it determines whether compressible flow features are present locally and therefore highlights the fact that compressibility effects cannot be ignored. The maximum wall y^+ monitorable provides the maximum wall y^+ at each time-step, which allows for checking whether the maximum y^+ value at each time-step falls below the maximum value of one.

For the residuals, certain criteria were set to ensure that the residuals fall below a certain threshold below progressing to the next time-step. The first criterion was that all of the main residuals (continuity, x-momentum, y-momentum, and energy) had to reach a residual value of 1.0×10^{-6} before progressing to the next time-step. The second criterion was that the standard deviation of the maximum velocity magnitude had to be within 1 m/s, which was based on the last 20 samples. If both criteria could not be achieved (due to convergence issues), then the maximum number of inner iterations was set to 400. This meant that the simulation would progress to the next time-step if the number of inner iterations exceeded 400 as a result of not meeting the requirements for the two set criteria.

The results for the residuals, maximum velocity magnitude, and the maximum wall y^+, for the rigid aerofoil using grid, G_3, is shown in Fig. 3.6. The residual results in Fig. 3.6a are presented against number of iterations, and only the last 2000 iterations are shown. The residual results have also been filtered to improve clarity of the visualisation. It is clear that all of the residuals fall below 1.0×10^{-6} before progressing to the next time-step, meaning that both criteria that were set for the residuals have been achieved. The results for the maximum y^+ at each time-step over a range of 10 pitch cycles is shown in Fig. 3.6b. It is shown that the wall y^+ is greater than 1 at specific points in each pitch cycle, which is due to the increase in local Cp_{min} at the leading-edge's suction surface, before the formation of the primary LEV. Figure 3.6c illustrates the maximum local velocity magnitude at each time-step for the full 10 pitch cycles. Again, it is shown for specific points of all pitch cycles that the maximum V_{mag} is within compressible flow regime ($Ma \geq 0.3$) which is again due to the large increase in Cp_{min} at the leading-edge's suction surface, shortly before the formation of the primary leading-edge vortex. This confirms that compressibility effects have to be modelled, even if the free-stream flow conditions are below $Ma \leq 0.3$.

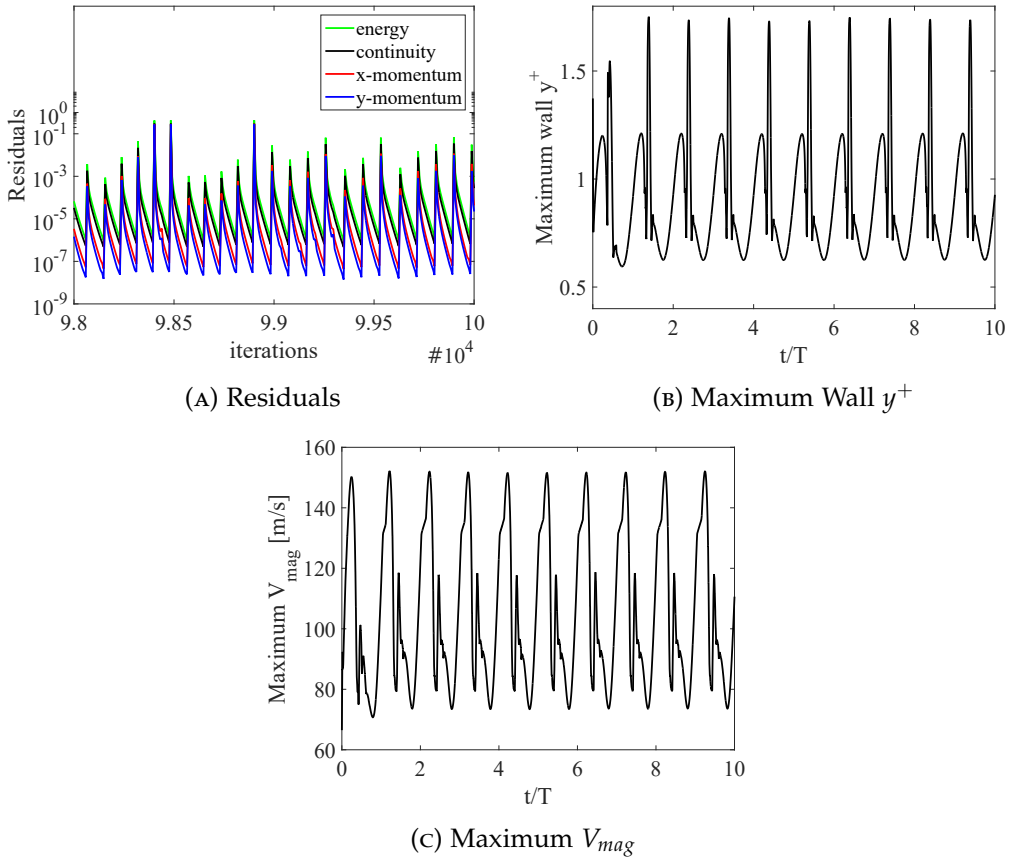

(A) Residuals

(B) Maximum Wall y^+

(C) Maximum V_{mag}

FIGURE 3.6: Grid G_3 results for the rigid aerofoil pitching over 10 cycles and illustrating key monitorables.

3.3 DYNAMIC STALL MESH VALIDATION

3.3.1 EFFECT OF GRID RESOLUTION

The CFD model is validated against previous dynamic stall experiments conducted at the University of Glasgow [102]. The Handley-Page low speed wind tunnel, a closed-return type with a 1.61 m by 2.13 m working test section was utilised. A range of static and dynamic tests were reviewed for various NACA 4-series aerofoils, however for this study the NACA0015 aerofoil is selected for analysis due to its prevalence in past research conducted on cycloidal rotor applications[13, 25, 38–40, 56, 103]. The NACA0015 aerofoil section's chord (c) and span (b) are 0.55 m and 1.61 m, respectively. The model was manufactured using a fibre-glass skin with an epoxy resin foam and bonded to an aluminium spar. The pitch axis was set at the aerofoil quarter chord, mounted vertically in the tunnel, and pivoted using a linear hydraulic actuator and crank mechanism. Quantitative measurements were performed by installing 30 pressure transducers below the surface center-span to record surface pressure measurements. The resultant normal and axial pressure forces exerted on the aerofoil test section were obtained and transformed to obtain the aerodynamic force coefficients.

For the dynamic test cases, sinusoidal oscillated pitching schedules were applied and surface pressure measurements were recorded to calculate the normal and axial forces acting on the aerofoil under deep-stall conditions. The reduced frequency, k, is a dimensionless parameter which relates the pitching motion of the aerofoil to the free-stream velocity. The reduced frequency is therefore defined as follows:

$$k = \frac{\omega c}{2U_\infty} \tag{3.4}$$

where ω is the aerofoil angular frequency in rad/s, and U_∞ is the free-stream velocity in m/s.

The operational conditions of the experimental test were: Reynolds number, Re = 1.48×10^6, Mach number, Ma = 0.12, and reduced frequency, k = 0.153. The aerofoil's transient motion was modelled as a sinusoidal function where the blade incidence angle, α, and blade incidence rate, $\dot{\alpha}$, equations are defined as:

$$\alpha(t) = \alpha_{amp} \sin(\omega t) + \alpha_M \tag{3.5}$$

$$\dot{\alpha}(t) = \alpha_{amp} \omega \cos(\omega t) \tag{3.6}$$

where α is the cyclic amplitude in degrees, α_M is the mean incidence angle in degrees, T is the period of the sinusoidal oscillation in seconds, and t is time in seconds. α_M and α_{amp} were set to 15° and 8.7° respectively which represents the actual incidence angles measured from the experiment [102]. It should be noted that in the experimental study, no corrections were applied to the surface pressure measurements such as wind tunnel blockage effects when calculating the aerodynamic pressure forces acting on the aerofoil [102].

A mesh independence study was first performed as part of the validation process to assess when the flow solution becomes independent of the mesh resolution. Four grids are assessed with grid, G_1, set as a base coarse grid to provide an initial solution and grid, G_4, set as the most refined grid. The total cell count for the background and overset meshes for all grids assessed are presented in Table 3.1.

Grid	Total cell count	Background cells	Overset cells
G1	88,500	64,400	24,100
G2	199,300	147,700	51,600
G3	446,600	347,400	99,200
G4	824,100	647,400	176,700

Table 3.1: Grid sensitivity study. Values rounded to the nearest 100.

The time-step was selected based on the non-dimensional time-step equation [86, 104], and is defined in relation to the reduced frequency as:

$$\Delta t = \frac{2k\Delta t^*}{\omega} \tag{3.7}$$

where Δt^* is the non-dimensional time-step and Δt is the time-step in seconds. A non-dimensional time-step of 0.02 was selected for the mesh independence study which results in a time-step of 2.64×10^{-4}s.

The phase-averaged aerodynamic coefficients are plotted against the various mesh grids and compared against the experimental results in Fig. 3.7. All grids assessed in Fig. 3.7 sufficiently generate key flow features of dynamic stall such as: the increase in dynamic lift in Fig. 3.7a, the dynamic lift overshoot loop in Fig. 3.7b, the drag-rise in Fig. 3.7c, and the moment stall in Fig. 3.7d. There are phase and magnitude discrepancies in the results at the stall and secondary vortex formation regions as it has been previously shown that the boundary layer grid resolution has a significant contribution on the secondary stall event [93].

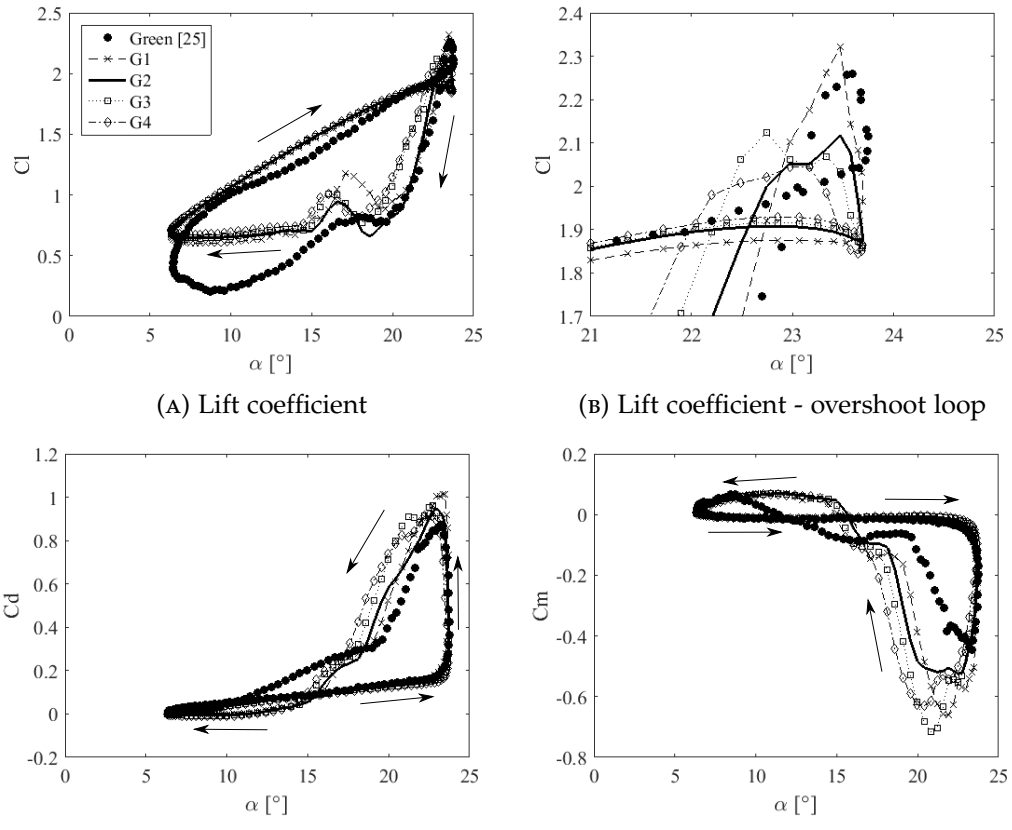

(A) Lift coefficient

(B) Lift coefficient - overshoot loop

(C) Drag coefficient

(D) Moment coefficient

Figure 3.7: Grid independence results for the aerofoil phase-averaged aerodynamic coefficients. Operational conditions: Re = 1.48×10^6, k = 0.153, $\alpha_M = 15°$, $\alpha_{amp} = 8.7°$.

The coefficient of determination, R^2, is used to determine which grids can be considered mesh independent and is defined as:

$$R^2 = 1 - \frac{\sum_{t=0}^{T}((C_{aero}(t) - C_{l_{aero_{ref}}}(t))^2}{\sum_{t=0}^{T}((C_{aero}(t) - C_{l_{aero_{av}}})^2} \tag{3.8}$$

where C_{aero} is the aerodynamic coefficient of the case being assessed, $C_{aero_{ref}}$ is the aerodynamic coefficient of the reference case being compared against, and $C_{aero_{av}}$ is the mean aerodynamic coefficient of the case being assessed. The coefficient of determination determines the level of variance between the differing mesh resolution grids where $R^2 \approx 1$ results in negligible differences between the two cases being evaluated [86]. All of the grids assessed are compared against the most refined grid, G_4, which is set as $C_{aero_{ref}}$.

The results for the coefficient of determination for the mesh independence phase-averaged aerodynamic coefficients are presented in Table 3.2. Grid G_3 achieves a low level of variance with $R^2 \geq 96\%$ for all aerodynamic coefficients when compared to grid G_4, while achieving an approximate 46 % reduction in the total cell count. Therefore, grid G_3 is determined as mesh independent as it produces an accurate resolution of the key dynamic stall flow features similar to grid G_4 and is therefore selected to use in the time-step independence study.

Grid	*Cl*	*Cd*	*Cm*
$R^2(G1)$	0.9272	0.8218	0.7788
$R^2(G2)$	0.9463	0.9121	0.8809
$R^2(G3)$	**0.9939**	**0.9798**	**0.9634**

Table 3.2: Grid independence results for the coefficient of determination, R^2.

3.3.2 Effect of time-step resolution

A time-step independence study was performed as part of the CFD model validation process. The non-dimensional time-step, Δt^*, was varied to determine the extent to which the aerodynamic coefficients are effected by a refinement in time-step for a fixed total mesh cell count using grid G_3. Four non-dimensional time-step values were evaluated, namely: $\Delta t_1^* = 0.04$, $\Delta t_2^* = 0.02$, $\Delta t_3^* = 0.01$, and $\Delta t_4^* = 0.005$.

Figure 3.8 presents the aerofoil's phase-averaged aerodynamic coefficients plotted against incidence angle for the four Δt^* cases and compared against the experimental results of Green [102]. There are minimal discrepancies in the aerodynamic coefficients for the majority of the upstroke for all Δt^*. Δt_1^* produces variations in the phase and magnitude of the dynamic stall as well as the secondary vortex formation and stall when compared to the remaining Δt^*, as shown in Fig. 3.8a. There are minimal differences in the phase-averaged aerodynamic coefficients at the flow reattachment stage at the end of the down-stroke for all Δt^*.

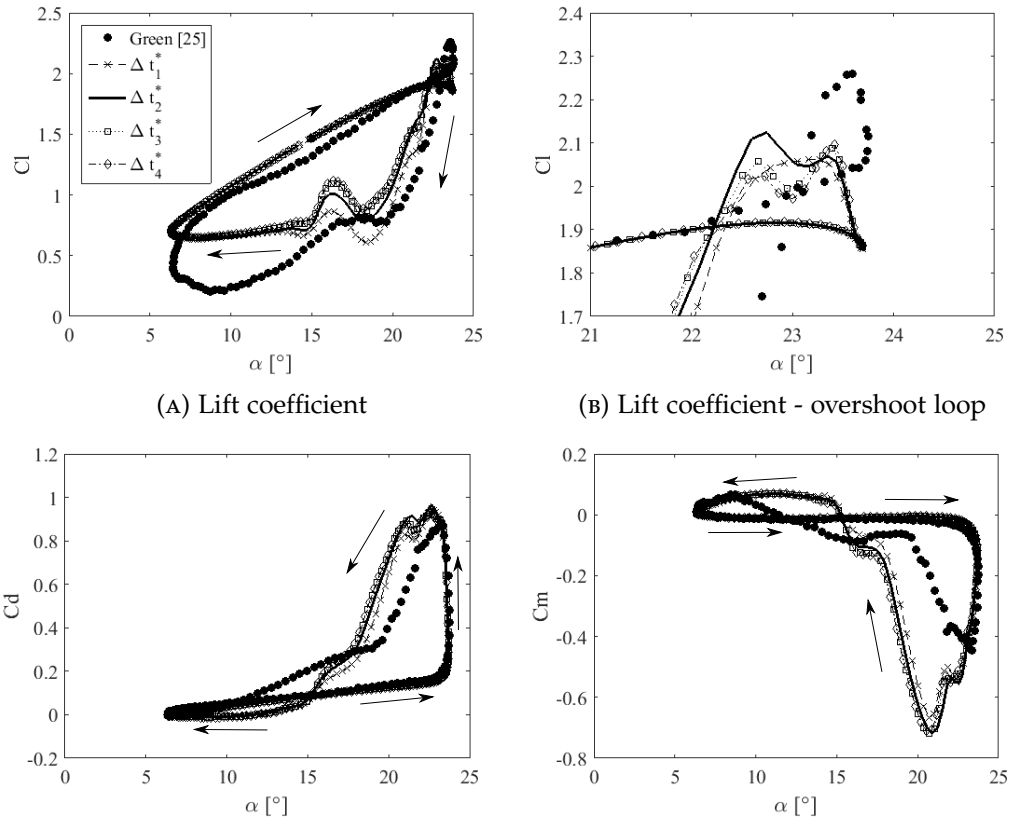

(a) Lift coefficient

(b) Lift coefficient - overshoot loop

(c) Drag coefficient

(d) Moment coefficient

Figure 3.8: Time-step independence results for the aerofoil phase-averaged aerodynamic coefficients. Operational conditions: Re = 1.48×10^6, $k = 0.153$, $\alpha_M = 15°$, $\alpha_{amp} = 8.7°$.

The coefficient of determination results from the time-step independence analysis are shown in Table 3.3. For all non-dimensional time-step values assessed, Δt_2^* and Δt_3^* accomplishes a low level of variance with $R^2 \geq 0.99$ for all aerodynamic coefficients when compared against the most refined non-dimensional time-step case Δt_4^*. There is an approximate 100 % increase in computational cost when comparing Δt_3^* to Δt_2^*, therefore the decision was made to use grid G_3 with Δt_2^* = 0.02 for the remainder of the simulations.

When comparing the phase-averaged aerodynamic coefficients from the CFD analysis to the experimental results in Fig. 3.8, the CFD results are shown to accurately predict key flow features of the dynamic stall process such as: the secondary vortex formation after the primary stall in Fig. 3.8a, the lift overshoot in Fig. 3.8b, the drag-rise in Fig. 3.8c, and the moment stall in Fig. 3.8d. There are discrepancies between the CFD and experimental results during the post stall and flow-reattachment stages of the down-stroke which is due to the limitations of the turbulence model used and has been observed from previous computational research [105]. Note, there are also experimental errors to consider as correction factors such as wind tunnel blockage effects were not applied to the aerodynamic coefficients obtained from the surface pressure measurements.

Non-dimensional time-step	Cl	Cd	Cm
$R^2(\Delta_{t1}^*)$	0.9600	0.9770	0.9494
$R^2(\Delta_{t2}^*)$	**0.9939**	**0.9974**	**0.9945**
$R^2(\Delta_{t3}^*)$	0.9977	0.9970	0.9971

Table 3.3: Time-step independence results for the coefficient of determination, R^2.

3.4 DYNAMIC STALL CONTROL WITH ACTIVE LEADING-EDGE MORPHING AND LEADING-EDGE FIXED DROOP

3.4.1 Effect of leading-edge morphing amplitude

Active leading-edge morphing is applied to a pitch oscillating NACA0015 aerofoil to investigate the effect it has on alleviating dynamic stall and its impact on aerodynamic performance. The leading-edge morphing amplitude, denoted as β_{max}, is defined positive in the anti-clockwise direction, as shown in Fig. 3.5. Active leading-edge droop morphing is initialised at α_M during the pitch upstroke, resulting in β_{max} occurring at α_{max}, which is where the dynamic stall takes place. The objective of actively deforming the leading-edge is to reduce the local incidence at the leading-edge with the aim of mitigating the full formation of the LEV. Four different β_{max} amplitudes are investigated to assess the level of dynamic stall suppression obtained when β_{max} is varied. The aerofoil's operational pitching parameters remain unchanged and the aerofoil's pitching schedule as well as the four β_{max} pulsed droop schedules are shown in Fig. 3.9.

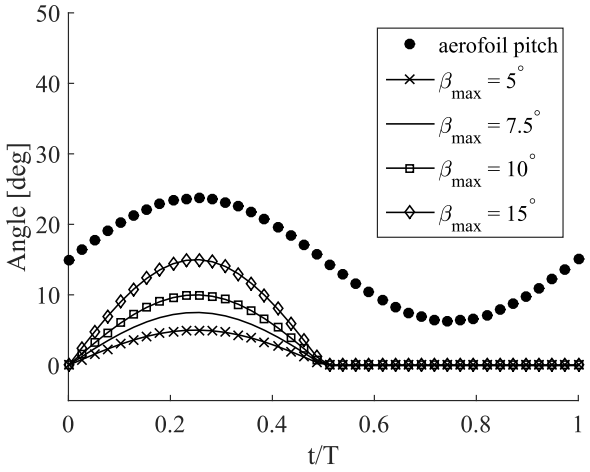

Figure 3.9: Aerofoil pitch and leading-edge morphing scheduling with a variation in the maximum leading-edge morphing amplitude for a single pitch cycle.

Figure 3.10 shows the phase-averaged results for the aerodynamic coefficients against incidence angle as well as the dynamic drag polar, with and without leading-edge morphing. For most of the pitch upstroke, it is clear that the aerodynamic forces are insensitive to the effect of leading-edge morphing. The effect of leading-edge morphing is more prominent at the end of the upstroke. For $22^\circ \leq \alpha \leq 24^\circ$, the overshoot in lift due to the effect of the LEV convecting across the aerofoil's upper surface is removed for all β_{max} as evident in Fig. 3.10a. The drag coefficient results in Fig. 3.10b show that the peak drag-rise is significantly reduced for all β_{max} and the level of reduction increases for a certain increase in β_{max}. The most effective cases are β_{max} = 5° and 10° where there are significant reductions in Cd_{max} of 55.5% and 59% respectively. There are also significant reductions in Cm_{min} when leading-edge morphing is applied, which vary depending on the value of β_{max} applied. The results in Fig. 3.10c indicate that reductions in Cm_{min} of 56.4% and 62.1% were achieved when applying β_{max} = 5° and 10°, respectively. Leading-edge morphing is still very effective but less so than for the lower morphing amplitudes in decreasing the peak drag and minimum moment coefficient with β_{max} = 15°, with 45.6 % and 43.8 % reductions respectively in comparison to the rigid aerofoil.

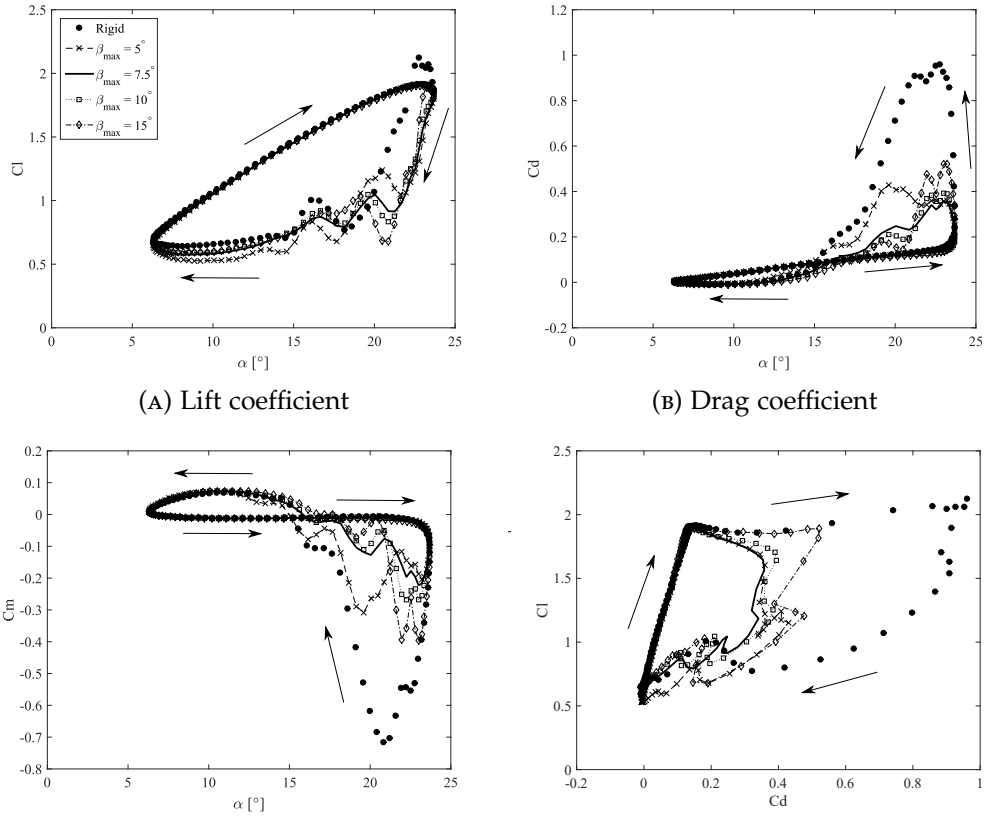

(A) Lift coefficient

(B) Drag coefficient

(C) Moment coefficient

(D) Drag polar

Figure 3.10: Aerofoil aerodynamic coefficient results against incidence angle for a variation in the leading-edge morphing amplitude. Comparison made against the rigid aerofoil. Operational conditions: Re = 1.48 × 10^6, k = 0.153, $\alpha_M = 15^\circ$, $\alpha_{amp} = 8.7^\circ$.

During the pitch downstroke, there are significant reductions in the drag and moment coefficient hysteresis loops when active leading-edge morphing is applied, as illustrated in Figs. 3.10b and 3.10c. The effect of leading-edge morphing on the lift coefficient during the downstroke is shown to increase the lift hysteresis loop as shown in Fig. 3.10a. This is due to the removal of the overshoot in lift which leads to a delay in dynamic stall for the rigid aerofoil and results in stall occurring earlier for the morphing cases. When inspecting drag during the down-stroke in Fig. 3.10b, all β_{max} amplitudes significantly reduce the positive drag hysteresis loop with a 39 % reduction in Cd_{mean} for all β_{max} amplitudes in comparison to the rigid aerofoil. The down-stroke results for the moment coefficient in Fig. 3.10c also show significant reductions in the negative hysteresis loops for all β_{max} amplitudes, resulting in a decrease in negative aerodynamic damping which is associated with structural fatigue issues. This leads to a 61 % reduction in $C_{m_{mean}}$ for all β_{max} in comparison to the rigid aerofoil. During the latter part of the pitch cycle down-stroke when active leading-edge morphing is not applied, there are minimal variations in the aerodynamic performance compared to the rigid aerofoil.

The aerodynamic efficiency is also significantly improved through the implementation of leading-edge morphing as visualised by the dynamic drag polar results in Fig. 3.10d. The aerodynamic efficiency is related to the ratio of the mean aerodynamic lift and drag, $(C_l/C_d)_{mean}$, with the rigid aerofoil producing an aerodynamic efficiency of 6.23. All β_{max} amplitudes generate an increase in the aerodynamic efficiency with the most effective case, $\beta_{max} = 10^\circ$ producing an aerodynamic efficiency of 11.6. The aerodynamic efficiency improvements are clearly shown in the drag polar curves in Fig. 3.10d due to the significant reductions in the dynamic drag polar hysteresis loops in comparison to the rigid aerofoil.

The effect that variation of the leading-edge morphing amplitude has on the aerodynamic performance characteristics is presented in Table 3.4. All of the tabulated results are normalised to the rigid aerofoil results. The tabulated results show that $\beta_{max} = 10^\circ$ is the most effective case in terms of improving the aerodynamic performance characteristics. This is due to achieving the largest reductions in Cd_{max} and Cm_{min} as well as achieving the largest increase in the aerodynamic efficiency, $Caero_{av}$, of 84.9 %. It is also shown that performance gains increase when varying the leading-edge morphing amplitude from 0 degrees up to 10 degrees, however the level of performance gains achieved reduces at $\beta_{max} = 15^\circ$.

β_{max} [deg]	Cl_{av}	Cd_{av}	Cm_{av}	Cl_{max}	Cd_{max}	Cm_{min}	$Caero_{av}$
Rigid	1.000	1.000	1.000	1.000	1.000	1.000	1.000
5	0.919	0.607	0.380	0.900	0.445	0.436	1.514
10	0.934	0.505	0.276	0.897	0.410	0.379	1.849
15	0.938	0.552	0.385	0.894	0.544	0.562	1.700

Table 3.4: Effect of the leading-edge morphing amplitude on the time-averaged and peak aerodynamic force and moment coefficients. Data has been normalised with respect to the rigid aerofoil.

The effect of applying active leading-edge morphing was also assessed quantitatively and qualitatively by visualising the pressure coefficient (Cp) scalar field and surface pressure coefficient distribution acting on the aerofoil at key stages of the pitch cycle. A comparison is made between the rigid NACA0015 aerofoil and the morphing aerofoil with $\beta_{max} = 10^{\circ}$ to observe how key dynamic stall flow features, such as the LEV, are affected by the application of pulsed, leading-edge morphing.

The minimum peak suction pressure coefficient occurs near the rigid aerofoil's leading-edge upper surface at approximately $\alpha = 23.3^{\circ} \uparrow$ as shown in Figs. 3.11a and 3.11c. Figure 3.11b illustrates that active leading-edge morphing reduces the extent of flow reversal travelling from the trailing-edge to leading-edge as well as decreasing Cp_{min} and increasing the area of low pressure at the trailing-edge. The reduction of Cp_{min} results in a decrease in the strength of the LEV after its formation. The effect of active leading-edge morphing is apparent in the surface pressure coefficient distribution in Fig. 3.11d, as shown by the presence of a kink on the aerofoil upper surface. The morphing is influential in preventing the increase in the minimum peak pressure coefficient. The surface pressure distribution at the aerofoil lower surface is insensitive to the deployment of leading-edge morphing.

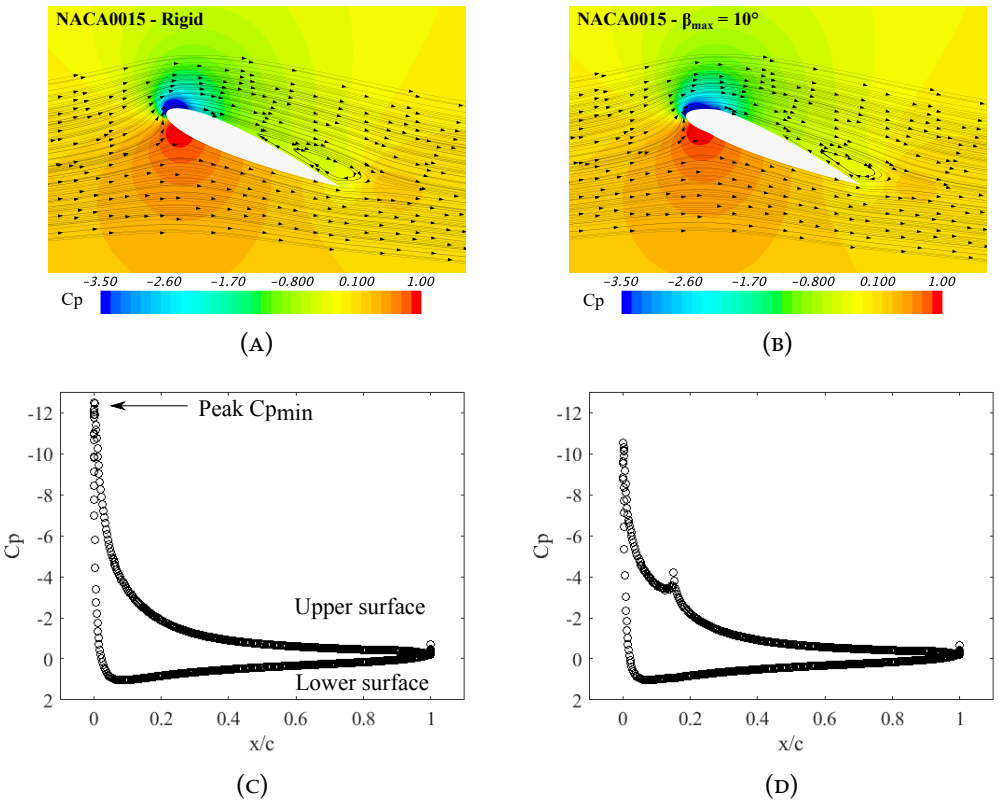

Figure 3.11: Pressure coefficient scalar visualisation and aerofoil surface pressure coefficient distribution. (a) & (c): Rigid NACA0015 aerofoil. (b) & (d): Morphing leading-edge amplitude, $\beta_{max} = 10°$. $\alpha = 23.3°\uparrow$, Re =1.48 $\times$ 10^6,k= 0.153,$\alpha_M = 15°$, $\alpha_{amp} = 8.7°$.

At α = 22.6° $\downarrow$, there is an overshoot in lift due to the convection of the LEV across the rigid aerofoil's upper surface, as shown in Fig. 3.12. In Fig. 3.12a, the LEV is visualised convecting across the rigid aerofoil's upper surface at approximately 0.6c, producing a large wake originating from the leading-edge. The convection of the LEV is also represented as a pressure ridge in the Cp surface distribution curve in Fig. 3.12c. When active leading-edge morphing is applied, the strength of the LEV is reduced and its full formation mitigated, as evident in Fig. 3.12b. In Fig. 3.12d, large levels of low pressure are maintained at the upper surface of the leading-edge due to the maintained attached flow at the morphed, leading-edge section. Moreover, the LEV convection ridge for the morphing aerofoil is smaller in comparison to the rigid aerofoil due to the aerofoil stalling earlier which is evident due to the formation of the TEV, as shown by the large level of suction pressure present at the trailing-edge.

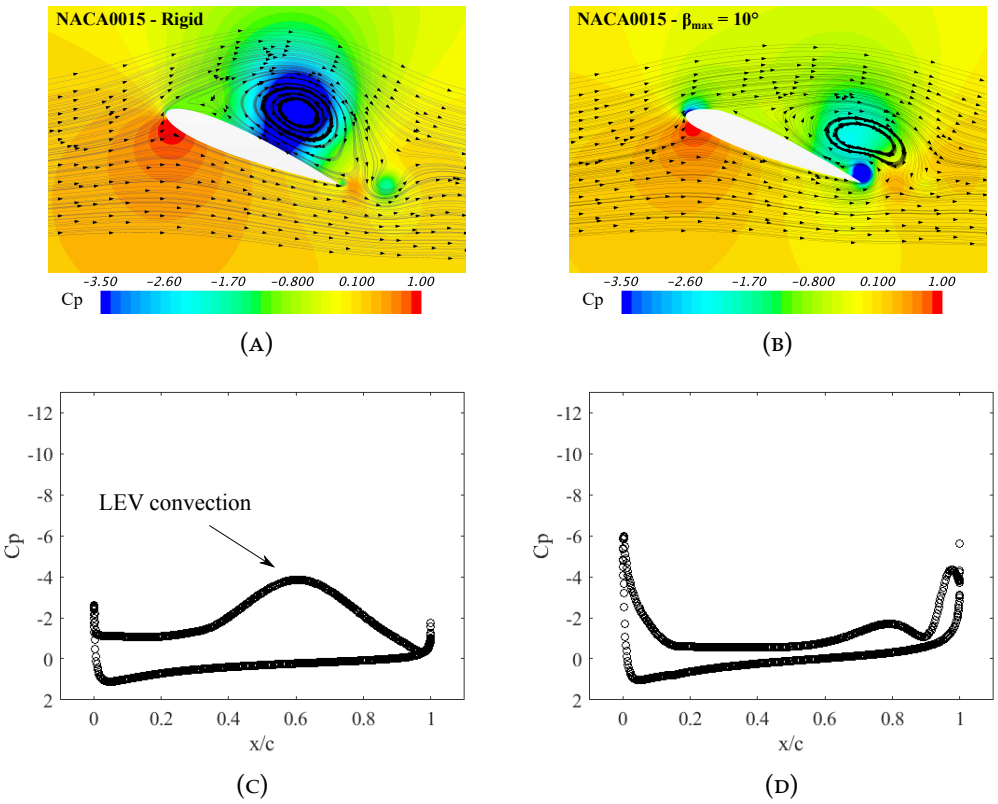

Figure 3.12: Pressure coefficient scalar visualisation and aerofoil surface pressure coefficient distribution. (a) & (c): Rigid NACA0015 aerofoil. (b) & (d): Morphing leading-edge amplitude, $\beta_{max} = 10°$. $\alpha = 22.6°\downarrow$, Re =1.48 $\times$ 10^6,k= 0.153,$\alpha_M = 15°$, $\alpha_{amp} = 8.7°$.

The point at which α = 21.27° $\downarrow$ indicates the shedding of the LEV as well as the formation of a strong TEV, as shown in Fig. 3.13. The interaction of the LEV and TEV produces large levels of suction near the aerofoil's trailing-edge in Figs. 3.13a & 3.13c, and is known to be the key driver for the generation of large negative pitching moments [71, 106]. In contrast, the active leading-edge morphing aerofoil demonstrates a reduction in the strength of the LEV and TEV, which decreased the level of suction at the trailing-edge, as shown in Figs. 3.13b & 3.13d. The flow is still attached at the morphed region's upper surface which results in the reduction in size of the wake as shown in Fig. 3.13b.

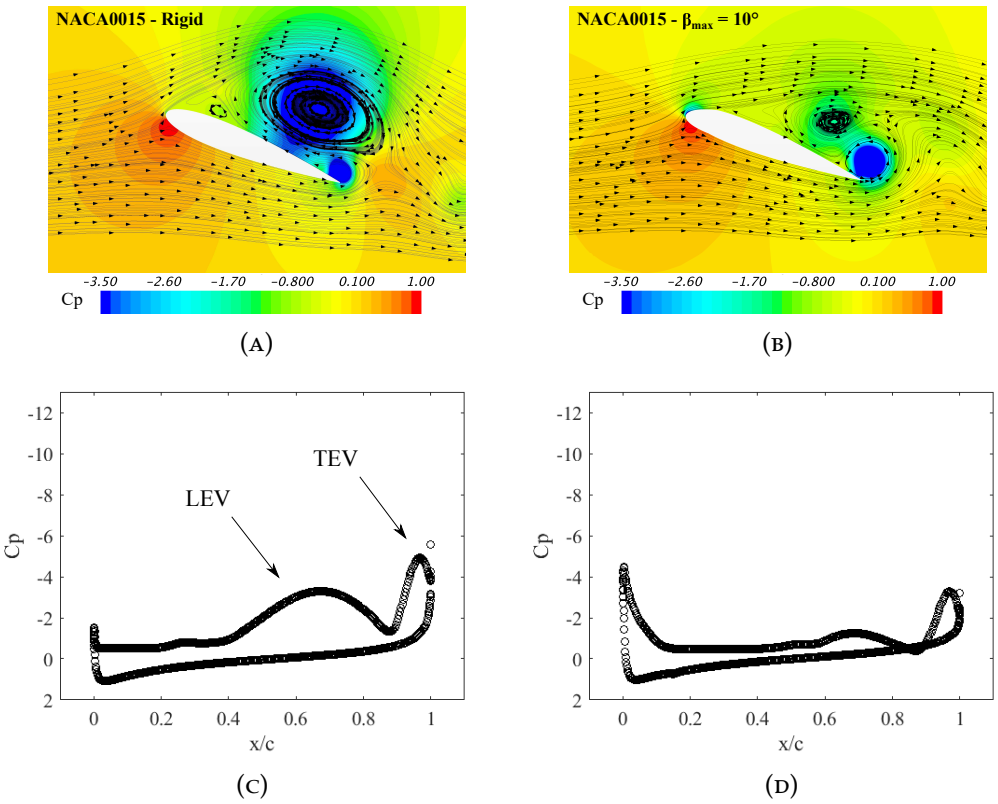

Figure 3.13: Pressure coefficient scalar visualisation and aerofoil surface pressure coefficient distribution. (a) & (c): Rigid NACA0015 aerofoil. (b) & (d): Morphing leading-edge amplitude, $\beta_{max} = 10°$. $\alpha = 21.7°\downarrow$, Re =1.48 $\times$ 10^6,k= 0.153,$\alpha_M = 15°$, $\alpha_{amp} = 8.7°$.

At α = 17.1° $\downarrow$ the convection of the secondary vortex and shedding of the TEV occurs at the rigid aerofoil's upper surface as illustrated in Fig. 3.14a. The magnitude of the secondary vortex as shown by the Cp ridge at x/c = 0.5 in Fig. 3.14c is much lower in comparison to the primary LEV. For the morphing aerofoil, the strength of the TEV and secondary vortex are much weaker still compared to the rigid aerofoil and have already separated, as shown in Figs. 3.14b and 3.14d. This results in a reduction in the time it takes for flow reattachment to occur as shown by the increase in the low levels of pressure produced at the upper surface of the aerofoil's morphed region.

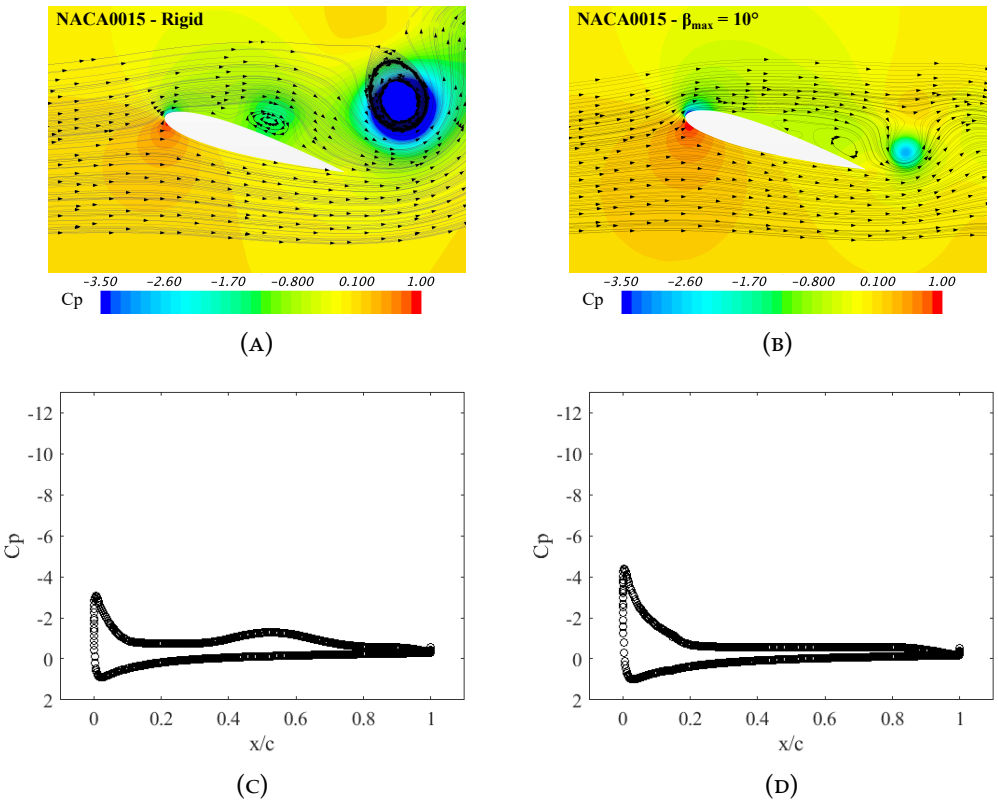

Figure 3.14: Pressure coefficient scalar visualisation and aerofoil surface pressure coefficient distribution. (a) & (c): Rigid NACA0015 aerofoil. (b) & (d): Morphing leading-edge amplitude, $\beta_{max} = 10°$. $\alpha = 17.1°\downarrow$, Re =1.48 $\times$ 10^6,k= 0.153,$\alpha_M = 15°$, $\alpha_{amp} = 8.7°$.

3.4.2 Effect of leading-edge fixed droop

Next, an assessment is made on the effect that variation of the leading-edge fixed droop amplitude, FD_{amp}, has on the dynamic stall control characteristics. A comparison is also made between the leading-edge fixed droop aerodynamic characteristics and the leading-edge morphing aerodynamic characteristics. The geometry of the leading-edge fixed droop cases is defined as the maximum leading-edge morphing amplitude, β_{max}, and remains fixed at this flap amplitude over the entire simulation. Three leading-edge fixed droop amplitudes are assessed which include, FD_{amp} = [5,10,15] °. All other operational conditions remained unchanged to maintain consistency.

The phase-averaged aerodynamic force and moment coefficient results for a variation in the leading-edge fixed droop amplitude is visualised is Fig. 3.15. During the pitch upstroke, there are apparent changes in the calculated lift, drag, and moment values for a change in FD_{amp}. This is evident when inspecting the moment coefficient results in Fig. 3.15c, which illustrates a reduction in Cm for an increase in FD_{amp}. This is due to a change in the physical camber of the aerofoil as a result of applying leading-edge fixed droop, which leads to a change in the overall aerofoil aerodynamic characteristics. At max incidence, all values of FD_{amp} are shown to remove the overshoot in lift as shown in Fig. 3.15a. This results in dynamic stall occurring earlier for

all FD_{amp} cases in comparison to the rigid aerofoil.

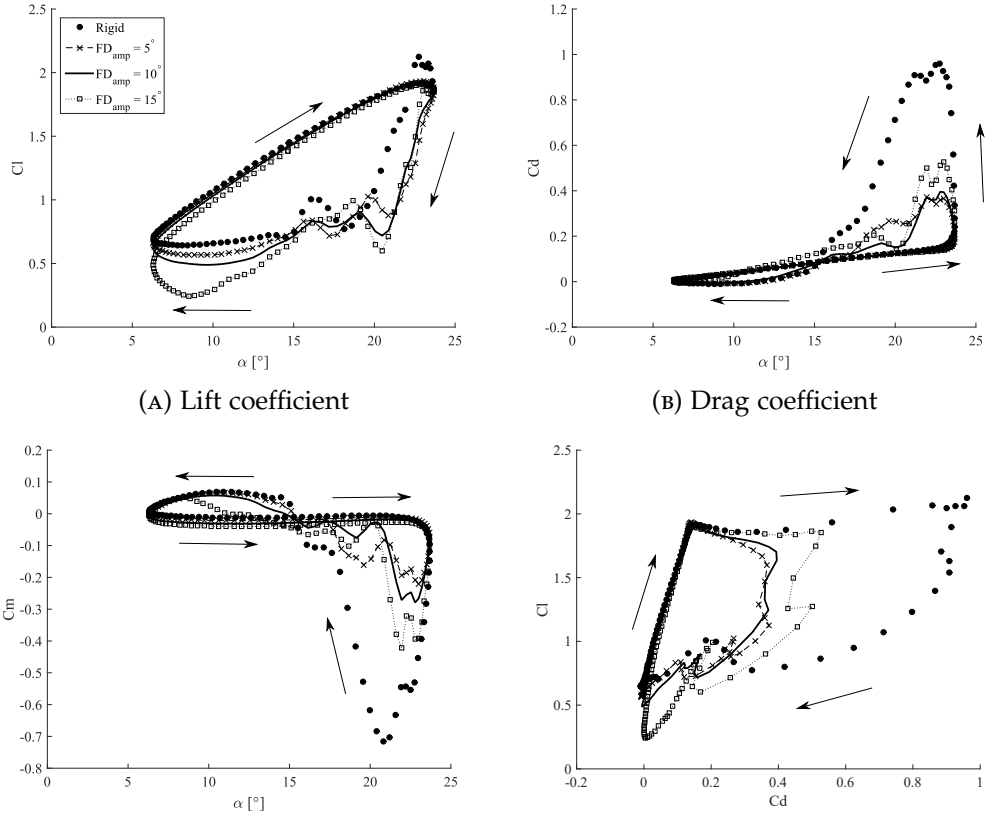

(A) Lift coefficient

(B) Drag coefficient

(C) Moment coefficient

(D) Drag polar

Figure 3.15: Aerofoil aerodynamic coefficient results against incidence angle for a variation in the leading-edge fixed droop amplitude. Comparison made against the rigid aerofoil. Operational conditions: Re = 1.48×10^6, k = 0.153, $\alpha_M = 15°$, $\alpha_{amp} = 8.7°$.

At the pitch downstroke where dynamic stall occurs, it is shown that all FD_{amp} cases are effective in achieving large reductions in the drag-rise (Fig. 3.15b) and peak negative pitching moment (Fig. 3.15c). For the lift coefficient results in Fig. 3.15a, the magnitude of the lift stall reduces for a decrease in FD_{amp}. It is shown that $FD_{amp} = 15°$ achieves a larger magnitude in lift stall in comparison to the rigid aerofoil. This means that even though the type of stall has changed (removal of the lift overshoot and delay in dynamic stall), the effective incidence at the morphing joint point on the suction surface still triggers a large magnitude in lift stall past the leading-edge fixed droop section. At the lower incidence range, there is a significant reduction in Cl when FD_{amp} increases. This is again due to the change in the aerofoil physical camber, which alters the overall aerodynamic characteristics of the aerofoil after flow reattachment occurs. The drag coefficient results in Fig. 3.15b show that similar Cd_{max} values are produced at 5 degrees and 10 degrees FD_{amp}. Figure 3.15c illustrates that Cm_{min} reduces for a decrease in FD_{amp}, with $FD_{amp} = 5°$ achieving the largest reduction in Cm_{min}. Another interesting feature is that the transition from negative to positive pitch damping is delayed as FD_{amp} increases, with $FD_{amp} = 15°$

achieving significantly smaller positive pitch damping characteristics in comparison the rigid aerofoil.

The dynamic, phase-averaged drag polar results are visualised in Fig. 3.15d. There is little change in the linear portion of the drag polar for a change in the leading-edge fixed droop amplitude. At the section where significant increase in drag occurs for a relatively constant lift value, there are significant reductions in drag for all values of FD_{amp}. It is evident that the most effective leading-edge fixed droop amplitude cases in terms of improving the aerodynamic efficiency is for FD_{amp} amplitudes of 5 and 10 degrees, due to the significant reductions in the drag polar hysteresis loops.

The effect of varying the leading-edge fixed droop amplitude has on the aerodynamic characteristics is further assessed by evaluating the time-averaged and peak aerodynamic coefficients as well as the time-averaged aerodynamic efficiency, as shown in Table 3.5. All of the tabulated results are normalised with respect to the equivalent rigid aerofoil results. The tabulated results show that the largest reduction in Cd_{max} and Cm_{min} is achieved at a leading-edge fixed droop amplitude $FD_{amp} = 5°$. The largest improvement in the time-averaged aerodynamic efficiency is achieved however at a leading-edge fixed droop amplitude of $FD_{amp} = 10°$, which is due to achieving the largest reduction in Cd_{av}. Both FD_{amp} values of 5 degrees and 10 degrees generate similar levels of reductions in Cl_{av} and Cl_{max}. The least effective leading-edge fixed droop amplitude case in terms of aerodynamic efficiency is at $FD_{amp} = 15°$.

FD_{amp} [deg]	Cl_{av}	Cd_{av}	Cm_{av}	Cl_{max}	Cd_{max}	Cm_{min}	$Caero_{av}$
Rigid	1.000	1.000	1.000	1.000	1.000	1.000	1.000
5	0.927	0.531	0.336	0.909	0.387	0.308	1.747
10	0.911	0.506	0.400	0.908	0.412	0.391	1.802
15	0.864	0.633	0.663	0.895	0.545	0.591	1.365

Table 3.5: Effect of the leading-edge fixed droop amplitude on the time-averaged and peak aerodynamic force and moment coefficients. Data has been normalised with respect to the rigid aerofoil.

A comparison is made between a single leading-edge fixed droop case against a single active leading-edge morphing case to assess the differences in aerodynamic characteristic improvements during dynamic stall. A flap amplitude of 10 degrees is selected for comparison as this leading-edge flap amplitude that was shown to be effective for both the β_{max} and FD_{amp} cases in terms of achieving large reductions in Cd_{max} and Cm_{min}. The phase-averaged aerodynamic force and moment coefficient results for comparing against the rigid aerofoil, leading-edge morphing, and leading-edge fixed droop is shown in Fig. 3.16. During the pitch upstroke, there is little difference in the calculated Cl for the rigid aerofoil, β_{max} aerofoil, and FD_{amp} aerofoil as visualised in Fig. 3.16a. At maximum incidence, both the β_{max} and the FD_{amp} methods remove the overshoot in lift and prevent the delay in dynamic stall.

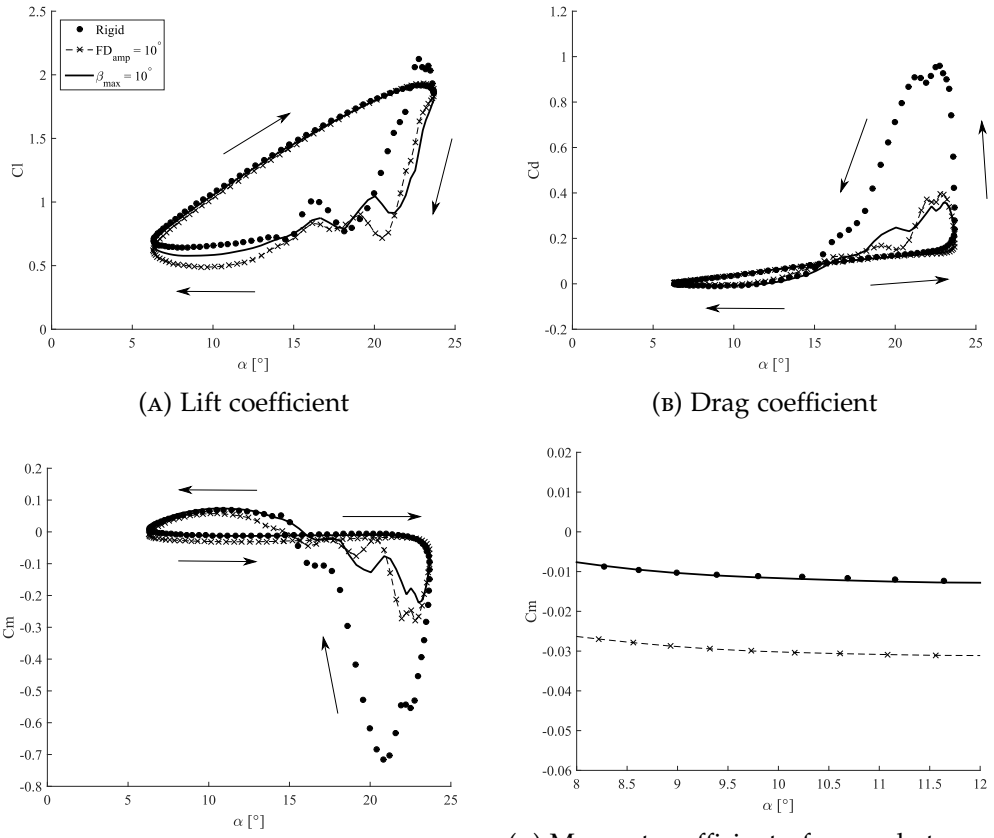

(A) Lift coefficient

(B) Drag coefficient

(C) Moment coefficient

(D) Moment coefficient - focussed at specific region

Figure 3.16: Comparison between leading-edge fixed droop and leading-edge morphing amplitude at 10 degrees amplitude. Comparison made against the rigid aerofoil. Operational conditions: Re = 1.48×10^6, $k = 0.153$, $\alpha_M = 15°$, $\alpha_{amp} = 8.7°$.

During the pitch down-stroke, the lift stall magnitude is larger for the FD_{amp} result than for the β_{max} result, as shown in Fig 3.16a. This also results in slightly larger values for Cm_{min} for $FD_{amp} = 10°$ compared to $\beta_{max} = 10°$. Figure 3.16b shows that both methods achieve similar levels of reduction in Cd_{max}, however the rate of reduction in Cd is larger for FD_{amp} in comparison to β_{max}. This is due to the decrease in the effective local incidence angle at the leading-edge suction surface as a result of a fixed leading-edge droop amplitude in comparison to larger local incidence angles for the leading-edge morphing method. The moment coefficient results in Fig. 3.16c show that both methods achieve a significant reduction in Cm_{min} when compared to the rigid aerofoil. The transition from negative to positive pitch damping occurs later for FD_{amp} in comparison to β_{max}, and it is shown that β_{max} produces similar levels of positive pitch damping when compared to the rigid aerofoil. This is due leading-edge morphing being inactive at the second half of the pitch cycle.

It has been shown that both the FD_{amp} and β_{max} methods achieve similar levels of reduction in Cd_{max} and Cm_{min} when compared against the rigid aerofoil. In terms of cycloidal rotor operation, it is preferable to only introduce physical camber change in the rotor's advancing side where dynamic stall features are present, and would not be

required for the rotor retreating side [44]. This means that leading-edge morphing would be better suited for implementing within cycloidal rotor operation as the motion can be activated at a specific instances of the rotor cycle only. Moreover, applying leading-edge fixed droop has shown to alter the aerodynamic force and moment characteristics when compared against the rigid aerofoil. This is clearly shown in the pitching moment coefficient plot in Fig. 3.16d which is focussed in the region at the start of the pitch upstroke (attached flow region). Here, the results show that there is no difference in the calculated Cm results between the rigid aerofoil and the leading-edge morphing method as leading-edge morphing is not activated within this section of the pitch cycle. The FD_{amp} results produces a negative shift in Cm which is due to the physical camber change in the aerofoil, and is therefore not representative of the rigid NACA0015 aerofoil. For cycloidal rotor operation, this would mean that performance gains would be achieved in the rotor retreating side when implementing FD_{amp}, however this could result in detrimental effects in the rotor advancing side, due to the introduction of negative physical camber. An analysis of the energy required to apply leading-edge morphing using a linear actuation system will be discussed in Chapter 4. The comparison for both the leading-edge morphing and leading-edge fixed droop methods for cycloidal rotor operation will be discussed further in Chapter 6.

3.4.3 Effect of leading-edge morphing chord size

The next part of this investigation assesses the effect that increasing the proportion of aerofoil chord with leading-edge morphing has on dynamic stall control. β_{max} was set to 10° as this was deemed to be the most effective morphing case in terms of improving the time-averaged lift, drag, and moment as well as reducing the effect of flow separation.

Three different morphing cases have been assessed, which are characterised based on the value of the morphing axis origin position as shown in Fig. 3.5, and are set as: x_{morph}/c = 0.15c, 0.20c, and 0.25c. The fixed points in Fig. 3.5 are also adjusted according to the value set for x_{morph}/c, which results in an increase in the proportion of aerofoil surface which has leading-edge morphing applied. The aerofoil's pitch axis remains unchanged at the quarter chord, as no other changes are applied to the operational conditions to maintain consistency.

The phase-averaged results for the aerodynamic coefficients against incidence angle as well as the dynamic drag polar for a variation in x_{morph}/c is presented in Fig. 3.17. In Fig. 3.17a, all values of x_{morph}/c prevent the overshoot in lift and reduce Cl_{max} by approximately 10.3 %. The level of reduction in Cl_{max} is insensitive to the increase in x_{morph}/c. The effect of varying x_{morph}/c is more effective in dynamic stall control during the pitch downstroke.

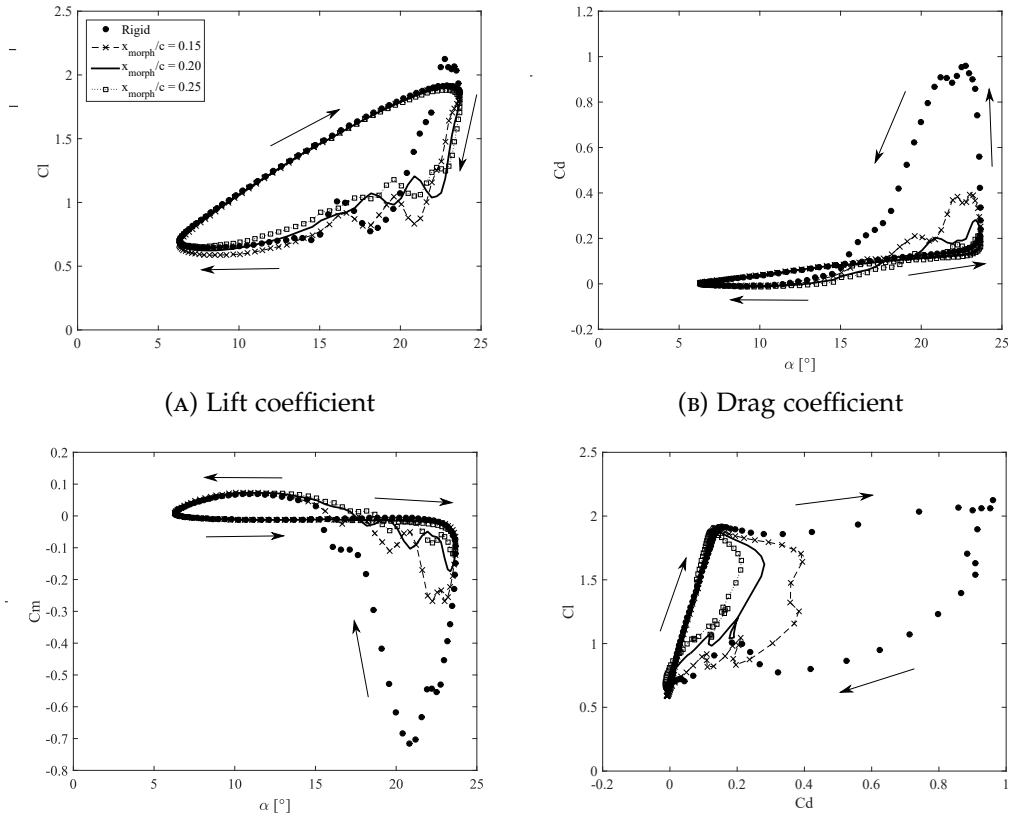

(A) Lift coefficient

(B) Drag coefficient

(C) Moment coefficient

(D) Drag polar

FIGURE 3.17: Aerofoil aerodynamic coefficient results against incidence angle for an increase in proportion of chord with active leading-edge morphing. Comparison made against the rigid aerofoil. Operational conditions: Re = 1.48×10^6, k = 0.153, $\alpha_M = 15°$, $\alpha_{amp} = 8.7°$.

The phase-averaged dynamic lift plot in Fig. 3.17a shows that the initiation of the primary stall occurs earlier for an increase in x_{morph}/c. The magnitude of the primary stall is also reduced for an increase in x_{morph}/c in comparison to the rigid aerofoil. Leading-edge morphing has a pronounced effect on the stall structure during the down-stroke for all x_{morph}/c. Two fluctuation peaks are produced for all x_{morph}/c, in comparison to the one fluctuation peak for the rigid aerofoil, which represents the secondary vortex from dynamic stall. This results in a reduction in the severity of the lift stall and achieves flow reattachment quicker in comparison to the rigid aerofoil. The effect of leading-edge morphing has no influence in reducing the lift hysteresis loop during stall. This results in a reduction in Cl_{mean} for all values of x_{morph}/c. The level of reduction in Cl_{mean} decreases for an increase in x_{morph}/c, with the most effective case, $x_{morph}/c = 0.25$, achieving a 4.7% reduction in Cl_{mean} in comparison to the rigid aerofoil.

There are significant improvements in performance in relation to the drag and moment coefficients when leading-edge morphing is applied for all values of x_{morph}/c. There are significant reductions in the drag-rise and negative nose-down pitching moment for all x_{morph}/c, as shown in Figs. 3.17b and 3.17c respectively. The level of

reduction in the drag-rise and the peak negative pitching moment increases for an increase in x_{morph}/c. There are reductions in Cd_{max} and Cm_{min} of approximately 78% and 83.1% respectively for the most effective leading-edge morphing case x_{morph}/c = 0.25. Leading-edge morphing also has a pronounced effect on reducing the drag and moment hysteresis loops during the pitch down-stroke, with the level of reduction increasing for an increase in x_{morph}/c. The significant decrease in the negative moment hysteresis loop in Fig. 3.17c is directly related to the decrease in structural fatigue of the blade. The positive damping hysteresis loop is also increased for all x_{morph}/c cases in comparison to the rigid aerofoil, which indicated that stall terminates earlier for the morphing aerofoil. Overall, this results in significant performance gains in Cd_{mean} and Cm_{mean} of 65.5% and 92.9% respectively when x_{morph}/c = 0.25.

The dynamic drag polar hysteresis loops illustrated in Fig. 3.17d show significant improvements in the aerodynamic efficiency for all x_{morph}/c cases assessed. This is due to the substantial decrease in drag, with the level of reduction increasing for an increase in x_{morph}/c. The most effective leading-edge morphing case, $x_{morph}/c = 0.25$, produces an aerodynamic efficiency equivalent to 17.3, which results in a 176% increase in aerodynamic efficiency in comparison to the rigid aerofoil.

The effect of increasing the leading-edge morphing chord size is further assessed by evaluating the aerodynamic performance characteristics as shown in Table 3.6. It is evident that there are significant improvements in the time-averaged and peak aerodynamic coefficients for an increase in x_{morph}/c. There is also an increase in aerodynamic efficiency for an increase in x_{morph}/c. This is primarily due to the large reductions in the drag-rise and the peak negative pitch moment as a result of weakening of the LEV's strength. Another reason for larger improvements in aerodynamic efficiency for an increase in x_{morph}/c is due to more of the aerofoil surface area near the leading-edge experiencing lower local incidence angles. This results in this section of the aerofoil maintaining attached flow as well as slowing down the forward movement of the separation point.

x_{morph}/c [deg]	Cl_{av}	Cd_{av}	Cm_{av}	Cl_{max}	Cd_{max}	Cm_{min}	$Caero_{av}$
Rigid	1.000	1.000	1.000	1.000	1.000	1.000	1.000
0.15	0.934	0.505	0.276	0.897	0.410	0.379	1.849
0.20	0.944	0.403	0.125	0.892	0.291	0.245	2.344
0.25	0.953	0.345	0.071	0.884	0.220	0.169	2.760

Table 3.6: Effect of the leading-edge morphing chord size on the time-averaged and peak aerodynamic force and moment coefficients. Data has been normalised with respect to the rigid aerofoil.

The effectiveness of leading-edge morphing with variation in x_{morph}/c is also assessed qualitatively through visualisation of the flowfield, in the form of the non-dimensional vorticity pitch cycle history ($\omega_z^* = \omega_z c/U_\infty$), as shown in Fig. 3.18. The leftmost column represents the non-dimensional vorticity history for the rigid aerofoil, whilst the rightmost column represents the largest x_{morph}/c case, $x_{morph}/c = 0.25$. At α = 23.25° ↑, minimum suction pressure occurs at the leading-edge for the rigid aerofoil which initiates the convection process of the LEV. This stage of the pitch cycle demonstrates that there is minimal influence in the vortex flow structure when x_{morph}/c is varied. At α = 23.75° ↑, the LEV is convecting across the rigid aerofoil's upper surface, which produces a large wake, originating at the leading-edge. The size of the wake is reduced when leading-edge morphing is applied, which is due to the upper surface of the morphing leading-edge section maintaining attached flow. The area of attached flow maintained at the leading-edge morphing section increases for an increase in x_{morph}/c. This also results in a modification of the stall process, with the morphing aerofoil wake more akin to classical vortex shedding. At α = 22.13° ↓, flow separation occurs for the rigid aerofoil due to shedding of the LEV interacting with a strong TEV, which results in the significant loss of lift, and the production of large nose-down pitching moments and drag. This vortex flow structure is not observed for the morphing aerofoil cases, which maintains a traditional Von Karman vortex shedding pattern which is common in static aerofoil stall. The vortex shedding increases for an increase in x_{morph}/c and the size of the wake is smaller in comparison to the rigid aerofoil. At α = 19.05° ↓, separation of the TEV occurs for the rigid aerofoil, which is followed by the formation of a secondary vortex at the leading-edge. For the morphing aerofoil cases, traditional vortex shedding is still produced, however the size of the wake is reduced for all x_{morph}/c. This indicates the beginning of the flow reattachment stage. Finally, at α = 11.03° ↓, both the rigid and leading-edge morphing aerofoils achieve flow reattachment with similar vortex flow structures. This is expected as the pulsed morphing of the leading-edge is terminated for the remainder of the pitch cycle. This supports the conclusion that leading-edge morphing is effective in improving the aerofoil's aerodynamic performance during the pitch downstroke due to alteration of the dynamic stall characteristics.

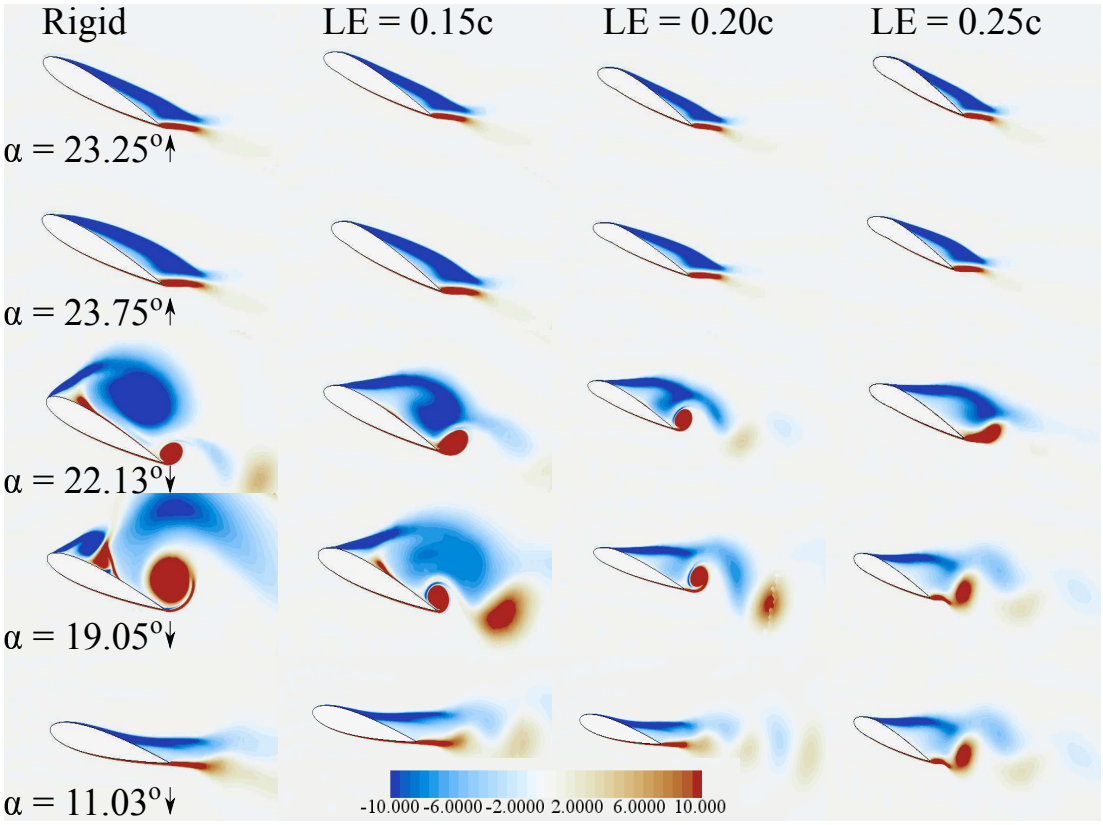

Figure 3.18: Non-dimensional vorticity scalar pitch cycle history ($\omega_z^* = \omega_z c / U_{inf}$). Left to right: Rigid NACA0015 aerofoil, morphing (LE = 0.15c), morphing (LE = 0.20c), morphing (LE = 0.25c). Operational conditions: Re = 1.48 $\times$ 10^6, k = 0.153, $\alpha_M = 15°$, $\alpha_{amp} = 8.7°$.

3.4.4 Effect of morphing type

The next part of this CFD investigation investigates the differences in dynamic stall control though modification of the active leading-edge morphing method. The current method uses control points which are rigidly rotated about a reference point and has fixed boundary points applied to the remainder of the aerofoil surface boundary. The current deformation scheme was also setup so that maximum deformation was applied at the leading-edge point, and the level of deformation decreased linearly towards the fixed boundary points. The alternative active leading-edge morphing method offers a simpler approach to simulate morphing motion and does not require control points as a function of time. Only a reference axis system is required to apply a rigid body rotation about. The alternative leading-edge morphing method is also better suited in representing the leading-edge morphing mechanism used in the experimental analysis which is discussed in Chapter 5.

An illustration of the various morphing methods is shown in Fig.3.19. MT_1 represents the current morphing method which utilises control points and fixed boundary points. MT_{2a} represents the alternative leading-edge morphing method where the morphing reference system is located at the same location as MT_1's reference axis system. The MT_{2a} method is the most representative of the leading-edge morphing mechanism implemented in the experimental analysis section in Chapter 5. MT_{2b} represents the alternative leading-edge morphing method similar to MT_{2a}, however, the morphing reference axis position is positioned below the lowest point on the aerofoil. For both alternative morphing methods, MT_{2a}, and MT_{2b}, a rigid body rotation is applied to the entire leading-edge flap section, which means that all node points that are associated with the leading-edge flap rotate at the same rate and displacement. A rigid body rotation is applied to the remainder of the aerofoil to represent the aerofoil's pitching motion. Finally an inbuilt morphing feature in STAR-CCM+, defined as floating boundary condition, is applied to the remainder of the aerofoil, which allows the remainder of the aerofoil's surface to adapt to the leading-edge flap deformation [83]. A detailed description of the floating boundary mechanism is provided in Section 2.4.

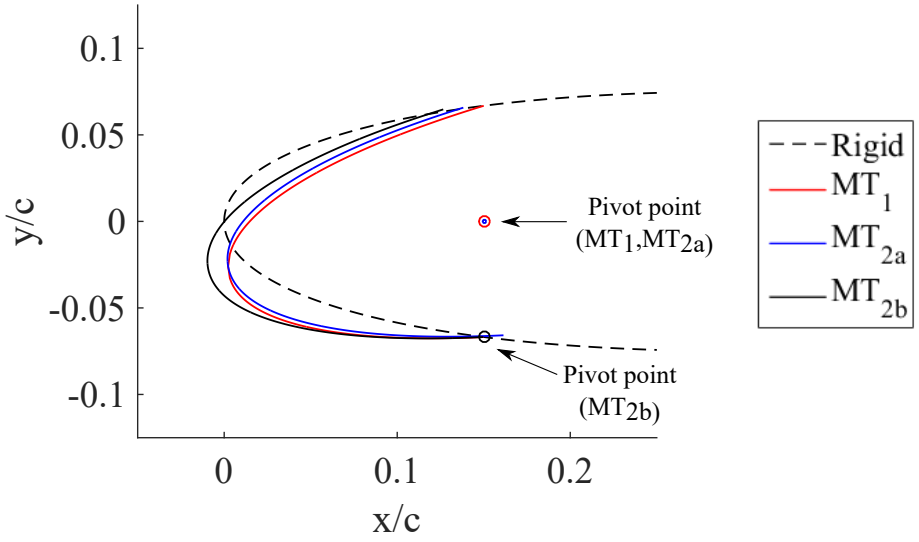

Figure 3.19: Alternative leading-edge morphing deformation methods visualisation.

The phase-averaged aerodynamic force and moment coefficient results for a change in the morphing method is shown in Fig. 3.20. There is minimal change in the aerodynamic coefficients during the pitch upstroke until the maximum incidence is reached for all morphing type methods assessed and when compared against the rigid aerofoil results. All leading-edge morphing methods demonstrate removal of the lift overshoot feature (Fig. 3.20a), which results in the weaker strength of the leading-edge vortex. The biggest differences between the different leading-edge morphing methods are present at the pitch downstroke region.

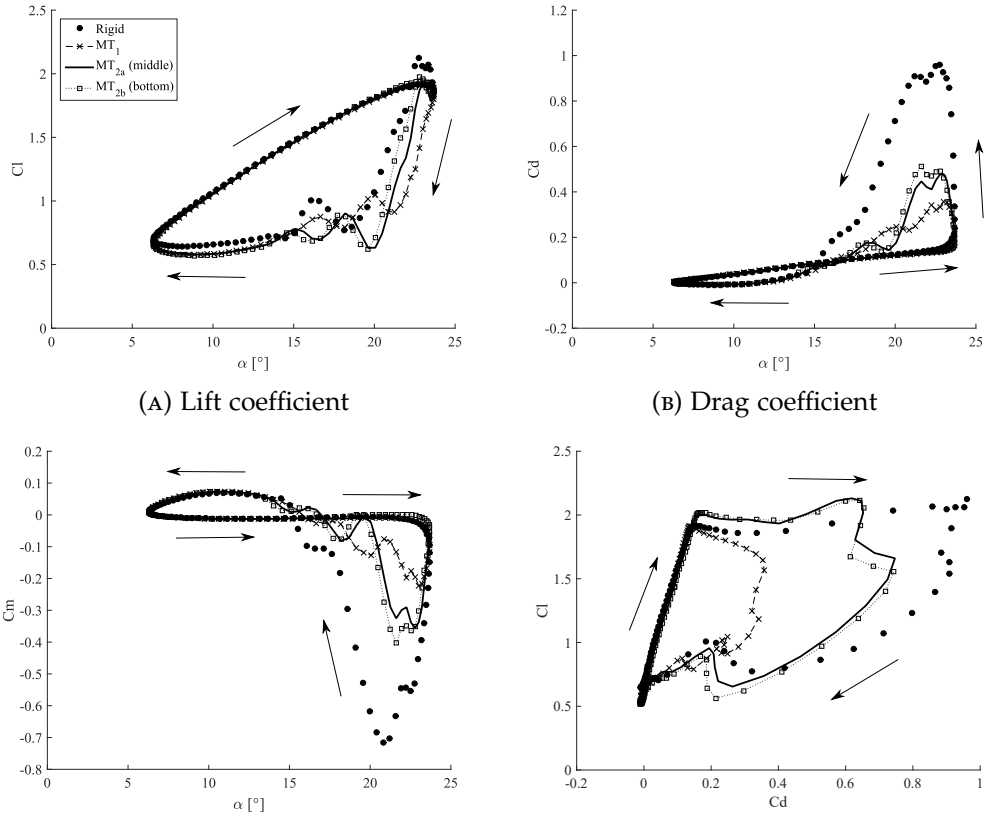

(A) Lift coefficient

(B) Drag coefficient

(C) Moment coefficient

(D) Drag polar

Figure 3.20: Aerofoil aerodynamic coefficient results against incidence angle for a variation in the morphing type method. Comparison made against the rigid aerofoil. Operational conditions: Re = 1.48×10^6, k = 0.153, $\alpha_M = 15°$, $\alpha_{amp} = 8.7°$.

During the pitch downstroke, there are multiple key features which highlight the differences in aerodynamic performance for a change in the leading-edge morphing method. Firstly, there is a change in the incidence angle where lift stall occurs for a change in the leading-edge morphing method, as shown in Fig. 3.20a. This largest delay in lift stall is achieved for MT_{2b}, followed by MT_{2a} and MT_1 respectively. The magnitude of loss in lift is similar for both MT_{2a} and MT_{2b}, which is greater than MT_1. The formation of a secondary leading-edge vortex is present for all leading-edge morphing methods as well as the rigid aerofoil. Once the motion of the leading-edge flap deformation has terminated, similar lift results are generated for all leading-edge morphing methods assessed.

There is also a significant decrease in the Cd_{max} and Cm_{min} for all leading-edge morphing methods assessed compared against the equivalent results for the rigid aerofoil. Figure 3.20b illustrates that the largest reduction in Cd_{max} is achieved when using MT_1, although MT_{2a} and MT_{2b} are shown to produce similar reductions in Cd_{max}. The moment coefficient results in Fig. 3.20c show that MT_1 achieves the largest reduction in Cm_{min}, with MT_{2a} and MT_{2b} producing similar levels of reduction. The transition from negative pitch damping to positive pitch damping occurs earlier for MT_{2a} and MT_{2b} than for MT_1. For the positive pitch damping loop, there are no differences when comparing all leading-edge morphing methods to the rigid aerofoil results.

The dynamic drag polar results for changes in the leading-edge morphing method is presented in Fig. 3.20d. During the linear rate increase portion, the morphing methods, MT_{2a+b} generate a larger increase in lift than for MT_1 and the rigid aerofoil. It is evident that the leading-edge morphing method, MT_1 produces the largest increase in the aerodynamic efficiency which is shown by achieving the largest reductions in the drag polar hysteresis loops. There is also an increase in aerodynamic efficiency for both leading-edge morphing methods MT_{2a} and MT_{2b}, and the drag-polar hysteresis loops are of similar magnitude.

The aerodynamic performance results for the different leading-edge morphing method are tabulated in Table 3.7. It is clear that the leading-edge morphing method, MT_1, achieves the largest improvements in aerodynamic performance when compared against MT_{2a} and MT_{2b}. All leading-edge morphing methods however achieve significant gains in aerodynamic performance when compared to the rigid aerofoil results. For the alternative leading-edge morphing method, it is shown that MT_{2a} produces larger reductions in Cd_{av}, Cd_{max}, and Cm_{min} when compared to MT_{2b}, although the differences are small. The aerodynamic efficiency increase is also slightly larger for MT_{2a} than for MT_{2b}, although MT_1 is shown to achieve a much larger increase in aerodynamic efficiency.

Morphing method	Cl_{av}	Cd_{av}	Cm_{av}	Cl_{max}	Cd_{max}	Cm_{min}	$Caero_{av}$
Rigid	1.000	1.000	1.000	1.000	1.000	1.000	1.000
MT_1	0.928	0.506	0.242	0.899	0.372	0.313	1.834
$MT_{2a}(middle)$	0.941	0.552	0.348	0.910	0.495	0.497	1.705
$MT_{2b}(bottom)$	0.954	0.571	0.337	0.933	0.529	0.563	1.673

Table 3.7: Effect of the leading-edge morphing type method on the time-averaged and peak aerodynamic force and moment coefficients. Data has been normalised with respect to the rigid aerofoil.

The differences in the aerodynamic performance characteristics for a changes in the leading-edge morphing method are further investigated by evaluating the change in the aerofoil's surface pressure distribution as well as the flow-field characteristics. Two key features of the flow-field characteristics are assessed which include the point at which Cp_{min} occurs for the rigid aerofoil, and the convection of the leading-edge vortex.

Visualisation of the Cp scalar and surface Cp distribution plots at Cp_{min} for a change in the leading-edge morphing method are shown in Fig. 3.21. It is evident that the flow-field features are similar for all leading-edge morphing methods when evaluating the Cp scalar plots (Figs. 3.21a, 3.21b and 3.21c), and the surface Cp distribution plots (Figs. 3.21d, 3.21e and 3.21f). When analysing the surface Cp distribution plots in (Figs. 3.21d, 3.21e and 3.21f), there are no changes to the curve trend features for both the pressure and suction surface when changing the leading-edge morphing method. The main difference is that Cp_{min} is slightly larger for MT_1 than for MT_{2a} and MT_{2b}, which can be linked to the change in the leading-edge morphing mechanism.

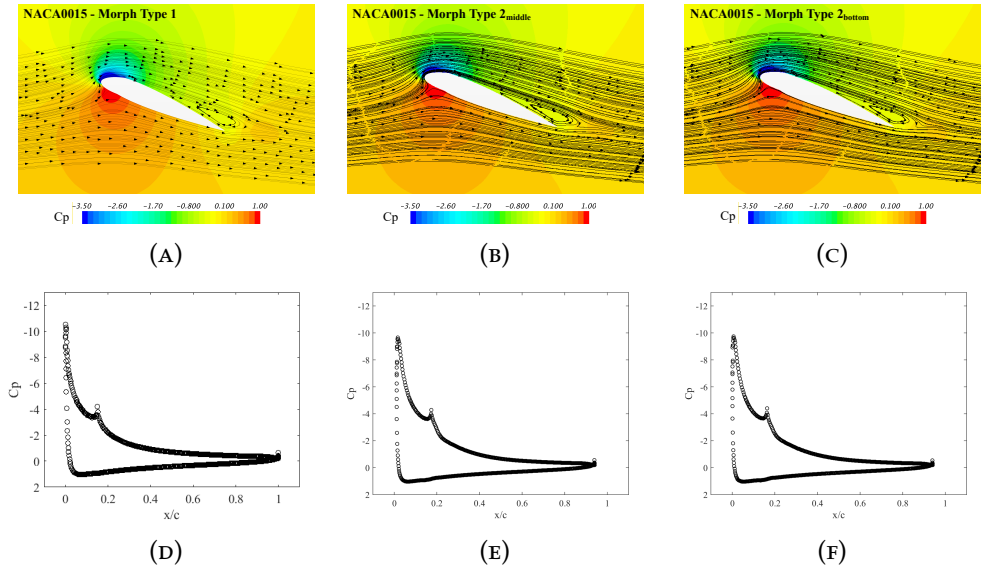

Figure 3.21: Pressure coefficient scalar visualisation and aerofoil surface pressure coefficient distribution. (a) & (c): Rigid NACA0015 aerofoil. (b) & (d): Morphing leading-edge amplitude, $\beta_{max} = 10°$. $\alpha = 23.3°\uparrow$, Re =1.48 $\times$ 10^6,k= 0.153,$\alpha_M = 15°$, $\alpha_{amp} = 8.7°$.

A visualisation of the Cp scalar and surface distribution plots for a change in the leading-edge morphing method, at the point of LEV convection, is shown in Fig. 3.22. The Cp scalar plots clearly demonstrate the separation of the LEV and formation of the TEV for MT_1 (Fig. 3.22a), whereas the only flow feature present for MT_{2a} and MT_{2b} is convection of the LEV, as shown in Figs. 3.22b and 3.22c. This confirms that there is a delay in the lift and moment stall when implementing the alternative leading-edge morphing method (MT_{2a} and MT_{2b}), in comparison to MT_1. The Cp surface distribution plots in Figs. 3.22d, 3.22e & 3.22f show that the flow remains attached at the leading-edge flap's suction surface for all leading-edge morphing methods assessed. The Cp surface distribution for MT_1 in Fig. 3.22d illustrates a negative Cp peak at the trailing-edge which highlights the formation of the TEV. This feature is not present for MT_{2a} and MT_{2b} as shown in Figs. 3.22e and 3.22f respectively. There is only a pressure ridge present for both MT_{2a} and MT_{2b} which highlights the convection of the LEV. There is no difference in the Cp surface distribution at the aerofoil's pressure surface for all leading-edge morphing methods assessed.

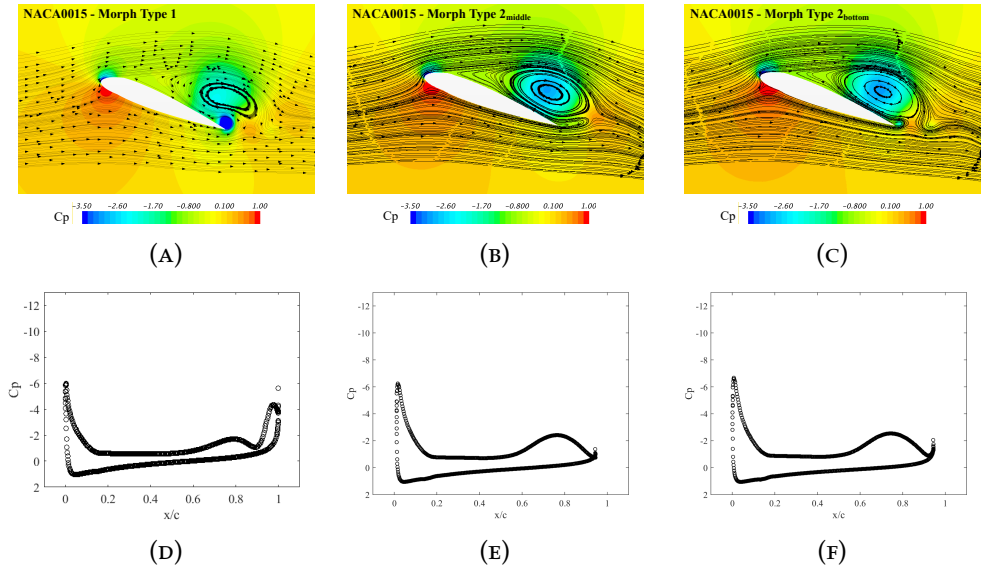

Figure 3.22: Pressure coefficient scalar visualisation and aerofoil surface pressure coefficient distribution. (a) & (c): Rigid NACA0015 aerofoil. (b) & (d): Morphing leading-edge amplitude, $\beta_{max} = 10°$. $\alpha = 22.6°\downarrow$, Re =1.48 $\times$ 10^6,k= 0.153,$\alpha_M = 15°$, $\alpha_{amp} = 8.7°$.

3.4.5 Effect of reduced frequency

The final part of this CFD study investigates the effect that variation of the reduced frequency has on the dynamic stall characteristics when active leading-edge morphing is applied. The CFD results previously discussed were performed using a reduced frequency value k = 0.153. Next, a lower reduced frequency value is assessed which has the value k =0.1021. This value was selected as it is the setting which is used in the experimental analysis in Chapter 5. A single leading-edge morphing amplitude is assessed, $\beta_{max} = 10°$ which was selected as it was deemed to be the most effective setting in terms of improving aerodynamic performance during dynamic stall. The morphing method MT_{2a} is utilized as it provides the most accurate representation of the leading-edge flap deformation for the experimental model as discussed in Chapter's 4 and 5. To maintain consistency, no other CFD operational parameters are changed.

The phase-averaged aerodynamic force and moment coefficient results for a variation in reduced frequency is shown in Fig. 3.23. At mean incidence during the pitch upstroke, there is little difference in the aerodynamic coefficients for a change in k when comparing against the rigid aerofoil and leading-edge morphing aerofoil. The lift overshoot feature is captured for both k values as shown in Fig. 3.23a, however the lower reduced frequency value (k = 0.1021) results in a small decrease in lift shortly before the overshoot. This also leads to the lift overshoot occurring earlier and consequently lift stall. Figure 3.23b illustrates that the significant drag-rise is predicted for both k values, however the onset of the drag-rise occurs at an earlier incidence angle for the lower reduced frequency, k = 0.1021. Moreover, the moment coefficient

results in Fig. 3.23c shows that the moment stall incidence angle occurs earlier for the lower reduced frequency in comparison to k = 0.153.

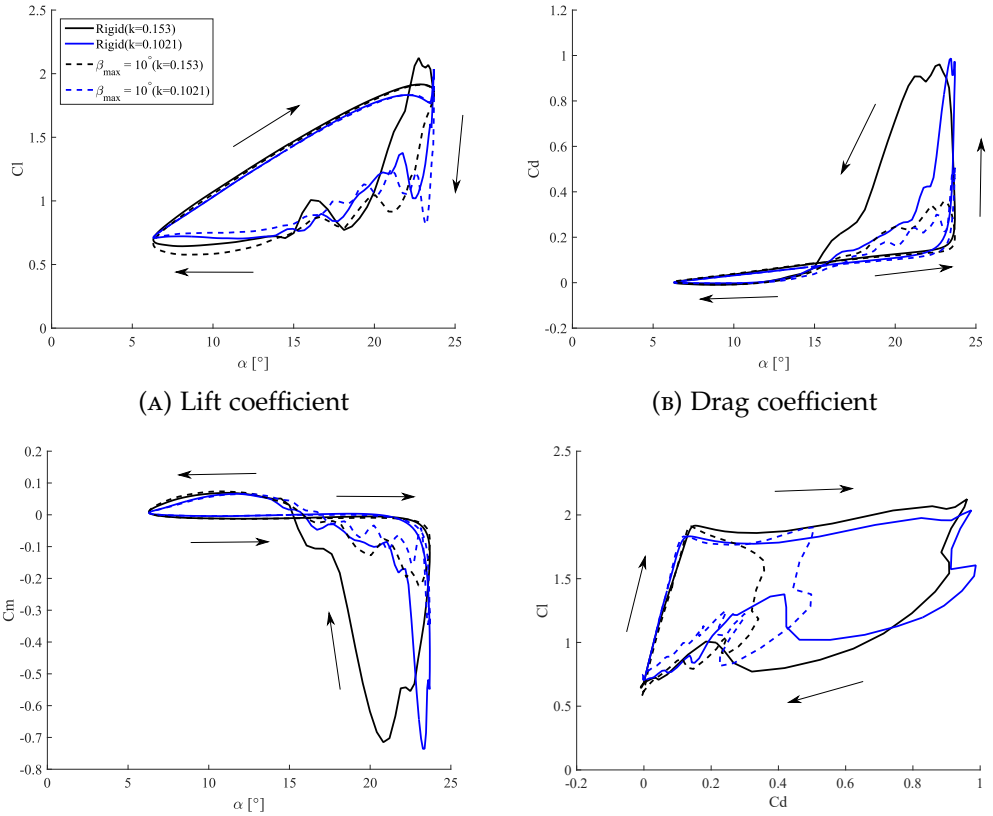

(A) Lift coefficient

(B) Drag coefficient

(C) Moment coefficient

(D) Drag polar

Figure 3.23: Aerofoil aerodynamic coefficient results against incidence angle for a variation in reduced frequency. Comparison made against the rigid aerofoil. Operational conditions: Re = 1.48×10^6, k = 0.153, $\alpha_M = 15°$, $\alpha_{amp} = 8.7°$.

During the pitch downstroke, there are similar trends in the aerodynamic curve features when comparing the rigid aerofoil aerodynamic coefficient results for a change in reduced frequency. The lift coefficient results in Fig. 3.23a show that a secondary vortex is generated for both reduced k values, however the lift overshoot loop is only predicted for k = 0.153. This implies that the increase in the pitch rate results in a delay of lift stall due to delaying the formation of the primary LEV. The delay in lift stall at k = 0.153 results in a larger production of drag and negative pitching moments for the rigid aerofoils during the pitch down-stroke as shown in Figs. 3.23b and 3.23c respectively. The transition from negative to positive pitch damping occurs earlier at k = 0.1021 which is due to the moment stall occurring earlier.

The implementation of active leading-edge morphing produces similar effects when applying a variation in reduced frequency. Figure 3.23a shows that leading-edge morphing prevents the lift overshoot feature for both reduced frequency values, although the level of reduction in lift hysteresis is similar when compared against the lift hysteresis loop for the rigid aerofoil. Leading-edge morphing is most effective

when assessing the changes in the drag and moment coefficients for both reduced frequency settings. There is a significant reduction in the drag-rise and peak negative moment coefficients for the leading-edge morphing results at both reduced frequency values.

The dynamic drag polar results in Fig. 3.23d demonstrate that leading-edge morphing is effective in improving aerodynamic efficiency for the two reduced frequency values assessed. At the linear section during the pitch upstroke, larger values of lift are generated at k = 0.153 for both the rigid and leading-edge morphing aerofoil. This results in higher lift being generated during the drag-rise section, however it is shown that maximum drag is larger at the lower reduced frequency setting, k = 0.1021. When comparing the leading-edge morphing aerofoil results, the improvement in aerodynamic performance is greater at k = 0.153 which is due to achieving the largest reduction in the drag polar hysteresis loop.

The effect of leading-edge morphing with a variation in reduced frequency is further assessed by evaluating the time-average and peak aerodynamic coefficients, as shown in Table 3.8. The results are normalised against the rigid aerofoil results at their respective reduced frequency setting. It is clear that the greatest improvements in the aerodynamic efficiency are achieved when the reduced frequency is increased (within the reduced frequency range explored). When assessing the time-averaged aerodynamic coefficients, the largest reductions in Cd_{av} and Cm_{av} are achieved at k = 0.1521. The largest reductions in Cd_{max} and Cm_{min} are also achieved at k = 0.1521 and also achieves the largest improvement in aerodynamic efficiency. It should be noted however that significant improvements in aerodynamic performance are also achieved at the lower reduced frequency setting, k = 0.1021.

Morphing method	Cl_{av}	Cd_{av}	Cm_{av}	Cl_{max}	Cd_{max}	Cm_{min}	$Caero_{av}$
Rigid	1.000	1.000	1.000	1.000	1.000	1.000	1.000
$\beta_{max} = 10^{\circ} (k = 0.1521)$	0.928	0.506	0.242	0.899	0.372	0.313	1.834
$\beta_{max} = 10^{\circ} (k = 0.1021)$	0.980	0.592	0.386	0.933	0.511	0.481	1.657

Table 3.8: Effect of reduced frequency variation on the time-averaged and peak aerodynamic force and moment coefficients. Data has been normalised with respect to the rigid aerofoil.

3.5 CONCLUSIONS

A CFD investigation of a single, pitch oscillating NACA0015 aerofoil with active leading-edge morphing has been performed under deep dynamic stall conditions. The main purpose of this study is to assess the effect of leading-edge morphing on the dynamic stall characteristics when compared against a rigid NACA0015 aerofoil. A detailed parametric study was performed which evaluated different parameters relating to leading-edge morphing.

Leading-edge morphing is very effective in achieving dynamic stall alleviation and improving the aerodynamic characteristics across the leading-edge morphing amplitude range assessed. There are significant reductions in the time-average and peak drag and moment coefficients when comparing the leading-edge morphing aerofoil against the rigid aerofoil. 10 degrees was the most effective leading-edge morphing amplitude setting due to achieving the largest increase in aerodynamic efficiency as well achieving the largest reductions in drag and pitching moment. The level of increase in aerodynamic efficiency gains when increasing the leading-edge morphing amplitude from 5 to 10 degrees.

Leading-edge fixed droop is also very effective in achieving dynamic stall alleviation and improving the aerodynamic characteristics across the deflection amplitude range assessed. There are similar improvements in the aerodynamic characteristics when comparing the leading-edge fixed droop method to the leading-edge morphing method. The rate of reduction in drag during dynamic stall is larger when applying leading-edge fixed droop in comparison to applying leading-edge morphing. This is due to the reduction in local incidence at the leading-edge surface as a result of the fixed-camber leading-edge section. The implementation of leading-edge fixed droop also leads to an overall change in the aerofoil's aerodynamic characteristics due to a change in the physical camber. When applying leading-edge fixed droop to blades of a cycloidal rotor, this means that performance gains could be achieved at the rotor advancing, however this could also lead to detrimental effects in performance at the rotor retreating side due to the introduction of negative physical camber.

There is an increase in the aerodynamic characteristics for an increase in the proportion of aerofoil chord which has leading-edge morphing applied. the level of improvements in aerodynamic efficiency increases for an increase in the leading-edge morphing chord size from 15 % to 25 %. The main reason for the performance gains for an increase in the leading-edge morphing chord size is due to the onset of the primary dynamic stall occurring earlier. This also leads to flow-reattachment occurring earlier for the larger leading-edge morphing chord size.

An alternative leading-edge morphing method was assessed which was simpler to implement and is more representative of the leading-edge morphing mechanism used in the experimental analysis (which is discussed in Chapter 5). The results showed that there is little difference in the aerodynamic characteristics between both leading-edge

morphing methods during the pitch upstroke. At the pitch downstroke, there is small modifications of the aerodynamic hysteresis loops and the incidence angle at which lift stall occurs. Both leading-edge morphing methods however demonstrate significant improvements in the aerodynamic characteristics when compared against the rigid aerofoil.

Finally, it was shown that increasing the reduced frequency (within the range assessed) improved the effect that leading-edge morphing had on the aerodynamic efficiency when compared against the rigid aerofoil. This is due to a delay in the formation of the leading-edge vortex because of the larger reduced frequency for the rigid aerofoil. This resulted in a larger generation of drag and negative pitching moment during the pitch downstroke.

CHAPTER 4

EXPERIMENTAL METHODOLOGIES

4.1 INTRODUCTION

Dynamic stall wind tunnel testing of a NACA0015 aerofoil section with an active leading-edge flap is performed to act as validation against the results obtained from the CFD analysis in Chapter 3. Key findings from the CFD analysis in Chapter 3 demonstrated that a NACA0015 aerofoil with a morphing leading-edge section of 15 % chord mitigated the negative effects of dynamic stall through: weakening of the LEV by reducing the peak minimum pressure coefficient, Cp_{min}, removal of the dynamic lift overshoot, reduction in the drag-rise, reduction in the peak negative moment and negative pitch damping loop, and reducing the level of aerodynamic hysteresis during the pitch downstroke. The main objective of this experimental study is to determine whether the leading-edge morphing performance enhancements which were predicted by the CFD model are captured with the leading-edge flap wind tunnel model. Details of the methods used in the experimental design process are discussed here.

4.2 WIND TUNNEL

Experimental dynamic stall testing is performed using the Handley-Page, low-speed wind tunnel at the University of Glasgow's wind tunnel test facility. The wind tunnel is of a closed return type with a 1.61 m by 2.13 m octagonal working section [102]. The aerofoil model is mounted vertically inside the wind tunnel test section and is pivoted about the quarter chord point using a linear hydraulic actuator and crank mechanism. An illustration of the Handley-Page wind tunnel schematic diagram as well as the schematic for the hydraulic actuator test rig is shown in Fig. 4.1. The wind tunnel turbulence intensity has been previously measured from similar experimental studies, with the results shown in Fig. 4.2 [102]. The wind tunnel maximum velocity is set to approximately 30 m/s for all test cases performed in this study, therefore the turbulence intensity is expected to be $\leq$ 2%.

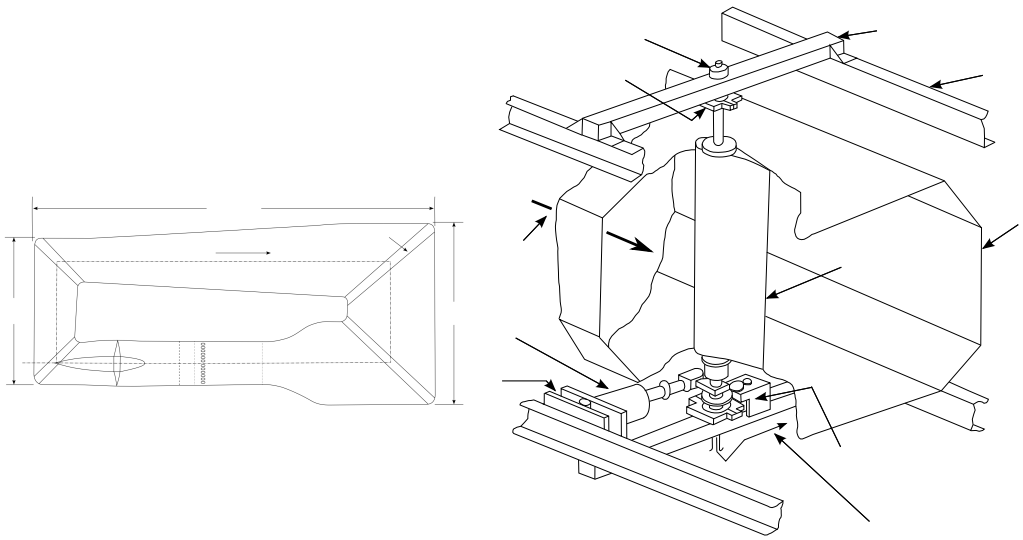

(a) Wind tunnel schematic (b) Hydraulic actuator test rig

Figure 4.1: Schematic diagram illustrations of the Handley-Page low speed wind tunnel and the hydraulic actuator test rig [102].

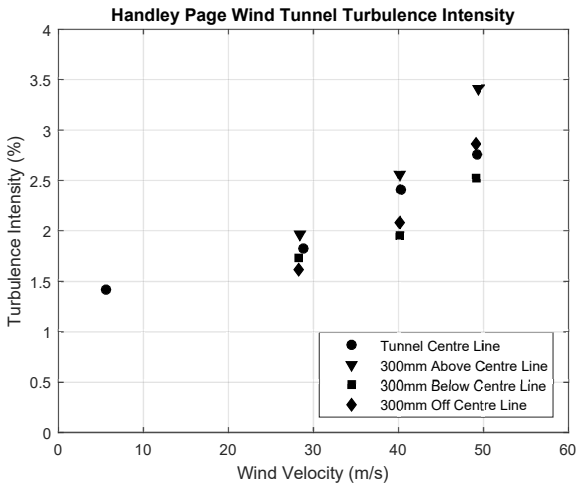

Figure 4.2: Wind tunnel turbulence intensity results against a variation in the wind tunnel velocity [102].

4.3 CAD MODEL DESIGN

The design of the NACA0015 leading-edge flap model was performed using the commercial CAD software package, SolidWorks. An illustration of the leading-edge flap NACA0015 aerofoil design is shown in Fig. 4.3. To simplify the morphing mechanism for the leading-edge morphing aerofoil, the leading-edge was split into two parts: a leading-edge flap which covered 15 % of the chord section, and the remainder of the aerofoil section. A circular recess is formed on the aerofoil section to allow for slotting of the leading-edge flap. The 1mm gap formed by the slot is sealed using thick, low coefficient friction tape, which is applied to the circular recess of the aerofoil section [107]. The leading-edge flap pitch motion is driven by a STA2510 linear Servotube Actuator (STA) which is supplied by Copley Motion Corp [108]. The active mechanism for the leading-edge flap consists of the STA, and a slider-yoke mechanism moment arm which is attached to the leading-edge flap's shaft. The main function of this mechanism is to transform the linear input motion applied by the STA into a rotational output motion which is applied to the leading-edge flap. The linear actuator and flap mechanism will be discussed later.

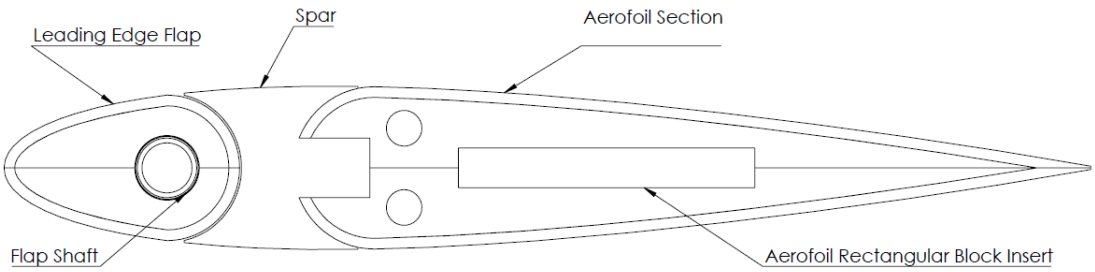

Figure 4.3: Leading-edge flap NACA0015 aerofoil design.

The leading-edge flap aerofoil model has a chord length, c = 0.55 m, and an effective span, b = 1 m. The total span of the model is 1.61 m which includes the actuator support attachments required for housing the linear actuator as well as mounting the model to the tunnel. The leading-edge flap's pitch axis is set at 15% of the chord and is supported by taper roller bearings and shaft clamp collars to prevent rotational friction. Circular end-plates are installed on the model to remove any three-dimensional effects caused by dynamic stall as well as interference from the external model attachments [72, 73]. The end plate diameter size, $D_{endplate}$, was set based on sizings from a previous experimental dynamic stall study, which used a ratio, $D_{endplate}/c$ = 2 [109]. The spacing between the leading-edge flap and the end plates was set to 1 mm to minimise any leakage of air flow through the gap.

The manufacturing process for the leading-edge flap and aerofoil section involved a mold layup design. Two molds were produced which contained the outer profiles of the leading-edge flap and aerofoil section. Six layers of fibreglass weave cloth with an approximate total thickness of 6 mm were bonded to the mold using vinyl-ester resin and cured. Once the fibreglass skin had set, the ribs were then bonded to the skin for both the leading-edge flap and aerofoil section. The material selected for the ribs was a high density foam supplied by SikaBlock (M330), which has been previously used in previous wind tunnel models tested at the University of Glasgow. The sizing of the outer and inner ribs were based on previous dynamic stall wind tunnel models developed at the University of Glasgow. The leading-edge flap shaft and the aluminium inserts for the aerofoil section are bonded to the models and both halves of each part are bonded together to seal the model. The pressure transducers which are used for the surface pressure measurements, are bonded to both the leading-edge flap and aerofoil section before the model is sealed. Filler foam was used for both the leading-edge flap and aerofoil section to prevent any external flow leakage, and both models had an air breather tube installed which allowed for atmospheric conditions inside the sealed model. A schematic of the aerofoil model layup design for the leading-edge flap and aerofoil section is shown in Fig. 4.4.

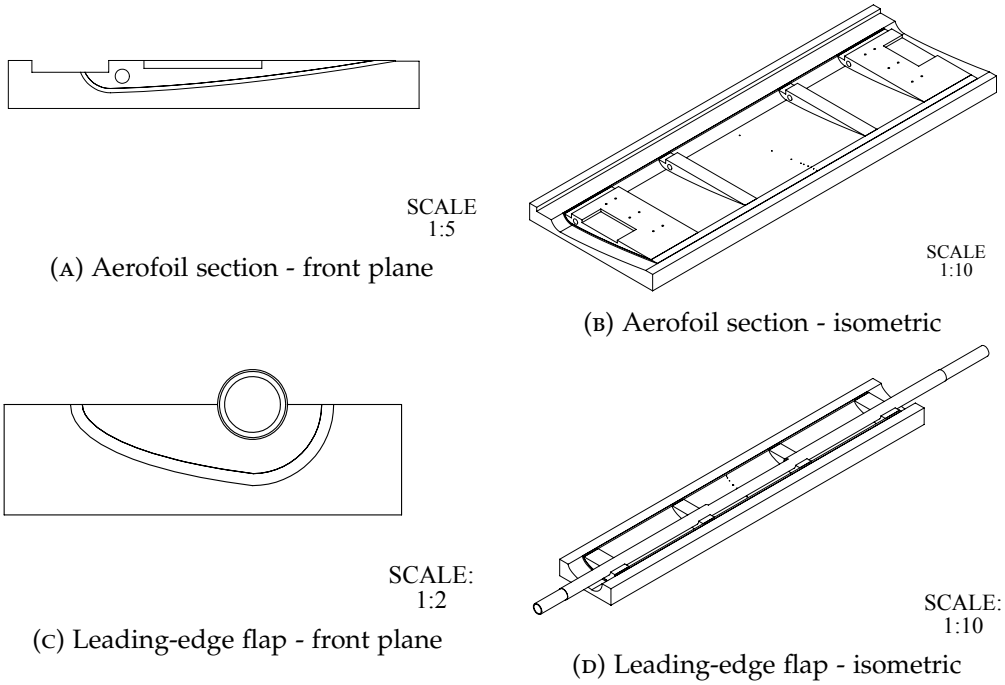

(a) Aerofoil section - front plane

(b) Aerofoil section - isometric

(c) Leading-edge flap - front plane

(d) Leading-edge flap - isometric

Figure 4.4: Wing model layup design.

Illustrations of the full model assembly are visualised in Fig. 4.5. Due to the design complexities of the circular recess for the aerofoil section, an aluminium spar with an extrusion was manufactured and bonded to the two halves of the aerofoil section ribs, as shown in Fig. 4.5a. This design choice simplified the mold layup process and ensured sufficient stiffness near the model's pitch axis. The linear actuator used to actuate the leading-edge flap is positioned at the top of the model and is fixed using an actuator support attachment, as illustrated in Fig. 4.5b. An illustration of the free-stream velocity direction, U_∞, is shown in Fig. 4.5c. The wind tunnel's hydraulic actuator system, which is positioned below the wind tunnel test section, drives the leading-edge flap model as well as the STA. The leading-edge flap motion which is provided by the STA is superimposed on the main pitch oscillation motion provided by the hydraulic actuator. An exploded view of the full model assembly is shown in Fig. 4.6. The bill of materials is presented in Appendix A.

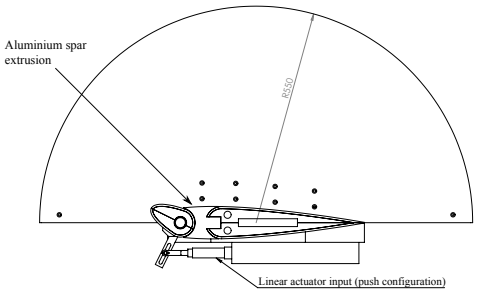

(a) Front plane

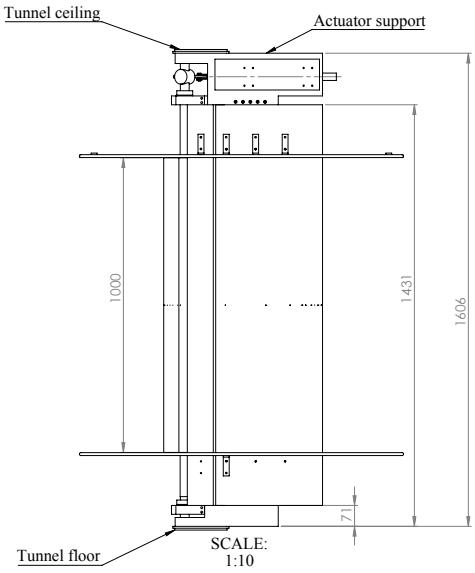

(b) Top plane

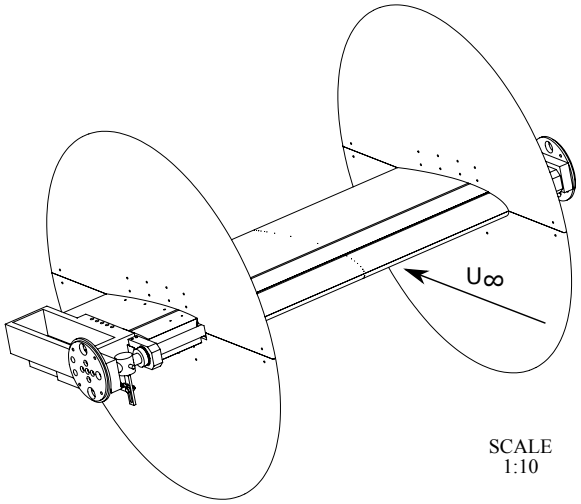

(c) custom view

Figure 4.5: Full model assembly.

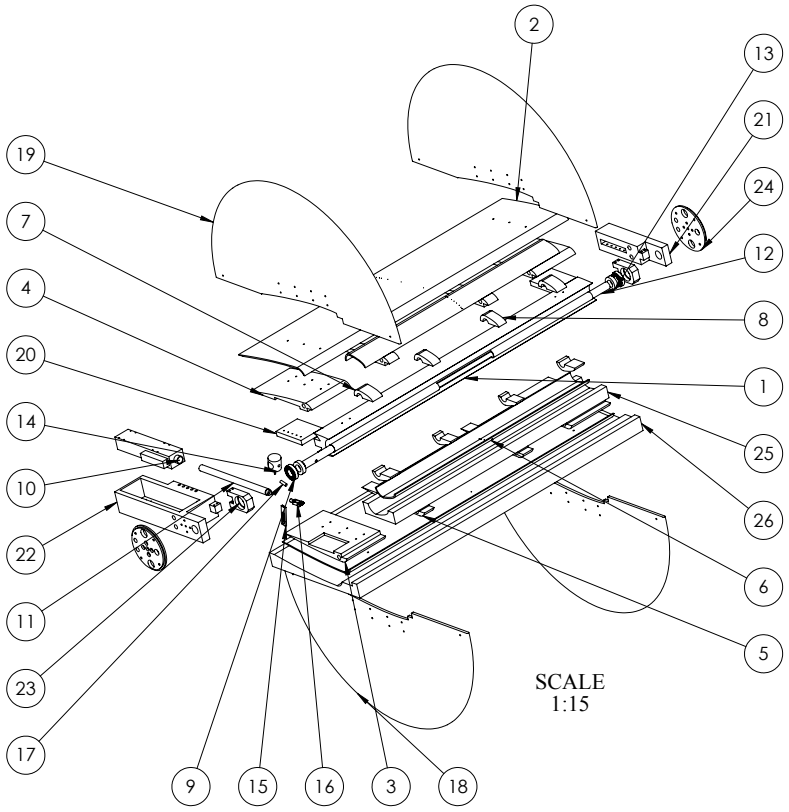

Figure 4.6: Exploded view visualising all parts featured in the leading-edge flap model.

A visualisation of the leading-edge flap NACA0015 aerofoil model, which is fully installed in the wind tunnel test section is shown in Fig 4.7. Additional steel support attachments were applied to the end plates which are connected to the model. This was implemented to improve the stiffness of the end plates and reduce the level of bending and vibration. The servotube actuator's cabling was secured to the end plates and guided out of the tunnel which is where the STA's amplifier was positioned.

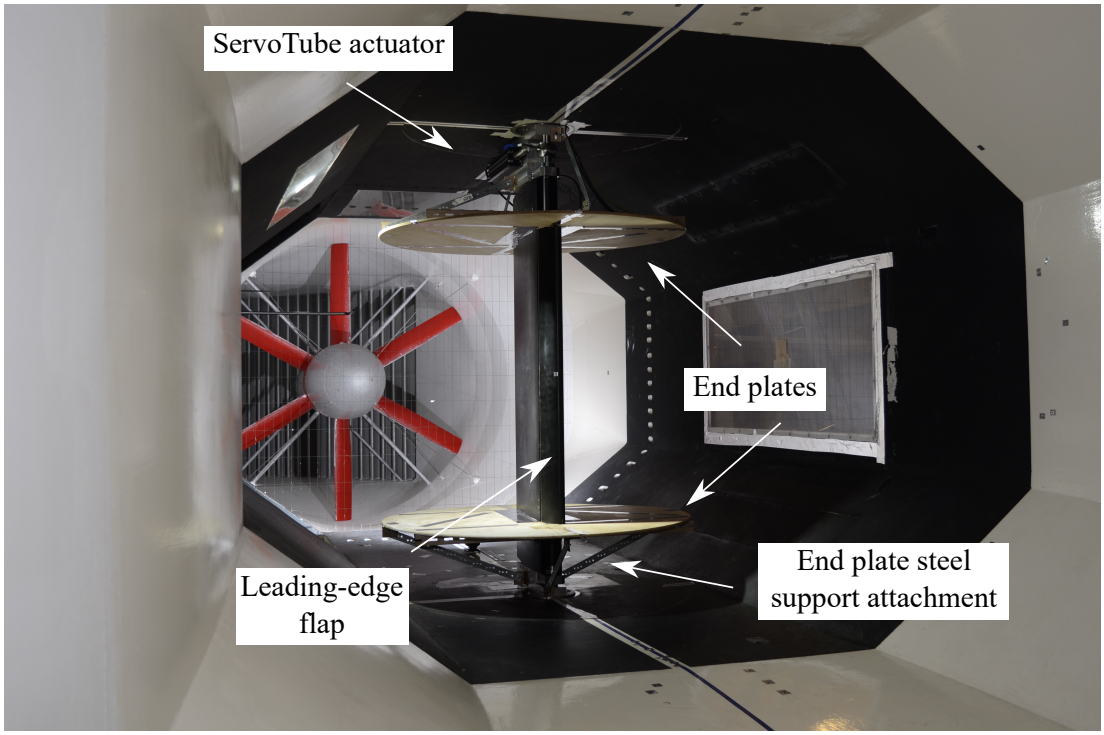

FIGURE 4.7: A visualisation of the leading-edge flap NACA0015 aerofoil model installed in the wind tunnel's test section.

4.4 CFD ANALYSIS - MODEL DESIGN CHECK

A CFD analysis of a single NACA0015 aerofoil with active leading-edge morphing (using the CFD model developed in Chapter 3) is performed and compared against previous experimental data obtained at the University of Glasgow. Both the clean aerofoil configuration and the 2 mm step aerofoil configuration are assessed to determine whether the step created by the implementation of the leading-edge flap alters the dynamic stall characteristics when compared against the clean configuration aerofoil.

For the operational conditions, the leading-edge morphing amplitude was set to $\beta_{max} = 10°$, as this setting was previously shown in the CFD results in Chapter 3 to achieve the largest improvements in aerodynamic performance. The proportion of the aerofoil chord section which has leading-edge morphing applied was set to $0.15c$. Pulsed, leading-edge morphing is initialised at the mean incidence angle, α_M, during the upstroke and terminates at α_M during the downstroke. The flow conditions used in this study are $Re = 1,008,100$, $\alpha_M = 17°$, $\alpha_{amp} = 8°$, and $k = 0.1021$. The flow condition set for this study is lower in comparison to the flow conditions set in Chapter 3. This is due to the physical limitations of the servotube actuator's force capability to hold the leading-edge flap at a fixed position. Therefore, the decision was made to reduce the size of the leading-edge flap, the wind-tunnel velocity, and the model pitch rate in order to reduce the required leading-edge flap actuator force, while still achieving fully turbulent flow conditions ($Re \geq 1,000,000$) and flow unsteadiness ($k \geq 0.1$). All computational simulations are performed over 10 periodic pitch cycles

and the aerodynamic characteristics are phase-averaged over the last five cycles.

The phase-averaged aerodynamic force and moment coefficient results for the rigid, clean aerofoil configuration as well as the 2 mm step rigid aerofoil configuration predicted by CFD is shown in Fig. 4.8. The addition of the 2 mm step on the suction and pressure surface of the aerofoil is shown to maintain the key features of dynamic stall and differences only occur for the predicted magnitude. There is little difference in the phase variation between the clean configuration and 2 mm step aerofoil configuration.

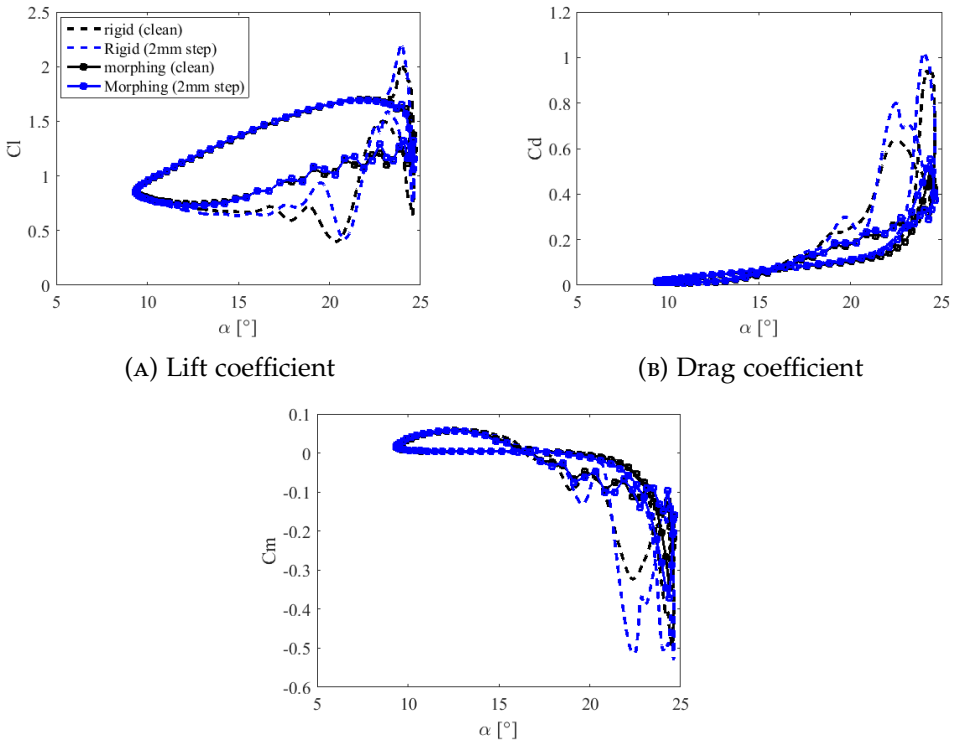

(A) Lift coefficient

(B) Drag coefficient

(C) Moment coefficient

FIGURE 4.8: Phase-averaged aerodynamic coefficient characteristics comparison against the rigid and leading-edge morphing NACA0015 aerofoil with and without an outer 2 mm step. Operational conditions: Re = 1,008,100, $\alpha_M = 17°$, $\alpha_{amp} = 8°$, k = 0.1021.

The effect of leading-edge morphing for both the clean surface aerofoil configuration and the 2 mm step surface aerofoil configuration are assessed to determine whether the inclusion of the step alters the performance benefits gained from leading-edge morphing. The phase-averaged aerodynamic characteristics for the clean surface aerofoil configuration and the 2 mm step aerofoil configuration with leading-edge morphing applied, is shown in Fig. 4.8. For the clean surface aerofoil configuration, the effect of leading-edge morphing is shown to remove the dynamic lift overshoot as well as reduce the level of lift hysteresis, as demonstrated in Fig. 4.8a. Moreover, there are significant reductions in Cd_{max} and Cm_{min}, as well as the level of hysteresis during the pitch downstroke when leading-edge morphing is applied, as shown in Figs. 4.8b & 4.8c respectively. The inclusion of the 2 mm step produces minor differences in the performance improvements due to leading-edge morphing when compared against the clean surface aerofoil configuration. This analysis concludes that the inclusion of the 2 mm step as a result of the experimental model design should not have a significant influence on the alteration of the dynamic stall results for both the rigid and morphing test cases.

Finally, the effect of the rigid, 2 mm step aerofoil configuration is further examined by qualitatively assessing the flowfield characteristics from the CFD analysis. An illustration of the non-dimensional velocity magnitude scalar plot is shown in Fig. 4.9. For the clean surface aerofoil configuration as visualised in Fig. 4.9a, the non-dimensional velocity magnitude scalar plot illustrates key flow features such as: large levels of suction at the leading-edge upper surface, stagnation pressure at the lower surface, and the development of the boundary layer along the aerofoil's upper surface during the pitch upstroke at $\alpha_M = 17^\circ$. The inclusion of the 2 mm step for the experimental model's surface in Fig. 4.9b shows little variation in the flowfield structure, with the only clear differences being the small areas of stagnation pressure regions created by the steps on both the upper and lower surface. Both of the stagnation pressure regions created by the 2 mm steps are shown to not produce any significant alterations to the boundary layer characteristics for the majority of the pitch cycle.

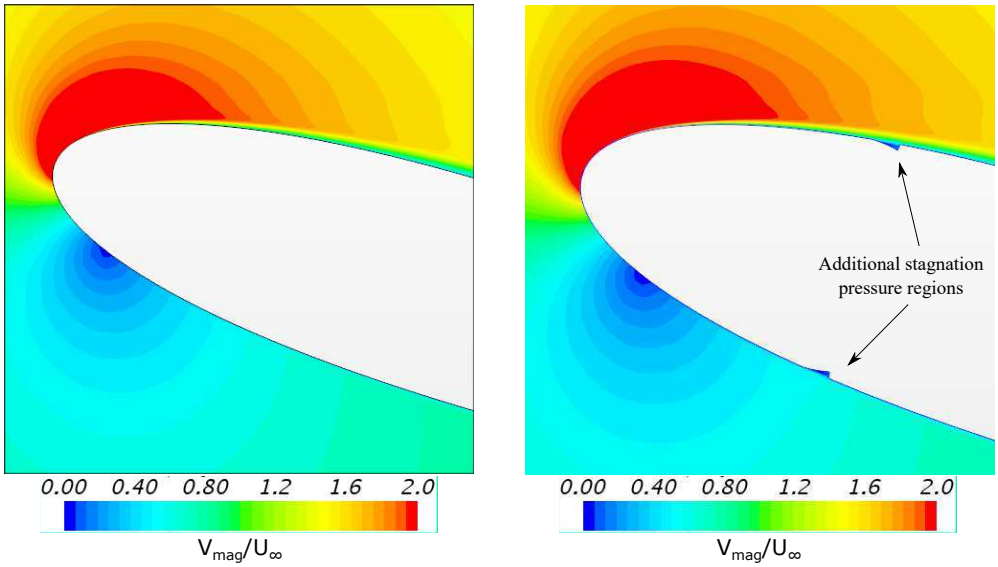

(A) Clean surface (B) 2mm step surface

FIGURE 4.9: CFD predicted non-dimensional velocity magnitude comparison between a rigid NACA 0015 aerofoil with and without a 2 mm step at 17 degrees incidence during the pitch upstroke. Operational conditions: Re = 1,008,100, $\alpha_M = 17°$, $\alpha_{amp} = 8°$ k = 0.1021

4.5 INSTRUMENTATION

WIND TUNNEL CONTROL ROOM OPERATION

A user-defined Graphical User Interface (GUI), which was developed in MATLAB, is used to setup, run, and record the measurements for the dynamic stall rig with the leading-edge flap model. Various inputs are required for the MATLAB dynamic stall GUI which include: details of the data acquisition channel settings and offset settings, the experimental condition settings (α_M, α_{amp}, Re, k), the model motion settings (static/dynamic) and the data acquisition trigger control. An event log is automatically produced and updated which keeps a record of all test cases that have been performed during the experimental test campaign. A visualisation of the key hardware implemented in this study is shown in Fig. 4.10 and will be discussed in this section.

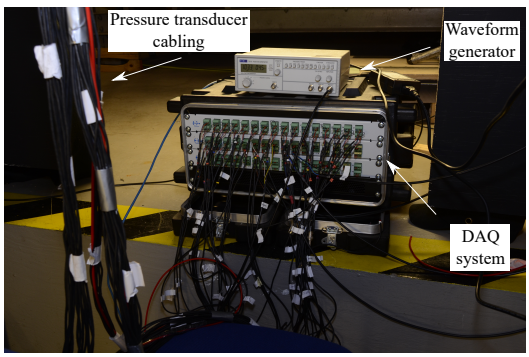

(A) Data acquisition system

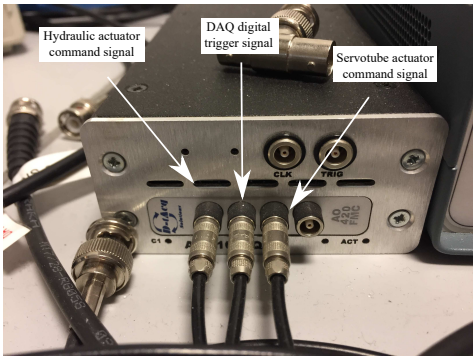

(B) Multi-channel analogue input module

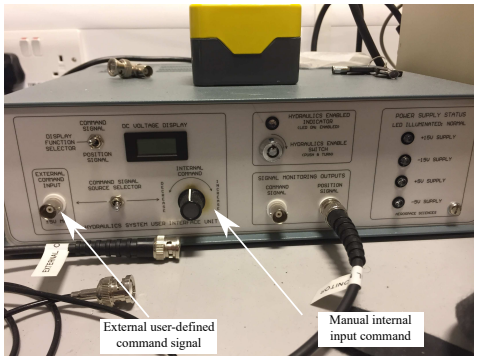

(C) Hydraulic actuator control system

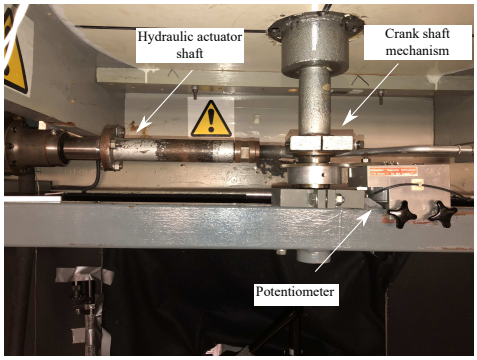

(D) Hydraulic actuator rig

FIGURE 4.10: Various hardware and instrumentation used in this experimental study.

DATA ACQUISITION SYSTEM

A multi-channel data acquisition system supplied by D-tacq (system model: DJ2006) was used to measure multiple readings such as: the wind-tunnel flow conditions, the leading-edge flap NACA0015 aerofoil model's surface pressure transducer measurements, and the hydraulic control system input/output signals [110]. A visualisation of the Data Acquisition System (DAQ) is illustrated in Fig. 4.10a. The MATLAB dynamic stall GUI is used to initialise the DAQ data recording, which was based on a sampling frequency of 10 kHz and a sampling duration which can be varied depending on whether the motion is static or dynamic. For static motion cases where the leading-edge flap model is fixed, the sampling duration was set to five seconds. For dynamic motion cases, the sampling duration was set for 10 periodic pitch cycles. Moreover, for the dynamic motion cases, a pulse trigger signal is sent to the DAQ to initialise the data recording when the model has reached the full pitch motion operation and after the initial transient effects have passed. Once the test run has finished successfully, the recorded results obtained by the DAQ are sent back to the GUI and are saved in a suitable format which is ready to use for post-processing.

For this experimental study, 47 channels were utilized by the data acquisition system which recorded the following: model pressure transducer readings (40 channels), the hydraulic control system's input command signal and the output position signal (2 channels), an arbitrary waveform generator signal (1 channel), and wind tunnel parameters such as the dynamic pressure, q, static temperature, T_{static}, total pressure,

P_{total}, and the tunnel static pressure, p (4 channels). The model pressure transducer readings are the individual surface pressure readings from the gauge pressure transducers. The hydraulic control system command signal is the input signal which drives the hydraulic motion, and the position signal is the output measurement for the hydraulic actuator which measures the hydraulic displacement. The signal generator has a generic sinusoidal motion which is sent to the data hydraulic system to check that there is no deviation in the output result. For the wind tunnel instrumentation, the dynamic pressure is recorded by a micro-manometer, the static temperature is measured by a thermocouple installed inside the test section, and the total and static pressure is measured by a pitot-static probe. The pitot static probe is placed inside the test section, and is located upstream of the model where the free-stream conditions are undisturbed by the model.

Multi-Channel Analogue Input Module

A 4 channel, analogue input module (D-Tacq/ACQ420FMC) was used to supply simultaneous user-defined generated waveform signals to control various hardware associated with the dynamic stall rig and the leading-edge flap actuation mechanism [111]. The analogue input module has a voltage range of +/- 10 V, and a resolution of 16 bits. The module's maximum sampling rate is 1 MHz, however the sampling frequency was set to 2 kHz due to the memory limitations when operating over a wide periodic pitch cycle duration. A visualisation of the multi-channel analogue module is shown in Fig. 4.10b.

The analogue input module receives various user-defined signals from the dynamic stall MATLAB GUI (sinusoidal, pulse, digital) which is then sent simultaneously to the hydraulic control system, the DAQ, and the linear actuator's amplifier. A user-defined sinusoidal wave signal is sent to the hydraulic control system which results in the hydraulic actuator executing a oscillatory motion which drives the leading-edge flap's pitching profile. A digital signal is sent to the DAQ which triggers the data recording when the system receives a high level voltage. A user-defined, analogue, pulsed motion signal is sent to the linear actuator's amplifier which results in actuation of the leading-edge flap.

Hydraulic Actuator Control System

A Hydraulics System User Interface (HSUI) unit is used to supply a control signal to the hydraulic actuator in order to drive the model pitch motion. Two types of signal can be sent to the HSUI: an internal command which allows the user to vary the voltage input manually via a turn command, and an external command input which receives an analogue input voltage signal which is sent by the multi-channel analogue input control module. The internal command is used when performing static runs and the external command input is used when performing oscillatory motion runs. The HSUI has a voltage range of +/- 4.5 V, which restricts the incidence range achievable

by the hydraulic actuator between a range, $-30^\circ \leq \alpha \leq 30^\circ$. An illustration of the HSUI unit is shown in Fig. 4.10c.

A calibration process is performed to determine the incidence angle output for a command signal input from the HSUI. There are two signals which are measured for this calibration process: a command signal and a position signal. The command signal is the input signal supplied by the HSUI to actuate the hydraulics, and the position signal is the output signal which is measured by a displacement transducer mounted at the hydraulic actuator rig. An illustration of the hydraulic actuator rig and the potentiometer used to measure the output displacement signal is shown in Fig. 4.10d. A measurement scale is positioned at the model's trailing-edge in the wind tunnel test section to measure the incidence angle. The calibration results for the command signal and position signal are shown in Fig. 4.11. There is a linear relationship for both the command signal and the position signal. The sensitivity values for the command signal and the position signal are 157.8 mV/deg, and -158.1 mV/deg, respectively.

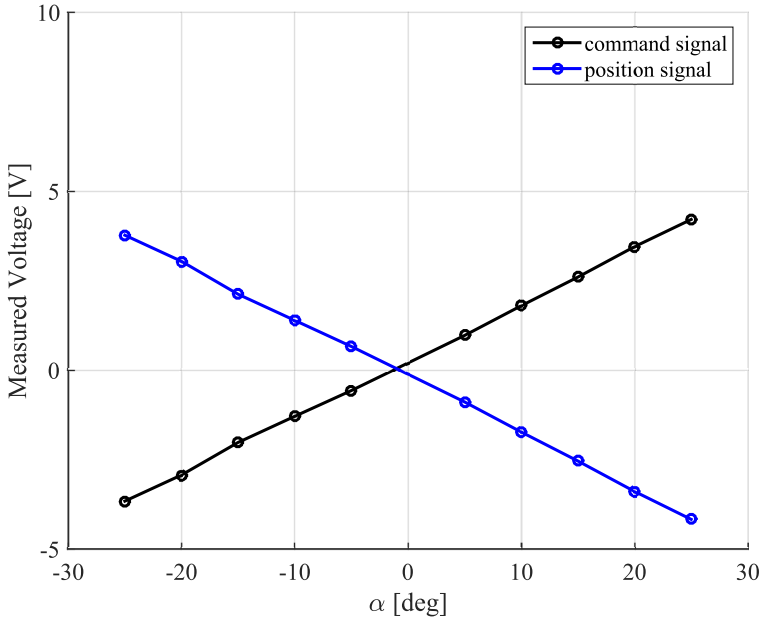

FIGURE 4.11: HSUI incidence angle calibration results.

SURFACE PRESSURE MEASUREMENTS

Surface pressure measurements are the primary form of instrumentation used in this experimental study to characterise and compare the leading-edge morphing performance characteristics between the measured experimental results and the predicted computational results. Forty gauge, bi-directional, pressure transducers were installed at the leading-edge flap model's centre span along the chord. The pressure transducers were supplied by First Sensor (specification number: HDI-G-M100-B-Y-8-P-5), which have a pressure and voltage range of 100 mbar and 5 V respectively [112]. A pressure range of 100 mbar was selected, based on a Cp_{min} value of 13, which was predicted from the dynamic stall CFD analysis for a free-stream velocity, U_∞ = 30 m/s.

All 40 pressure transducers were calibrated before being installed in the leading-edge flap wind tunnel model. The portable pressure calibrator Druck dpi 615 was used to perform the calibration procedure of the pressure transducers by supplying a steady pressure [113]. The pressure transducer calibration test procedure is shown in Fig.4.12. The pressure calibrator allows the user to apply both a positive and negative pressure to the pressure transducer, which enables an assessment of the full bi-directional capability. The DAQ was used to measure the output pressure from the transducer, which was sampled at a frequency and duration of 10 kHz and 5 s, respectively. The raw voltage data generated by the pressure transducer is filtered at 2 kHz to remove any unwanted signals (noise), and a mean voltage is determined.

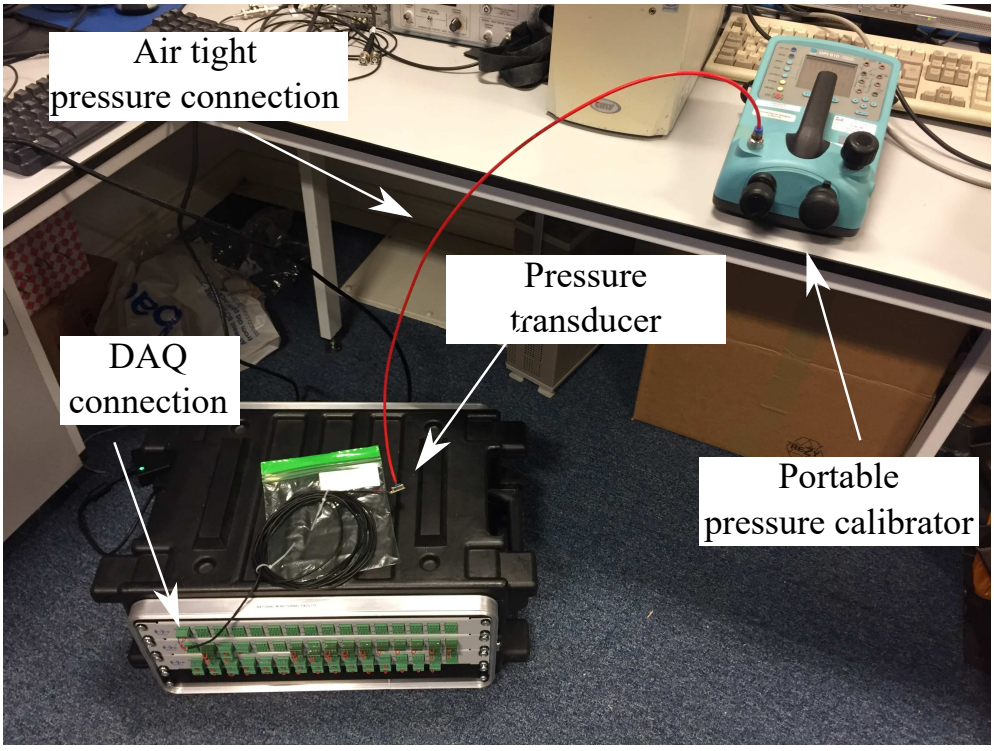

FIGURE 4.12: Illustration of the pressure calibration test procedure.

The mean voltage results for all 40 individual pressure transducers assessed against the applied input pressure from the pressure calibrator is shown in Fig. 4.13. The output results supplied by the manufacturer (First Sensor) are also shown in the results for comparison [112]. Figure 4.13a demonstrates that there is a linear trend for all pressure transducers assessed. There is little variance in the measured mean voltage results between all transducers over the input pressure range assessed. Figure 4.13b illustrates the same pressure transducer calibration results, but is focussed near the 0 mbar pressure region. This result shows that there is a larger offset in the output mean voltage for all pressure transducers assessed in comparison to the results produced by First Sensor. At 0 mbar gauge pressure, there is also a slight variance between the output mean voltage between all transducers against the averaged transducer reading (highlighted by the colour red). Due to this variance, the sensitivity and offset value of every pressure transducer will be slightly different and is accounted for when converting from output voltage to pressure. An example of the sensitivity reading taken for pressure transducer number 1 is 20.364 mV/mbar. The offset voltage for each of the pressure transducers is recorded before each test case to ensure consistency in the measurement readings as a result of varying ambient conditions.

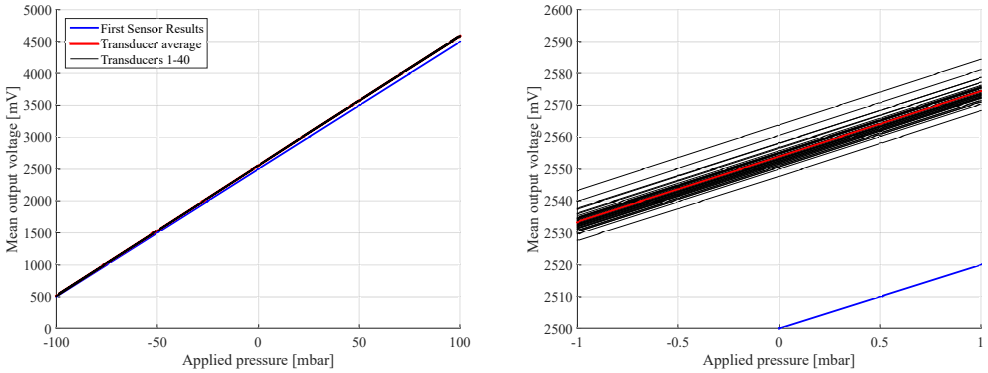

(A) Full applied pressure range (B) Focussed at the 0 mbar pressure region

Figure 4.13: Pressure transducer calibration results for all 40 pressure transducers assessed. Results supplied by First Sensor are also shown for comparison [112].

When installing the gauge pressure transducers into the aerofoil model, the majority of transducers were directly bonded to the surface, meaning that tubing was not required. Brass inserts and tubing were required for a few transducers which were positioned close to leading-edge or trailing-edge where available spacing was limited. The maximum tubing length for these specific transducers was limited to 4 cm to minimise any loss from the dynamic pressure signal. The response time of the gauge pressure transducers is 0.5 ms (2000 Hz), as quoted by First Sensor [112]. The diameter size of all pressure taps is 0.9 mm which is based on previous experimental wind tunnel models manufactured at the University of Glasgow.

4.6 DETERMINING PRESSURE TRANSDUCER POSITIONS

To determine an effective arrangement to position the pressure transducers, pressure distribution results are extracted from the dynamic stall CFD analysis and applied to various pressure transducer arrangement configurations to assess the accuracy of the interpolated pressure distributions. The dynamic stall CFD results for the rigid clean surface aerofoil configuration from Section 4.4 is used for this study, and is assessed at the point where convection of the LEV occurs.

Three different pressure transducer configurations were assessed, using the surface pressure data obtained from the CFD result, and interpolated to assess it's accuracy in comparison to the CFD's computed results. The three pressure transducer arrangement configurations tested are: uniform spacing, cosine spacing, and user-defined spacing, as shown in Fig. 4.14. Uniform spacing in Fig. 4.14a equally spaces the pressure transducers along the aerofoil's upper and lower surfaces. Figure 4.14b demonstrates that cosine spacing is a more efficient distribution method as the resolution of points are increased at the leading-edge and trailing-edge of the aerofoil to ensure an accurate representation of key features such as: large levels of suction near the leading-edge upper surface, stagnation pressure at the lower surface, and pressure gradients at the trailing-edge. User-defined spacing in Fig. 4.14c is a modification of the cosine-spacing distribution which takes into account constraints from the experimental model such as the inclusion of the spar and spacing issues at the trailing-edge for installation of the pressure transducers. 25 pressure transducers are allocated for the aerofoil's upper surface, and 15 for the lower surface to ensure an accurate representation of the interpolation for key flow features associated with dynamic stall at the aerofoil's upper surface.

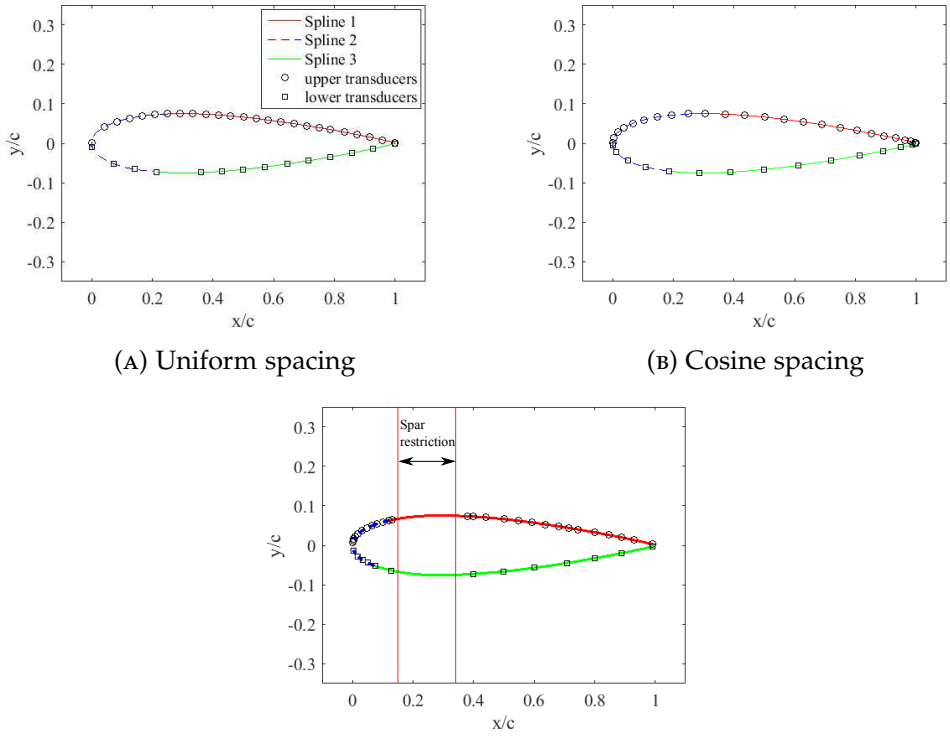

(A) Uniform spacing

(B) Cosine spacing

(C) User-defined

FIGURE 4.14: Various pressure transducer arrangement configurations.

The lift coefficient, C_l, drag coefficient, C_d, and moment coefficient, C_m, are used to assess the accuracy of interpolation for the uniform, cosine, and user-defined pressure transducer arrangement configurations in comparison to the computed CFD pressure distribution. A description of the derivation process to calculate the aerodynamic force and moment coefficients, based on the pressure coefficient is provided in Appendix B.

The flow-field visualisations for convection of the LEV on the aerofoil's upper surface from the CFD analysis is shown in Fig. 4.15. The Cp scalar plot in Fig. 4.15a illustrates the convection of a fully formed LEV along the aerofoil's upper surface which results in the overshoot in lift. The non-dimensional vorticity plot in Fig. 4.15b also illustrates the initial formation of the TEV.

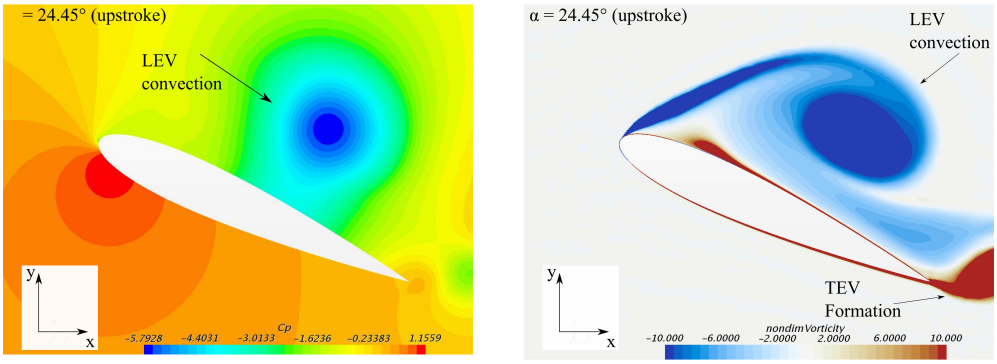

(A) Cp scalar

(B) Non-dimensional vorticity, ω_z^*

FIGURE 4.15: Flow-field visualisation scalar plots of the LEV convection along the aerofoil's upper surface. Operational conditions: Re = 1,008,100, $\alpha_M = 17°$, $\alpha_{amp} = 8°$ k = 0.1021

The interpolated surface Cp distribution against the non-dimensional chord position for the three pressure transducer arrangement configurations are shown in Fig. 4.16 along with their pressure transducer positions. Figure 4.16c highlights the restriction created by the aluminium spar for the experimental model which restricts the installation of pressure transducers within that region. All three pressure transducer configurations accurately represent the convection of the LEV through interpolation as shown by the presence of a low pressure ridge on the upper surface. Next, the interpolated pressure distribution produced by all pressure transducer configurations are compared against the surface Cp distribution from the CFD results as shown in Fig. 4.17. There are minor differences in the surface Cp distribution accuracy for the uniform and user-defined spacing configurations as shown in Figs. 4.17a and 4.17c respectively. This is due to the decrease in resolution of the pressure transducer points for the uniform spacing configuration as well as the restriction of the pressure transducer points within the spar region for the user-defined spacing configuration.

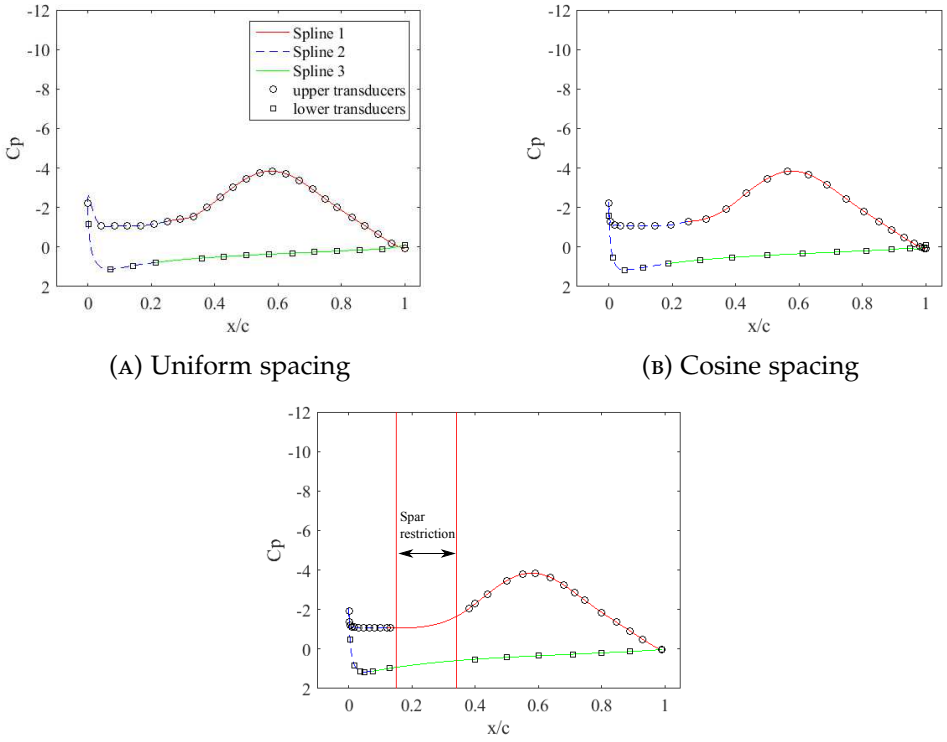

(A) Uniform spacing

(B) Cosine spacing

(C) User-defined spacing

FIGURE 4.16: Cp distribution against non-dimensional chord position for three pressure transducer arrangement configurations with pressure transducer positions highlighted.

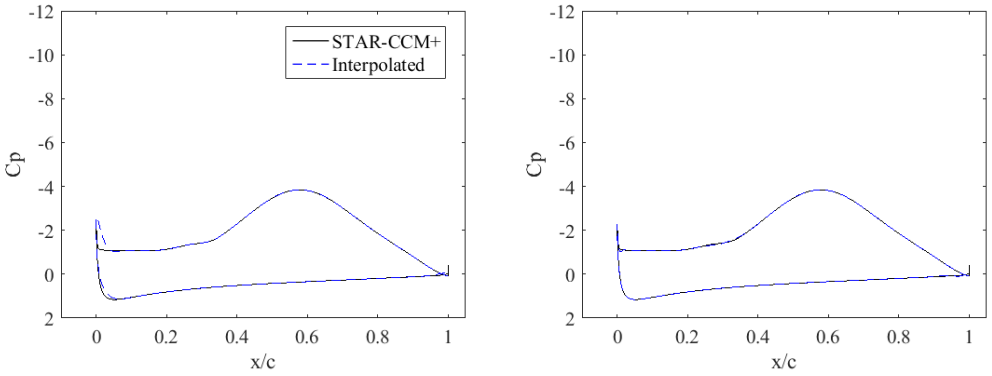

(A) Uniform spacing

(B) Cosine spacing

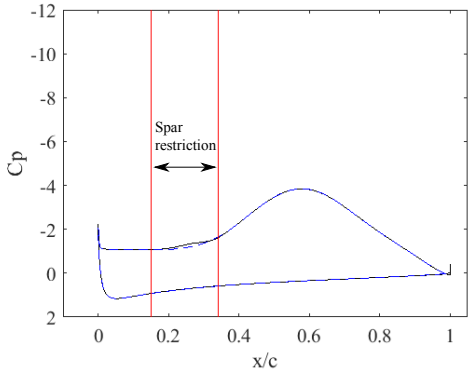

(C) User-defined spacing

FIGURE 4.17: Cp distribution against non-dimensional chord position comparison against CFD results for three pressure transducer arrangement configurations.

Next, an assessment in the level of the accuracy in predicting the drag coefficients between the three pressure transducer arrangements is made and compared against the CFD predicted surface Cp distribution. The interpolated surface Cp distribution against y/c for the three pressure transducer arrangement configurations along with their pressure transducer positions highlighted, are shown in Fig. 4.18. The comparison between the three interpolated pressure transducer arrangement configurations against the CFD pressure distribution are shown in Fig. 4.19. There are clear differences in the representation of the interpolated pressure distribution when comparing the uniform spacing configuration to the computed CFD results in Fig. 4.19a. Both the interpolated surface Cp distribution curves for the cosine and user-defined spacing configurations demonstrate minor differences in comparison to the computed CFD results in Fig. 4.19b and 4.19c respectively.

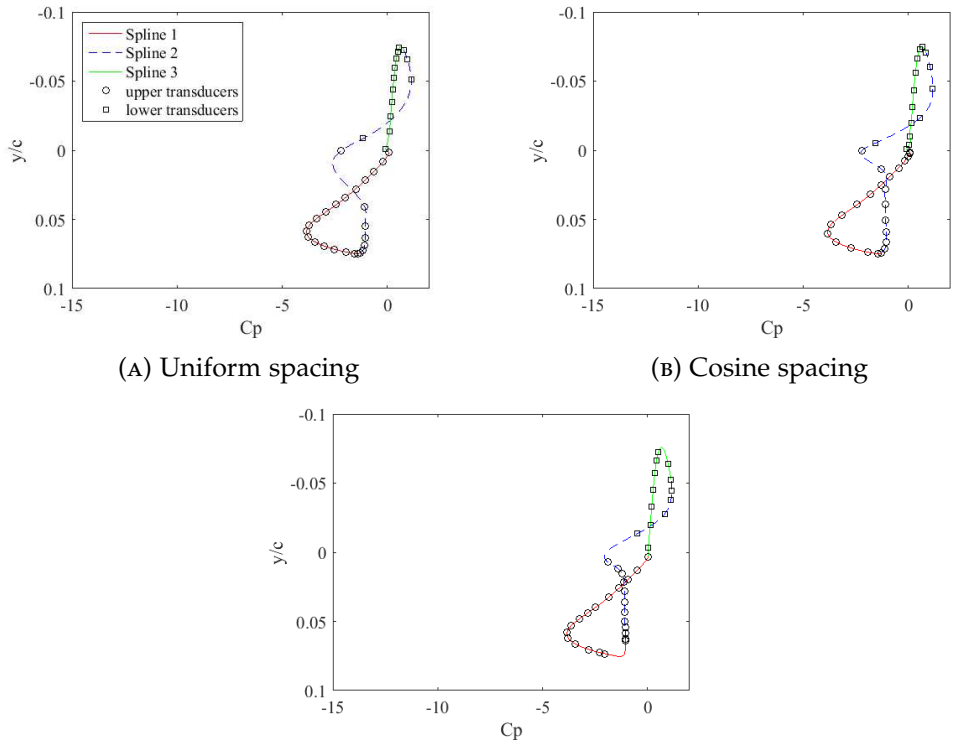

(A) Uniform spacing

(B) Cosine spacing

(C) User-defined spacing

FIGURE 4.18: non-dimensional thickness position against Cp distribution for three pressure transducer arrangement configurations with pressure transducer positions highlighted.

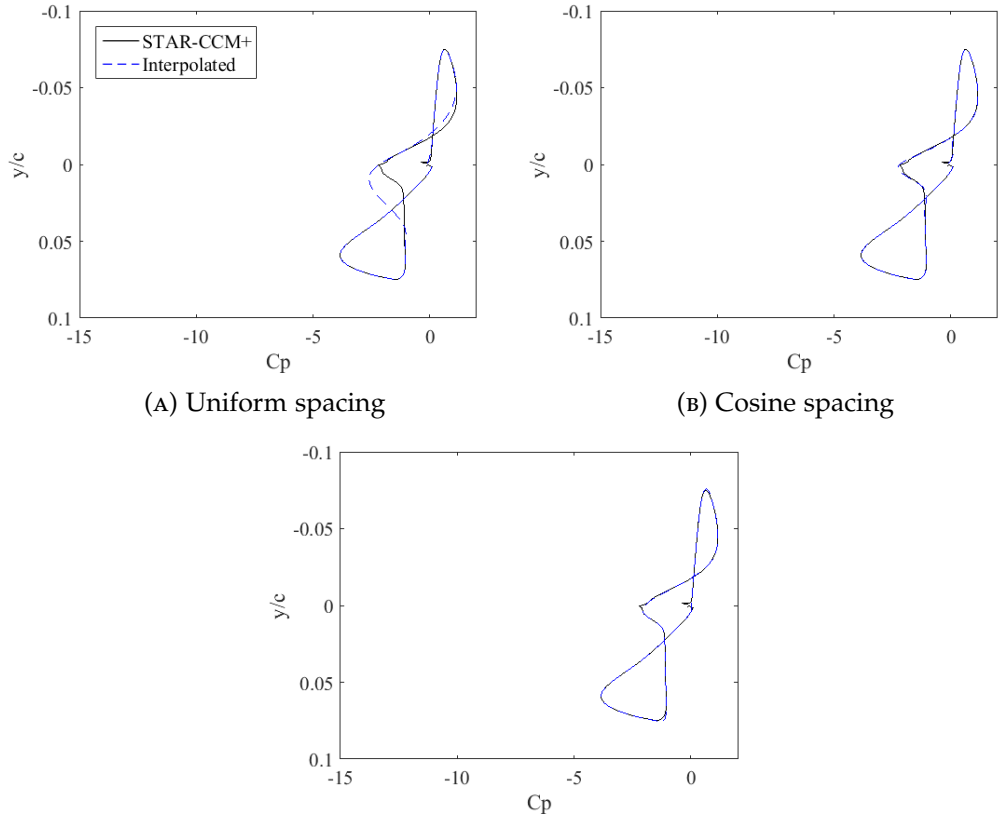

(A) Uniform spacing

(B) Cosine spacing

(C) User-defined spacing

FIGURE 4.19: non-dimensional thickness position against Cp distribution comparison against CFD results for three pressure transducer arrangement configurations.

The integrated force and moment coefficients for the three pressure transducer configurations as well as the CFD predicted results are presented in Table 4.1. Cosine-spacing is the best performing configuration due to achieving minor differences in the aerodynamic force and moment coefficients when compared against the CFD result. Uniform spacing is the worst performing configuration which under predicts Cd by approximately 2.5 %. The user-defined spacing configuration under predicts all of the aerodynamic coefficients by approximately 0.4 % due to the presence of the spar restriction. The user-defined pressure transducer arrangement configuration is however sufficient to use for the experimental model. The positions of the pressure transducers which are installed in the leading-edge flap model is provided in Appendix C. The pressure transducers are positioned at the centre of the effective model span.

Case	Cl	Cd	Cm_{LE}	$Cm_{1/4}$
STAR-CCM+	2.170	1.072	-1.159	-0.616
Uniform spacing	2.192	1.044	-1.159	-0.608
% diff	**1.017**	**-2.540**	**0.000**	**-1.311**
Cosine spacing	2.170	1.071	-1.159	-0.616
% diff	**-0.001**	**-0.037**	**0.000**	**0.026**
User-defined	2.161	1.069	-1.157	-0.617
% diff	**-0.398**	**-0.226**	**-0.134**	**0.091**

Table 4.1: Interpolated aerodynamic coefficient results comparison between the equivalent CFD results for three pressure transducer arrangement configurations.

4.7 LEADING-EDGE FLAP ACTUATION - LINEAR SERVOMOTOR

Active control of the leading-edge flap is achieved through implementation of a linear servotube actuator (model specification: STA2510), supplied by Copley Motion Corp [108]. The STA has a continuous force rating of 102.4 N and can achieve maximum velocity rates up to 5.9 m/s. The servotube actuator incorporates an IP67 rated forcer and a sealed stainless steel thrust rod enclosing rare-earth magnets [108]. The STA has two separate cable connections for the forcer and position feedback and is connected to an amplifier which is used to drive and control the STA.

A Xenus amplifier (specification number: XSL-230-18) is used to provide power and analogue control to the STA [114]. The amplifier receives user-defined position commands via the multi-channel analogue input module. The input position signal is used by the amplifier to drive the STA with the desired motion profile. The analogue command input for the amplifier requires only one channel and has a voltage range of +/- 10 V. The amplifier has a resolution and bandwidth of 12 bit and 7 kHz respectively.

The STA and the Xenus amplifier had to be configured before being operational in the wind tunnel test campaign. The software package supplied by Copley Motion, CME 2, was used for the configuration process, which allowed for a fast and simple configuration setup between the amplifier and the STA [115]. The amplifier can be configured for both digital input commands (requires 2 channels) and analogue input commands (requires 1 channel), however the analogue input signal command was selected due to the simpler input command signal required. The calculation function in CME 2 was used which uses the motor and encoder values entered to calculate the initial feedback loop gains (position, velocity, and current) as well as the limits. Auto-phasing and auto-tuning procedures were finally performed as instructed in the CME 2 user-guide which fine tunes the position, velocity, and current gains.

An illustration of the experimental test bench which was used for configuring the STA with the Xenus amplifier is shown in Fig. 4.20. The amplifier is mounted onto a board to allow for simple connection of the input command signals as well

as activating and deactivating the actuator manually. The oscilloscope feature in the CME 2 software package was used to record the STA's displacement during operation, which can be compared against the input command signal. The input command voltage signal is transformed into electrical counts which is measured by the STA, and is derived using the following expression:

$$counts = \frac{V_{input}}{0.00244} \tag{4.1}$$

The output displacement signal is measured in electrical counts, which can be converted into a displacement value by calculating the following:

$$X_{amp} = \frac{counts}{800} \tag{4.2}$$

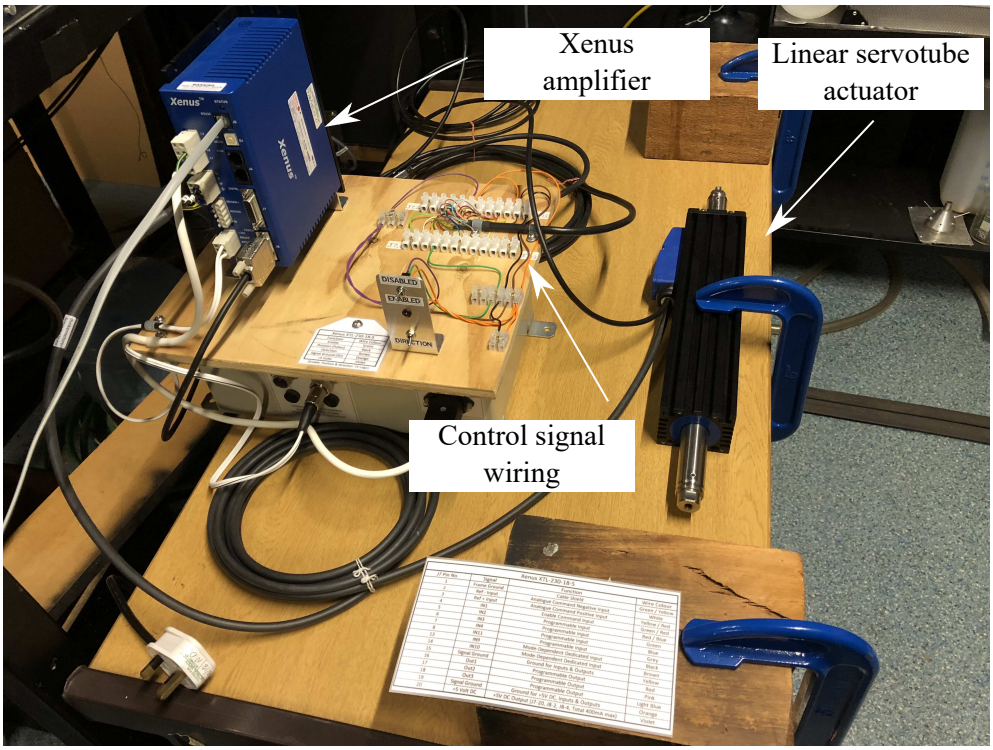

FIGURE 4.20: Illustration of the configuration setup procedure between the linear servotube actuator and the Xenus amplifier.

A leading-edge flap mechanism was designed to transform the input linear motion from the STA to the output rotational motion of the leading-edge flap. This involved a slide-yoke mechanism design which allowed for movement in two degrees of freedom and is visualised in Fig. 4.21. A clevis end rod is attached to the end of the thrust rod, which is connected to the slide-yoke mechanism. The slide-yoke mechanism is fixed to the leading-edge flap's shaft, and acts as the flap's moment arm. The leading-edge flap deflection angle, β, with units in degrees, can be determined by calculating:

$$tan\beta = \frac{X_{amp}}{R_{ac_y}} \tag{4.3}$$

where is X_{amp} is the STA's thrust rod displacement in metres, and R_{ac_y} is the leading-edge flap's moment arm length in metres. The moment arm length was set to 0.077 m, due to the operational range of the STA's continuous force. The moment arm length was determined though a leading-edge flap kinematics analysis which is discussed in the next section.

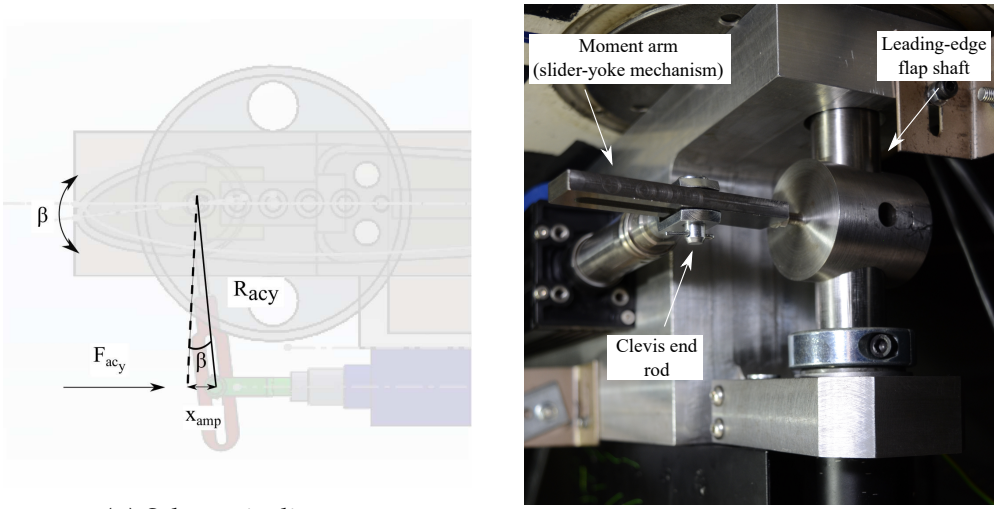

(A) Schematic diagram

(B) Installed flap mechanism

FIGURE 4.21: Leading-edge flap actuation mechanism visualisation.

4.8 FLAP KINEMATICS ANALYSIS - DETERMINING REQUIRED ACTUATOR FORCES AND MOMENT ARM SIZE

The objective of the two-dimensional leading-edge flap kinematics analysis is to determine the required forces for the linear actuator while under hold and leading-edge morphing conditions. This analysis will also determine the moment arm lengths which are suitable for the experiment. The operational conditions for the flap kinematics analysis for the rigid case are identical to those defined in Section 4.4, which are: $Re = 1,008,100$, $\alpha_M = 17^\circ$, $\alpha_M = 8^\circ$, and $k = 0.1021$.

The coordinate system for the leading-edge flap kinematics is shown in Fig. 4.22. The coordinate system origin is located at the aerofoil's pitch axis, where $\vec{R_0}$ is defined as the position vector from the aerofoil's pitch axis to the flap's pitch axis. $\vec{R_F}$ is defined as the position vector from the flap's pitch axis to the flap's centre of mass. α is the aerofoil incidence angle and β is the leading-edge flap deflection angle.

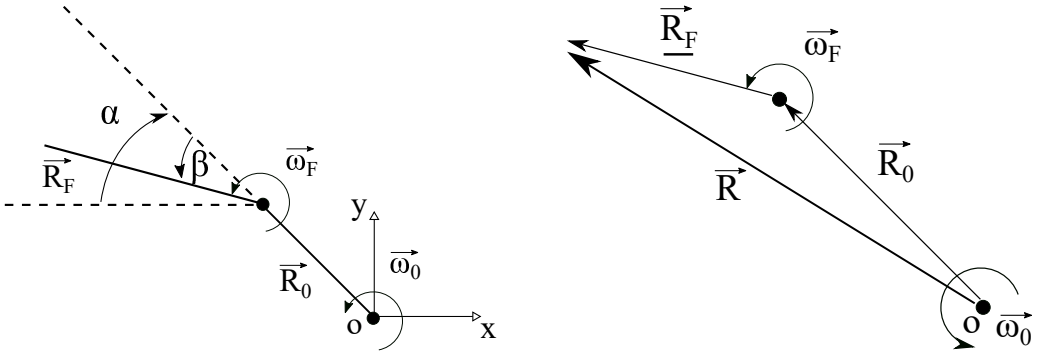

(A) Coordinate system (B) Position vectors

FIGURE 4.22: Leading-edge flap model coordinate system for flap kinematics analysis and an illustration of the position vectors.

The actuator forces required by the linear actuator to either hold or actuate the leading-edge flap can be obtained through calculation of the angular momentum of the leading-edge flap model as a function of time. First the relative position, velocity, and acceleration vectors of the leading-edge flap model are derived. The relative position vector, $\vec{R}$, as shown in Fig.4.22 is defined as follows:

$$\begin{aligned} \vec{R} &= \vec{R_0} + \vec{R_F} \\ \begin{bmatrix} R_x(t) \\ R_y(t) \end{bmatrix} &= \begin{bmatrix} R_{0_x}(t) \\ R_{0_y}(t) \end{bmatrix} + \begin{bmatrix} R_{F_x}(t) \\ R_{F_y}(t) \end{bmatrix} \end{aligned} \tag{4.4}$$

From Fig. 4.22a, $\vec{R_0}$ and $\vec{R_F}$ can be transformed into component form:

$$\begin{aligned} R_{0_x} &= -R_0 cos(\alpha) \\ R_{0_y} &= R_0 sin(\alpha) \end{aligned} \tag{4.5}$$

$$\begin{aligned} R_{F_x} &= -R_F cos(\alpha - \beta) \\ R_{F_y} &= R_F sin(\alpha - \beta) \end{aligned} \tag{4.6}$$

The relative position vector as a function of time can then be solved as:

$$\begin{bmatrix} R_x(t) \\ R_y(t) \end{bmatrix} = \begin{bmatrix} -R_0(t)cos(\alpha(t)) \\ R_0(t)sin(\alpha(t)) \end{bmatrix} + \begin{bmatrix} -R_F(t)(cos(\alpha(t))Cos(\beta(t)) + sin(\alpha(t))Sin(\beta(t)) \\ R_F(t)(sin(\alpha(t))Cos(\beta(t)) - sin(\alpha(t))Cos(\beta(t)) \end{bmatrix} \tag{4.7}$$

The relative velocity vector, $\vec{V}$, is derived through differentiation of $\vec{R}$ as follows:

$$\begin{aligned} \vec{V} = \dot{\vec{R}} &= \dot{\vec{R_F}} + \dot{\vec{R_0}} \\ &= \vec{\omega_F} \times \vec{R_F} + \vec{\omega_0} \times \vec{R_F} + \vec{\omega_F} \times \vec{R_0} \end{aligned} \tag{4.8}$$

As the flap kinematics analysis is two-dimensional, specific conditions can be set which simplifies the derivation such as:

$$\begin{aligned} \vec{\omega} &= \omega \hat{k} \\ \vec{\omega} \cdot \vec{R} &= 0 \\ \omega_0 = \dot{\alpha}, &\quad \dot{\omega_0} = \ddot{\alpha} \\ \omega_F = -\dot{\beta}, &\quad \dot{\omega_F} = \ddot{\beta} \end{aligned} \tag{4.9}$$

where $\dot{\alpha}$ is the incidence angle rate (rad/s), $\ddot{\alpha}$ is incidence angle acceleration (rad/s^2), $\dot{\beta}$ is the leading-edge flap deflection rate (rad/s), and $\ddot{\beta}$ is the leading-edge flap deflection acceleration (rad/s^2).

The relative velocity vector as a function of time can then be solved as:

$$\begin{bmatrix} V_x(t) \\ V_y(t) \end{bmatrix} = \dot{\alpha} \begin{bmatrix} (R_{0_y}(t) + R_{F_y}(t)) \\ (R_{0_x}(t) + R_{F_x}(t)) \end{bmatrix} + \quad \dot{\beta} \begin{bmatrix} R_{F_y}(t) \\ -R_{F_x}(t) \end{bmatrix} \tag{4.10}$$

The relative acceleration vector, $\vec{A}$, is derived through differentiation of $\vec{V}$ as follows:

$$\vec{A} = \dot{\vec{R}} = (\vec{\omega_0} \times \vec{R_0}) + (\vec{\omega_0} \times \dot{\vec{R_0}}) + (\vec{\omega_0} \times \dot{\vec{R_F}}) + (\vec{\omega_0} \times \dot{\vec{R_F}}) + (\vec{\dot{\omega_0}} \times \vec{R_F}) + (\vec{\omega_F} \times \dot{\vec{R_F}}) \tag{4.11}$$

The relative acceleration vector as function of time can then be solved as:

$$\begin{aligned} \begin{bmatrix} A_x(t) \\ A_y(t) \end{bmatrix} = \ddot{\alpha}(t) \begin{bmatrix} -(R_{0_y}(t) + R_{F_y}(t)) \\ R_{0_x}(t) + R_{F_x}(t) \end{bmatrix} + \quad \dot{\alpha}^2(t) \begin{bmatrix} R_{0_x}(t) + R_{F_x}(t) \\ R_{0_y}(t) + R_{F_y}(t) \end{bmatrix} \\ + \dot{\beta}^2(t) \begin{bmatrix} R_{F_x}(t) \\ R_{F_y}(t) \end{bmatrix} + \ddot{\beta}(t) \begin{bmatrix} R_{F_y}(t) \\ -R_{F_x}(t) \end{bmatrix} \end{aligned} \tag{4.12}$$

The leading-edge flap model angular momentum equation as a function of time is defined as:

$$\vec{M_{inertial}} = \vec{M_{aero}} + \vec{M_{flap}} \tag{4.13}$$

where:

$$\begin{aligned} \vec{M_{inertial}} &= M_F(\vec{R_F} \times \vec{A}) \\ \vec{M_{flap}} &= (\vec{R_{ac}} \times \vec{F_{ac}}) \end{aligned} \tag{4.14}$$

where M_F is the flap mass in kg, $\vec{R_F}$ is the flap centre of mass vector in metres, $\vec{A}$ is the relative acceleration vector with units m/s^2, $\vec{M_{aero}}$ is the blade pitch aerodynamic moment about the quarter chord with units Nm, $\vec{R_{ac}}$ is the flap actuator moment arm vector in metres, and $\vec{F_{ac}}$ is the flap actuator force vector with units N. An illustration of the moments acting about the aerofoil model as well as the leading-edge flap is shown in Fig. 4.23.

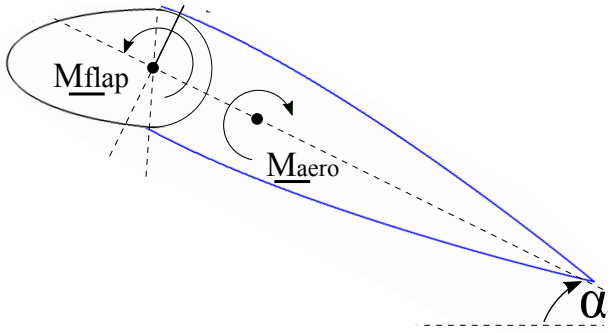

FIGURE 4.23: Coordinate system for the moments acting on the aerofoil, flap, and linear actuator.

All moments are specified in the k-direction due to the two-dimensional conditions, therefore the components, $\vec{M_{inertial}}$ and $\vec{M_{aero}}$ are set as:

$$\vec{M_{inertial}} = \begin{bmatrix} 0 \\ 0 \\ M_{inertial} \end{bmatrix} \tag{4.15}$$

$$\vec{M_{aero}} = \begin{bmatrix} 0 \\ 0 \\ M_{aero} \end{bmatrix} \tag{4.16}$$

$\vec{M_{aero}}$ from eq. (4.13) is the aerofoil's aerodynamic moment as a function of time which is obtained from the CFD analysis.

The orientation of the shaft moment arm, $\vec{R_{ac_y}}$, and direction of the linear actuator force, $\vec{F_{ac}}$, are illustrated in Fig. 4.21a Both parameters can be transformed into their component form as a function of incidence as follows:

$$\vec{R_{ac}} = \begin{bmatrix} 0 \\ Moment \quad arm \quad distance \\ 0 \end{bmatrix} = \begin{bmatrix} 0 \\ R_{ac_y} cos(\alpha) \\ 0 \end{bmatrix} \tag{4.17}$$

$$\vec{F_{ac}} = \begin{bmatrix} Linear & actuator & force \\ & 0 & \\ & 0 & \end{bmatrix} = \begin{bmatrix} -F_{ac_x} cos(\alpha) \\ 0 \\ 0 \end{bmatrix} \tag{4.18}$$

Since the angular momentum equation is now fully derived, the equation can be re-arranged to determine the required actuator forces for different leading-edge flap operational conditions (hold, pulse flap motion) as follows:

$$F_{ac_x}(t) = (M_{aero} + M_{flap}(R_{F_x} A_y - R_{F_y} A_x))/R_{ac_y}(Cos(\alpha))^2 \tag{4.19}$$

The results for the required actuator forces as a function of time with a variation in the moment arm length and for both rigid and morphing profiles is shown in Fig. 4.24. The maximum required actuator force occurs near the mean incidence during the pitch upstroke for all moment length sizes assessed. For both the hold and motion profiles, there is a reduction in the required actuator force for an increase in the moment arm length. It is clear that a moment arm length of 5 cm fails to maintain the required actuator force below the linear actuator force rating (100 N). All other moment arm lengths are successful in reducing the peak required actuator force to below 100 N. Therefore, a moment arm length of 0.077 m was selected and manufactured for the experimental model. This analysis concludes that the linear actuator should be able to safely perform the hold and pulse motion actuated profiles during wind tunnel operation for free-stream velocities upto approximately 30 m/s.

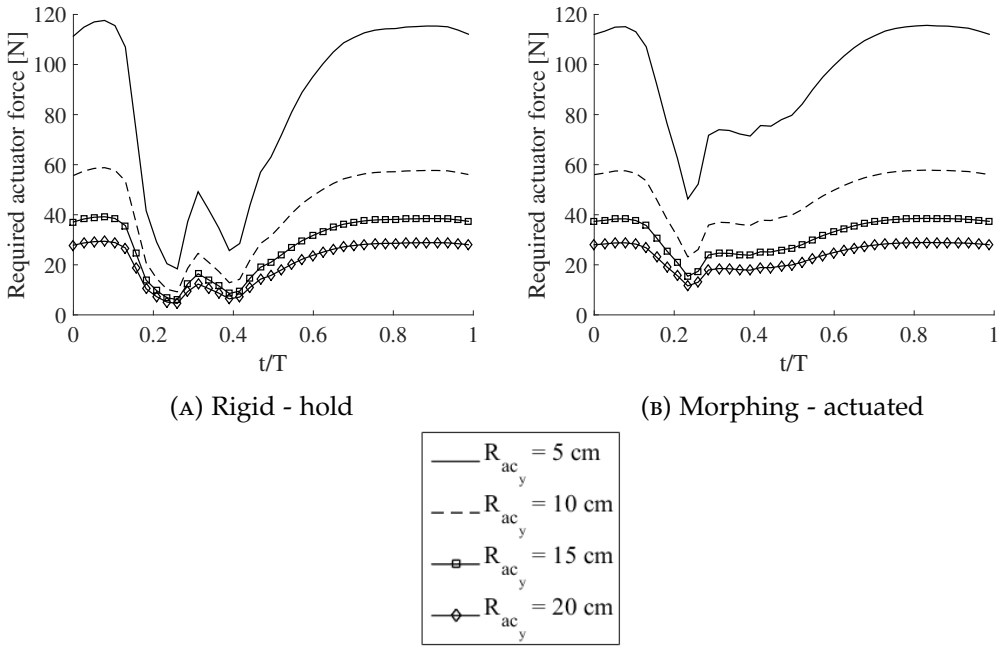

(A) Rigid - hold (B) Morphing - actuated

FIGURE 4.24: Effect of the moment arm length on the actuator forces required to either operate under rigid-hold or morphing-actuated conditions.

The energy required to actuate the leading-edge morphing mechanism will have a detrimental effect on the power reduction savings. The energy required for the linear actuator can be determined through multiplying the actuator force by the moment arm length. The linear actuator power can then be calculated by dividing the linear actuator energy by time. The aerofoil aerodynamic power, P, can by calculated as follows:

$$P = M_{(0.25c)}\omega \tag{4.20}$$

where M is the aerofoil moment about the quarter chord with units, Nm.

The power reduction savings for a leading-edge morphing system whilst considering the power required to actuate leading-edge morphing can be determined as follows:

$$\Delta P_{morphing} = P_{morphing_{(0.25c)}} - (P_{rigid_{(0.25c)}} + P_{actuator_{(0.15c)}}) \tag{4.21}$$

For the leading-edge fixed droop system, the power reduction savings (which does not require actuation) can be determined as follows:

$$\Delta P_{fixeddroop} = P_{fixeddroop_{(0.25c)}} - P_{rigid_{(0.25c)}} \tag{4.22}$$

The overall power assessment of the leading-edge morphing system which includes the power required to actuate the leading-edge morphing section has not been considered for this study. Further simulations will have to be performed in order to quantify the effect of the power required for the leading-edge morphing actuation in order to include its effect in the power reduction calculations.

4.9 MEASUREMENT UNCERTAINTY ANALYSIS

Details and results for all of the measurement uncertainties associated to this experimental study are presented in Appendix D. The maximum relative uncertainty error for the lift, drag, and moment coefficient for all experimental test cases are 2.72 %, 4.13 % and -6.7 % respectively. A key factor associated to the measurement uncertainty is linked to leakage of flow which has a detrimental effect on the surface pressure measurements. This effect will be discussed in greater detail in Chapter 5.

CHAPTER 5

DYNAMIC STALL WIND TUNNEL TESTING OF NACA0015 AEROFOIL WITH ACTIVE LEADING-EDGE FLAP

5.1 INTRODUCTION

Dynamic stall wind tunnel testing for a NACA0015 aerofoil model with an active leading-edge flap has been performed using the Handley-Page low-speed, closed return, wind tunnel. The main purpose of this experimental study is to assess the effect that active leading-edge flap control has on the aerodynamic force and moment characteristics for both static and dynamic motion. It will also be used to validate the CFD model developed in Chapter 3, which predicted dynamic stall alleviation for both the leading-edge morphing and leading-edge fixed droop methods.

5.2 EXPERIMENTAL PLAN

The experimental investigation is comprised of two main sections which include static and dynamic analysis. A list of the test cases for the static analysis is presented in Table 5.1. checks are performed on the instrumentation in terms of measurement accuracy. Also, the static aerodynamic force and moment coefficients are measured and compared against the experimental results for a clean NACA0015 aerofoil to assess the changes in the aerodynamic characteristics due to the implementation of the leading-edge flap. Wind tunnel corrections are applied to the aerodynamic force and moment coefficients which takes into account the effects of solid blockage, wake blockage, and streamline curvature effects. Next, the effect of varying the leading-edge fixed droop amplitude is investigated to assess its effect on the static aerodynamic force and moment coefficients as well as the change in the static stall angle. Finally, the measured corrected aerodynamic force and moment coefficients are compared against the static computational results for selected incidence angles using the CFD model developed in Chapter 3. Static RANS modelling was used for 4 and 8 degrees incidence (pre-stall), and URANS was performed at 16 degrees incidence.

The dynamic analysis consists of three sections which include: attached flow, light stall, and deep stall. A list of the test cases for the dynamic analysis are presented in Table 5.2. In the attached flow regime, the effects of leading-edge morphing and leading-edge fixed droop are not investigated, therefore the flap is locked at the zero degree flap amplitude setting. The measured rigid, phase-averaged aerodynamic force and moment coefficients are compared against the equivalent CFD results at different reduced frequencies to use for validation. In the light dynamic stall regime, pitching profiles are set so that mild dynamic stall effects are produced with small levels of hysteresis. The effect of applying active leading-edge morphing or leading-edge fixed droop is then investigated to assess the dynamic stall alleviation characteristics. The effect of reduced frequency on dynamic stall production as well as the change in dynamic stall alleviation from either leading-edge morphing or leading-edge fixed droop is also evaluated. Finally, the dynamic stall alleviation effects are then quantified and normalised using the measured aerodynamic force and moment coefficients which are then used for validation against the equivalent CFD results. In the deep dynamic stall regime, the pitching profiles are set so that large hysteresis effects from dynamic stall are produced. The effect of applying either active leading-edge morphing or leading-edge fixed droop is investigated to determine it's effect on reducing the level of aerodynamic hysteresis and improving aerodynamic performance. The dynamic stall alleviation effects from leading-edge morphing and leading-edge fixed droop flap methods are assessed through variation of the reduced frequency. Finally, the effects of leading-edge morphing and leading-edge fixed droop on deep dynamic stall reduction are used as validation for the CFD model developed in Chapter 3.

Test case	α_{start} [°]	α_{end} [°]	α_{inc} [°]	Flap motion ( )	Flap amplitude [°]
Effect of pressure transducer leakage	-4	4	4	(Rigid)	0
Wind tunnel blockage effects (CFD validation)	0	24	2	(Rigid)	0
Effect of leading-edge fixed droop	0	24	2	(Fixed droop)	10 15 -10 -15

Table 5.1: List of static motion experimental test cases.

Flow regime	Test case	α_M [°]	α_{amp} [°]	Reduced frequency	Flap motion ( )	Flap amplitude [°]
Attached flow	Effect of reduced frequency (CFD validation)	5	5	0.025 0.1021	(Rigid)	0
Light dynamic stall	Effect of cyclic amplitude	12	8 10	0.1021	(Rigid)	0
Light dynamic stall	Effect of leading-edge morphing (CFD validation)	12	10	0.1021	(Morphing)	5 10 15
Light dynamic stall	Effect of leading-edge fixed droop (CFD validation)	12	10	0.1021	(Fixed droop)	5 10 15
Light dynamic stall	Effect of reduced frequency	12	10	0.025	(Rigid) (Morphing) (Fixed droop)	0 5 10 15 5 10 15
Deep dynamic stall	Effect of cyclic amplitude	16	8 10	0.1021	(Rigid)	0
Deep dynamic stall	Effect of leading-edge morphing (CFD validation)	16	10	0.1021	(Morphing)	5 10 15
Deep dynamic stall	Effect of leading-edge fixed droop (CFD validation)	16	10	0.1021	(Fixed droop)	5 10 15
Deep dynamic stall	Effect of reduced frequency	16	10	0.025	(Rigid) (Morphing) (Fixed droop)	0 5 10 15 5 10 15

Table 5.2: List of dynamic motion experimental test cases.

5.3 STATIC ANALYSIS

Static analysis was first performed to assess the measurement accuracy of the surface pressure measurements as well as evaluating the effect that the leading-edge flap NACA0015 mode has on the aerodynamic force and moment coefficients when compared against a clean NACA0015 aerofoil. The measured static aerodynamic force and moment coefficients are then compared against the static computational results from the CFD model at various incidence angles.

5.3.1 Effect Of Pressure Transducer Leakage

The gauge type pressure transducers were assessed in terms of measured Cp output and compared against predicted Cp distribution at various static incidence angles from the CFD model. The Reynolds number was set to approximately 1 million and the surface pressure measurements were sampled for five seconds at a sampling rate of 10 kHz for all transducers. All of the recorded surface pressure measurements are then filtered to 2 kHz using a low-pass filter, time-averaged, and integrated to obtain the pressure components of the aerodynamic force and moment coefficients. A static incidence angle sweep, $-4^\circ \leq \alpha \leq -16^\circ$, was used in increments of four degrees. A short time was set to allow the flow to settle before sampling at each individual incidence angle and to remove any transient effects from the model motion.

The surface pressure measurement results using all of the baseline pressure transducers at various incidence angles is visualised in Fig. 5.1. The RANS CFD results at incidence angles of 4, 8, and 16 degrees are also shown to use as a comparison against the measured surface pressure coefficient results. There is a good agreement between the measured Cp values at the aerofoil section of the model when compared against the CFD results for all incidence angles assessed. The pressure transducers used at the leading-edge flap for the "all transducer case" however generates surface Cp results that fail to show good agreement with the predicted CFD results. This is apparent when comparing the stagnation Cp values in Table 5.3, as the experimental results show measured Cp stagnation values greater than one. Moreover, the measured stagnation Cp increases for an increase in incidence whereas the CFD results are shown to predict Cp values close to one for all incidence angles assessed.

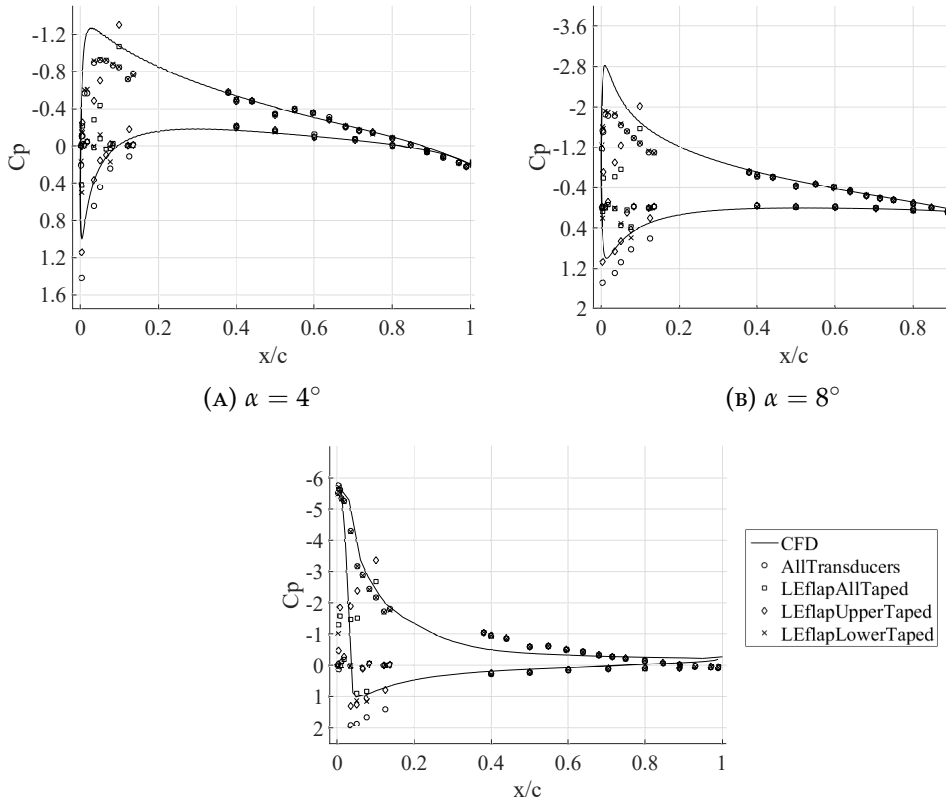

(a) $\alpha = 4°$ (b) $\alpha = 8°$

(c) $\alpha = 16°$

Figure 5.1: Effect of flow leakage on the surface Cp measurements with transducer ports blocked off at various surfaces of the leading-edge flap.

α [°]	Cp (CFD) [1]	Cp (Exp - AllTransducers) [1]	Percentage difference [%]
4	1.000	1.419	41.900
8	1.000	1.488	48.800
16	1.005	1.917	90.746

Table 5.3: Effect of flow leakage on the measured stagnation pressure coefficient for an increase in incidence angle.

The potential presence of flow leakage within the leading-edge flap was investigated to determine whether this feature was the reason for the significantly larger values in the measured stagnation Cp. The effect of flow leakage was initially evaluated by blocking off the pressure transducer ports at various sections of the leading-edge flap using tape, and re-running the static cases. The various sections of the leading-edge flap which had pressure transducer ports blocked include: all of the transducer ports, all of the transducer ports on the suction surface, and all of the transducer ports on the pressure surface.

The surface Cp distribution at various incidence angles and with different sections of the leading-edge flap's transducer ports blocked, is shown in Fig. 5.1. There is little effect on the measured Cp values on the suction surface when the transducer ports on the pressure surface are blocked for all incidence angles. There is a variation in the measured Cp values when all of the leading-edge flap transducer ports are blocked, which suggests that flow leakage is present within the volume of the leading-edge flap. Moreover, there is a significant reduction in the stagnation Cp when all of the transducer ports at the suction surface are blocked. The level of reduction in the measured stagnation Cp increases for an increase in incidence. This is due to reducing the level of negative pressure within the leading-edge flap volume, which has an effect on the readings from the gauge type pressure transducers (which expects ambient pressure conditions inside the leading-edge flap's volume). This leads to an offset in the pressure transducer readings at the leading-edge flap when all of the active pressure transducer ports at the suction surface are exposed. The effect of flow leakage inside the volume of the leading-edge flap is further investigated by blocking off all leading-edge flap transducer ports individually. Each pressure transducer port was blocked and pressure measurements taken and compared against the Cp distribution from the CFD results.

The effect that blocking each of the individual pressure transducer ports at the leading-edge flap has on the surface pressure coefficient measurements at various incidence angles is visualised in Fig. 5.2. A list of the pressure transducer numbering and positioning convention is presented in Table 4.3. It is evident that blocking the pressure transducer port 17 has a significant effect on the surface Cp measurements at the leading-edge flap for all incidence angles. There is also a better agreement when comparing the experimental surface Cp results against the computational results, and there is also a reduction in $Cp_{stagnation}$. Fig. 5.2a shows that there is a good agreement against the experimental and computational Cp_{min} at four degrees incidence, however there are larger differences between both methods at 8 degrees (Fig. 5.2b) and 16 degrees incidence (Fig. 5.2c). A potential reason for the differences between both the experimental and computational results is due to the presence of negative flow leakage within the volume of the leading-edge flap.

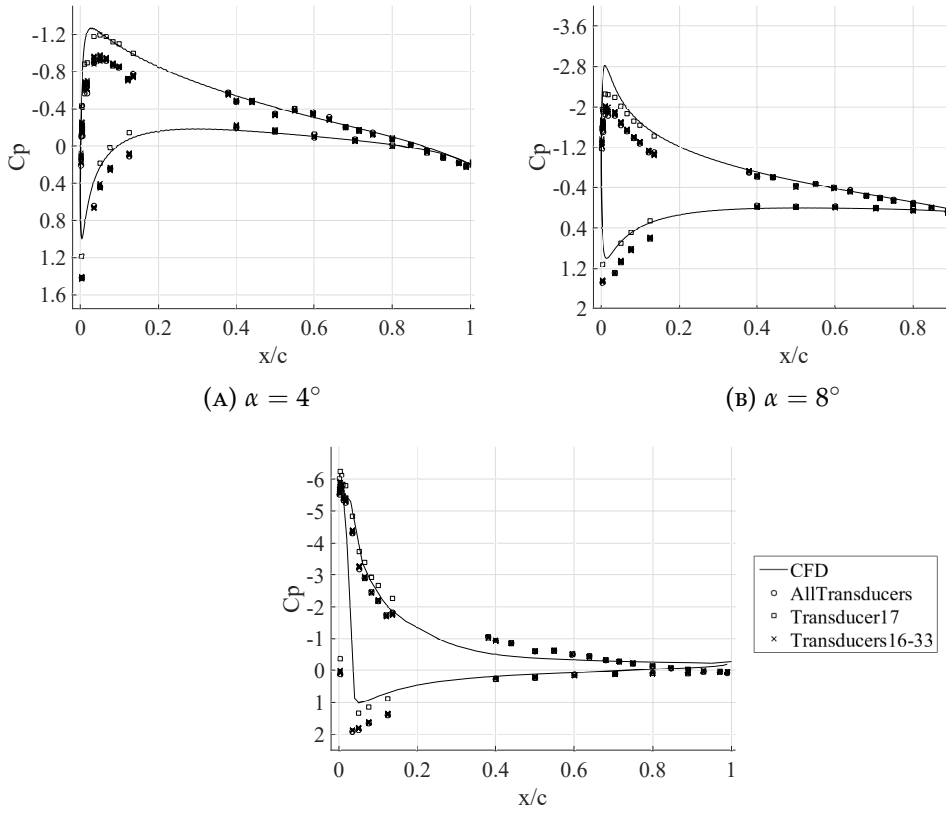

(a) $\alpha = 4°$

(b) $\alpha = 8°$

(c) $\alpha = 16°$

Figure 5.2: Effect of flow leakage on the surface Cp measurements with all of the leading-edge flap transducer ports blocked off individually.

The effect that flow leakage from each of the leading-edge flap's transducer ports has on the static aerodynamic force and moment coefficients is shown in Fig. 5.3. The results are also compared against the clean NACA0015 aerofoil model under the same operational conditions [102]. Note: no wind tunnel corrections have been applied to the aerodynamic force and moment coefficients at this stage.

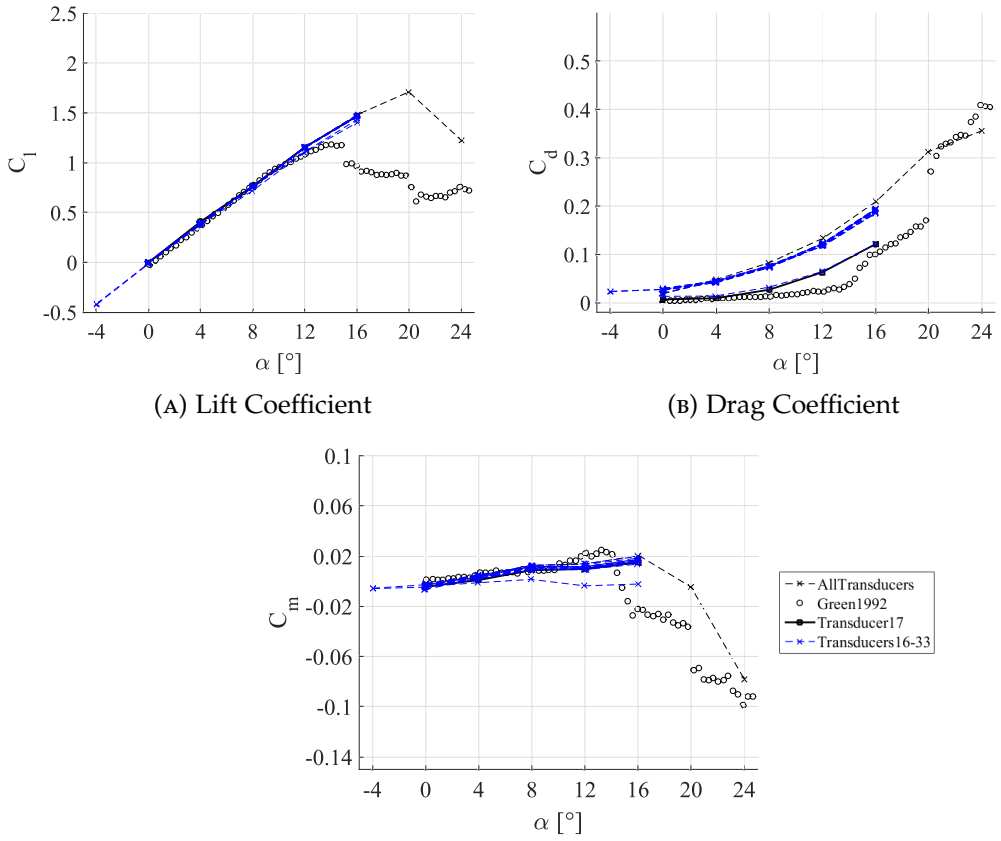

(A) Lift Coefficient

(B) Drag Coefficient

(C) Moment Coefficient

Figure 5.3: Effect of blocking the individual leading-edge flap transducer ports on the static aerodynamic force and moment coefficients. NOTE: results are compared against experimental results for a clean NACA0015 aerofoil [102].

There is a good agreement between the leading-edge flap model and the clean NACA0015 aerofoil when evaluating the lift coefficient results up to 12 degree incidence as shown in Fig. 5.3a. This result shows that the effect of flow leakage inside the leading-edge flap chamber has a minimum effect on the measured Cl values. There is a significant difference in the static stall angle when comparing the leading-edge flap model to the clean NACA0015 model by approximately 5 degrees. The delay in the static stall angle between both models could be potentially due to flow leakage from the leading-edge slot for the leading-edge flap model. Previous research has shown that leading-edge flap slots can produce a delay in separation due to flow from the pressure surface to the suction surface, which slows down the movement of the separation point from the trailing-edge to the leading-edge [116, 117].

The effect of flow leakage inside the leading-edge flap has a more prominent effect on the drag coefficient results as shown in Fig. 5.3b. There is a significant shift in the drag coefficient values when transducer port 17 is blocked, which improves the agreement between the leading-edge flap model and the clean NACA0015 Cd results at the lower incidence range. For incidence values greater than 5 degrees, the measured Cd results with transducer port 17 blocked are larger than for the clean

NACA0015 aerofoil which is due to flow leakage and the level of negative pressure inside the leading-edge flap chamber increasing. The moment coefficient results in Fig. 5.3c show that there is minimal change in the measured values for all individual pressure transducer port blocked cases.

It is shown that the presence of flow-leakage inside the leading-edge flap chamber has a detrimental effect on the measured Cp distribution as well as the aerodynamic force characteristics, with transducer port 17 on the suction surface showing significant levels of flow leakage. It is therefore concluded that the pressure transducer port 17 at the suction surface of the leading-edge flap has a significant effect on the measured surface Cp at the leading-edge flap due to the effect of negative flow leakage within the flap volume. This transducer port is therefore blocked and set as inactive for the remainder of the experimental study.

5.3.2 Wind Tunnel Corrections

Wind tunnel corrections are applied to the static aerodynamic force and moment coefficient results, based on the theory developed by Barlow et al [118]. The main effects of wind tunnel corrections taken into account include solid blockage, wake blockage, and streamline curvature effects. The solid blockage effect, which is represented as the ratio of the relative size of the test article and the test section, is represented by considering the "blockage" to generate an effective change in oncoming flow or dynamic pressure. The wake blockage effect is a result of the finite size of a body wake where the magnitude of the correction for wake blockage increases with an increase of wake size, leading to an increase in drag. The streamline curvature effect refers to modification of the streamline curvature about a body in a wind tunnel in contrast to the corresponding curvature in an infinite free-stream.

The solid blockage factor, ϵ_{sb}, is approximated using the theory developed by Thom [118] using the following expression:

$$\epsilon_{sb} = \frac{K1(Vol_{model})}{A^{3/2}_{testsection}} \tag{5.1}$$

where $K1$ is a factor which represents a model spanning a tunnel height ($K1 = 0.52$), Vol_{model} is the aerofoil model volume (approximated as 0.7 x model thickness x model chord x model span = 0.015901 m^3), and $A_{testsection}$ is the wind tunnel test section cross-sectional area ($A_{testsection} = 2.94\ m^2$).

To apply a correction for the wake blockage effect, ϵ_{wb}, Maskell [118] investigated the flow outside of the wake, and how higher speeds result in reduced pressure over the rearward portion of the model. From this, the wake blockage correction was defined as:

$$\epsilon_{wb} = \frac{(c/h)}{2} C_{d_{un}} \tag{5.2}$$

where c is the aerofoil chord in metres, and h is the test section width of the wind tunnel in metres, and Cd_{un} is the uncorrected value for the drag coefficient.

The total effect of blockage from the wind-tunnel test-section and experimental model, ϵ, is defined as the summation of the solid and wake blockage effects:

$$\epsilon = \epsilon_{sb} + \epsilon_{wb} \tag{5.3}$$

The measurement parameters which have wind-tunnel corrections applied include the incidence angle, lift coefficient, drag coefficient, and the moment coefficient. The corrected incidence angle, α, in radians, is calculated as follows:

$$\alpha = \alpha_u + \frac{57.3\sigma}{2\pi}(C_{l_{un}} + 4C_{m1/4_{un}}) \tag{5.4}$$

where the subscript, $_{un}$, denotes the uncorrected value for the values of incidence angle, lift and moment coefficients. σ is a factor derived from the stream-line curvature effects and is defined as:

$$\sigma = \frac{\pi^2}{48}\frac{c}{h}^2 \tag{5.5}$$

Finally, the corrected values for the lift, drag, and moment coefficients can be calculated using the following expressions:

$$C_l = C_{l_{un}}(1 - \sigma - 2\epsilon) \tag{5.6}$$

$$C_d = C_{d_{un}}(1 - 3\epsilon_{sb} - 2\epsilon_{wb}) \tag{5.7}$$

$$C_m = C_{m_{un}}(1 - 2\epsilon) + 0.25\sigma C_l \tag{5.8}$$

A comparison between the uncorrected and corrected static aerodynamic force and moment coefficients is shown in Fig. 5.4. For incidence angles, $\alpha \leq 10^{\circ}$, blockage effects are minimal therefore similar results are achieved when comparing the uncorrected and corrected aerodynamic coefficients. Blockage effects are shown to begin for incidence angles, $\alpha \geq 10^{\circ}$. There are reductions in Cl_{max}, Cd_{max}, and Cm_{min} when blockage effects are taken into account in comparison to the uncorrected values. It therefore shows that blockage effects from the wind tunnel have an effect on the static aerodynamic force and moment coefficients at the larger incidence angles, however the difference in magnitude is small when compared against the uncorrected aerodynamic coefficients. Table 5.4 presents the tabulated aerodynamic force and moment coefficient results for the uncorrected and corrected cases (the results are normalised using the uncorrected dataset). There are reductions in all of the average and peak aerodynamic coefficients when applying blockage correction factors.

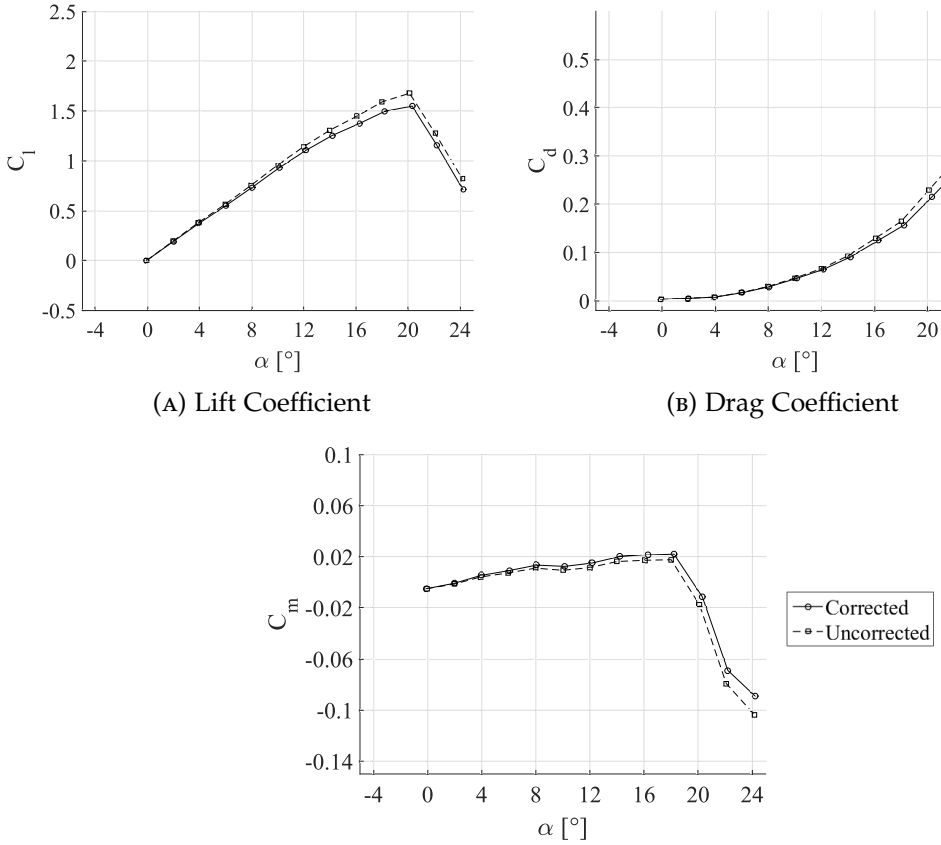

(A) Lift Coefficient

(B) Drag Coefficient

(C) Moment Coefficient

Figure 5.4: Effect of wind tunnel static corrections applied to the aerodynamic force and moment coefficients.

Case	$C_{l_{av}}$	$C_{d_{av}}$	$C_{m_{av}}$	$C_{l_{max}}$	$C_{d_{max}}$	$C_{m_{min}}$
Uncorrected	1.000	1.000	1.000	1.000	1.000	1.000
Corrected	0.943	0.929	0.535	0.924	0.880	0.858

Table 5.4: Effect of wind tunnel blockage on the measured static aerodynamic force and moment coefficients. Note: the results are normalised with respect to the uncorrected dataset.

5.4 EFFECT OF LEADING-EDGE FIXED DROOP AMPLITUDE ON THE STATIC STALL ANGLE

The effect of the delay in the static stall angle for the leading-edge flap NACA0015 model is further investigated by varying the leading-edge fixed droop amplitude (aerofoil physical camber). Positive and negative values of the leading-edge fixed droop amplitude were set and the static aerodynamic force and moment coefficients were measured to determine the change of the onset of the static stall angle. The range of values selected for the fixed droop amplitude, FD_{amp}, include: $FD_{amp} = [-15, -10, 0, +10, 15]^{\circ}$.

The variation of static aerodynamic force and moment coefficient results with leading-edge fixed droop amplitude is shown in Fig. 5.5. The clean NACA0015 aerofoil results are also shown for comparison [102]. At leading-edge fixed droop amplitudes $FD_{amp} \leq 15^{\circ}$, there is no change in the measured Cl values for a wide incidence range, as shown in Fig. 5.5a. There is an increase in Cl_{max} when $FD_{amp} = 15^{\circ}$, and the positive leading-edge fixed droop amplitude has little effect on the static stall angle when compared against the zero degree flap setting. In Fig. 5.5b, there is a small increase in the Cd for an increase in positive FD_{amp} for a large range of incidence angles. The improvement in static stall recovery however results in a reduction in Cd_{max} for leading-edge fixed droop amplitudes, $FD_{amp} \geq 10^{\circ}$.

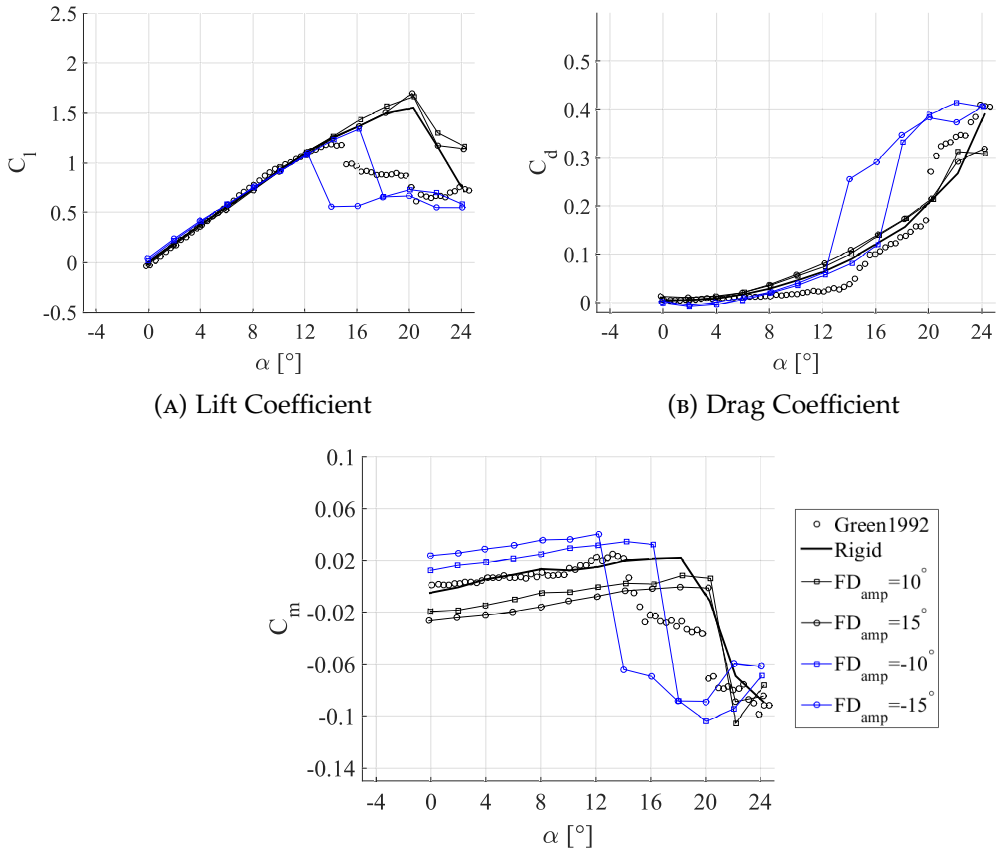

(A) Lift Coefficient

(B) Drag Coefficient

(C) Moment Coefficient

Figure 5.5: Effect of the leading-edge fixed droop amplitude on the static, corrected aerodynamic force and moment coefficients. Note: results are compared against the experimental results for the clean NACA0015 aerofoil [102].

There is a significant change in the static angle onset when negative leading-edge fixed droop deflections are applied, as shown in Fig. 5.5a. There is a decrease in the static stall angle onset for an increase in -ve FD_{amp}, which results in a decrease in Cl_{max}. This reduction in the static stall angle onset also results in an earlier instance of the drag rise, as illustrated in Fig. 5.5b. There is a plateau in Cd_{max} near the maximum incidence angle for both negative leading-edge fixed droop amplitudes, which represents the full extent of the model wake. At α_{max}, both negative FD_{amp} settings are shown to produce similar levels of Cd, which suggests that the wake domains are of similar size.

The effect of leading-edge fixed droop has a significant influence on the moment coefficient results shown in Fig. 5.5c. This is due to the variation in aerofoil camber which results in a change in the Cm polar results. At $\alpha = 10°$, an increase in +ve FD_{amp} results in a decrease in Cm, whereas an increase in -ve FD_{amp} leads to an increase in Cm. When comparing the clean NACA0015 aerofoil against the leading-edge flap NACA0015 model ($FD_{amp} = 0°$), the moment coefficient results are similar for incidence angles, $\alpha \leq 13°$. This confirms that the leading-edge flap NACA0015 model with the flap set to zero degrees is similar to the clean NACA0015 model,

with minor differences in the measured *Cm* being associated either to flow leakage within the leading-edge flap volume, measurement uncertainty, or from differences due to the leading-edge flap model geometry. Moreover, at maximum incidence, the leading-edge flap model achieves similar values of *Cm* when compared against the clean NACA0015 aerofoil model.

Another reason for the delay in the static stall onset angle for the leading-edge flap NACA0015 aerofoil in comparison to the clean NACA0015 aerofoil could be due to the leading-edge flap model design. There is a 1mm gap between the leading-edge flap and the recess to the aerofoil section which is sealed using low coefficient of friction tape. It has previously been shown in experimental studies however that airflow in leading-edge slots from the pressure side to the suction side can lead to a delay in static and dynamic stall [116, 117].

5.4.1 CFD and experimental validation

For the final part of the static analysis section, a comparison is made between the computational and wind-tunnel corrected experimental aerodynamic force and moment coefficients at selected incidence angles to use as part of the validation process. The time-averaged force and moment coefficient results for both methods is shown in Fig. 5.6, along with the results for the clean NACA0015 aerofoil [102]. There is a good agreement between the experimental and computational results when assessing *Cl* and *Cm* at incidence angles, $\alpha \leq 8^{\circ}$. There is a poorer agreement between both methods when comparing the drag coefficient results, however the computational predicted values for Cd are shown to be similar to the clean NACA0015 aerofoil for incidence angles $\alpha \leq 8^{\circ}$. This further shows that the presence of flow leakage within the leading-edge flap volume generates a significant positive offset in the measured Cd values. At $\alpha = 16^{\circ}$, there is a good agreement between the leading-edge flap experimental and computational results when assessing Cl as shown in Fig. 5.6a. In Fig. 5.6c, the measured Cm for the leading-edge flap model is lower in comparison to the computational predicted Cm, which is partly due to the larger offset in drag as visualised in Fig. 5.6b.

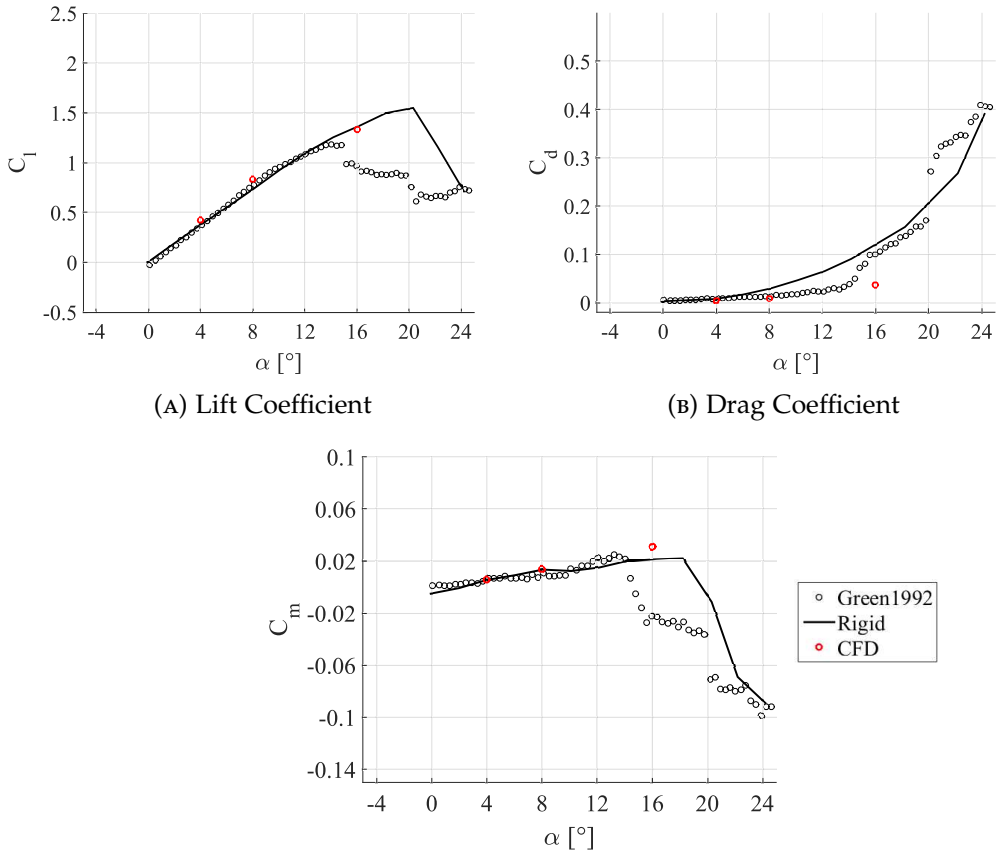

(A) Lift Coefficient

(B) Drag Coefficient

(C) Moment Coefficient

Figure 5.6: Validation comparison between the experimental and computational static aerodynamic coefficients. Note: results are compared against experimental results for the clean NACA0015 aerofoil [102].

5.5 DYNAMIC ANALYSIS - ATTACHED FLOW

5.5.1 Effect of Reduced Frequency

The first stage of the dynamic analysis is to assess the dynamic response of the pressure transducers for the leading-edge flap NACA0015 model under attached flow conditions. The dynamic response of the pressure transducers are assessed against two values of reduced frequency for one sinusoidal pitch motion profile. The operational conditions for the attached flow runs were: Re = 1,010,000, $\alpha_M = 5°$, and $\alpha_{amp} = 5°$. No effects of leading-edge morphing or leading-edge fixed droop are included in the dynamic attached flow stage, therefore the leading-edge flap is set to zero degrees. This allows for the leading-edge flap model to be comparable against the clean NACA0015 model. The measured aerodynamic force and moment coefficients are compared against the equivalent CFD results, using the CFD model developed in chapter 3, which will form part of the validation process for the model predicting attached dynamic flow conditions.

During the attached flow runs, the sampling rate for the data acquisition was kept constant at 10 kHz. There was however a change in the sampling duration time

depending on the value of reduced frequency being assessed. At k = 0.025, the last five periodic pitch cycles were used for the sampling duration, whereas 10 cycles were used for k = 0.1021. The difference in the total number of pitch cycles recorded was due to the memory limitations for both the analogue waveform generator and the data acquisition system. A low pass filter is applied to the raw sampled data to remove any interference noise from the signal. For k = 0.025, the signal is filtered at 250 Hz, and for k = 0.1021, the signal is filtered at 1000 Hz.

The phase-averaged aerodynamic force and moment coefficient results comparison between the experimental and computational methods at k = 0.025, is shown in Fig. 5.7. There is a good agreement in the Cl-α linear rate trends between the experimental and computational results as illustrated in Fig. 5.7a. There is also a good agreement in Cm between both methods as shown in Fig. 5.7c. The level of hysteresis in Cl and Cm between both methods are also similar. There is however, a large difference between the experimental and CFD methods when assessing the drag coefficient. This is evident when analysing the time-averaged and peak aerodynamic coefficients in Table 5.5, which shows a 61.8 % and 54.7 % difference in Cd_{av} and Cd_{max} respectively. The differences in both methods could be due to the effect of flow leakage from the leading-edge flap for the experimental result, which was previously shown in the static analysis to generate a significant offset in the measured Cd. As a result, there is a significant increase in Cd_{max} for the experimental result in comparison to the computational result.

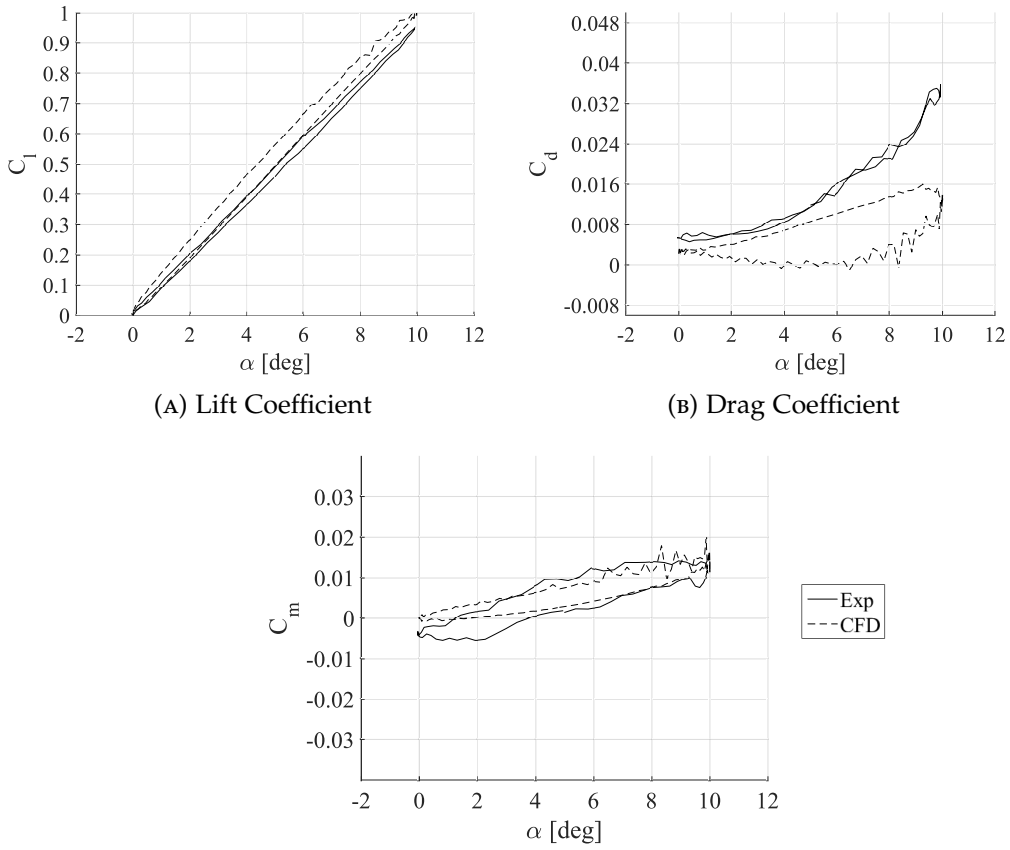

(a) Lift Coefficient

(b) Drag Coefficient

(c) Moment Coefficient

Figure 5.7: Phase-averaged aerodynamic force and moment coefficient comparison between the experiment and computational results under dynamic, attached flow conditions. Operational conditions: $\alpha_M = 5°$, $\alpha_{amp} = 5°$, $k = 0.025$, $Re = 1,010,000$.

Case	$C_{l_{av}}$	$C_{d_{av}}$	$C_{m_{av}}$	$C_{l_{max}}$	$C_{d_{max}}$
Experiment	1.000	1.000	1.000	1.000	1.000
CFD	1.096	0.382	1.408	1.069	0.543

Table 5.5: Time-averaged aerodynamic force and moment coefficient comparison between the experiment and computational results under dynamic, attached flow conditions. Operational conditions: $\alpha_M = 5°$, $\alpha_{amp} = 5°$, $k = 0.025$, $Re = 1,010,000$. Note: data is normalised with respect to the experimental results.

There is a better agreement in the phase-averaged aerodynamic coefficients between the experimental and computational methods when increasing the reduced frequency from 0.025 to 0.1021, as shown in Fig. 5.8. The linear increase in the lift coefficient is similar between both methods as shown in Fig. 5.8a. The time-averaged and peak aerodynamic force and moment coefficient results in Table 5.6 demonstrate a 5.9 % and 2.1 % difference in Cl_{av} and Cl_{max} respectively between the CFD and experimental results. At $\alpha = 0°$, there is an offset in lift for both the experimental and computational results which is due to the increase in pitch rate. The drag coefficient

results in Fig. 5.8b shows similar trends when increasing the reduced frequency. At lower incidence angles, there is a close match between the experimental and computational Cd, however for incidence angles $\alpha \geq 4°$, there is a larger increase in drag from the experimental result. The main difference between both methods is due to the presence of flow leakage in the experiment, which was shown from the static analysis section to have a significant influence on the measured Cd values at the higher incidence angles. When assessing the phase-averaged moment coefficient results in Fig. 5.8c, there is a good agreement between both methods. Both the experimental and CFD methods demonstrate that the flow remains attached as well as showing no negative pitch damping loop when the aerofoil transitions from the pitch upstroke to the pitch downstroke. The difference in Cm_{av} between the experiment and CFD is approximately 0.6 %.

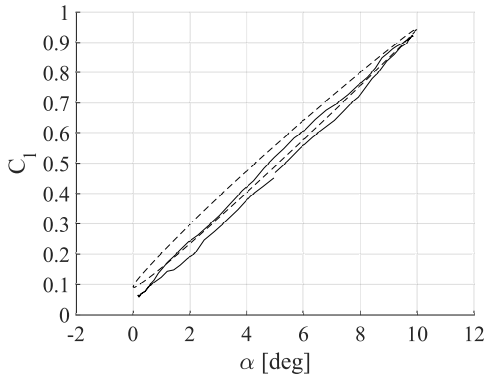

(A) Lift Coefficient

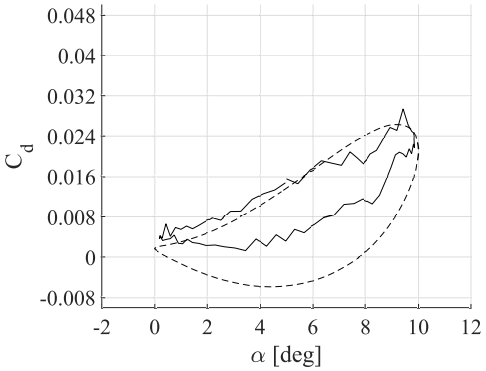

(B) Drag Coefficient

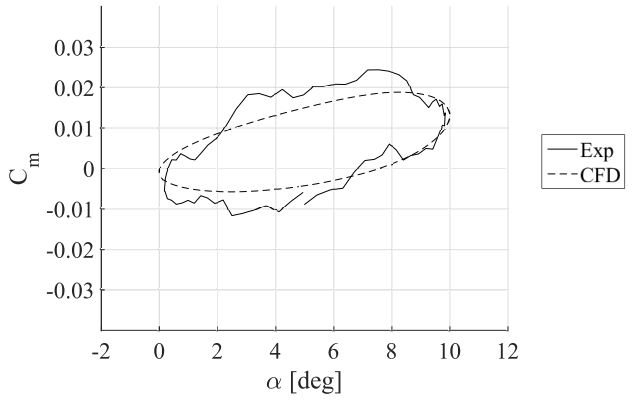

(C) Moment Coefficient

Figure 5.8: Phase-averaged aerodynamic force and moment coefficient comparison between the experiment and computational results under dynamic, attached flow conditions. Operational conditions: $\alpha_M = 5°$, $\alpha_{amp} = 5°$, $k = 0.1021$, $Re = 1,010,000$.

Case	$C_{l_{av}}$	$C_{d_{av}}$	$C_{m_{av}}$	$C_{l_{max}}$	$C_{d_{max}}$
Experiment	1.000	1.000	1.000	1.000	1.000
CFD	1.059	0.668	1.006	1.021	0.894

Table 5.6: Time-averaged aerodynamic force and moment coefficient comparison between the experiment and computational results under dynamic, attached flow conditions. Operational conditions: $\alpha_M = 5^\circ$, $\alpha_{amp} = 5^\circ$, $k = 0.1021$, $Re = 1,010,000$. Note: data is normalised with respect to the experimental results.

It has been shown for both reduced frequency values assessed under dynamic, attached flow conditions that there is a good agreement in the lift and moment coefficient when comparing the experimental result against the CFD result. There is a poorer agreement between both methods when comparing the drag coefficient results for both reduced frequency values, which is due to the effect of flow leakage affecting the surface pressure measurements from the experimental method. Due to the effect of flow leakage, the measured values for the drag coefficient should only be used to compare against the CFD predicted measurements qualitatively, as the presence of flow leakage produces an offset in the measure experimental drag coefficient.

5.6 DYNAMIC ANALYSIS - LIGHT STALL

The effect that leading-edge morphing and leading-edge fixed droop have on improving aerodynamic performance under light dynamic stall conditions is investigated in this section. Different pitch profiles are assessed to determine when light dynamic stall effects are produced, which can then be used when performing the leading-edge morphing and leading-edge fixed droop runs. Next, the effect of leading-edge morphing and leading-edge fixed droop on alleviating the negative effects of dynamic stall is assessed for a range of flap amplitudes. The performance benefit of both flap methods are also evaluated for a variation in reduced frequency. Finally, a comparison is made between the experimental and computational results with regards to validating the effect that leading-edge morphing and leading-edge fixed droop have on alleviating the adverse effects of light dynamic stall.

The majority of the operational conditions for the light dynamic stall cases remain the same from the dynamic attached flow cases. The Reynolds number is kept constant at Re = 1,010,000. At a reduced frequency of k = 0.1021, the sampling rate and sampling duration time remains the same at 10 kHz and 10 periodic pitching cycles, respectively. At k = 0.025, the sampling duration time is for only 5 periodic pitching cycles due to the memory limitations from the analogue waveform generator and the data acquisition system.

5.6.1 Effect of cyclic amplitude

The effect of incidence is first investigated to determine which pitch motion profiles exhibit features of light dynamic stall conditions. This is achieved by varying the cyclic amplitude for two settings, α_{amp} = [8,10]° at one mean incidence angle, $\alpha_{mean} = 12°$. The reduced frequency is set to the larger value k = 0.1021, and the leading-edge flap is set to zero degrees, which represents the clean NACA0015 aerofoil configuration.

The phase-averaged aerodynamic force and moment coefficient results with a variation in cyclic amplitude under light dynamic stall conditions is shown in Fig. 5.9. The lift coefficient results in Fig. 5.9a demonstrated that the linear rate increase in Cl is independent of the cyclic amplitude during the pitch upstroke. Light dynamic stall conditions are shown to be produced at $\alpha_{amp} = 10°$ due to the formation of a negative pitch damping loop as visualised in Fig. 5.9c. Moreover, at $\alpha_{amp} = 10°$, the level of hysteresis during the light dynamic stall is larger and results in an increase in Cd_{max} and Cm_{min}. There is a delay in flow re-attachment due to the light dynamic stall characteristic features at $\alpha_{amp} = 10°$, near the end of the pitch downstroke. After flow reattachment occurs, there is little change in the aerodynamic force and moment coefficients for a change in α_{amp}.

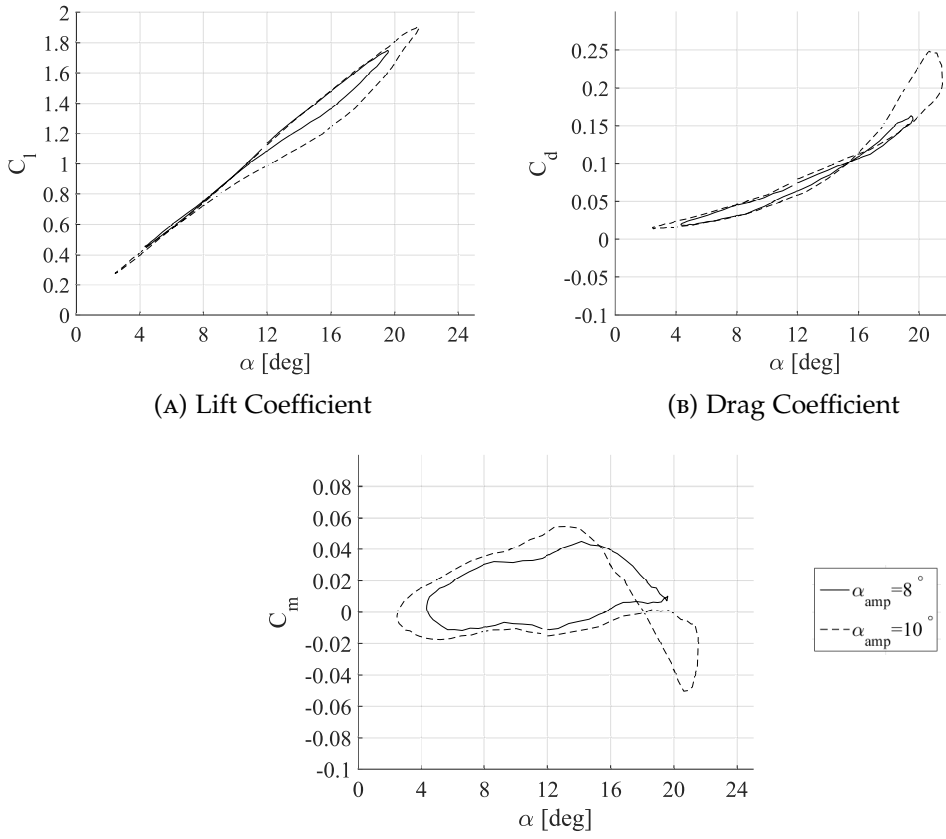

(a) Lift Coefficient

(b) Drag Coefficient

(c) Moment Coefficient

Figure 5.9: Effect of cyclic variation on the phase-averaged aerodynamic force and moment coefficients under light dynamic stall conditions. Operational conditions: $\alpha_M = 12°$, $k = 0.1021$, $Re = 1,010,000$.

5.6.2 Effect of Leading-Edge Morphing

The effect of the leading-edge morphing amplitude on reducing the adverse effects of light dynamic stall is investigated for the pitch profile condition: $\alpha_M = 12^\circ$, $\alpha_{amp} = 10^\circ$, and at a reduced frequency of k = 0.1021. The leading-edge flap motion is initiated at the mean incidence during the pitch upstroke, and follows a pulsed motion profile. This means that the flap achieves maximum deflection at α_{max}, and returns to the zero degree flap deflection at α_M during the pitch downstroke. The flap then remains at the zero degree setting for the remainder of the pitch cycle. The effect of variation in the leading-edge morphing amplitude β_{max}, is assessed with the following settings, $\beta_{max} = 5, 10, 15^\circ$, and is compared against the zero degree flap deflection (rigid NACA0015 aerofoil).

The effect that the leading-edge morphing amplitude has on the phase-averaged aerodynamic force and moment coefficients under light dynamic stall conditions is shown in Fig. 5.10. For all values of β_{max} assessed, there are reductions in the aerodynamic hysteresis loops when compared against the rigid aerofoil. During the pitch upstroke, leading-edge morphing has an minimal effect on the lift characteristics when compared against the rigid aerofoil, as shown in Fig. 5.10a. During the pitch downstroke, the level of reduction in the lift hysteresis loop increases for an increase in β_{max}.

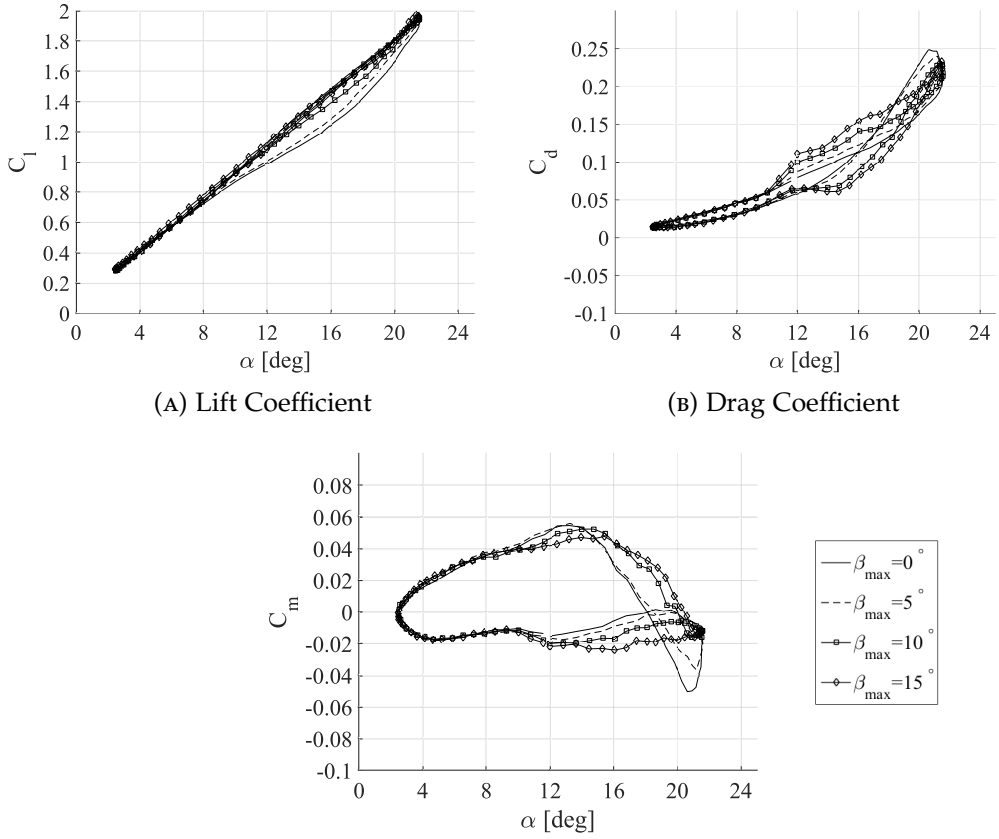

(A) Lift Coefficient

(B) Drag Coefficient

(C) Moment Coefficient

Figure 5.10: Effect of leading-edge morphing variation on the phase-averaged aerodynamic force and moment coefficients under light dynamic stall conditions. Operational conditions: $\alpha_M = 12°$, $\alpha_{amp} = 10°$, $k = 0.1021$, $Re = 1,010,000$.

The drag coefficient results in 5.10b show an interesting feature where there is a sudden, large increase in drag when actuation of the leading-edge flap is initiated. Possible reasons for this feature could be due to the flow leakage from the leading-edge flap, or the initial transient effects in the flap motion during each cycle. The drag coefficient results should therefore be taken with caution, as it was shown in the static analysis section that flow leakage has a significant impact on the measured drag. Similar to the lift coefficient results, there is no change in the drag coefficient when the flap actuation has finished at the mean incidence angle during the downstroke.

The leading-edge morphing benefits are better illustrated when analysing the moment coefficient results in Fig. 5.10c. The negative pitch damping loop is significantly reduced for all values of β_{max}. The transition point to positive pitch damping also occurs earlier when leading-edge morphing is applied except for $\beta_{max} = 5°$ which occurs similar to the rigid aerofoil.

Table 5.7 presents the time-averaged and peak aerodynamic force and moment coefficient results for a variation in the leading-edge morphing amplitude. It is shown that all leading-edge morphing amplitudes assessed have no effect on Cl_{av} and Cl_{max} when compared against the rigid aerofoil. The most effective leading-edge morphing amplitude setting is at $\beta_{max} = 10^{\circ}$, as it achieves the largest reductions in Cd_{max} and Cm_{min} of 8.1 % and 61.4 % respectively when compared against the rigid aerofoil. The level of reduction in Cd_{max} and Cm_{min} decreases when β_{max} is increased from 10 to 15 degrees. This feature of leading-edge morphing was also predicted in the CFD analysis previously performed in Chapter 3.

Case	$C_{l_{av}}$	$C_{d_{av}}$	$C_{m_{av}}$	$C_{l_{max}}$	$C_{d_{max}}$	$C_{m_{min}}$
$\beta_{max} = 0^{\circ}$	1.000	1.000	1.000	1.000	1.000	1.000
$\beta_{max} = 5^{\circ}$	1.016	1.007	5.200	1.013	0.955	0.671
$\beta_{max} = 10^{\circ}$	1.033	0.989	8.400	1.024	0.919	0.386
$\beta_{max} = 15^{\circ}$	1.044	1.000	6.800	1.034	0.932	0.461

Table 5.7: Effect of leading-edge morphing variation on the time-averaged and peak aerodynamic force and moment coefficients under light dynamic stall conditions. Operational conditions: $\alpha_M = 12^{\circ}$, $\alpha_{amp} = 10^{\circ}$, $k = 0.1021$, $Re = 1,010,000$. Note: data is normalised with respect to the rigid aerofoil results.

5.6.3 Effect of Leading-Edge Fixed Droop

The effect that variation of the leading-edge fixed droop has on alleviating the adverse effects of light dynamic stall is next investigated. The operational conditions for the leading-edge fixed droop cases are set as the same as the leading-edge morphing cases. The leading-edge fixed droop amplitude, FD_{amp}, is varied to assess the change in dynamic stall control at the following settings, FD_{amp} = [5,10,15]$^{\circ}$. Note: before the dynamic runs are performed for the leading-edge fixed droop cases, the leading-edge flap is set to the desired flap angle, and remains locked in the current position for the run duration.

The effect that variation of the leading-edge fixed droop amplitude has on the phase-averaged aerodynamic force and moment coefficients under light dynamic stall conditions is shown in Fig. 5.11. The lift coefficient results in Fig. 5.11a illustrate that leading-edge fixed droop has little effect on Cl during the pitch upstroke which is consistent with the leading-edge morphing method. There is however an offset in the linear increase section of Cl for leading-edge fixed droop amplitudes, $FD_{amp} \geq 10^{\circ}$, due to the physical camber change of the aerofoil. During the pitch downstroke, there is a reduction in lift hysteresis for all values of FD_{amp}.

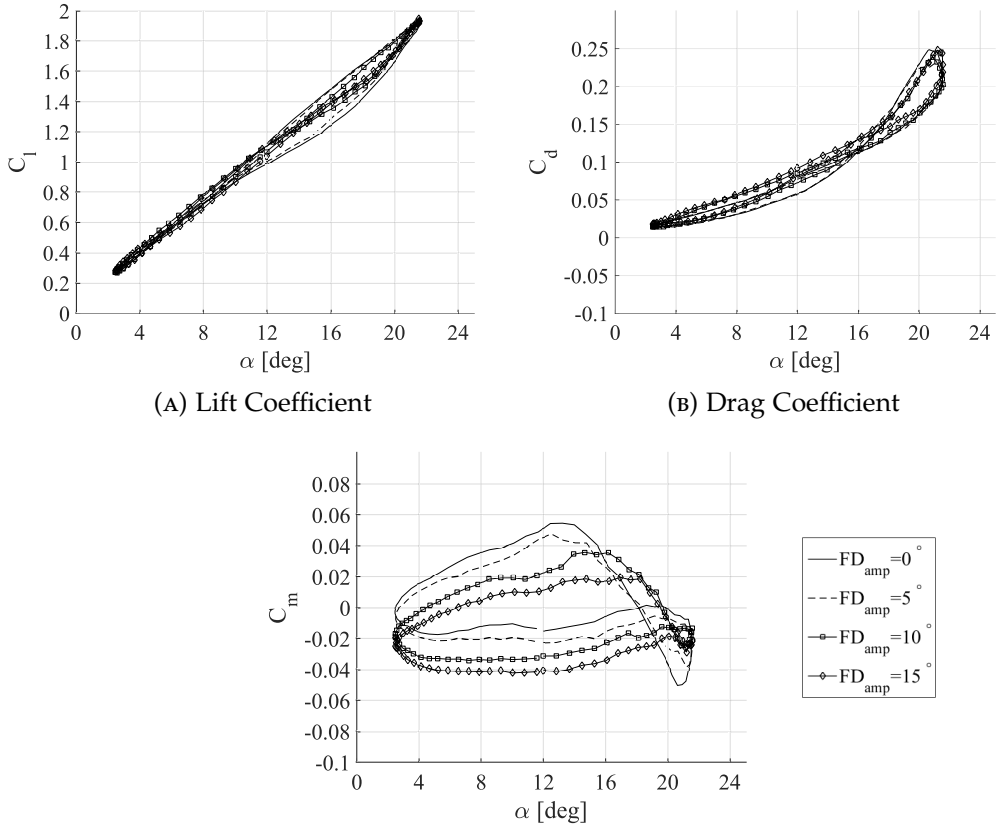

(A) Lift Coefficient

(B) Drag Coefficient

(C) Moment Coefficient

Figure 5.11: Effect of leading-edge positive fixed droop variation on the phase-averaged,aerodynamic force and moment coefficients under light dynamic stall conditions. Operational conditions: $\alpha_M = 12^\circ$, $\alpha_{amp} = 10^\circ$, $k = 0.1021$, $Re = 1,010,000$.

The drag coefficient results in Fig. 5.11b show that there is a positive offset in the measured Cd when FD_{amp} increases during the pitch upstroke. There is a reduction in the peak drag coefficient for all FD_{amp} amplitudes assessed and none of the leading-edge morphing amplitudes were able to achieve a significant reduction in the positive drag hysteresis loop during the pitch downstroke.

The moment coefficient results in Fig. 5.11c show that there is a modification of the pitch moment characteristics during the pitch upstroke for a change in the leading-edge fixed droop amplitude. This characteristic has been observed in previous numerical and experimental research on dynamic stall with cambered-variation aerofoils [74–76].During the pitch upstroke, at the mean incidence angle, there is a reduction in the measured Cm for an increase in FD_{amp}. During the pitch downstroke, there is a significant reduction in the negative pitch damping loop for all FD_{amp} cases, compared to the rigid aerofoil case. The transition point from negative pitch damping to positive pitch damping occurs earlier for all FD_{amp} cases assessed. However, there is also a reduction in positive Cm for an increase in FD_{amp}, due to the aerofoil's physical camber change. This can introduce undesired performance changes to the aerofoil when applied to propulsion systems such as cycloidal rotors as the results deviate

from the rigid NACA0015 aerofoil.

Table 5.8 presents the time-averaged and peak aerodynamic force and moment coefficient results for a variation in the leading-edge fixed droop amplitude. Similar to leading-edge morphing, it is shown that leading-edge fixed droop has no effect on the lift characteristics when compared against the rigid aerofoil. The largest reduction in Cd_{max} of 6.6 % is achieved at $FD_{amp} = 5°$, however the level of reduction in Cd_{max} decreases for an increase in FD_{amp} to 15 degrees. There is also an increase in Cd_{av} at $FD_{amp} \geq 10°$, which is due to the physical camber change that is applied throughout the entire pitch cycle. All leading-edge fixed droop amplitudes also achieve significant reductions in Cm_{min}, with the largest reduction of 35.1 % achieved at $FD_{amp} = 10°$. There is also a significant change in the time-averaged moment coefficient due to applying leading-edge fixed droop, which results in an overall change to the aerodynamic characteristics in comparison to the rigid NACA0015 aerofoil.

Case	$C_{l_{av}}$	$C_{d_{av}}$	$C_{m_{av}}$	$C_{l_{max}}$	$C_{d_{max}}$	$C_{m_{min}}$
Rigid	1.000	1.000	1.000	1.000	1.000	1.000
$FD_{amp} = 5°$	1.010	0.988	-7.600	1.012	0.934	0.728
$FD_{amp} = 10°$	1.018	1.015	-18.600	1.010	0.951	0.649
$FD_{amp} = 15°$	1.010	1.086	-34.000	1.021	0.988	0.783

Table 5.8: Effect of leading-edge positive fixed droop variation on the phase-averaged,aerodynamic force and moment coefficients under light dynamic stall conditions. Operational conditions: $\alpha_M = 12°$, $\alpha_{amp} = 10°$, $k = 0.1021$, $Re = 1,010,000$. Note: data is normalised with respect to the rigid aerofoil results.

5.6.4 Comparison between leading-edge fixed droop and leading-edge morphing

A comparison is made between the effect of leading-edge morphing and leading-edge fixed droop for the most effective flap angle, 10 degrees, with the phase-averaged aerodynamic force and moment coefficient results shown in Fig. 5.12. The lift coefficient results in Fig. 5.12a show a small decrease in lift during the pitch upstroke when comparing the leading-edge fixed droop flap method against the rigid NACA0015 aerofoil. There is also no difference in Cl_{max} when comparing against both flap methods. During the pitch downstroke, both leading-edge flap methods achieve a reduction in lift hysteresis, with leading-edge morphing achieving a greater reduction in comparison to leading-edge fixed droop. Near the end of the downstroke, leading-edge fixed droop produces a positive offset in lift generated due to the positive camber change to the model. When comparing leading-edge morphing to the rigid aerofoil near the end of the pitch downstroke, there is no change in the measured Cl due to the morphing being inactive at this phase of the pitch cycle.

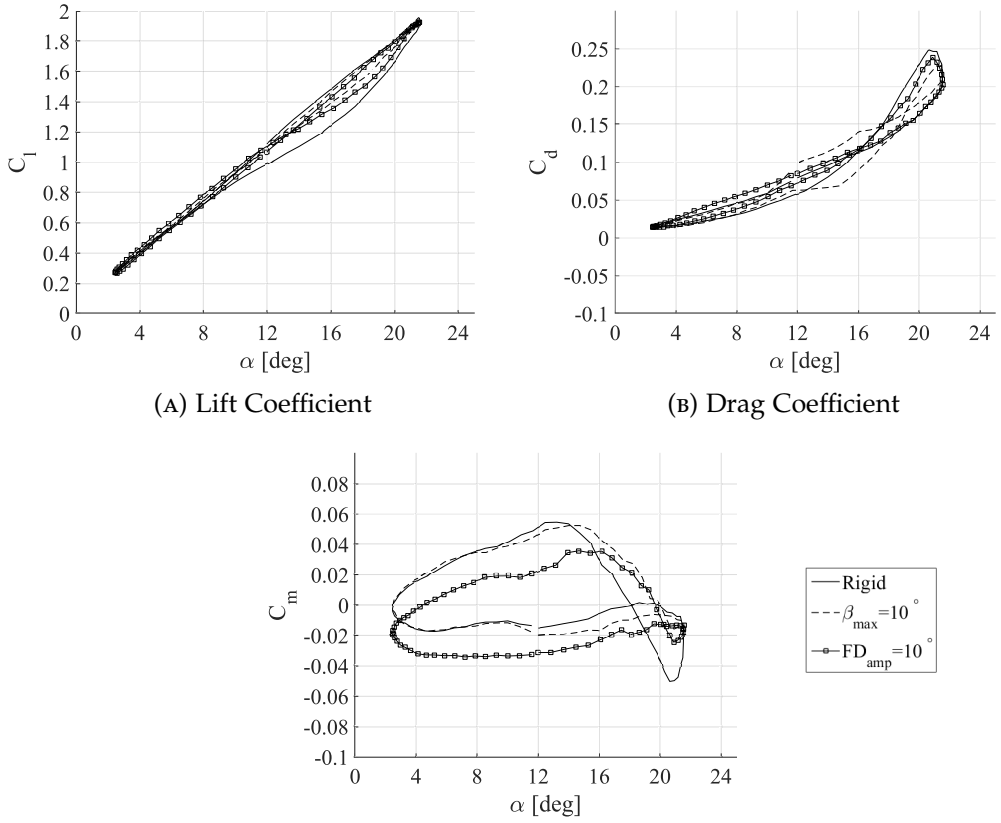

(A) Lift Coefficient

(B) Drag Coefficient

(C) Moment Coefficient

Figure 5.12: Comparison between leading-edge morphing and fixed droop amplitude effects under light dynamic stall conditions. Operational conditions: $\alpha_M = 12°$, $\alpha_{amp} = 10°$, $k = 0.1021$, $Re = 1,010,000$.

The drag coefficient results in Fig. 5.12b show that both flap methods generate an increase in drag at the mean incidence during the pitch upstroke. The increase in drag is much larger for leading-edge morphing than for leading-edge fixed droop which may be due to the initial transient effect from flap motion. There is a reduction in Cd_{max} for both flap methods when compared against the rigid aerofoil. During the initial phase of the pitch downstroke, leading-edge morphing generates a greater reduction in drag in comparison to leading-edge fixed droop. Once leading-edge morphing has terminated at the mean incidence, similar drag results are generated when compared to the rigid NACA0015 aerofoil. The leading-edge fixed droop flap method however generates an increase in drag due to the aerofoil's physical camber change. This also leads to an offset increase in drag at the beginning of the pitch upstroke, and towards the mean incidence angle.

There is a significant difference in the moment coefficient for both flap methods as visualised in Fig. 5.12c. The physical camber change for leading-edge fixed droop results in a negative offset in the measured Cm for the entire pitch upstroke. In contrast, there is only a small change in Cm when leading-edge morphing is initiated at the mean incidence. Both flap methods are shown to decrease Cm_{min} as well as

reducing the negative pitch damping loop. This also results in transitioning from negative pitch damping to positive pitch damping occurring earlier for both leading-edge flap methods, in comparison to the rigid aerofoil. The pitch damping transition point occurs at the same incidence angle during the pitch downstroke for both flap methods. Similar positive Cm values are produced for leading-edge morphing and the rigid aerofoil when leading-edge morphing has terminated at the mean incidence during the pitch downstroke. There is a significant decrease in positive Cm for leading-edge fixed droop during the pitch downstroke due to the aerofoil's physical camber change. This concludes that by activating leading-edge morphing only where dynamic stall characteristics are present, improvements in aerodynamic performance can be gained as well as maintaining the original NACA0015 aerodynamic performance characteristics for the second half of the pitch cycle. Leading-edge fixed droop has shown to alleviate the negative effects of light dynamic stall, however, it also alters the aerodynamic performance characteristics for the remainder of the pitch cycle due to the change in the aerofoil's physical camber. This can have a detrimental effect when applying leading-edge fixed droop to a cycloidal rotor configuration, as the cambered blades would induce dynamic stall at the rotor's advancing side.

5.6.5 Effect of Reduced Frequency

A comparison is made between both leading-edge flap methods in alleviating the negative effects of light dynamic stall for a variation in reduced frequency. The effect of reduced frequency is assessed for two conditions which include k = [0.025, 0.1021]. The flap amplitude range remains unchanged for both leading-edge flap methods, which are $\beta_{max} = FD = 0, 5, 10, 15°$. Note: the zero degree flap amplitude represents the rigid NACA0015 aerofoil. All other operational conditions remain unchanged to maintain consistency between the other case studies.

To evaluate the effect of leading-edge morphing and leading-edge fixed droop for a change in reduced frequency, a delta is calculated for both the average and maximum aerodynamic force and moment coefficients, and normalised as follows:

$$\Delta C_{aero_{av}} = \frac{C_{aero_{av(flapamplitude)}} - C_{aero_{av(rigid)}}}{C_{aero_{av(rigid)}}} \tag{5.9}$$

$$\Delta C_{aero_{max}} = \frac{C_{aero_{max(flapamplitude)}} - C_{aero_{max(rigid)}}}{C_{aero_{max(rigid)}}} \tag{5.10}$$

where $C_{aero_{av(flapamplitude)}}$ is the average aerodynamic force or moment coefficient at a desired flap amplitude, $C_{aero_{av(rigid)}}$ is the average force or moment coefficient for the rigid NACA0015 aerofoil (zero degree flap amplitude), and the subscript $C_{aero_{max}}$ represents the maximum force or moment coefficient. Note: $C_{aero_{max}}$ for the moment coefficient represents the peak negative moment coefficient, Cm_{min}.

The delta lift coefficient results for variations in reduced frequency under light dynamic stall conditions is shown in Fig. 5.13. There is an increase in both the average and maximum ΔCl for both flap motion methods and for all of the flap amplitude range. The average delta lift coefficient results in Fig. 5.13a show that both flap methods produce a positive increase at k = 0.025, in comparison to k = 0.1021. This is due to a larger hysteresis in lift at k = 0.025 as a result of the onset of dynamic stall whereas the increase in flow unsteadiness at k = 0.1021 lessens the effect due to maintaining attached flow at the higher incidence angles. Moreover, leading-edge morphing produces a greater increase in ΔCl_{av} in comparison to leading-edge fixed droop at both reduced frequencies. At a flap amplitude of five degrees, there is little difference in ΔCl_{av} between both leading-edge flap methods. The maximum delta lift coefficient results in Fig. 5.13b illustrates a larger increase in ΔCl_{max} for both leading-edge flap methods when k is increased. Moreover, both leading-edge flap methods are shown to increase the lift coefficient over the entire flap amplitude range for both reduced frequencies. At k = 0.025, leading-edge morphing produces a larger increase in Cl_{max} compared to leading-edge fixed droop for all flap amplitudes. This trend is similar at k = 0.1021, however it is shown that leading-edge fixed droop generates a slightly larger increase in Cl_{max} at a flap amplitude of 10 degrees, in comparison to leading-edge morphing.

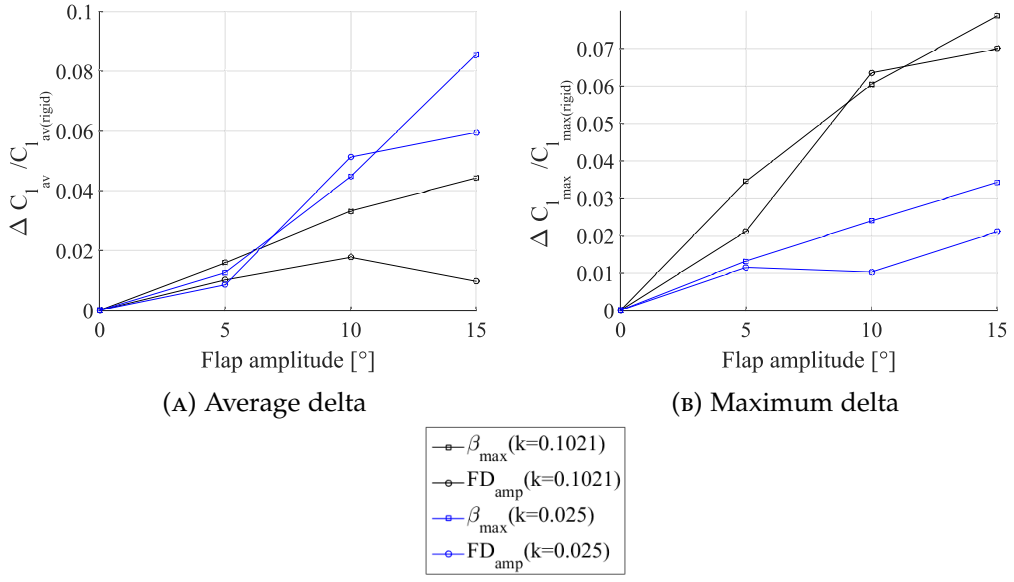

(A) Average delta

(B) Maximum delta

Figure 5.13: Effect of reduced frequency comparison between normalised ΔCl for leading-edge morphing and fixed droop under light dynamic stall conditions. Operational conditions: $\alpha_M = 12°$, $\alpha_{amp} = 10°$, $Re = 1,010,000$.

The drag coefficient delta results for a change in reduced frequency under light dynamic stall conditions is shown in Fig. 5.14. In Fig. 5.14a, there is a non linear trend for the average delta drag coefficient for both the flap methods and for both reduced frequencies. At five degrees flap amplitude, there is reduction in Cd_{av} at both reduced frequencies for leading-edge fixed droop whereas leading-edge morphing is shown to produce a small increase in Cd_{av}. The level of increase in Cd_{av} increases for an increase in reduced frequency for both leading-edge flap methods. As the flap amplitude increases, there is a significant increase in Cd_{av} for leading-edge fixed droop at both reduced frequencies. At 15° flap amplitude, leading-edge morphing produces a small decrease in Cd_{av}. Moreover there is decrease in Cd_{av} for a decrease in reduced frequency for both flap methods. The maximum delta drag coefficient results in Fig. 5.14b show that at a flap amplitude of five degrees, there are reductions in Cd_{max} for both flap methods at k = 0.025. At k = 0.1021, both flap methods generate an increase in Cd_{max} at this flap amplitude. Reductions in Cd_{max} are achieved for both flap methods at a reduced frequency of 0.025 for all flap amplitudes assessed. At k = 0.1021, there are reductions in Cd_{max} for flap amplitude values $\geq 10°$ for leading-edge morphing and at 15° only for leading-edge fixed droop. The largest reduction in Cd_{max} is achieved for leading-edge fixed droop at a flap amplitude and reduced frequency of 15° and 0.1021 respectively.

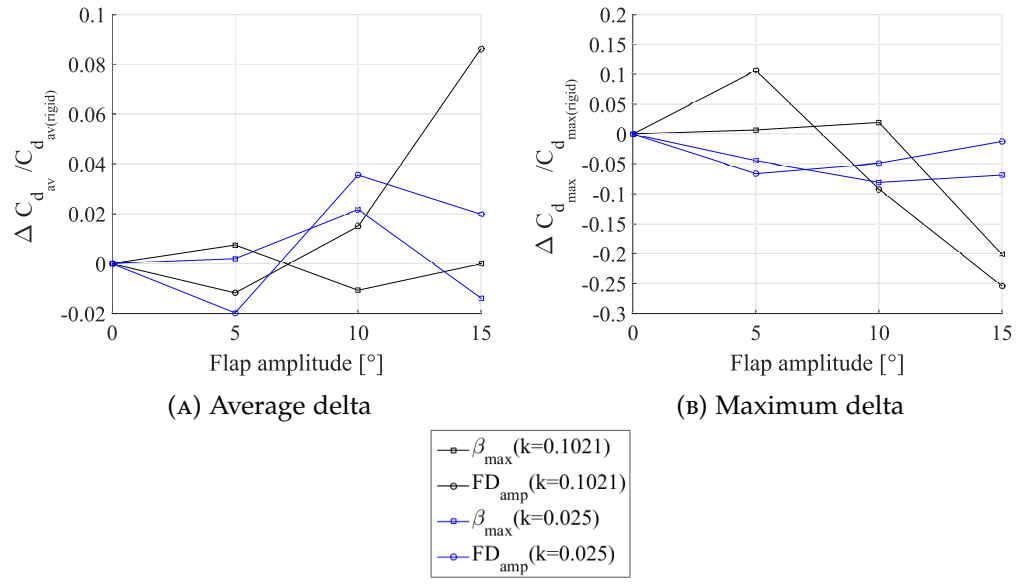

(A) Average delta

(B) Maximum delta

Figure 5.14: Effect of reduced frequency comparison between normalised ΔCd for leading-edge morphing and fixed droop under light dynamic stall conditions. Operational conditions: $\alpha_M = 12°$, $\alpha_{amp} = 10°$, $Re = 1,010,000$.

The moment coefficient delta results for a change in reduced frequency under light dynamic stall conditions is shown in Fig. 5.15. The average delta moment coefficient results in Fig. 5.15a show that an increase in reduced frequency results in a greater change in Cm_{av} for both leading-edge flap methods. At k = 0.1021, there is a significant increase in Cm_{av} for leading-edge morphing whereas there is a significant decrease in Cm_{av} for leading-edge fixed droop. The difference in Cm_{av} for both flap methods is significantly reduced for a decrease in reduced frequency to k = 0.025. Figure 5.15b visualises the minimum delta moment coefficient results for both flap methods with a variation in reduced frequency. At k = 0.025, there are reductions in Cm_{min} for both leading-edge flap methods at all flap amplitudes assessed. Both flap methods produce the greatest reduction at a flap amplitude of 10 degrees, with leading-edge morphing generating a larger decrease in Cm_{min} in comparison to leading-edge fixed droop. At k = 0.1021, there are reductions in Cm_{min} for both flap methods except for a flap amplitude of 5 degrees for leading-edge fixed droop. The largest reduction in Cm_{min} is achieved at a flap amplitude of 15 degrees for both flap methods and leading-edge morphing is shown to produce the largest reduction in Cm_{min} at this flap amplitude and reduced frequency value.

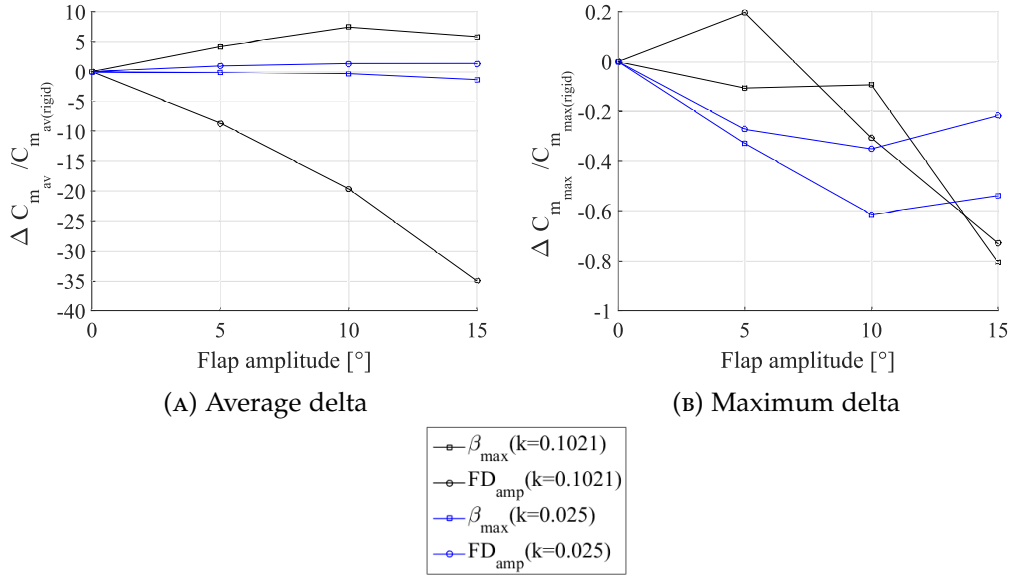

(A) Average delta

(B) Maximum delta

Figure 5.15: Effect of reduced frequency comparison between normalised ΔCm for leading-edge morphing and fixed droop under light dynamic stall conditions. Operational conditions: $\alpha_M = 12°$, $\alpha_{amp} = 10°$, $Re = 1,010,000$.

5.6.6 CFD Validation

The final assessment of the light dynamic stall analysis is to compare the experimental results against the equivalent computational results to serve as part of the validation process. CFD simulations were performed using the model developed in Chapter 3 for the rigid aerofoil, as well as leading-edge morphing and leading-edge fixed droop. The simulations were performed for a range of flap amplitudes to assess the prediction of the dynamic stall alleviation effects. The comparison of leading-edge morphing and leading-edge fixed droop between the experimental and CFD results are compared through calculating the delta (average and maximum) aerodynamic force and moment coefficients as previously defined in Section 5.6.4.

Comparison between the experimental and computational rigid aerofoil aerodynamic lift and moment coefficient under light dynamic stall conditions is shown in Fig. 5.16. For the computational results at $\alpha_M = 12^\circ$, there is a delay in the dynamic stall initiation at the beginning of the pitch downstroke due to the initial formation of the LEV. This results in a significant loss of lift during the pitch downstroke (Fig. 5.16a) as well as a significant increase in Cm_{min} and the negative pitch damping loop (5.16b). The experimental results in contrast do not show a delay in lift stall and the level of increase in negative pitching moment is much less in comparison to the computational results. This confirms that the LEV has not fully formed for the experimental case, which leads to a weaker form of dynamic stall. The delay in the dynamic stall process could potentially be due to the leading-edge flap model design as airflow could possibly leak from the recess gap of the leading-edge flap. Previous studies have shown that airflow in leading-edge slots from the pressure side to the suction side can lead to a delay in dynamic stall [116, 117].

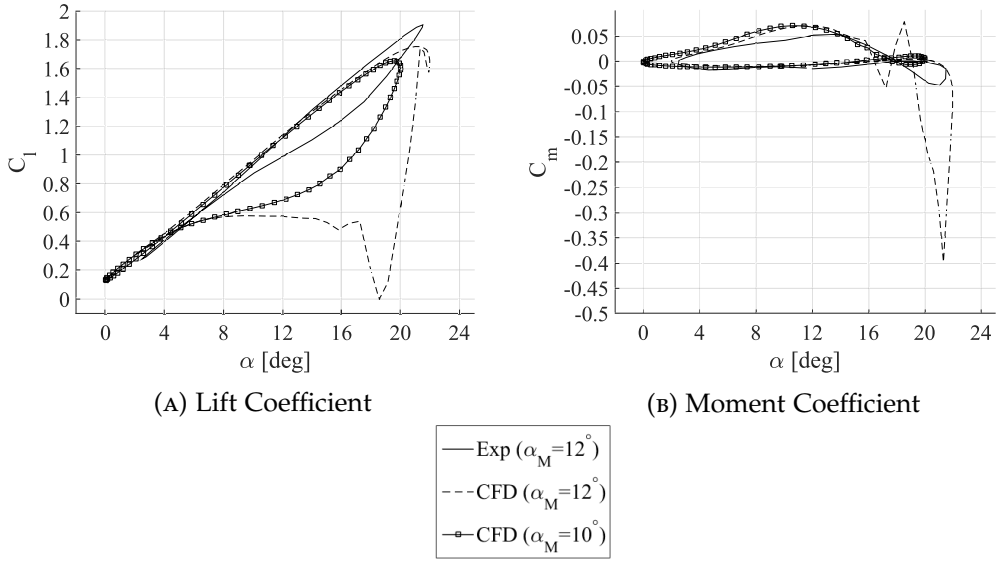

(a) Lift Coefficient (b) Moment Coefficient

Figure 5.16: Comparison between experimental and CFD rigid aerofoil aerodynamic coefficient results under light dynamic stall conditions. Operational conditions: $\alpha_M = 12^\circ$, $\alpha_{amp} = 10^\circ$, $k = 0.1021$, $Re = 1,010,000$.

Due to the significant differences in the dynamic stall characteristics between the experimental and computational results, a further CFD simulation was performed for the rigid aerofoil by reducing the mean incidence angle by two degrees to take into account the delay in dynamic stall from the experiment. The lift coefficient results in Fig. 5.16a show that the lift curve profile is similar to the experimental results as the type of stall is altered (the delay in lift due to the LEV formation is removed). During the pitch downstroke, the computational result predicts larger lift hysteresis in comparison to the experimental result and flow re-attachment occurs later. The moment coefficient results in Fig. 5.16b show that there is a significant reduction in the negative pitching moment when compared to the CFD result for 12 degrees mean incidence, however the formation of a negative pitch damping loop is still captured. It was therefore decided to use a mean incidence angle of 10 degrees to perform the computational simulations for leading-edge morphing and leading-edge fixed droop to use and compare against the equivalent experimental results.

The results for the delta lift coefficients, comparing the experimental and computational results under light dynamic stall conditions is shown in Fig. 5.17. There is a good agreement in the curve trends for both the average and maximum delta lift coefficients for all flap amplitudes except for a flap amplitude of 15 degrees. In Fig. 5.17a, there is an increase in Cl_{av} for all cases assessed up to a flap amplitude of 10 degrees. Moreover, the computational results illustrate that leading-edge morphing generates a larger increase in Cl_{av} than for leading-edge fixed droop, which is in agreement with the experimental findings. When evaluating the maximum delta lift coefficient results in Fig. 5.17b, there is a small increase in computational Cl_{max} for both leading-edge flap motion methods up to a flap amplitude of 10 degrees. At 15 degrees flap amplitude, there is a poor agreement in Cl_{max} between the experimental and computation results.

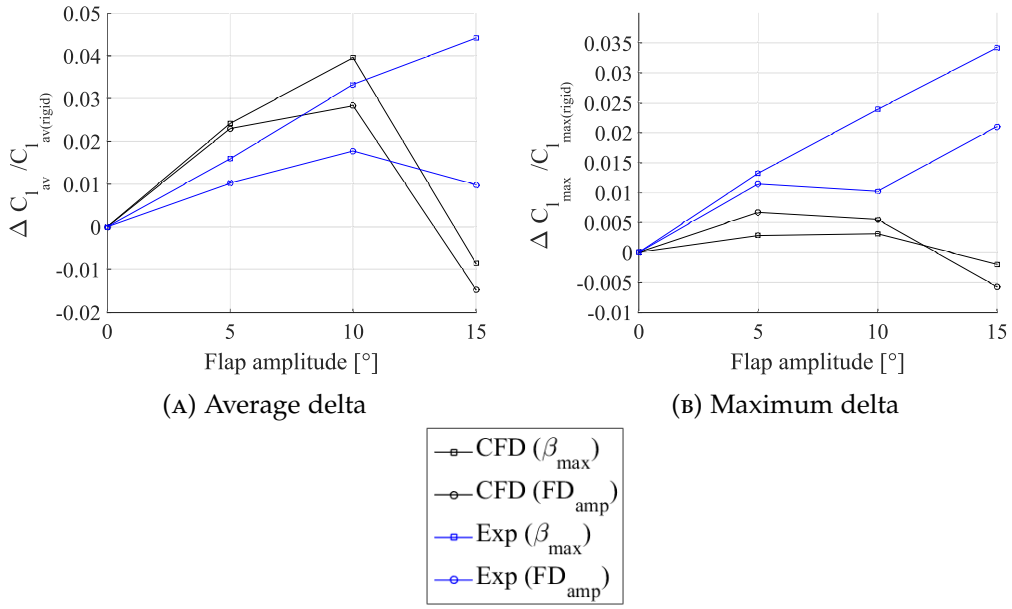

(A) Average delta

(B) Maximum delta

FIGURE 5.17: Comparison between experimental and CFD normalised ΔCl for leading-edge morphing and fixed droop under light dynamic stall conditions. Operational conditions: $\alpha_M = 12°$, $\alpha_{amp} = 10°$, $k = 0.1021$, $Re = 1,010,000$.

The results for the delta drag coefficients, comparing the experimental and computational results under light dynamic stall conditions is shown in Fig. 5.18. There is a poor agreement in Cd_{av} between the experimental and computational results for both leading-edge flap methods as illustrated in Fig. 5.18a. The computational results show a significant reduction in Cd_{av} for an increase in flap amplitude up to 10 degrees for both flap methods. The experimental results show that there is little change in Cd_{av} up to 10 degrees flap amplitude, however there is a significant increase in Cd_{av} at 15 degrees flap amplitude for the experimental leading-edge fixed droop. This is due to the increase in the aerofoil physical camber producing a positive offset in the measured drag. Again there is a poor agreement in Cd_{av} between the experimental and computational results at a flap amplitude of 15 degrees for both flap methods. There is a better agreement between the experimental and computational results for both flap methods (up to 10 degrees flap amplitude) when comparing the maximum delta drag coefficients in Fig. 5.18b.

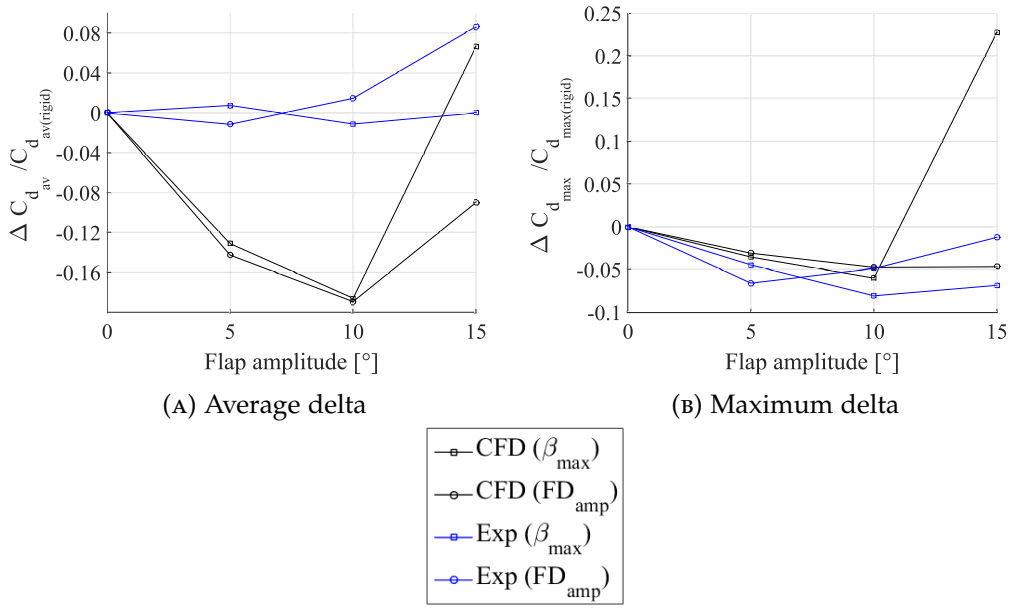

(A) Average delta

(B) Maximum delta

Figure 5.18: Comparison between experimental and CFD normalised ΔCd for leading-edge morphing and fixed droop under light dynamic stall conditions. Operational conditions: $\alpha_M = 12°$, $\alpha_{amp} = 10°$, $k = 0.1021$, $Re = 1,010,000$.

The results for the delta moment coefficients, comparing the experimental and computational results under light dynamic stall conditions are shown in Fig. 5.19. There is a poor agreement between the experimental and computational results for both delta moment coefficients. The computational results in Fig. 5.19a demonstrate that for both flap methods, an increase in the flap amplitude has a negligible effect on Cm_{av}. This is due to the predicted minimum moment coefficient and negative pitch damping loop being smaller than what was measured experimentally. Moreover, this is the reason why there is no reduction in Cm_{min} from the computational results for both flap methods due the low negative Cm value for the rigid aerofoil (Fig. 5.19b). Due to this, a comparison between the experimental and computational results the effect of leading-edge morphing and leading-edge fixed droop on the moment coefficient under light stall conditions cannot be made. Moreover, for all aerodynamic force and moment coefficients, a comparison between the experimental and computational results at 15 degrees flap amplitude for both flap methods cannot be made due to the large discrepancies in results.

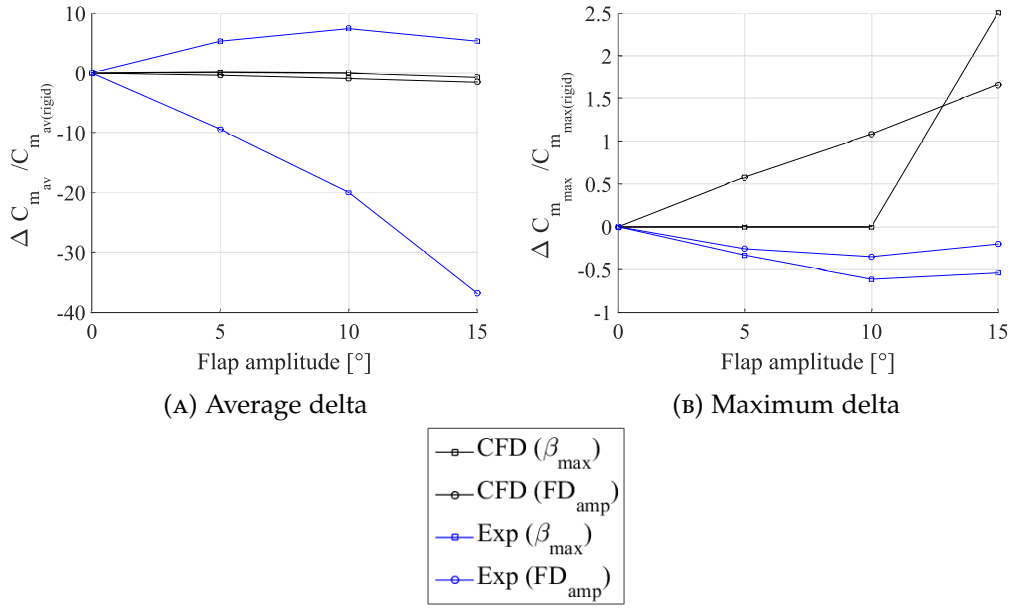

(A) Average delta

(B) Maximum delta

FIGURE 5.19: Comparison between experimental and CFD normalised ΔCm for leading-edge morphing and fixed droop under light dynamic stall conditions. Operational conditions: $\alpha_M = 12°$, $\alpha_{amp} = 10°$, $k = 0.1021$, $Re = 1,010,000$.

5.7 DYNAMIC ANALYSIS - DEEP STALL

The effect of leading-edge morphing and leading-edge fixed droop in alleviating the adverse effects of dynamic stall under deep dynamic stall conditions are evaluated for the final part of this experimental study. Deep dynamic stall conditions are significant in both rotorcraft and cycloidal rotor applications, which result in severe blade-wake interference effects as well as significant loss in performance [55, 119]. The effect of incidence is first evaluated to determine the pitch profile which produces significant dynamic stall hysteresis. Next, the effect of leading-edge morphing and leading-edge fixed droop is assessed in terms of its ability to alleviate the negative effects of deep dynamic stall. The effect of reduced frequency on leading-edge morphing and leading-edge fixed droop performance effects are also assessed. Finally, a comparison between the predicted computational results and the measured experimental results relating to the performance effects of leading-edge morphing and leading-edge fixed droop is made for validation purposes.

5.7.1 EFFECT OF CYCLIC AMPLITUDE

Deep dynamic stall conditions for the rigid aerofoil setting (zero degrees flap angle) for two pitch motion profiles have been measured to assess the extent of the hysteresis effect on the aerodynamic coefficients. The mean incidence angle is set to $\alpha_M = 16°$, and two values for the cyclic amplitude are selected, α_{amp} = [8,10]°. The Reynolds number remains constant at approximately Re 1,010,000, and the reduced frequency is set to k = 0.1021. The unsteady surface pressure measurements are sampled over the last 10 periodic pitch cycles and a phase average is taken to determine the phase-

averaged aerodynamic force and moment coefficients.

The phase-averaged aerodynamic force and moment coefficient results for a variation in cyclic amplitude under deep dynamic stall conditions is shown in Fig. 5.20. During the attached flow phase of the pitch upstroke, there are minimal differences in the aerodynamic coefficients for a change in α_{amp}. There is an increase in Cl_{max} for an increase in α_{amp} with the dynamic stall initiation beginning at the start of the pitch downstroke, as illustrated in Fig. 5.20a. No overshoot in lift is measured, meaning that the full formation of the LEV did not occur. The increase in Cl_{max} due to the increase in α_{amp} also results in an increase in the drag-rise (Fig. 5.20b) and the peak negative pitching moment (Fig. 5.20c).

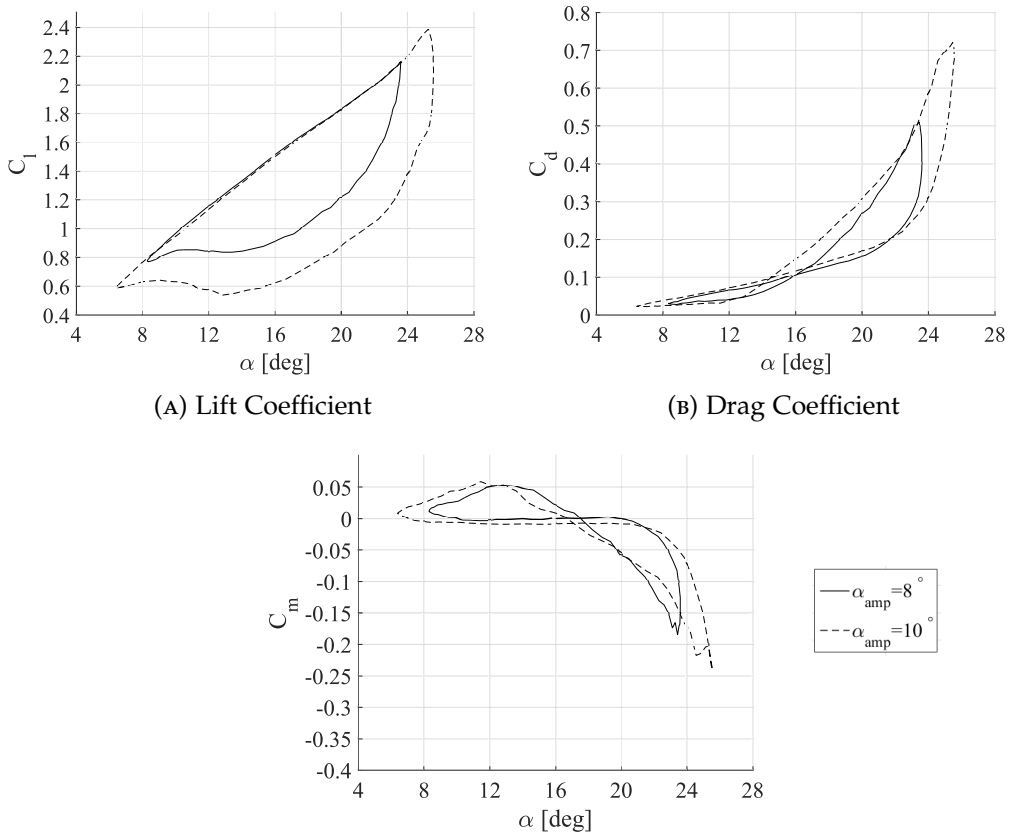

(A) Lift Coefficient

(B) Drag Coefficient

(C) Moment Coefficient

Figure 5.20: Effect of cyclic amplitude variation on the phase-averaged aerodynamic force and moment coefficients under deep dynamic stall conditions. Operational conditions: $\alpha_M = 16°$, $k = 0.1021$, $Re = 1,010,000$.

During the downstroke phase of the pitch cycle, it is shown that an increase in α_{amp} results in an increase in the level of lift hysteresis as shown in Fig. 5.20a. There is also a delay in flow re-attachment for an increase in α_{amp}, and both cyclic amplitudes are shown to not achieve flow reattachment until the beginning of the pitch upstroke. There is also a delay in the transition from negative pitch damping to positive pitch damping for the larger α_{amp} setting.

It is clear that an increase in the cyclic amplitude, α_{amp}, results in the larger production of deep dynamic stall. Therefore, to assess the effect that leading-edge morphing and leading-edge fixed droop has on alleviating the negative effects of deep dynamic stall, the cyclic amplitude, $\alpha_{amp} = 10^{\circ}$, is selected.

5.7.2 Effect of Leading-Edge Morphing

The effect of variation in the leading-edge morphing amplitude on reducing the negative impacts of deep dynamic stall is investigated in this section. The pitch profile selected was the one that exhibited the largest levels of aerodynamic hysteresis during the pitch downstroke, which includes a mean incidence $\alpha_M = 16^{\circ}$ and $\alpha_{amp} = 10^{\circ}$. Three values of leading-edge morphing amplitude are assessed which include, β_{max} = [5,10,15] degrees. All other operational conditions such as the Reynolds number, reduced frequency, and the sampling duration remain unchanged.

The phase-averaged aerodynamic force and moment coefficient results for a change in the leading-edge morphing amplitude under deep dynamic stall conditions are shown in Fig. 5.21. It is shown that leading-edge morphing has a significant influence in alleviating the negative effects of dynamic stall for all values of β_{max} assessed. The lift coefficient results in Fig. 5.21a show that there is minimal change in lift when morphing is initiated at the mean incidence during the pitch upstroke for all β_{max} values. The effect of leading-edge morphing is more effective during the pitch downstroke where dynamic stall and hysteresis in lift occurs. Figure 5.21a visualises a reduction in the lift hysteresis for an increase in β_{max}. At the beginning of the pitch upstroke, there is no change in the measured lift when comparing the β_{max} cases to the rigid aerofoil as the morphing motion is terminated at the mean incidence during the pitch downstroke.

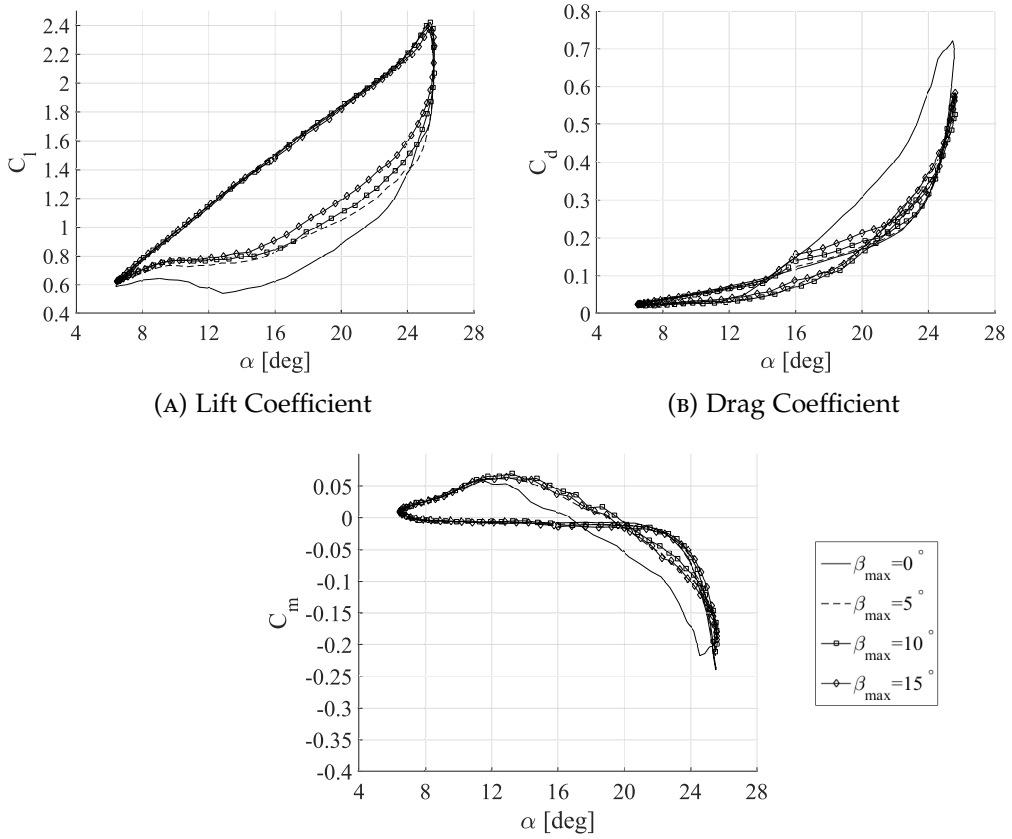

(A) Lift Coefficient

(B) Drag Coefficient

(C) Moment Coefficient

Figure 5.21: Effect of leading-edge morphing amplitude variation on the phase-averaged aerodynamic force and moment coefficients under deep dynamic stall conditions. Operational conditions: $\alpha_M = 16°$, $\alpha_{amp} = 10°$ $k = 0.1021$, $Re = 1,010,000$.

The drag coefficient results in Fig. 5.21b illustrate a large rate increase in drag when leading-edge morphing is initiated at the mean incidence during the upstroke. The amount of rate increase in drag increases for an increase in β_{max}. At α_{max}, there is a significant reduction in Cd_{max} for all values of β_{max}, with all morphing cases producing similar levels of reduction. During the pitch downstroke, there is a significant reduction in the positive drag loop for all β_{max}, compared to the rigid aerofoil. Similar values in drag are produced at an incidence of approximately 13 degrees for all cases assessed, which is after the leading-edge morphing motion has terminated.

The moment coefficient results in Fig. 5.21c show that there are minimal changes in the measured pitching moment and the onset angle of the negative pitching moment during the pitch upstroke for all values of β_{max}. There is a significant reduction in Cm_{min} for an increase in β_{max} and the effect of leading-edge morphing also leads to a reduction in the negative pitch damping loop during the initial stage of the pitch downstroke. The transition from negative to positive pitch damping also occurs earlier for the leading-edge morphing cases in comparison to the rigid aerofoil. Similar moment values between the rigid aerofoil and the leading-edge morphing results

are achieved at approximately 11 degrees at the pitch downstroke which is after the leading-edge morphing motion has been terminated.

Table 5.9 presents the time-averaged and peak aerodynamic force and moment coefficient results for a variation in the leading-edge morphing amplitude. There is a small increase in Cl_{av} for all leading-edge morphing amplitudes assessed and the level of increase in Cl_{av} increases for an increase in β_{max}. There is minimal change in Cl_{max} for all β_{max} amplitudes assessed. All leading-edge morphing amplitudes achieve significant reductions in the time-averaged and peak drag and moment coefficients when compared against the rigid aerofoil. The large reductions in Cd and Cm have also been predicted in the CFD analysis previously performed in Chapter 3 for a NACA0015 aerofoil pitching under deep dynamic stall conditions. The largest reduction in Cd_{max} is achieved at a leading-edge morphing amplitude, $\beta_{max} = 10^{\circ}$, which achieves a 20.6 % decrease in comparison to the rigid aerofoil. The level of reduction in Cm_{min} increases for an increase in β_{max}, with a 20.1 % reduction in Cm_{min} achieved at a leading-edge morphing amplitude, $\beta_{max} = 15^{\circ}$.

Case	$C_{l_{av}}$	$C_{d_{av}}$	$C_{m_{av}}$	$C_{l_{max}}$	$C_{d_{max}}$	$C_{m_{min}}$
Rigid	1.000	1.000	1.000	1.000	1.000	1.000
$\beta_{max} = 5^{\circ}$	1.048	0.778	0.665	1.008	0.795	0.903
$\beta_{max} = 10^{\circ}$	1.068	0.761	0.518	1.016	0.794	0.869
$\beta_{max} = 15^{\circ}$	1.087	0.822	0.586	0.996	0.809	0.799

Table 5.9: Effect of leading-edge morphing amplitude variation on the time-averaged and peak aerodynamic force and moment coefficients under deep dynamic stall conditions. Operational conditions: $\alpha_M = 16^{\circ}$, $\alpha_{amp} = 10^{\circ}$ $k = 0.1021$, $Re = 1,010,000$. Note: data is normalised with respect to the rigid aerofoil results.

5.7.3 Effect of Leading-Edge Fixed Droop

Next, the effect that variation in the leading-edge fixed droop amplitude has on reducing the negative effects of deep dynamic stall is investigated. The changes in the aerodynamic coefficients for the leading-edge fixed droop is also compared against the leading-edge morphing amplitude results to determine which flap method is more effective. Three values of leading-edge fixed droop amplitude are assessed which include: FD_{amp}= [5,10,15] degrees. All other operational conditions such as the Reynolds number, reduced frequency, and the sampling duration remain unchanged.

The phase-averaged aerodynamic coefficients for a variation in the leading-edge fixed droop amplitude under deep dynamic stall conditions are presented in Fig. 5.22. The results show overall that leading-edge fixed droop has a pronounced effect on the aerodynamic performance characteristics over the entire pitch cycle when compared against the rigid NACA0015 aerofoil. During the pitch upstroke at α_M, there is a reduction in Cl for an increase in FD_{amp}, as shown in Fig. 5.22a. During the pitch downstroke, there is a reduction in the lift hysteresis for all leading-edge fixed droop amplitudes when compared against the rigid aerofoil setting. An interesting feature for the leading-edge fixed droop case is that flow re-attachment occurs earlier for an increase in FD_{amp}, which is shown by a intermittent increase in lift. Moreover, there is a positive offset in the measured minimum lift for all leading-edge fixed droop amplitudes, due to the aerofoil physical camber change.

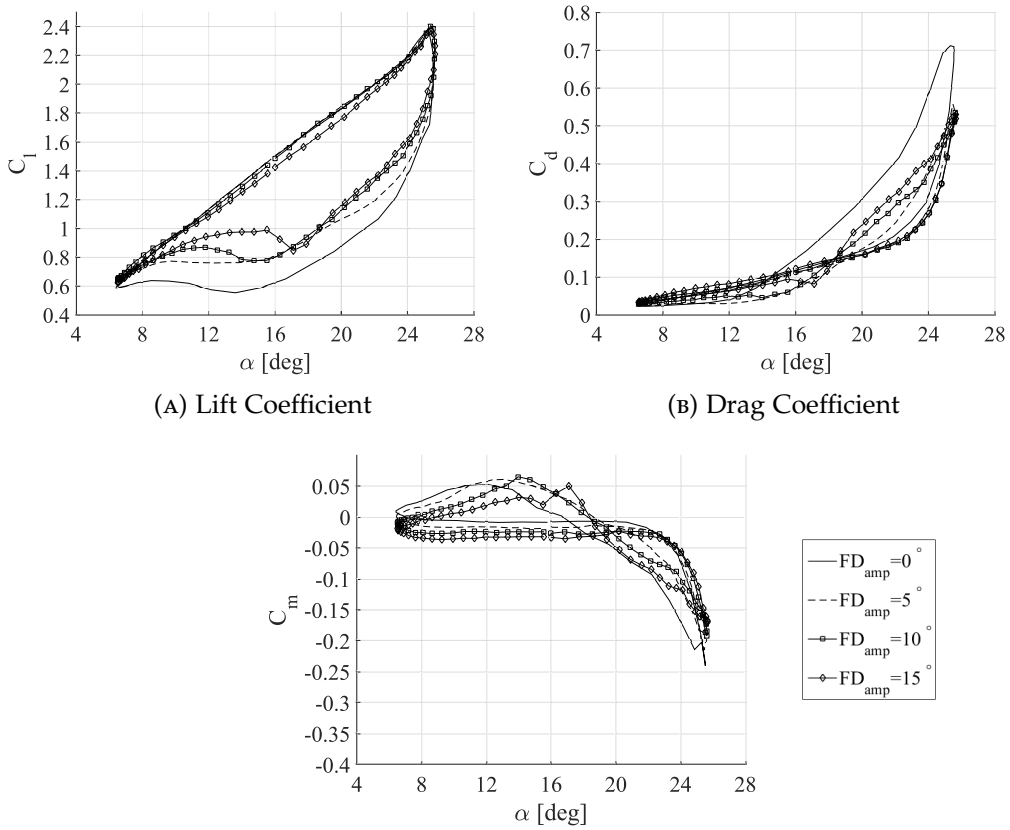

(A) Lift Coefficient

(B) Drag Coefficient

(C) Moment Coefficient

Figure 5.22: Effect of leading-edge fixed-droop amplitude variation on the phase-averaged aerodynamic force and moment coefficients under deep dynamic stall conditions. Operational conditions: $\alpha_M = 16°$, $\alpha_{amp} = 10°$ $k = 0.1021$, $Re = 1,010,000$.

The drag coefficient results in Fig. 5.22b shows that there is a small change in drag when comparing all leading-edge fixed droop cases against the rigid aerofoil at α_M during the pitch upstroke. There is a small delay in the drag-rise onset angle for all FD_{amp} cases compared to the rigid aerofoil, which is due to two reasons: 1) the reduction in the negative surface C_p due to the reduction in local incidence for the leading-edge flap and, 2) delay in the separation point from the TE to LE. Near the maximum incidence angle, there is a significant decrease in Cd_{max} for all FD_{amp} values assessed, with the level of reduction increasing for an increase in FD_{amp}. During the pitch downstroke, there is a reduction in the positive drag hysteresis loop for all FD_{amp}. It is shown however that the level of reduction in the positive drag loop decreases for an increase in FD_{amp}. This is due to the significant increase in local incidence at the joint gap due to the physical camber change introduced by the leading-edge fixed droop.

The moment coefficient results in Fig. 5.22c illustrates a negative offset shift in Cm at α_M, during the pitch upstroke for all values of FD_{amp}. The negative offset shift in Cm increases for an increase in FD_{amp}, which is due to the physical camber change introduced at the leading-edge. The onset of the negative pitching moment occurs earlier for the rigid aerofoil in comparison to the leading-edge fixed droop cases. This is due to the leading-edge flap change producing a delay in the separation point travelling from the TE to LE. More importantly, there is a significant decrease in Cm_{min} for an increase in FD_{amp}. This also leads to a reduction in the negative pitch damping loop, however the level of reduction decreases for an increase in FD_{amp}. Transition from negative to positive pitch damping occurs earlier for all leading-edge fixed droop amplitude cases compared to the rigid aerofoil, however the measured Cm values at the end of the pitch downstroke differ because of the physical camber change introduced by the leading-edge fixed droop amplitude change.

Table 5.10 presents the time-averaged and peak aerodynamic force and moment coefficient results for a variation in the leading-edge fixed droop amplitude. Similar to leading-edge morphing, there is a small increase in Cl_{av} for an increase in FD_{amp} whilst having an minimal effect on Cl_{max} in comparison to the rigid aerofoil. There are significant reductions in both the time-averaged and peak drag and moment coefficients for all FD_{amp} amplitudes assessed. The level of reduction in Cd_{max} and Cm_{min} increases for an increase in FD_{amp}. This results in a decrease in Cd_{max} and Cm_{min} of 26.9 % and 27.8 % respectively at $FD_{amp} = 15°$.

Case	$C_{l_{av}}$	$C_{d_{av}}$	$C_{m_{av}}$	$C_{l_{max}}$	$C_{d_{max}}$	$C_{m_{min}}$
Rigid	1.000	1.000	1.000	1.000	1.000	1.000
$FD_{amp} = 5^\circ$	1.055	0.754	0.769	1.007	0.774	0.903
$FD_{amp} = 10^\circ$	1.085	0.770	0.858	1.010	0.744	0.793
$FD_{amp} = 15^\circ$	1.089	0.823	1.058	1.001	0.731	0.722

Table 5.10: Effect of leading-edge fixed-droop amplitude variation on the time-averaged and peak aerodynamic force and moment coefficients under deep dynamic stall conditions. Operational conditions: $\alpha_M = 16^\circ$, $\alpha_{amp} = 10^\circ$ $k = 0.1021$, $Re = 1,010,000$. Note: data is normalised with respect to the rigid aerofoil results.

5.7.4 Comparison between leading-edge fixed droop and leading-edge morphing

A comparison is made between the effect of leading-edge morphing and leading-edge fixed droop for a flap angle of 10 degrees, with the results for the phase-averaged aerodynamic coefficients shown in Fig. 5.23. The lift coefficient results in Fig. 5.23a illustrate that there is little change in Cl at the mean incidence during the pitch upstroke for both flap methods when compared against the rigid aerofoil. Moreover, both flap methods are shown to have little effect on Cl_{max} and dynamic stall occurs at approximately the same incidence angle during the start of the pitch downstroke. Differences between both flap methods exist during the downstroke phase, where flow-reattachment occurs earlier for leading-edge fixed droop in comparison to leading-edge morphing. This is due to the leading-edge morphing motion terminating at the mean incidence, whereas the positive flap camber change for the leading-edge fixed droop case, leads to to local flow-reattachment at the flap because of the reduction in local incidence. Both flap methods are shown to generate a similar level of reduction in lift hysteresis in comparison to the rigid aerofoil case.

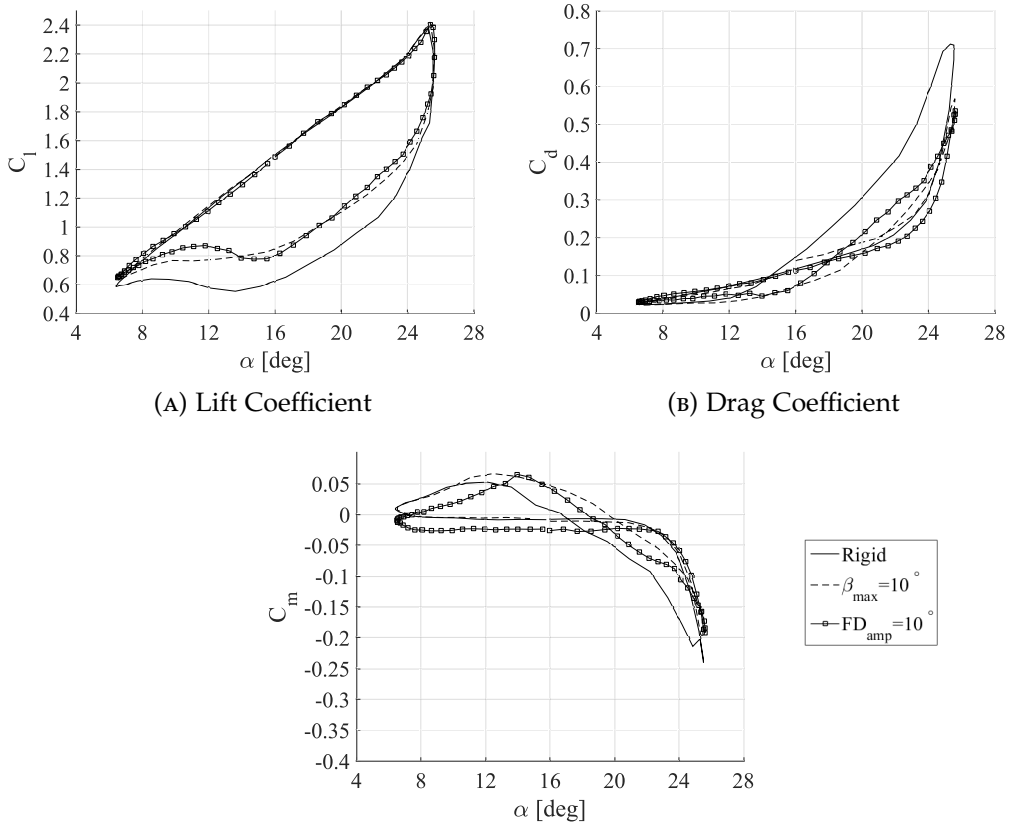

(A) Lift Coefficient

(B) Drag Coefficient

(C) Moment Coefficient

Figure 5.23: Comparison between leading-edge morphing and fixed droop effects for the phase-averaged aerodynamic force and moment coefficients under deep dynamic stall conditions: $\alpha_M = 16°$, $\alpha_{amp} = 10°$ $k = 0.1021$, $Re = 1,010,000$.

The drag coefficient results in Fig. 5.23b, show noticeable differences between both flap methods during the pitch upstroke at mean incidence. When leading-edge morphing is initiated at α_M, there is a large increase in drag; this feature is not captured for the leading-edge fixed droop case and may be due to transients effect from the leading-edge flap motion. Moreover, the drag-rise occurs at approximately the same incidence angle when comparing against the leading-edge morphing case and the rigid aerofoil. Leading-edge fixed droop is shown to produce a small delay on the onset angle for the drag-rise. Both flap methods generate similar levels of reductions in Cd_{max}. During the pitch downstroke, leading-edge fixed droop is shown to produce a larger positive drag loop in comparison to leading-edge morphing. Also, near the end of the pitch downstroke, leading-edge morphing is shown to produce similar values of drag in comparison to the rigid aerofoil as the leading-edge morphing motion has been terminated at the mean incidence. The leading-edge fixed droop amplitude is shown however to have an increase in drag at the end of the pitch downstroke, due to the physical change in camber at the leading-edge.

The moment coefficient results in Fig. 5.23c show clear differences between both flap methods at the mean incidence angle during the pitch upstroke. Leading-edge

morphing is shown to produce similar Cm values when compared to the rigid aerofoil, however leading-edge fixed droop produces a negative offset shift in Cm. This is due to the positive camber change which also leads to a slight delay in the onset of the negative pitching moment compared to the rigid aerofoil and leading-edge morphing. During the pitch downstroke, both flap methods achieve a similar reduction in Cm_{min} however leading-edge morphing has a greater effect in reducing the negative pitch damping loop in comparison to leading-edge fixed droop. This also results in the transition from negative to positive damping occurring earlier for leading-edge morphing over leading-edge fixed droop. Near the end of the pitch downstroke, similar Cm values are achieved when comparing the leading-edge morphing method to the rigid aerofoil, however the leading-edge fixed droop method is shown to decrease the level of positive damping.

5.7.5 Effect of Reduced Frequency

A comparison is made between the alleviation effects of deep dynamic stall for both leading-edge morphing and leading-edge fixed droop for a variation in reduced frequency. Two cases of reduced frequency, similar to the light dynamic stall analysis, are considered: k = [0.025,0.1021]. The flap amplitude points remain unchanged which are: $\beta_{max} = FD_{amp}$ = [0,5,10,15] $^{\circ}$, where zero degrees represents the rigid NACA0015 aerofoil. The effect of leading-edge morphing and leading-edge fixed droop is quantified through calculating the average and maximum deltas for the aerodynamic coefficients, as defined in Section 5.6.4.

The lift coefficient average and maximum delta results for a variation in reduced frequency under deep dynamic stall conditions is shown in Fig. 5.24. The average delta lift coefficient results in Fig. 5.24a illustrate similar curve trends when assessing the change in reduced frequency for both leading-edge flap methods. Both flap methods are shown to have an increase in Cl_{av} for an increase in flap amplitude, and the level of increase is similar when comparing against both flap methods. Moreover, both flap methods have a greater effect on increasing Cl_{av} at the lower reduced frequency, k = 0.025. This is due to the reduction in flow unsteadiness which leads to the formation of a larger deep dynamic stall, whereas the larger reduced frequency delays the formation of the LEV by reducing the effective incidence angle [120]. Figure 5.24b also illustrates that both flap methods produce a larger increase in Cl_{max} at the lower reduced frequency value, k = 0.025. The main reason for the larger improvement is due to the delay in dynamic stall through implementation of the aerofoil camber change. The Cl_{max} isn't as effective for k = 0.1021, which is due to significant flow unsteadiness effects maintaining attached flow up to the start of the pitch downstroke [120]. Another key difference in the reduced frequency results is that both flap methods show a reduction in improving Cl_{max} at k = 0.1021, with leading-edge morphing producing a decrease in Cl_{max}.

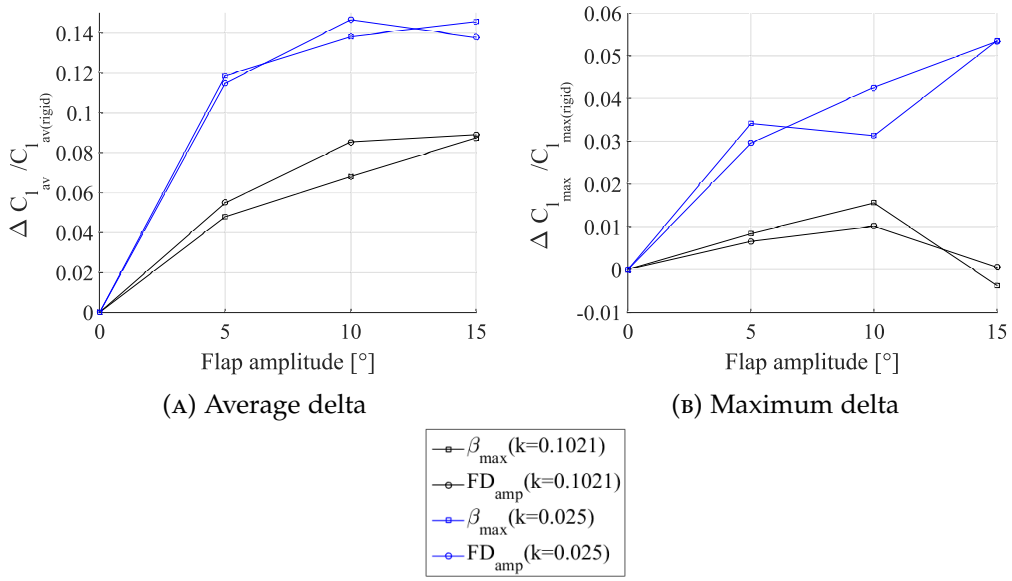

(A) Average delta

(B) Maximum delta

Figure 5.24: Effect of reduced frequency comparison between normalised ΔCl for leading-edge morphing and fixed droop under deep dynamic stall conditions. Operational conditions: $\alpha_M = 16°$, $\alpha_{amp} = 10°$, $Re = 1,010,000$.

The delta drag coefficient results for a variation in reduced frequency for both leading-edge flap methods is shown in Fig. 5.25. The delta average drag coefficient results in Fig. 5.25a illustrate similar curve trends for both reduced frequency values as well as for both flap methods. There is a reduction in Cd_{av} for both leading-edge flap methods for all FD_{amp} and k values assessed. The reduction in Cd_{av} is greater for the larger reduced frequency value, k = 0.1021, with the most effective flap amplitude being 10 degrees. In terms of the maximum delta drag coefficient results (Fig. 5.25b), both flap methods are shown to have a greater effect in decreasing Cd_{max} at the larger reduced frequency value, k = 0.1021. For flap amplitudes up to 10 degrees, the reduction in Cd_{max} is more effective for leading-edge morphing at the lower reduced frequency, k = 0.025, whereas leading-edge fixed droop is more effective at k = 0.1021. At 15 degrees flap amplitude, there is a small increase in Cd_{max} for the leading-edge morphing flap method, and there is also a smaller reduction in Cd_{max} for the leading-edge fixed droop method at k = 0.025.

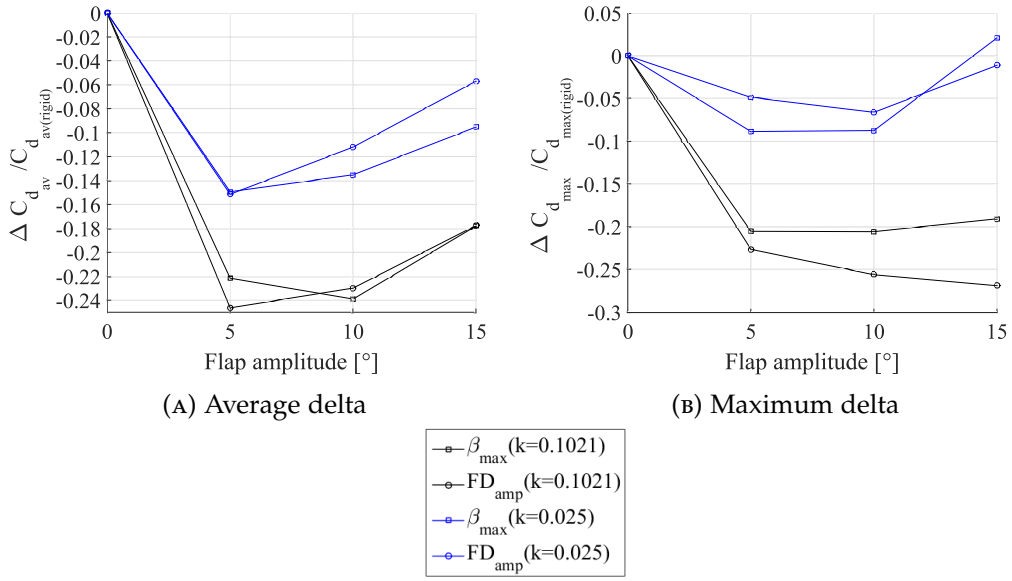

(A) Average delta

(B) Maximum delta

FIGURE 5.25: Effect of reduced frequency comparison between normalised ΔCd for leading-edge morphing and fixed droop under deep dynamic stall conditions. Operational conditions: $\alpha_M = 16°$, $\alpha_{amp} = 10°$, $Re = 1,010,000$.

The delta moment coefficient results for a variation in reduced frequency for both flap methods is shown in Fig. 5.26. For both leading-edge flap methods, an increase in reduced frequency has a greater effect in improving Cm_{av} as visualised in Fig. 5.26a. Moreover, the curve trends for both flap methods are similar for both values of reduced frequency. The leading-edge morphing flap method has an greater effect in improving Cm_{av} in comparison to the leading-edge fixed droop method. The maximum delta moment coefficient results in Fig. 5.26b illustrate significant differences in curve trends when comparing the two flap methods for both values of reduced frequency. At k = 0.1021, both flap methods produce a significant reduction in Cm_{min}, with the largest reductions achieved by the leading-edge fixed droop method. At k = 0.025 however, the leading-edge fixed droop method shows varying trends in Cm_{min}, and is shown to generate larger Cm_{max} values compared to the rigid aerofoil. The leading-edge morphing flap method is shown to have a reduction in Cm_{max} for flap amplitudes up to 10 degrees at k = 0.025. At 15 degrees flap amplitude however, there is a significant increase in Cm_{max} (similar to the measured leading-edge fixed droop method), which could be as a result of separation at the joint on the suction surface, separating at the aerofoil section instead of at the leading-edge flap.

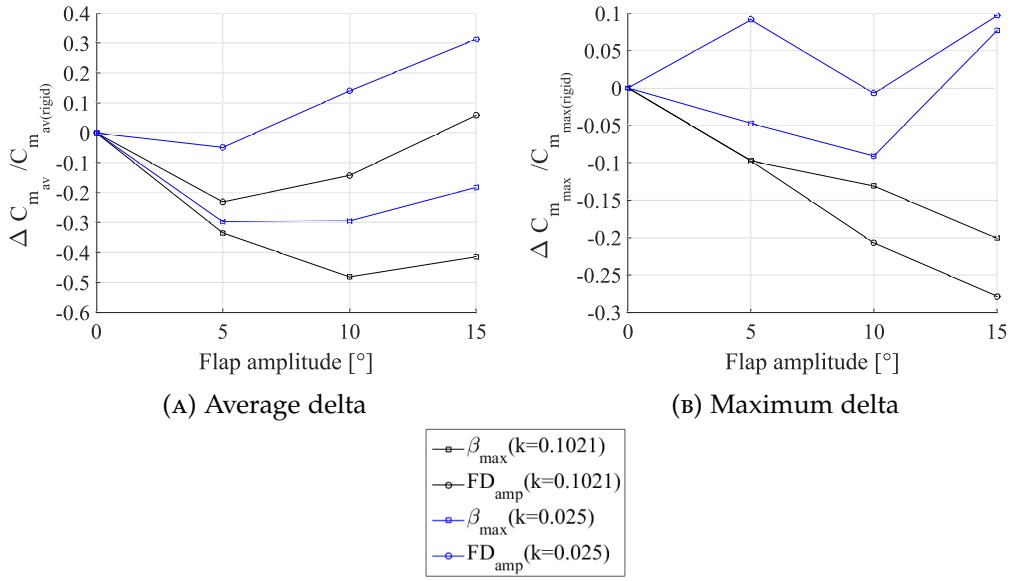

(A) Average delta

(B) Maximum delta

FIGURE 5.26: Effect of reduced frequency comparison between normalised ΔCm for leading-edge morphing and fixed droop under deep dynamic stall conditions. Operational conditions: $\alpha_M = 16°$, $\alpha_{amp} = 10°$, $Re = 1,010,000$.

5.7.6 CFD Validation

The final part of the deep dynamic stall analysis is to compare the aerodynamic characteristic changes achieved by both leading-edge morphing and leading-edge fixed droop for both the experimental and computational results. CFD simulations were performed at a deep dynamic stall pitch profile for a rigid aerofoil, as well as both flap methods at a range of flap amplitudes. The comparison of the leading-edge morphing and leading-edge fixed droop flap method's effect on alleviating dynamic stall is assessed through calculation of the average and maximum delta aerodynamic coefficients.

A comparison between the experimental and computational rigid aerofoil aerodynamic coefficients under deep dynamic stall conditions is shown in Fig. 5.27. Due to the experimental results shown to have a delay in stall for both static and dynamic conditions, an offset was applied to the mean incidence for the CFD simulations. An offset angle of 2 degrees (same value applied in Section 5.6.5) was applied to the mean incidence which results in $\alpha_M = 14°$. The cyclic amplitude remains the same at 10 degrees.

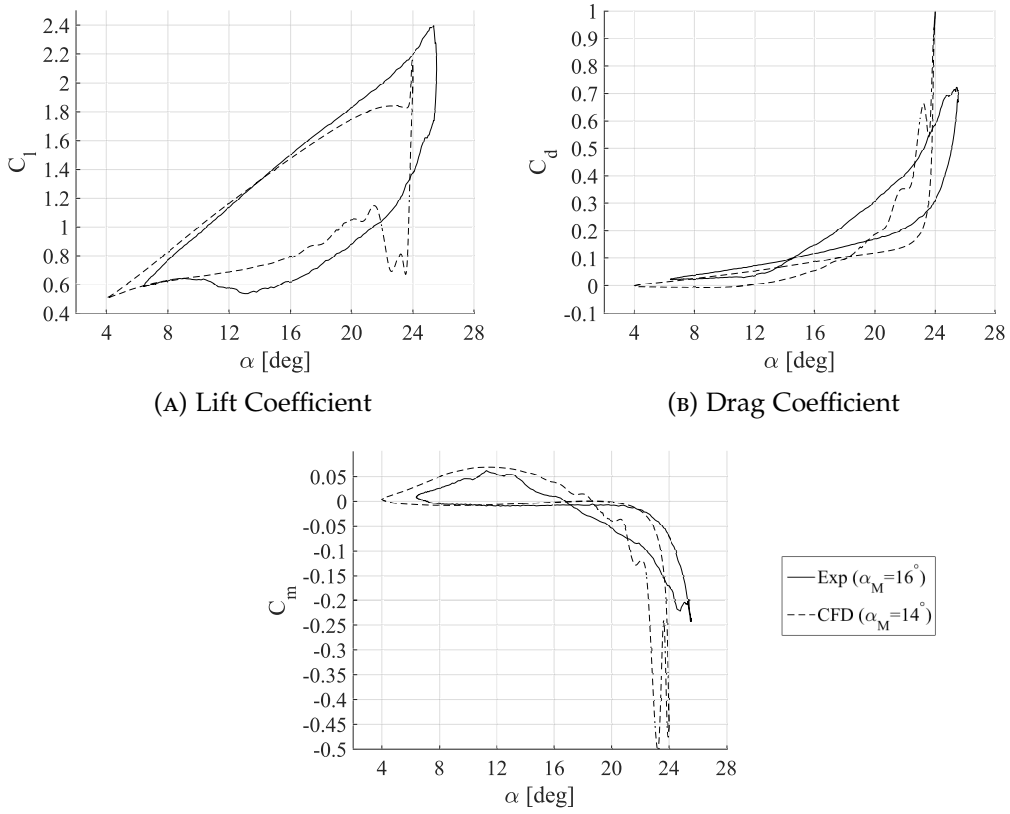

(A) Lift Coefficient

(B) Drag Coefficient

(C) Moment Coefficient

Figure 5.27: Comparison between experimental and CFD rigid aerofoil aerodynamic coefficient results under deep dynamic stall conditions. Operational conditions: $\alpha_M = 16°$, $\alpha_{amp} = 10°$, $k = 0.1021$, $Re = 1,010,000$.

The main reasons for the differences between the experimental and computational results is due to the delay in stall from the experiment and the poor predictions of dynamic stall during the pitch downstroke from the computational result. The phase-averaged aerodynamic force and moment coefficients, comparing the experimental result against the computational result is shown in Fig. 5.27. Figure 5.27a shows that at maximum incidence, the computational results predicts an overshoot in lift which represents the formation and convection of a LEV across the suction surface. However the experimental results show a continual increase in lift which means that the LEV has not formed. During the pitch downstroke, there is a larger loss of lift for the computational results in comparison to the experimental results. For the computational results, there is also another increase in lift at approximately 22° incidence, which represents the formation of a secondary vortex at the leading-edge which again is not measured from the experiment. The level of hysteresis is similar for both methods.

The drag coefficient results in Fig. 5.27b, show similar trends between the computational and experimental results. During the pitch upstroke, both methods show a steady increase in drag as well as generating a significant drag-rise up to maximum incidence. The computational results predict a significantly larger value for Cd_{max}

in comparison to the experimental result, due the prediction of the full formation of the LEV (which is not measured from the experimental result). The experimental results also show an offset in the measured drag coefficient which is due to the offset from flow leakage from the leading-edge flap, therefore a comparison between the experimental and computational results should be assessed qualitatively only. Both methods capture a positive drag damping loop and negative drag damping loop.

The moment coefficient results in Fig. 5.27c illustrates that both the experimental and computational results show similar trends, such as both capturing the negative and positive pitch damping loop. The computational results predict a larger value of Cm_{min} in comparison to the experimental result which is due to the CFD simulation predicting the full formation of the LEV which is not captured by the experimental result.

The average and maximum delta lift coefficient comparison between the experimental and computational results for both flap methods is visualised in Fig. 5.28. There is a good agreement between the experiment and computational results when comparing the average delta lift coefficient results for leading-edge morphing, as shown in Fig. 5.28a. Both the experimental and computational methods show an increase in Cl_{av} for an increase in the leading-edge morphing flap amplitude. There is a poor agreement between both sets of results when comparing the delta average lift coefficient results for leading-edge fixed droop. The experimental results show an increase in Cl_{av} for an increase in flap amplitude, whereas the CFD predicts a reduction in Cl_{av} at the larger flap amplitudes. Moreover, there are large differences between the experimental and computational results when comparing the maximum delta lift coefficient results for both flap methods (Fig. 5.28b). The experimental results demonstrate an increase in Cl_{max} for an increase in the leading-edge fixed droop amplitude, and leading-edge morphing is shown to approximately maintain Cl_{max} values when compared against the rigid aerofoil. The computational results on the other hand show a reduction in Cl_{max}, which is due to the removal of the lift overshoot, which in effect reduces the strength of the LEV. The lift overshoot feature is not represented in the experimental results, which may be due to the LEV not fully forming as a result of stall delay from the experimental model setup.

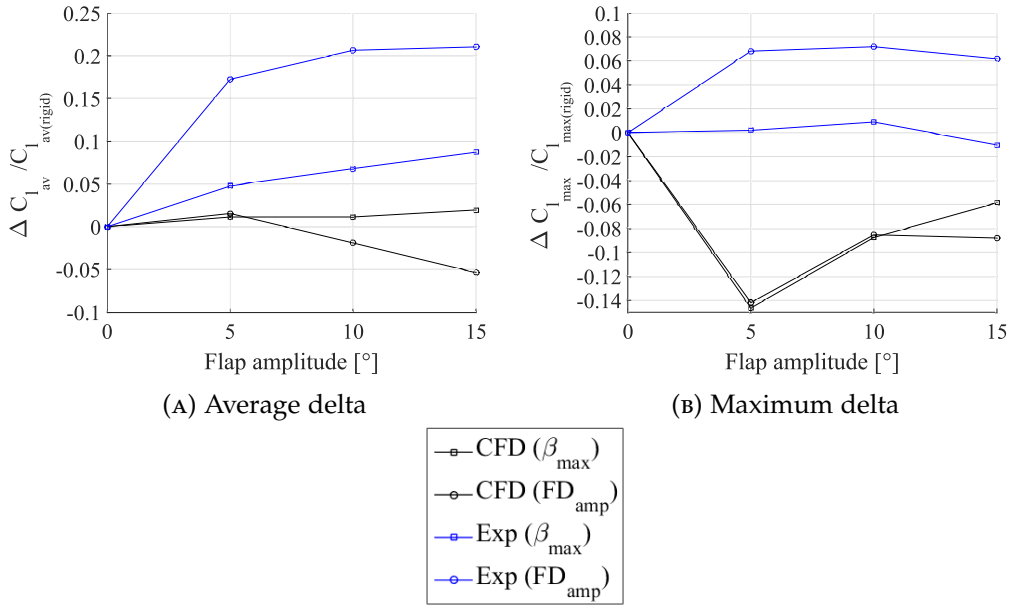

(A) Average delta (B) Maximum delta

Figure 5.28: Comparison between experimental and CFD normalised ΔCl for leading-edge morphing and fixed droop under deep dynamic stall conditions. Operational conditions: $\alpha_M = 16°$, $\alpha_{amp} = 10°$, $k = 0.1021$, $Re = 1,010,000$.

There is a better agreement between the experimental and computational results when evaluating the delta drag coefficient results, as shown in Fig. 5.29. Both sets of results are shown to achieve reductions in the average and maximum drag coefficients for both leading-edge morphing and for leading-edge fixed droop. The average delta drag coefficient results in Fig. 5.29a show that for five degrees flap amplitude, the computational results under-predict the reduction in Cd_{av} in comparison to the experimental results, when assessing both the leading-edge morphing and leading-edge fixed droop flap methods. The computational results show however that leading-edge morphing achieves a greater reduction in Cd_{av} in comparison to the leading-edge fixed droop method, which is also measured from the experiment. Figure 5.29b illustrates that the computation results predict that both leading-edge flap methods produces similar levels of reduction in Cd_{max} over the flap amplitude range. The experimental results on the other hand, show that leading-edge fixed droop has a greater effect on decreasing in Cd_{max} in comparison to the leading-edge morphing flap method.

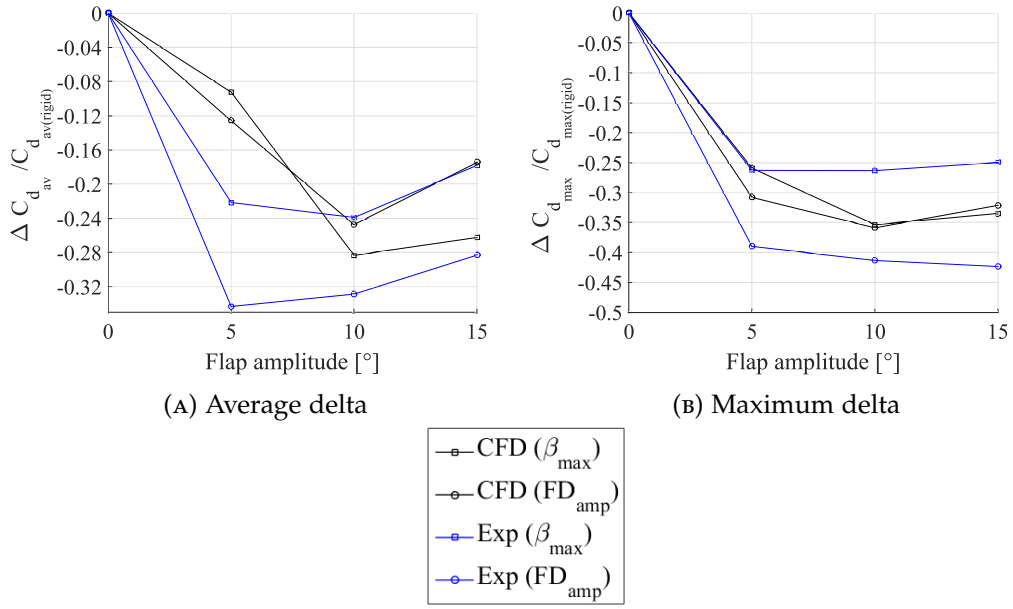

(A) Average delta (B) Maximum delta

FIGURE 5.29: Comparison between experimental and CFD normalised ΔCd for leading-edge morphing and fixed droop under deep dynamic stall conditions. Operational conditions: $\alpha_M = 16°$, $\alpha_{amp} = 10°$, $k = 0.1021$, $Re = 1,010,000$.

The average and delta moment coefficient comparison between the experimental and computational results is visualised in Fig. 5.30. The average delta moment coefficient results in Fig. 5.30a shows that there is a good agreement between both sets of results for both leading-edge flap methods at all flap amplitudes except at 5 degrees. The computational results predict a negative impact on Cm_{av} at a flap amplitude of five degrees for both flap methods; the experimental results generate a positive impact in Cm_{av} for both flap methods. A better agreement in the delta curve trends between the experimental and computational results is achieved for flap amplitudes 10 degrees and above. Here the computational and experimental results show that the leading-edge morphing flap method improves Cm_{av} in comparison to the leading-edge fixed droop method. The CFD method under-predicts the effect of leading-edge morphing, however there is a adequate prediction of the effect of the leading-edge fixed droop flap method, when compared against the experimental result. There is a poorer agreement when comparing the experimental and computational results for the maximum delta moment coefficient results in Fig. 5.30b over the flap amplitude range. At the lower flap amplitude of five degrees, both sets of results generate a reduction in Cm_{max} for both leading-edge flap methods, however the difference in reduction between for both flap methods is greater in the experimental result than for the computational result. As the flap amplitude increases, the level of reduction in Cm_{min} decreases for both flap methods, whereas the level of reduction in Cm_{min} increases significantly for both flap methods for the experimental results.

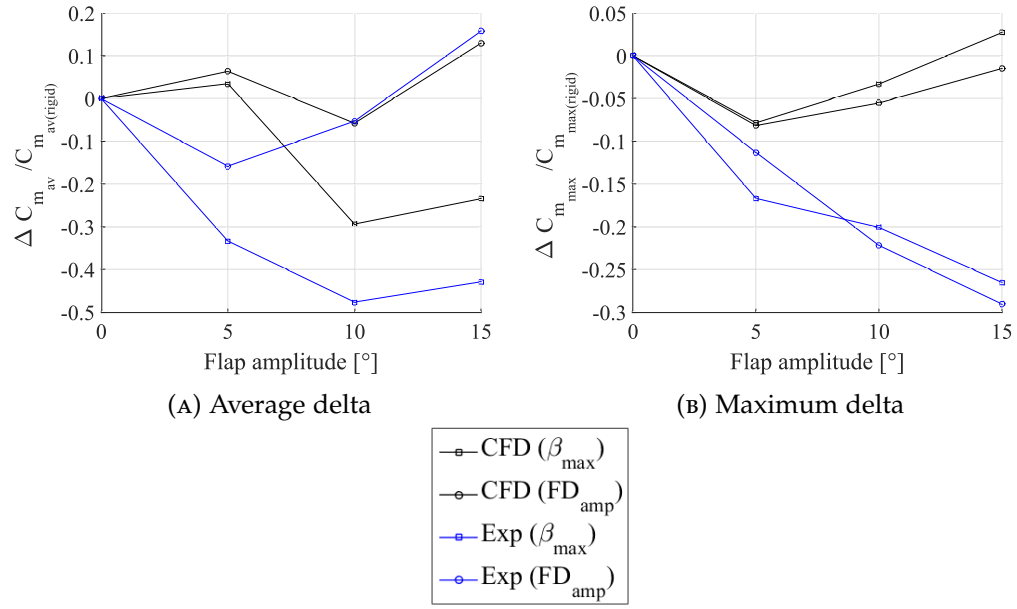

(A) Average delta

(B) Maximum delta

FIGURE 5.30: Comparison between experimental and CFD normalised ΔCm for leading-edge morphing and fixed droop under deep dynamic stall conditions. Operational conditions: $\alpha_M = 16°$, $\alpha_{amp} = 10°$, $k = 0.1021$, $Re = 1,010,000$.

5.8 CONCLUSIONS

Dynamic stall wind tunnel testing for a NACA0015 aerofoil model with an active leading-edge flap has been performed using the Handley-Page low-speed, closed return wind tunnel. The main purpose of this experimental study was to determine whether the effects of leading-edge morphing and leading-edge fixed droop on the aerodynamic performance which were predicted by CFD, can also be accurately represented in an equivalent experimental leading-edge flap wind tunnel model. This study involves assessing the effect of active leading-edge flap control on the aerodynamic force and moment characteristics for both static and dynamic motion. For the dynamic motion, three different types of flow regime were investigated which include: attached flow, light dynamic stall, and deep dynamic stall. For each experimental section, specific cases were selected to use as validation against the CFD model developed in Chapter 3.

For the static motion analysis, there was a good agreement in the lift and moment coefficient at the lower incidence angle range (upto approximately 8 degrees) between the experimental and CFD methods. There was a poorer agreement between both methods when assessing the drag coefficient, which was demonstrated to be linked to flow leakage within the volume of the leading-edge flap. The effect of flow leakage resulted in a significant offset in the surface pressure measurements due to the leakage of negative pressure from the aerofoil's suction surface. The negative impact of flow leakage increased for an increase in incidence, which led to larger offsets in the measured stagnation pressure. It was also shown that wind tunnel blockage effects were more noticeable at the larger range, however the difference on

the measured aerodynamic force and moment coefficients was small when compared to the uncorrected results.

Another key difference between the experimental and CFD results from the static motion analysis was the large delay in the static stall onset angle from the experiment. An investigation was performed to determine the effect that variation of the leading-edge fixed droop amplitude had on the static aerodynamic characteristics as well as the static stall onset angle. It was shown that applying negative leading-edge fixed droop increased the overall moment coefficient as well as decreasing the static stall onset angle; applying positive leading-edge fixed droop resulted in a decrease in the moment coefficient and an increase in the static stall angle. At a leading-edge flap amplitude of zero degrees, there was a good agreement in the static lift and moment coefficients when compared against a clean NACA0015 model, however the static stall onset angle was larger for the leading-edge flap model. A possible reason for the delay in the static stall onset angle for the leading-edge flap model could be due to airflow passing through the recess section between the leading-edge flap and aerofoil section. It has been shown in previous experimental studies that airflow in leading-edge slots from the pressure side to the suction side can lead to a delay in the static and dynamic stall.

In the dynamic attached flow analysis, for all reduced frequency values assessed, there is a good agreement between the experiment and CFD results when comparing the lift and moment coefficients. There is a poorer agreement when comparing the drag coefficient due to the effect of flow leakage at the larger incidence angles from the experiment.

In the light dynamic stall analysis, both leading-edge morphing and leading-edge fixed droop were shown to achieve a significant reduction in the level of aerodynamic hysteresis, as well as significantly reducing the peak drag and moment coefficients. All leading-edge morphing amplitudes assessed achieved an earlier transition from negative to positive pitch damping during the pitch downstroke in comparison to the rigid aerofoil. The largest reduction in the peak drag and negative moment coefficients was achieved at a leading-edge morphing amplitude of 10 degrees. For all leading-edge fixed droop amplitudes assessed, there was an improvement in dynamic stall alleviation however the physical change in aerofoil camber also resulted in an overall change to the aerofoil's aerodynamic characteristics when compared to the original NACA0015 aerofoil. When assessing the reduced frequency, it was shown that the larger reduced frequency led to larger reductions in the peak drag and moment coefficients for both the leading-edge morphing and leading-edge fixed droop methods.

The CFD simulations showed that for the same light dynamic stall pitch profile conditions, the dynamic stall characteristics differ when compared to the experiment. The computational results predicts the formation of the LEV which results in a significant loss in lift and large increases in the drag-rise and the negative moment

coefficient. These features are not measured in the experiment which may be due to the delay in stall from flow leakage through the leading-edge flap recess.

In the deep dynamic stall analysis, leading-edge morphing has a significant effect in alleviating the negative effects of deep dynamic stall for all values of β_{max} assessed. Moreover, activating leading-edge morphing within the first half of the pitch cycle has shown to reduce the impact of dynamic stall (hysteresis effects and the negative pitch damping loop), whilst achieving aerodynamic performance characteristics similar to the rigid NACA0015 aerofoil in the second half of the pitch cycle. Leading-edge fixed droop is also shown to have a significant effect on alleviating the negative effects of dynamic stall when compared to the rigid NACA0015 aerofoil. Differences in aerodynamic performance between both leading-edge flap methods occur during the pitch downstroke. Once leading-edge morphing has terminated, the aerodynamic results produced are similar to the rigid NACA0015 aerofoil characteristics. This is not true for the leading-edge fixed droop aerodynamic performance characteristics, due to the aerofoil physical camber change. An increase in reduced frequency results in greater reductions in the maximum drag coefficient and minimum moment coefficient for both leading-edge flap methods. Leading-edge fixed droop achieves greater reductions at the larger reduced frequency in comparison to leading-edge morphing.

The deep dynamic stall CFD simulation results with the two degrees negative offset in the mean incidence is shown to predict the LEV formation, as well as the secondary vortex formation. In contrast, the experimental results are shown to produce larger hysteresis effects, but no formation of the LEV occurs. There is a good agreement in the average delta lift, drag, and moment coefficients between the computational and experimental results for β_{max} values greater than 5 degrees. There is also a good agreement between both methods when assessing the curve trend reductions in the maximum drag coefficient. There is a poorer agreement between the experimental and computational results when comparing the maximum lift coefficient and minimum moment coefficient. The computational results showed both leading-edge flap methods preventing the formation of the leading-edge vortex which removed the lift overshoot feature. Both leading-edge flap methods for the experimental results are shown to maintain attached flow until the start of the downstroke which results in an increase in the maximum lift coefficient.

In summary, the experiment and CFD methods both capture similar effects of leading-edge morphing and leading-edge fixed droop for an aerofoil operating under deep dynamic stall conditions. Both leading-edge flap methods achieve significant reductions in the time-averaged and peak drag and negative moment coefficients in comparison to the rigid aerofoil. There is also a significant reduction in the negative pitch damping loop and the transition from negative to positive damping occurs earlier for both leading-edge flap methods. Moreover, both the experiment and CFD methods show that leading-edge morphing can maintain similar aerodynamic characteristics to the rigid aerofoil when morphing is inactive. Both methods also

show that applying leading-edge fixed droop results in an overall change to the aerodynamic characteristics when compared to the rigid NACA0015 aerofoil.

CHAPTER 6

CFD ANALYSIS - ACTIVE, LEADING-EDGE MORPHING OF A CYCLOIDAL ROTOR UNDER HOVER CONDITIONS

6.1 INTRODUCTION

A two-dimensional, unsteady CFD analysis of a cycloidal rotor operating under hover conditions and with active leading-edge morphing blades is performed. The hover operational condition has been selected as a result from a previous computational study which assessed the cycloidal rotor performance characteristics under hover conditions whilst varying the symmetric aerofoil profile thickness and rotor solidity [44]. The CFD input parameters are similar to the settings used in the single aerofoil CFD model developed in Chapter 3 to maintain consistency in the mesh strategy implemented. The main objective of this study is to evaluate the effect that active leading-edge morphing of the cycloidal rotor blades has on key cycloidal rotor features such as: dynamic stall, blade-wake interference, and the rotor performance characteristics. Another key objective of this study to determine whether a correlation can be made in the performance benefits gained from leading-edge morphing between a single cycloidal rotor orbiting blade and a single pitch oscillating aerofoil.

The CFD analysis consists of a detailed parametric study which contains various sections. A description of the mesh construction method for a 4-blade cycloidal rotor is provided as well as the input settings used to set up the flow physics for the CFD model. A grid independence and time-step independence study is conducted to determine the adequate grid and time-step settings. The effect of implementing different turbulence models for closure of the URANS equations is also assessed. The results from the grid and time-step independence study, as well as the results for the effect of different turbulence models are compared against computational results obtained from a previous cycloidal rotor study.

Next, an assessment is made into the effect that a single cycloidal rotor blade has on the rotor performance characteristics as well as the blade aerodynamic characteristics

in comparison to a rigid blade. A correlation is then made between a cycloidal rotor blade and a pitch oscillating aerofoil with active leading-edge morphing applied.

For the parametric study, multiple parameters are investigated in order to gain an understanding of the effect that active leading-edge morphing has on the cycloidal rotor performance characteristics as well as the level of blade-wake interference. First, The effect of varying the rotor azimuthal position for initialising leading-edge morphing is assessed to determine which rotor azimuth positions are effective in improving rotor performance. A variation in the leading-edge morphing amplitude is then applied and the results generated are compared against the results for a cycloidal rotor with rigid blades. This is then followed by assessing a cycloidal rotor with fixed droop amplitudes applied to the blades in order to make a comparison between using either active leading-edge morphing blades or fixed (cambered) cycloidal rotor blades. The effect of the rotor solidity is then assessed to determine the effect that active leading-edge morphing has on rotor performance as the total number of blades decreases.

6.2 MODEL SETUP DESCRIPTION

A description of the input conditions used for the setup of this CFD model for simulating a two-dimensional, 4-blade cycloidal rotor with active leading-edge morphing blades is discussed here.

6.2.1 Geometry

The geometry structure for the background and overset mesh domains is similar to the structure used in the single aerofoil dynamic stall CFD model developed in Chapter 3. A visualisation of the cycloidal rotor coordinate system used in this study is shown in Fig. 6.1. The origin of the coordinate system is located at the rotor centre where the rotor thrust (side force), F_x, and the rotor lift (vertical force), F_y, with units, N, are defined positive in the negative x-direction and positive y-direction respectively. M_{rotor} is the rotor moment with units, Nm, and is defined positive in the clockwise direction. Ω is the rotor rotational velocity with units, rpm, and has positive rotation in the anti-clockwise direction. The blade azimuthal position, ψ, with units in degrees, defines the position of a cycloidal rotor blade along the rotor orbit. θ_{max} is the maximum blade pitch amplitude, with units in degrees, and is defined as the angle between the aerofoil chord line and the tangent line to the rotor trajectory. Sinusoidal blade pitch motion is applied to each of the cycloidal rotor blades and is initialised at $\psi = 0^{\circ}$. This results in a cycloidal rotor blade achieving positive and negative θ_{max} at the upper and lower surface of the cycloidal rotor respectively.

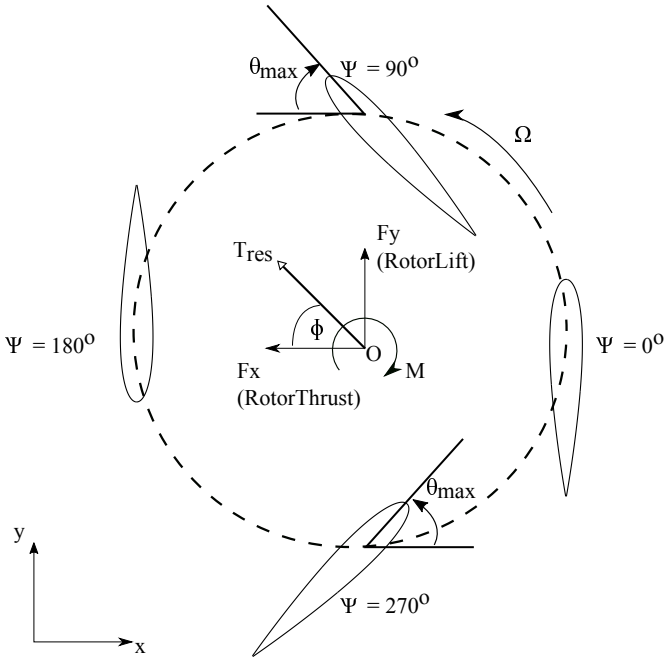

Figure 6.1: Cycloidal rotor coordinate system.

6.2.2 Mesh

A two-dimensional hybrid mesh was constructed, consisting of a unstructured polygonal mesher and a structured prism layer mesher applied at the aerofoil surface, which is used to effectively model the boundary layer characteristics. The grid type is the same as that used in the CFD model developed in Chapter 3, with a rectangular grid applied to both the flowfield (background domain) and the overset mesh boundary domain as shown in Fig. 6.2. The background domain was extended 50 chord lengths in all directions. Simulating the rotational motion of the cycloidal rotor blades as well as the blade pitch-oscillating motion was achieved through used of the overset mesh technique. The overset mesh method has been previously utilized in the CFD model developed in Chapter 3.

Volumetric mesh refinement controls were applied to both the background mesh and overset mesh in order to increase the density of cells in the regions where complex flow features such as blade-wake interference and blade boundary layer effects occur. For the overset mesh, curve refinement controls were also applied to increase the number of nodes representing the leading-edge and trailing-edge curvature of the NACA0015 aerofoil geometry. For construction of the prism layer mesh from the blade surface, the wall thickness distribution method was selected as it allows for defining the near wall prism layer cell height. This prism layer distribution method was used as it allows for fixing the wall y+ value when performing the grid independence study. The near wall prism layer height was set to 0.0000075c and the total number of prism layers was set to 30 (was previously set in Chapter 3). The prism layer total height was set to 0.01c, similar the CFD model developed in Chapter 3. The cell surface growth rate for both the background and overset mesh was set to 1.2 (as set in Chapter 3).

A base size was set for both the background mesh and overset mesh which was used to control the grid density. All of the volumetric, surface, and curve refinement controls were modified relative to a change in the base size. Two volumetric mesh refinement controls were applied to the background mesh which were 50% and 25% relative to the background's base size, and is visualised in Fig. 6.2a.

For the overset mesh, the base size was set 20% smaller than the cell target size for the background 25 % volumetric refinement region to ensure that there were enough overlapping cells which is required for sufficient interpolation of the overset boundary to the static background boundary [83]. A volumetric and surface refinement control was applied at the blade surface to increase the grid density of the core mesh near the aerofoil boundary and at the aerofoil surface. An illustration of the aerofoil surface volume grid refinement is shown in Fig. 6.2c. This was set to 10 % relative to the overset mesh's base size (as set in Chapter 3). A further surface refinement was applied at the aerofoil's leading-edge and trailing-edge surface to increase the node curvature resolution, with the target surface size set to 3 % relative to the overset mesh's base size (as set in Chapter 3). An illustration of the resultant leading-edge refinement mesh for one of the cycloidal rotor blades is shown in Fig. 6.2d. A key advantage of using the overset mesh technique in STAR-CCM+ is that only one overset mesh had to be generated which reduced the total time taken to achieve the desired mesh. The generated overset mesh which represents a single blade is then duplicated three times to produce the complete four blade cycloidal rotor. The four overset meshes are then translated and rotated into their correct positions as shown in Fig. 6.2b.

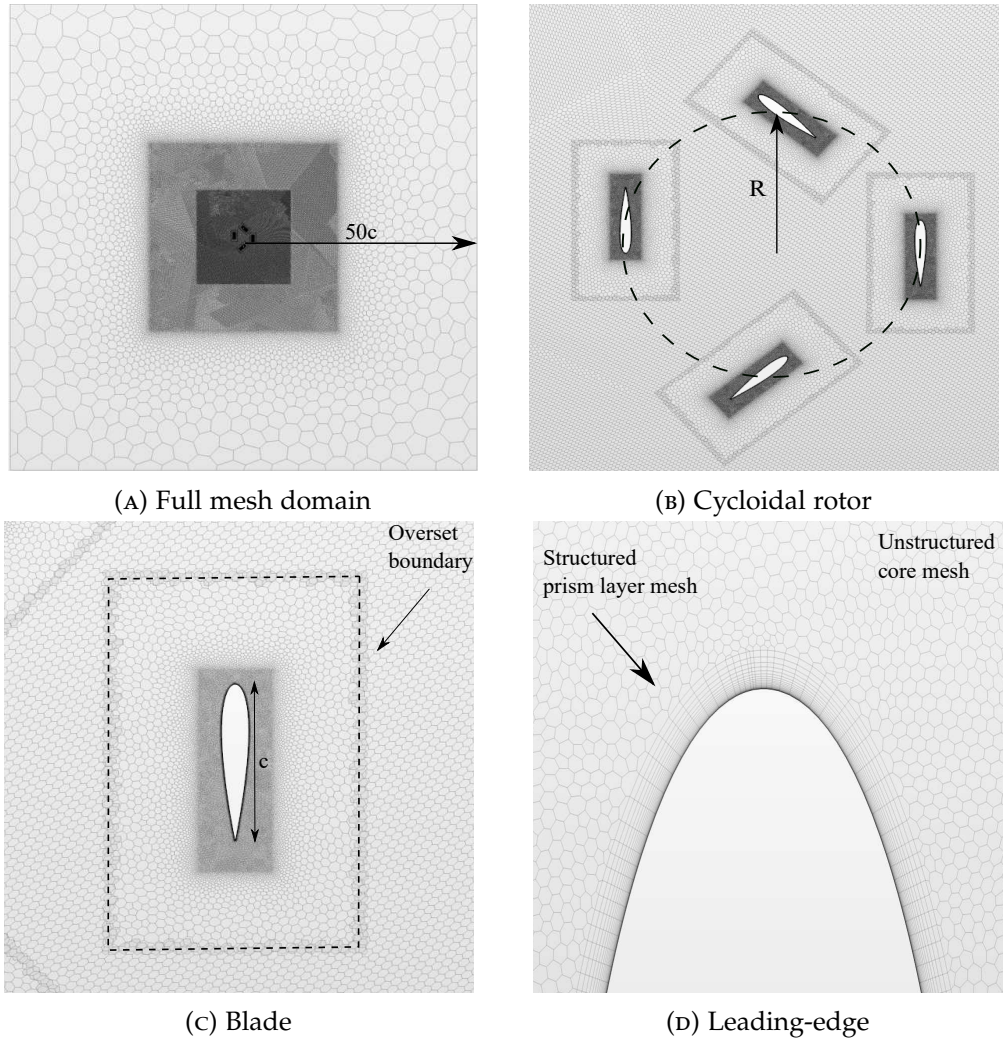

(A) Full mesh domain

(B) Cycloidal rotor

(C) Blade

(D) Leading-edge

FIGURE 6.2: CFD mesh domain for a four blade cycloidal rotor. Grid, *G*2 used as the example.

6.2.3 FLOW PHYSICS AND SOLVER

URANS equations are solved with air modelled as an ideal, compressible gas. The dynamic viscosity, μ, was set to $1.789\,72 \times 10^{-5}$ Pa-s which is the default setting used in STAR-CCM+. The default setting was used for the Turbulent Prandtl number, with the value set to 0.9. A pressure-energy based coupled solver was applied using second order spatial discretisation, and gradients were calculated using the default Hybrid Gauss LSQ method. Pressure outlet boundary conditions were extrapolated at the background boundaries due to simulating hover conditions for the cycloidal rotor. All flow computations are fully turbulent with comparisons made against the $k-\omega$-SST and Spalart-Almaras (SA) turbulence models which are used for turbulence closure of the URANS equations. The effects of turbulence were characterised by the turbulence intensity, I, and the turbulence length scale, L_{scale}, which were set to 0.02 and 0.02c respectively (as previously set in Chapter 3).

The temporal resolution was set to 2nd order and all of the computations were

performed for 10 rotor rotational cycles (which was phase-averaged from the fifth cycle onwards). The Courant number was set to 50 to improve on the convergence acceleration at each time-step without causing divergence of the residuals. The under-relaxation factors for the $k-\omega$ turbulence, SA turbulence, and turbulent viscosity parameters were set to the default parameters of 0.9.

6.2.4 Motion and morphing settings

Multiple rigid rotational motions were applied to the overset meshes in order to simulate typical cycloidal rotor motions, using STAR-CCM+'s built-in motion capability. The aerofoil's pitch axis origin is located at the quarter chord as shown in Fig. 6.1, and is defined positive in the clock-wise direction. Each blade has its own pitch axis coordinate system and is fixed to the blade which allows for sinusoidal pitching for each of the blades. Each blade of the four blade cycloidal rotor has a pitch-oscillating motion applied as a sinusoidal response where the blade pitch angle, θ, and the blade pitch rate, $\dot{\theta}$ are defined as:

$$\theta(t) = \theta_{max} sin(\Omega t + \psi_0) \tag{6.1}$$

$$\theta\dot{(t)} = \theta_{max} \Omega cos(\Omega t + \psi_0) \tag{6.2}$$

where θ_{max} is the blade pitch amplitude in degrees, Ω is the rotor rotational velocity in rad/s, t is the time in seconds, and ψ_0 is the blade's initial azimuth angle (phase angle) in degrees.

An additional rotor rotational motion is applied to the blade which rotates all of the individual blade pitch axis coordinate systems about the rotor centre. There is also a leading-edge morphing axis system (as developed in the CFD model in Chapter 3) applied to each of the blades which is used as the pivot point when applying leading-edge deformation. The leading-edge morphing axis system is fixed to the blade, therefore this axis system is rotated relative to the blade's pitch axis system.

Morphing of the blade's leading-edge is performed directly in STAR-CCM+, which uses a multi-quadratic radial splines morphing method to interpolate the displaced wall boundary surfaces [83]. In Chapter 3, two morphing methods were presented: one that used pre-defined tables which contained control points at different time-steps and a simpler method which only required the surface to be deformed about a reference pivot point. Both morphing methods presented in Chapter 3 were shown to achieve similar results in terms of generating similar performance trends in relation to the aerofoil's aerodynamic characteristics. Hence, the decision was made to implement the simpler morphing method to apply active leading-edge morphing to each of the four blades as it does not require pre-defined tables. Details of the alternative morphing method is discussed in Chapter 3.

6.2.5 Monitorables and convergence

The main monitorables used in this study include the rotor vertical force, F_y, the rotor side force, F_x, and the rotor moment, M_{rotor}, which are generated by the blades of the cycloidal rotor.

The rotor forces and moment generated by each of the blades are used to calculate rotor performance characteristics such as: the power-loading (PL), the disk-loading (DL), the rotor aerodynamic power (P), the resultant thrust vector (T_{res}), and it's direction (ϕ). The power-loading (PL) is the ratio of the rotor resultant thrust to the rotor aerodynamic power (with units N/kW), and is defined as:

$$PL = T_{res}/P \tag{6.3}$$

The disk-loading (DL) is the ratio of the rotor resultant thrust to the rotor disk area (with units N/m^2), and is defined as:

$$DL = T_{res}/A \tag{6.4}$$

The disk area, A, is determined from the blade span and the rotor radius as follows:

$$A = 2bR \tag{6.5}$$

where b is the blade span with units, m, and R is the rotor radius with units, m.

To calculate the resultant thrust vector, the total rotor vertical force and side force are calculated using the following expressions:

$$Fy = Fy_{blade1} + Fy_{blade2} + Fy_{blade3} + Fy_{blade4} \tag{6.6}$$

$$Fx = Fx_{blade1} + Fx_{blade2} + Fx_{blade3} + Fx_{blade4} \tag{6.7}$$

The resultant thrust vector, T_{res}, and its direction, ϕ, as shown in Fig. 6.1, can then be obtained as follows:

$$T_{res} = \sqrt{Fx^2 + Fy^2} \tag{6.8}$$

$$\phi = arctan\left(\frac{Fy}{Fx}\right) \tag{6.9}$$

where *Tres*, Fx, and Fy have the units, N, and ϕ has the units, degrees.

The aerodynamic power generated by the cycloidal rotor, P, with the units, W, is calculated using the following expression:

$$P = M_{rotor}\Omega \tag{6.10}$$

where M_{rotor} is the rotor moment with units, Nm, and Ω is the rotor rotational velocity with units, rad/s.

Dimensionless parameters are introduced to assess the aerodynamic performance characteristics of the cycloidal rotor (previously introduced in Chapter 1): the Thrust Coefficient, C_T, and the Power Coefficient, C_P. The thrust and power coefficients are defined as:

$$C_T = \frac{T_{res}}{0.5\rho V_t^2 A} \tag{6.11}$$

$$C_P = \frac{P}{0.5\rho V_t^3 A} \tag{6.12}$$

where V_t is the rotor tangential velocity with units m/s. The rotor tangential velocity is defined as:

$$V_t = \Omega R \tag{6.13}$$

For the residuals, certain criteria were set to ensure that the residuals fall below a certain threshold before progressing to the next time-step. The first criteria was that all of the main residuals (continuity, x-momentum, y-momentum, and energy) are required to reach a residual value of 1.0×10^{-6} before progressing to the next time-step. The second criteria was that the standard deviation of the maximum velocity magnitude had to be within 0.005 m/s, which was based on the last 75 samples. If both criteria set could not be achieved (due to convergence issues), then the maximum number of inner iterations was set to 400. This meant that the simulation would progress to the next time-step if the number of inner iterations exceeded 400 due to not meeting the requirements for the two set criteria.

6.3 VERIFICATION ANALYSIS

The CFD model is verified against computational cycloidal rotor performance results obtained by Xisto et al [44]. Their computational model was validated against experimental results produced for an IAT21 L3 cycloidal rotor and their CFD model was able to predict the rotor performance characteristics for a wide range of rotor rotational velocities with adequate accuracy. In this study however, the power-loading and disk-loading performance characteristics for the four-blade NACA0015 rotor test

case will be used for verification due to previous use of this aerofoil profile in the CFD model developed in Chapter 3. The blade's NACA0015 aerofoil section chord, c, and span, b, are 0.25 m and 1 m respectively. The blade's pitch axis was set to the quarter chord and the rotor radius, R, was set to 0.5 m.

6.3.1 Effect of grid resolution

A grid independence study was first performed to determine when the flow solution became independent for an increase in the grid density. A list of the various grids assessed in this study is presented in Table 6.1. A comparison was also made between the $k-\omega$ SST and SA turbulence models using the base grid G_1, as the SA turbulence model was utilised in the computational study performed by Xisto et al [44]. However it has been previously shown that the $k-\omega$ SST turbulence model can accurately model the key flow mechanisms of dynamic stall such as providing a reliable prediction of the flow-separation due to the significant adverse pressure gradients [104, 121]. The initial time-step was set to Δt = T/720, where T is the period of the rotor rotational cycles in seconds. Four different rotor rotational velocities were assessed for the grid independence analysis which were: Ω = 200, 400, 600, and 800 rpm.

Grid	Total cell count	Background cells	Overset cells (1 blade)
G_1	268,400	164,200	26,100
G_2	453,400	293,100	40,100
G_3	859,100	547,100	78,000

Table 6.1: Grid sensitivity study. Values rounded to the nearest 100.

The cycloidal rotor time-averaged performance results from the grid independence analysis are shown in Fig. 6.3. All grids assessed accurately predict the performance curve trends in comparison to the computational results obtained by Xisto [44]. Both the $k-\omega$ SST and SA turbulence models accurately predict the resultant thrust magnitude within 5% accuracy as shown in Fig. 6.3a for the range of rotor rotational velocities assessed. The aerodynamic power results in Fig. 6.3b illustrate that the SA turbulence model achieves an accurate prediction for the majority of rotor rotational velocities, however all grids using the $k-\omega$ SST turbulence model over-predict the aerodynamic power at the larger rotor rotational velocities. Similarly, when assessing the power-disk loading distribution in Fig. 6.3c, grid G_1 which uses the SA turbulence model, achieves a closer match when compared against Xisto's results over the full rotor rotational velocity range. However, both grids which utilise the $k-\omega$ SST turbulence model under-predict the PL by approximately 11 % in comparison to Xisto's results, when averaged over the rotor rotational velocity range. The coefficient of determination, R^2, which was previously defined in Chapter 3, is used to determine the difference in the rotor performance results for a change in grid density. The grid

independence R^2 results in Table 6.2 show that the power-loading is the most sensitive to an increase in grid density. It also shows that grid G_2 achieves a close match to G_3 for all of the cycloidal rotor performance parameters assessed whilst also achieving an approximate 14 % reduction in the computational time required to complete the simulation. Therefore, the decision was made to use the grid, G_2 for the time-step independence study.

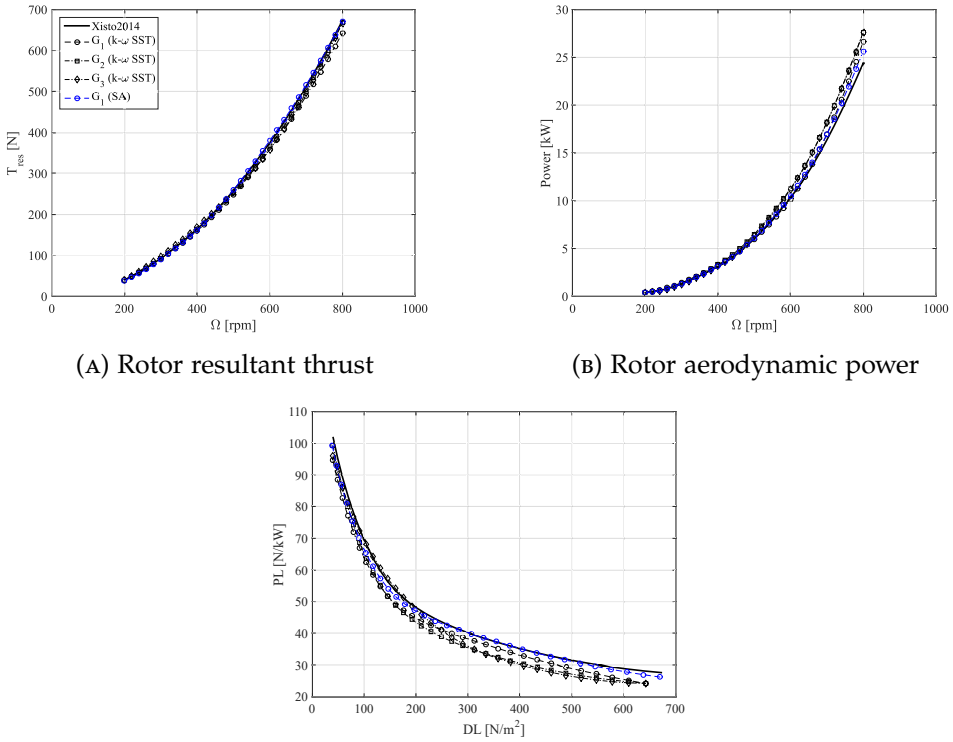

(A) Rotor resultant thrust

(B) Rotor aerodynamic power

(C) Rotor performance

Figure 6.3: Time-averaged grid independence results for a 4-blade cycloidal rotor against rotor rotational velocity and disk-loading. Results are time-averaged over the last five rotational cycles.

Grid	DL	PL	P_{total}
G_1	0.9976	0.9646	0.9901
G_2	0.9991	0.9808	0.9998
G_3	1.0000	1.0000	1.0000

Table 6.2: Grid independence results for the coefficient of determination, R^2.

6.3.2 Effect of turbulence modelling

A qualitative assessment was performed to compare the flow-field characteristics at the cycloidal rotor region when implementing either the $k-\omega$ SST or SA turbulence model for grid, G_1. Figure 6.4 visualises the instantaneous non-dimensional vorticity scalar in the k-direction for both turbulence models. The $k-\omega$ SST turbulence case in Fig. 6.4a illustrates the shedding of a primary LEV and TEV which have previously been shown to be the key flow features associated to dynamic stall for a single, pitch oscillating aerofoil [71, 121]. In fig. 6.4b, there is a modification of the vortical flow structure when using the SA turbulence model as visualised by an increase in the generation and shedding of counter-rotating vortices. This variation of the flow-field alters the blade-wake interaction acting on the succeeding blade which results in the modification of the force distribution. Due to the less accurate representation of the dynamic stall flow features when implementing the SA turbulence model, the decision was made to use grid G_2 with the $k-\omega$ SST turbulence model for the time-step independence study.

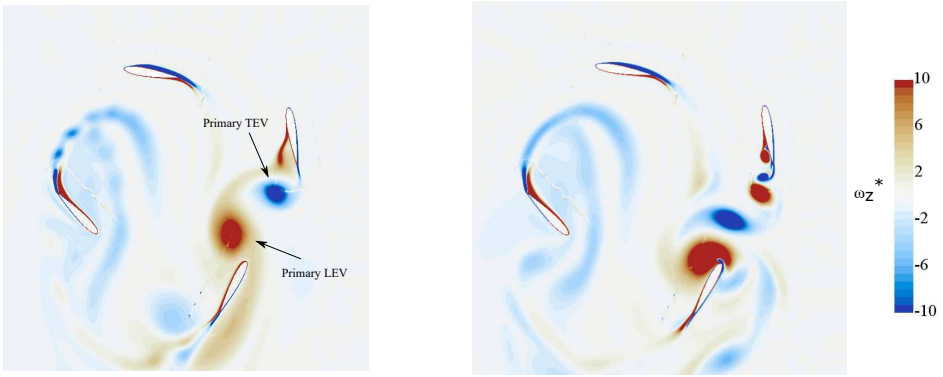

(a) $k-\omega$ SST

(b) Spalart Almaras

Figure 6.4: Non-dimensional vorticity, ($\omega_z^* = \frac{\omega_z c}{V_t}$), scalar comparison between the $k-\omega$ SST and Spalart-Almaras (SA) turbulence models. Vorticity results are scaled to improve the qualitative representation. Operational conditions: Ω = 600 rpm at t/T = 0.824 of 10^{th} cycle.

6.3.3 Effect of time-step refinement

A time-step independence study was performed as the final part of the CFD verification process. Three different values of time-step were assessed including $\Delta\ t_0$ = T/360, $\Delta\ t_1$ = T/720, $\Delta\ t_2$ = T/1000, where $\Delta\ t_1$ = T/720 was previously used for the grid independence analysis. Grid G_2 with $k-\omega$ SST turbulence modelling was used for the remainder of the simulations due to a more accurate representation of the key flow features of dynamic stall.

The time-averaged, cycloidal rotor performance results produced from the time-step independence analysis are shown in Fig. 6.5. All values of Δt accurately capture the rotor performance trends for the majority of rotor rotation velocities in comparison to the computational results obtained by Xisto et al [44]. The time-averaged rotor resultant thrust magnitude results in Fig. 6.5a show that all Δt under-predict T_{res} at the higher range of rotor rotation velocities. Moreover, all Δt were shown to over-predict the aerodynamic power by approximately 10% as shown in Fig. 6.5b, when averaged over the rotor rotational velocity range. The time-step independence R^2 results in Table 6.3 demonstrate that all Δt cases achieve similar results in all cycloidal rotor performance parameters assessed. It was therefore decided that Δt_1 is sufficient to use for the remainder of the CFD case simulations performed in this study.

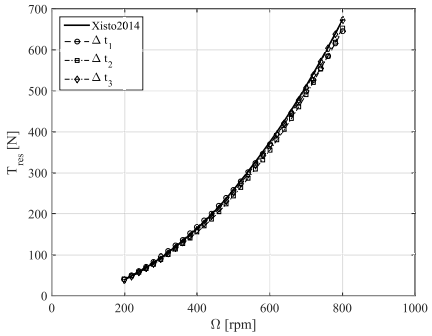

(a) Rotor resultant thrust

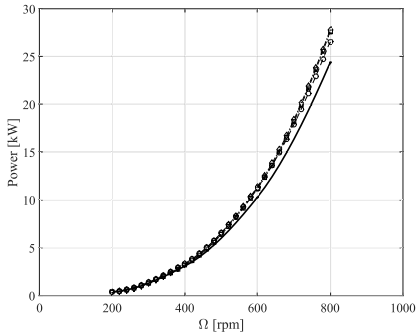

(b) Rotor aerodynamic power

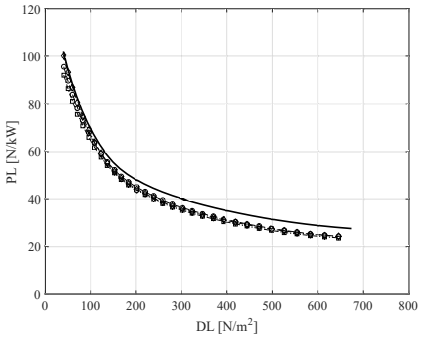

(c) Rotor performance

Figure 6.5: Time-averaged time-step independence results for a 4-blade cycloidal rotor against rotor rotational velocity and disk-loading. Results are time-averaged over the last five rotational cycles.

Grid	DL	PL	P_{total}
Δt_1	0.9976	0.9958	0.9975
Δt_2	0.9961	0.9835	0.9997
Δt_3	1.0000	1.0000	1.0000

Table 6.3: Time-step independence results for the coefficient of determination, R^2.

6.4 CORRELATION BETWEEN A SINGLE CYCLOIDAL ROTOR BLADE AND A SINGLE PITCH-OSCILLATING BLADE WITH ACTIVE LEADING-EDGE MORPHING

The single cycloidal rotor blade operates differently in comparison to a pitch oscillating aerofoil. The pitch oscillating aerofoil experiences an incoming uniform flow velocity across the blade, with no blade-wake interference effects occurring. The cycloidal rotor blade however rotates and pitches in an orbit about the rotor centre, which results in parts of the blade experiencing different directions of the local velocity. This curvilinear flow can be represented as the virtual camber effect which alters the blade aerodynamic performance as the blade orbits about the rotor domain. The cycloidal rotor blade also interacts with the wake which is produced from the previous rotational cycle. The aim of this section is to quantify the leading-edge morphing results of a single cycloidal rotor blade and to compare the differences in performance trends in comparison to a pitch-oscillating aerofoil.

An illustration of the single cycloidal rotor blade axis system which represents the blade aerodynamic forces is shown in Fig. 6.6. The blade axis system is fixed to the blade, and represents the blade lift coefficient, Cl, and drag coefficient, Cd. Cl is perpendicular to the rotor tangential velocity, V_t, and Cd is parallel to V_t. The rotor operational conditions are set the same as was set in the CFD study in Chapter 3 to assess whether there are similar performance trends between the cycloidal rotor blade and the pitch oscillating aerofoil.

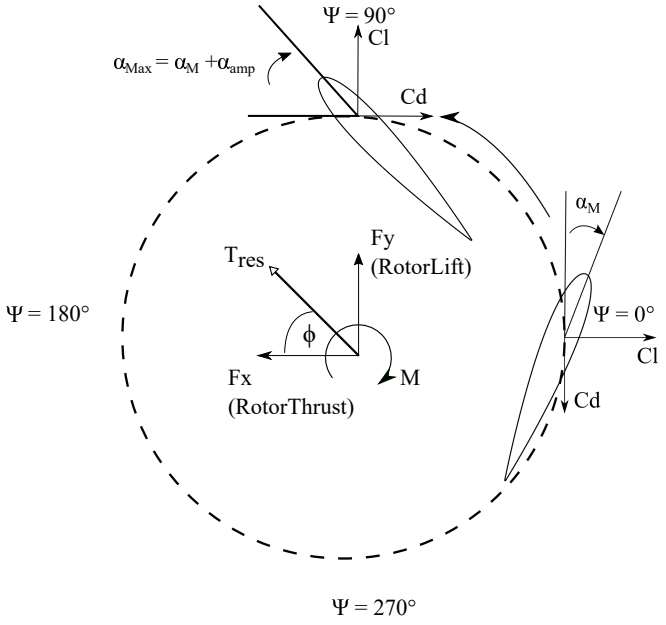

Figure 6.6: Cycloidal rotor coordinate system for a single blade which highlights the blade's aerodynamic axes system.

The sinusoidal pitch motion profile is defined as:

$$\alpha(t) = \alpha_M + \alpha_{amp} sin(\Omega t) \tag{6.14}$$

where α_M is the blade mean incidence angle with units, *deg*, α_{amp} is the blade incidence amplitude with units, *deg*, Ω is the blade angular frequency (equal to the rotor rotational speed) with units, rad/s, and t is the time in seconds. α_M and α_{amp} were set to 15 and 10 degrees respectively to represent similar settings used in the CFD analysis in Chapter 3. At the beginning of the rotor cycle ($\psi = 0°$), the blade is at mean incidence, and achieves max incidence at $\psi = 90°$, which is illustrated in Fig. 6.6.

The rotor rotational velocity (and blade pitch rate) was set at 800 rpm as this setting was deemed to produce the largest levels of blade-wake interference in the 4-blade cycloidal rotor cases. The reduced frequency, k, when applied to a cycloidal rotor, can be defined as:

$$k = \frac{c}{2R} \tag{6.15}$$

where c is the blade chord in metres, and R is the rotor radius in metres. A reduced frequency value, $k = 0.15$, was selected based on a similar reduced frequency setting used in the CFD analysis in Chapter 3. This results in an increase in the rotor radius from 0.5 m to 0.8333 m (blade chord remains constant) in comparison to the four blade cycloidal rotor. A comparison is made between a single rigid blade and a single

leading-edge morphing blade at an amplitude, $\beta_{max} = 10°$, which was selected based on achieving the largest improvements in cycloidal rotor performance. No other operational conditions are changed in the CFD model setup.

The phase-averaged cycloidal rotor performance characteristics for a single rigid and leading-edge morphing blade is shown in Fig. 6.7. Markers are included in the plots to highlight the region where leading-edge morphing actuation is implemented, which covers the rotor upper region ($0° \leq \psi \leq 180°$). The vertical force results in Fig. 6.7a show that there are small differences in the vertical force magnitude or distribution between the rigid and leading-edge morphing blade in the morphing actuation region ($0° \leq \psi \leq 180°$). At the rotor lower region where leading-edge morphing actuation is not implemented ($180° \leq \psi \leq 360°$), there is a small phase change in the vertical force distribution when comparing both blades.

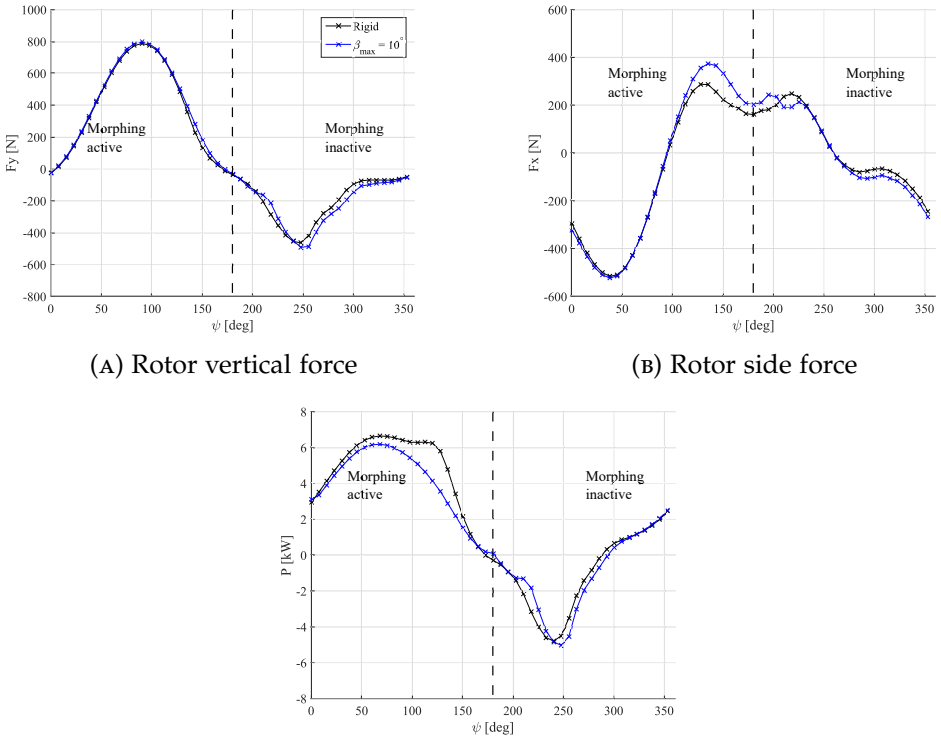

(A) Rotor vertical force

(B) Rotor side force

(C) Rotor power

Figure 6.7: Phase-averaged rotor force and power results for a single rigid and leading-edge morphing blade.

The phase-averaged rotor side force for the rigid and leading-edge morphing blade is shown in Fig. 6.7b. At the morphing actuation region ($0^\circ \leq \psi \leq 180^\circ$), there is no change in the side force results during the pitch upstroke section ($0^\circ \leq \psi \leq 90^\circ$), between both blades. During the pitch downstroke section ($90^\circ \leq \psi \leq 180^\circ$), there is an increase in the peak positive horizontal force for the leading-edge morphing blade in comparison to the rigid blade, however there is no change in the side force distribution. There is little difference in the side force distribution at the rotor lower region ($180^\circ \leq \psi \leq 360^\circ$) between the leading-edge morphing blade and the rigid blade as the morphing actuation is not performed at this region.

The phase-averaged rotor aerodynamic power results for the rigid and leading-edge morphing blade is shown in Fig. 6.7c. At the rotor upper region ($0^\circ \leq \psi \leq 180^\circ$), the level of power absorption is larger for the rigid blade in comparison the leading-edge morphing blade. This is due to dynamic stall occurring for the rigid blade which delays the stall process and results in a flatter distribution in the power absorption. At the rotor lower region ($180^\circ \leq \psi \leq 360^\circ$), similar aerodynamic power results are generated by the rigid and leading-edge morphing blade as no morphing actuation is performed at this region.

The phase-averaged, blade aerodynamic force and moment coefficient characteristics for both the rigid and leading-edge morphing blade is shown in Fig. 6.8. The blade lift coefficient results in Fig. 6.8a show that during the pitch upstroke in the active morphing region, there is no difference in Cl when comparing both rigid and morphing blade results (Cl_{max} is approximately the same). During the pitch downstroke, there is a reduction in the blade lift hysteresis loop for the leading-edge morphing blade in comparison to the rigid blade. The reduction in the lift hysteresis loop has been previously demonstrated in both the CFD analysis in Chapter 3, as well as the experimental analysis in Chapter 5.

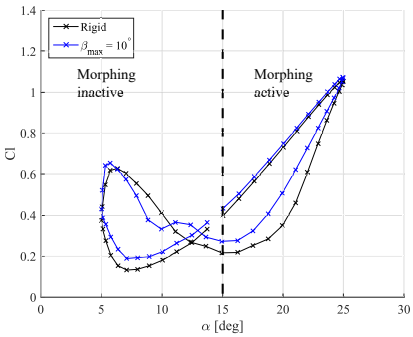

(A) Blade lift coefficient

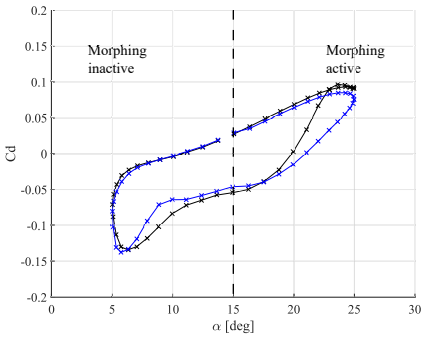

(B) Blade drag coefficient

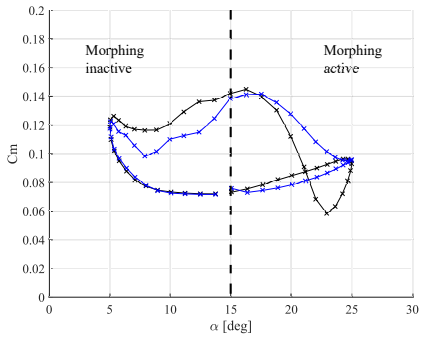

(C) Blade moment coefficient

FIGURE 6.8: Phase-averaged blade aerodynamic forces and moment coefficient results for a single rigid and leading-edge morphing blade.

The phase-averaged blade drag coefficient results for both the rigid and leading-edge morphing blade is shown in Fig. 6.8b. During the pitch upstroke, the leading-edge morphing blade achieves a small reduction in Cd_{max} compared to the rigid blade. Moreover, during the pitch downstroke, there is a significant reduction in Cd for the leading-edge morphing blade in comparison to the rigid blade as a result of the formation of an LEV for the rigid blade which results in a delay in the drag reduction. In the morphing inactive region, there is little difference in Cd between both the rigid blade and leading-edge morphing blade. Note, negative Cd values have been predicted due to the downwash flow produced by the single blade cycloidal orbit.

The phase-averaged blade moment coefficient results for both the rigid and leading-edge is shown in Fig. 6.8c. In the morphing active region, leading-edge morphing is shown to have a significant effect on the pitching moment characteristics in comparison to the rigid blade. The negative pitch damping loop produced by the rigid blade has been removed by the leading-edge morphing blade which results in a reduction in blade structural fatigue. The effect of leading-edge morphing reducing the size of the negative pitch damping loop has previously been demonstrated in the CFD analysis in Chapter 3 as well as the experimental analysis in Chapter 5.

6.5 ACTIVE LEADING-EDGE MORPHING OF CYCLOIDAL ROTOR BLADES

6.5.1 Effect of morphing actuation azimuthal position

Active leading-edge morphing is applied to each blade of the 4-blade cycloidal rotor to determine its effectiveness on rotor performance and alleviating the detrimental effects of dynamic stall. An initial study into the effectiveness of leading-edge morphing on the cycloidal rotor performance is assessed by varying the blade azimuth position for initialising the leading-edge morphing actuation. The leading-edge morphing amplitude, β_{max} was set to 10° as this was previously demonstrated in Chapter 3 to be effective in terms of alleviating the impact of dynamic stall on a single, pitch oscillating aerofoil. The pivot point, MT_{2a}, was selected as this was more representative of the leading-edge deflection method implemented in the experimental analysis in Chapter 5. Both positive and negative droop leading-edge morphing actuation schedules are assessed. An example of initialising both positive and negative pulsed leading-edge morphing at blade azimuth angle, $\psi = 180°$ is illustrated in Fig. 6.9. Operational conditions such as the rotor rotational speed is kept constant at Ω = 600 rpm due to the large levels of power absorption observed from the CFD verification analysis in Section 6.3.

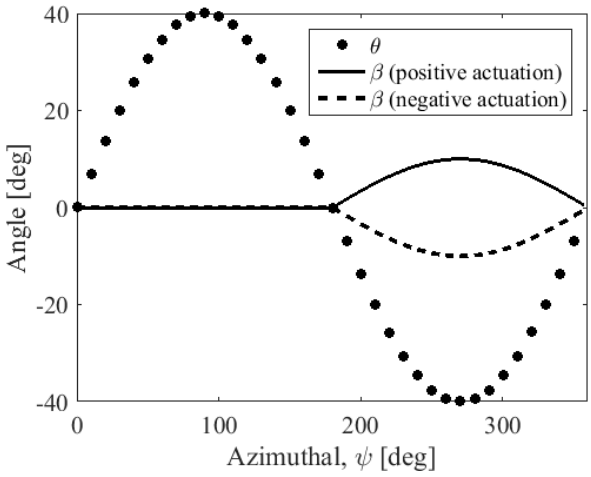

Figure 6.9: Blade pitch and leading-edge morphing schedule (with positive and negative pulsed actuation schedules).

The phase-averaged cycloidal rotor performance results for a single blade with positive and negative pulsed, leading-edge morphing, initialised at various blade azimuth positions is shown in Fig. 6.10. It is evident that leading-edge morphing actuation in the upper region of the cycloidal rotor ($0 \leq \psi \leq 180°$) has a minimal effect on the blade loading characteristics in comparison to the rigid rotor. At the lower region of the rotor, ($180 \leq \psi \leq 360°$), where dynamic stall and blade-wake interference effects are more significant due to the effects of virtual camber, only specific cases of leading-edge morphing had a positive effect on the blade loading distribution.

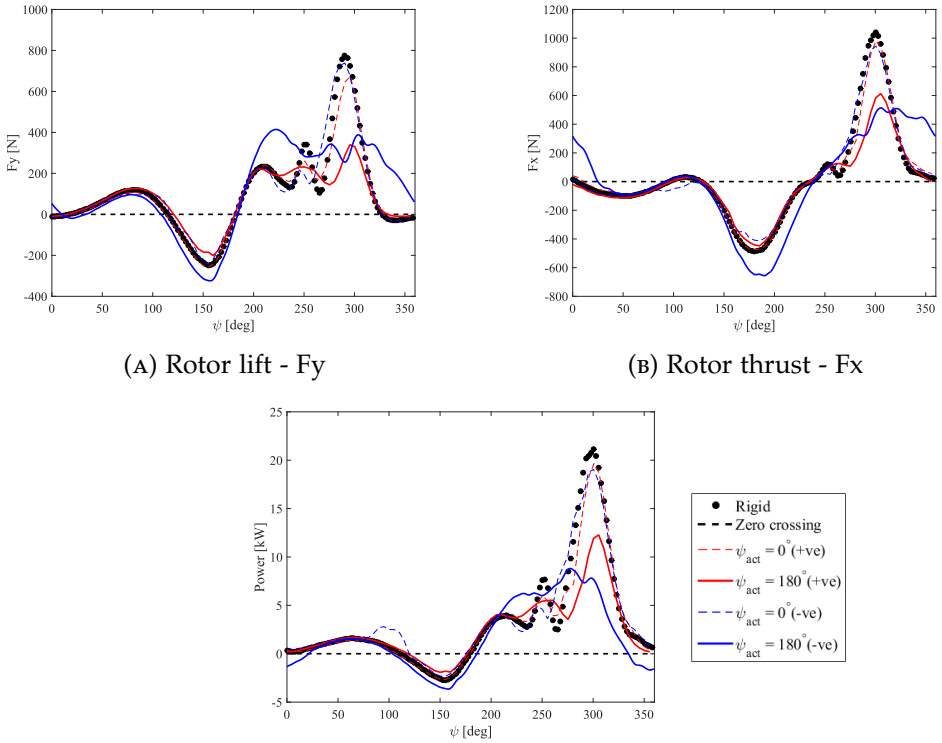

(A) Rotor lift - Fy

(B) Rotor thrust - Fx

(C) Rotor aerodynamic power

FIGURE 6.10: Phase-averaged cycloidal rotor aerodynamic performance results for a single blade at various initial morphing actuation azimuthal positions. Operational conditions: Ω = 600 rpm, $\beta_{max} = 10°$. Results are phase-averaged over the last five of the 10 rotation cycles.

The phase-averaged rotor vertical force results for a single blade with rigid and morphing conditions (initialised at various blade azimuth angles) is shown in Fig. 6.10a. For the rigid blade, the peak vertical force generated at the rotor's upper region is significantly less in comparison to the peak vertical force generated at the rotor's lower region. This is due to the effect of blade virtual camber which is generated by the blade's orbital trajectory resulting in a variation of the incoming flow velocity along the blade's chord position. This results in the blade achieving negative virtual camber on the rotor's upper region and positive virtual camber on the rotor lower region. The only effective morphing case in terms of mitigating the dynamic stall effect is when leading-edge morphing is initialised at $\psi_{act} = 180^{\circ}(-ve)$. This results in the blade achieving β_{max} at $\psi = 270^{\circ}$ which is where the blade is pitched at the minimum blade pitch amplitude. The morphing case, $\psi_{act} = 180^{\circ}(-ve)$, is shown to maintain an increase in rotor vertical force for an increase in negative blade pitch amplitude in contrast to the remainder of cases. This is due to leading-edge morphing delaying the progression of reversed flow towards the leading-edge which delays the onset of the LEV formation and convection. The peak rotor vertical force generated at the rotor lower region for $\psi_{act} = 180^{\circ}(-ve)$ is reduced by 46.48 % which occurs earlier at $\psi = 222^{\circ}$ in comparison to the rigid blade. This leads to a flatter positive vertical force distribution for $270 \leq \psi \leq 360^{\circ}$ with a gradual reduction in vertical force due to the reduction in θ_{max}.

When analysing the phase-averaged rotor side force results in Fig. 6.10b for a single rigid blade, there is a larger production of side force generated at the right half of the rotor in comparison to the left half. This results in fluctuations in the horizontal axis which creates a periodic side force instability. The majority of morphing cases tested had little influence on reducing the periodic side force instability except for when positive and negative leading-edge morphing is initialised at $\psi_{act} = 180^{\circ}$. The morphing case $\psi_{act} = 180^{\circ}(-ve)$ improved on the side force stability by reducing the maximum positive side force on the right half of the rotor whilst increasing the peak negative side force on the left half of the rotor. This resulted in an increase in the side force balance on the left and right half of the rotor which resulted in a reduction in the periodic side force instability.

Figure 6.10c visualises the phase-averaged cycloidal rotor aerodynamic power for a single blade with rigid and morphing settings initialised at various blade azimuth angles. Both positive and negative peaks in aerodynamic power are generated by both the rigid and morphing blade at the rotor's upper region ($0 \leq \psi \leq 180^{\circ}$). Negative aerodynamic power relates to power extraction which means that the blade extracts energy from the flow due to a reduction in flow velocity [122]. There is a 31.52% increase in power extraction when leading-edge morphing is initialised at $\psi_{act} = 180^{\circ}(-ve)$ compared to the rigid blade which indicates that the level of power extraction is dependent upon the modification of blade-wake interference. There are significant reductions in the peak power absorption when leading-edge morphing is active at the rotor's lower surface. A 58.34% reduction in peak power absorption is

achieved when leading-edge morphing is initialised at $\psi_{act} = 180°(-ve)$ and occurs earlier at $\psi_{act} = 278°$ in contrast to the rigid blade at $\psi_{act} = 300°$. This is related to the peak vertical force generated by the morphing blade occurring earlier in comparison to the rigid blade. At ($335 \leq \psi \leq 360°$), the only leading-edge morphing setting able to achieve power extraction is when leading-edge morphing is initialised at $\psi_{act} = 180°(-ve)$.

The effect of initialising leading-edge morphing at various blade azimuth positions has been further investigated quantitatively and qualitatively to determine the flow mechanisms responsible for the associated improvements in cycloidal rotor performance. The time-averaged performance characteristics for the four-blade cycloidal rotor with both rigid and morphing blades is presented in Table. 6.4. For the rigid blade rotor, the time-averaged PL and DL produced are 31.82 N/kW and 366 N/m^2 respectively. This results in the rotor achieving an equivalent value of 0.61 for C_T and C_P when operating at 600 rpm. The direction of the resultant thrust for the rigid blade rotor is $\phi = 84.25°$ which leads to skewness in the flow-direction of the downwash flow. The instantaneous non-dimensional vorticity in the z-direction, ω_z^*, and velocity magnitude flow-field plots for the rigid and morphing rotor cases, $\psi_{act} = 180°(-/+ve)$ are presented in Fig. 6.11 to illustrate the effect of leading-edge morphing on the modification of blade-wake interference. The non-dimensional vorticity flow-field for the rigid rotor in Fig. 6.11a shows the presence of a LEV and TEV produced by blade, B1. The wake of the LEV and TEV from the proceeding blade is also shown which contributes towards the high level of blade-wake interference exerted onto the succeeding blade.

Case	PL $[N/kW]$	DL $[N/m^2]$	ϕ $[deg]$	C_T [1]	C_P [1]
Rigid	31.82	366.00	84.25	0.61	0.61
ψ_{act} = 0° (+ve)	31.31	352.54	78.56	0.58	0.59
ψ_{act} = 180° (+ve)	28.61	350.29	76.36	0.58	0.65
ψ_{act} = 0° (-ve)	31.36	358.45	81.07	0.59	0.60
ψ_{act} = 180° (-ve)	**64.01**	**427.13**	**86.67**	**0.71**	**0.35**

Table 6.4: Time-averaged performance results for a 4-blade cycloidal rotor with rigid and morphing blades, initialised at various blade azimuthal positions. Results are time-averaged over the last five of the 10 rotation cycles and is at a rotor rotational velocity, Ω = 600 rpm.

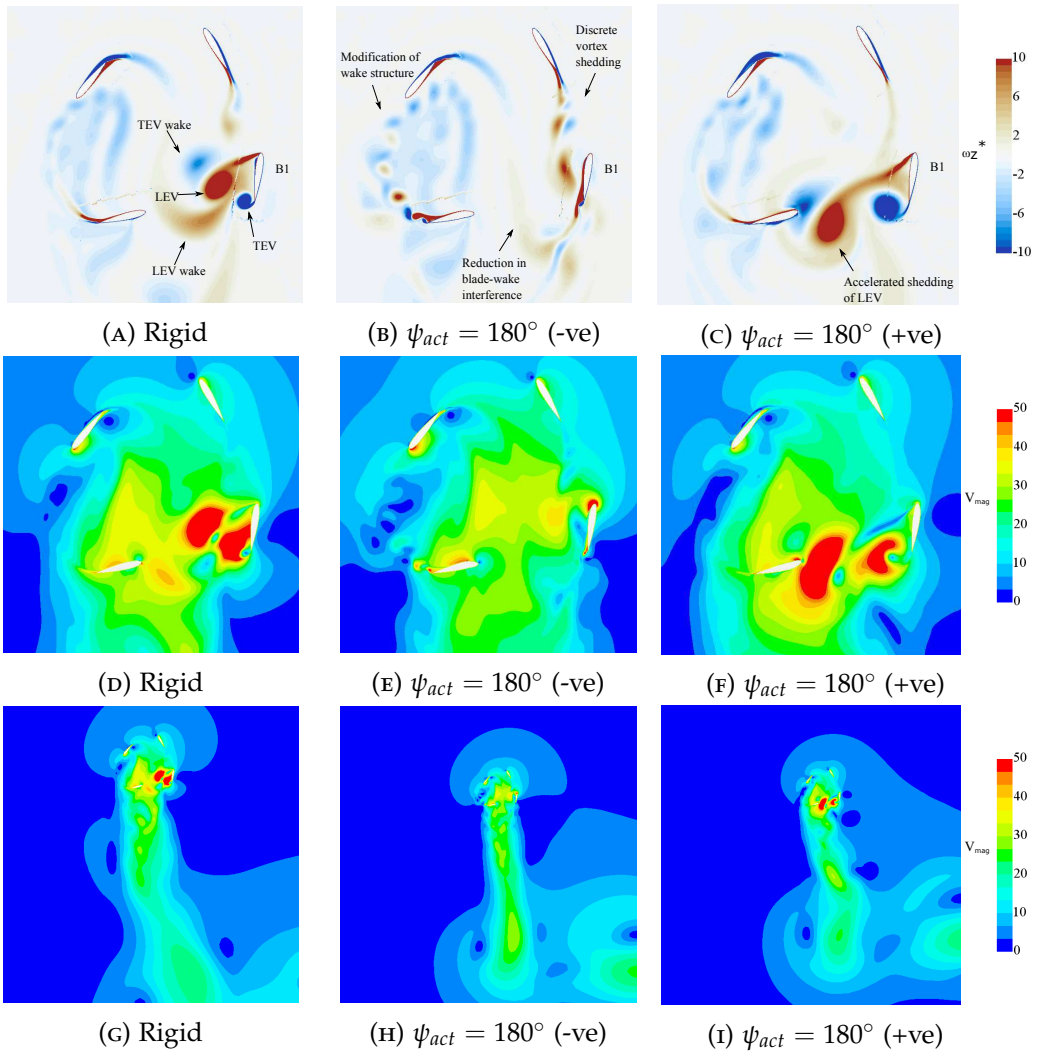

(A) Rigid (B) $\psi_{act} = 180°$ (-ve) (C) $\psi_{act} = 180°$ (+ve)

(D) Rigid (E) $\psi_{act} = 180°$ (-ve) (F) $\psi_{act} = 180°$ (+ve)

(G) Rigid (H) $\psi_{act} = 180°$ (-ve) (I) $\psi_{act} = 180°$ (+ve)

FIGURE 6.11: Visualisation of the flow-field characteristics for the cycloidal rotor under the operational conditions: Ω = 600rpm at t/T = 0.935 of 10th cycle. (a-c) - non-dimensional vorticity (($\omega_z^* = \frac{\omega_z c}{V_t}$)). (d-f) - Velocity magnitude (zoomed in). (g-h) - velocity magnitude (zoomed out).

The most effective morphing case is when leading-edge morphing is initialised at $\psi_{act} = 180°(-ve)$, which achieves significant improvements in PL and DL of 101.2% and 16.7% respectively, in comparison to the rigid blade rotor. There is also a significant reduction in C_P by approximately 42% as well as an increase in C_T by approximately 16.7% when initialising leading-edge morphing at $\psi_{act} = 180°(-ve)$. This is due to the reduction in strength of the LEV and TEV as well as the effects of blade-wake interference as shown in the non-dimensional vorticity plot in Fig. 6.11b. In Fig. 6.11b, there is a delay in the formation and convection of the LEV for blade B1, which leads to a break down of the large LEV structure as shown by the wake shedding produced by the preceding blade. Furthermore, the wake-structure within the rotor domain is less influential as shown by the minimal velocity gradient changes in Fig. 6.11e, which confirms the reduction in the level of blade-wake interference. Finally, the flow of the rotor downwash is shown to be less skewed in comparison to

the rigid rotor as visualised in Fig. 6.11h.

The least effective morphing case when compared to the rigid blade rotor is when leading-edge morphing is initialised at $\psi_{act} = 180°(+ve)$, with reductions in PL and DL of 10.1 % and 4.31 % respectively. This also results in an increase in C_P by approximately 6.3% and a decrease in C_T by approximately 4.3% when compared against the rigid blade rotor. The primary reason for the reduction in rotor performance is due to the implementation of physical negative camber applied to the blades when operating at the rotor's lower region. The effect of physical negative camber causes an earlier formation of a larger LEV in comparison to the rigid blade, as shown in the non-dimensional vorticity plot in Fig. 6.11c. The convection of the larger LEV generates a stronger TEV which results in an increase in the level of blade-wake interference acting on the succeeding blade as shown in the velocity magnitude flow-field in Fig. 6.11f. Furthermore there is an increase in the flow direction skewness of the downwash flow for $\psi_{act} = 180°(+ve)$ which is confirmed by the reduction in T_{res} from 84.25° to 79.18° when compared to the rigid blade rotor.

Overall, determining the optimal blade azimuth angle to initialise the pulsed leading-edge morphing is crucial in terms of improving the cycloidal rotor performance. At the lower region of the cycloidal rotor where the effects of blade-wake interference and dynamic stall effects are more significant, large improvements in rotor performance are gained when leading-edge morphing actuation is initialised at $\psi_{act} = 180°(-ve)$. This is primarily due to the delay and reduction in strength of the LEV which leads to a reduction in the level of blade-wake interference acting on the succeeding blade. Applying leading-edge morphing at the upper region of the cycloidal rotor had little influence on the rotor performance characteristics.

6.5.2 Effect of leading-edge morphing amplitude

Once the effective blade azimuthal position to initialise the leading-edge morphing actuation was determined, the next step was to assess the effect that variation of the leading-edge morphing amplitude has on the cycloidal rotor performance. Four different leading-edge morphing amplitudes are assessed, which include β_{max} = 5°, 7.5°, 10°, and 15°. A visualisation of the blade pitch and negative droop leading-edge morphing schedules is shown in Fig. 6.12. No other changes are applied to the operational conditions and the rotor rotational velocity remains constant at $\Omega = 600$ rpm.

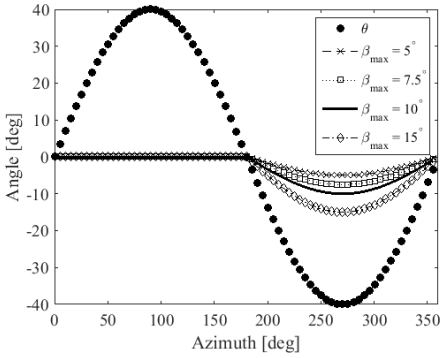

FIGURE 6.12: Blade pitch and leading-edge morphing schedules for a variation in β_{max}.

The phase-averaged rotor performance characteristics for both a rigid blade and morphing blade with differing β_{max} amplitudes is shown in Fig. 6.13. All β_{max} amplitudes evaluated with the exception to β_{max} = 5° are shown to have a significant positive influence on the rotor performance in comparison to the rigid blade. The level of increase in rotor performance when β_{max} is increased from 7.5° to 15° is small in comparison to the significant increase in rotor performance for a small increase in β_{max} from 5° to 7.5°.

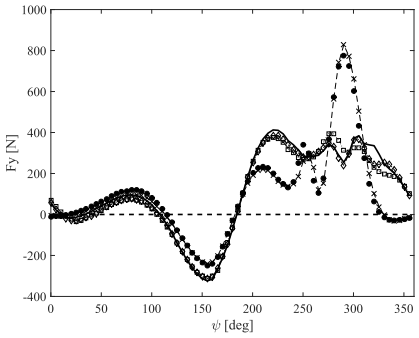

(A) Rotor lift - Fy

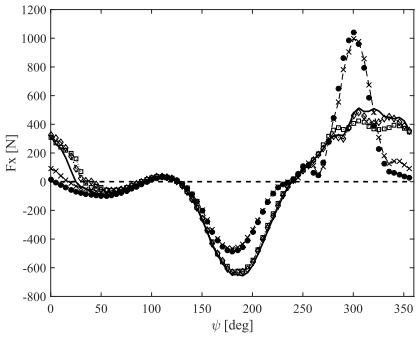

(B) Rotor thrust - Fx

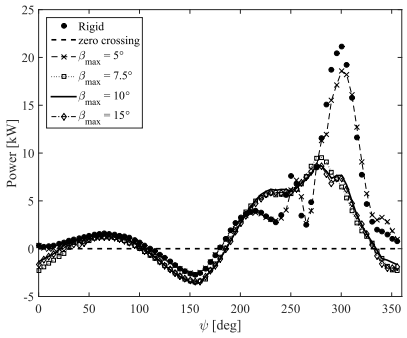

(C) Rotor aerodynamic power

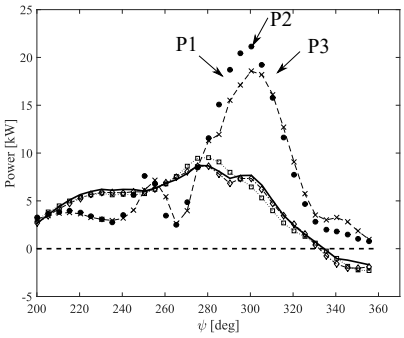

(D) Rotor aerodynamic power - zoomed in

FIGURE 6.13: Phase-averaged cycloidal rotor aerodynamic performance results for a single blade at various β_{max} amplitudes. Operational conditions: Ω = 600 rpm, $\psi_{act} = 180°$(-ve). Results are phase-averaged over the last five of the 10 rotation cycles.

The phase-averaged rotor vertical force results in Fig. 6.13a demonstrates that the dynamic overshoot is removed and positive vertical force is produced over the entire lower region of the rotor for $7.5 \leq \beta_{max} \leq 15^{\circ}$. In contrast, $\beta_{max} = 5^{\circ}$ is unsuccessful in removing the dynamic overshoot and actually results in an increase in the rotor's lower region peak vertical force by approximately 7 % in comparison to the rigid blade. The phase-averaged rotor side force plot in Fig. 6.13b illustrates an improvement in the side force equilibrium for $7.5 \leq \beta_{max} \leq 15^{\circ}$. The rigid blade generates a periodic side force imbalance of approximately 46 N where as the morphing blade, $\beta_{max} = 7.5^{\circ}$ reduces the imbalance by 20.47 N. The morphing blade, $\beta_{max} = 5^{\circ}$, however generates a side force imbalance of approximately 83 N which results in a increase in periodic side force instability.

Significant improvements are gained in mitigating the aerodynamic power absorption produced as an effect of dynamic stall modification for the majority of β_{max} amplitudes assessed as shown in Fig. 6.13c. At the rotor upper region ($0 \leq \psi \leq 180^{\circ}$), there is an increase in aerodynamic power extraction upto 30 % for $7.5 \leq \beta_{max} \leq 15^{\circ}$ in comparison to the rigid blade. This implies that modification of the blade-wake interference at the rotor lower region due to leading-edge morphing has an effect on the rotor's performance at the upper region where no morphing actuation is applied. At the rotor lower region ($180^{\circ} \leq \psi \leq 360^{\circ}$), peak power absorption occurs for the rigid blade due to the detrimental effects of dynamic stall. There is a significant decrease in the peak power absorption at $7.5^{\circ} \leq \beta_{max} \leq 15^{\circ}$ and occurs at an earlier blade azimuthal position when compared to the rigid blade due to the delay in lift stall. The rate of power absorption reduction begins at the same blade azimuthal position for leading-edge morphing amplitudes assessed, which is due to the reduction in the blade-pitch amplitude. However, the rate of power absorption reduction is less severe for $7.5^{\circ} \leq \beta_{max} \leq 15^{\circ}$ which suggests the level of blade-wake interference effects has reduced.

The time-averaged cycloidal rotor performance results for both the rigid and morphing 4-blade rotor with differing β_{max} amplitudes is presented in Table 6.5. There are improvements in the power-loading efficiency and power coefficient for all β_{max} amplitudes assessed in comparison to the rigid blade rotor. This level of improvement increases for an increase in β_{max} although there is a slight reduction in performance when β_{max} is increased from 10° to 15°. Moreover, all leading-edge morphing amplitudes assessed with the exception of $\beta_{max} = 5^{\circ}$ are shown to improve on the thrust coefficient and the disk-loading characteristics as well as the direction of the resultant thrust vector.

Case	PL $[N/kW]$	DL $[N/m^2]$	ϕ $[deg]$	C_T [1]	C_P [1]
Rigid	31.82	366.00	84.25	0.61	0.61
$\beta_{max} = 5°$	33.67	365.02	81.97	0.60	0.57
$\beta_{max} = 7.5°$	59.65	412.99	85.92	0.68	0.36
$\beta_{max} = 10°$	**64.01**	**427.13**	**86.67**	**0.71**	**0.35**
$\beta_{max} = 15°$	62.07	419.42	86.37	0.69	0.36

Table 6.5: Time-averaged performance results for a 4-blade cycloidal rotor with rigid and morphing blades with a variation in the leading-edge morphing amplitude. Results are time-averaged over the last five of the 10 rotation cycles and is at a rotor rotational velocity, Ω = 600 rpm.

An analysis of the flow-field and blade surface pressure coefficient (Cp) distribution at key blade azimuthal positions was performed to explain why β_{max} = 5° was the least effective morphing case in terms of improving the cycloidal rotor performance. Three key points were assessed, as marked on the phase-averaged power plot in Fig. 6.13d. The points were selected at the cycloidal rotor lower region where the effects of dynamic stall are significant.

The instantaneous Cp and ω_z^* scalar plots as well as the surface Cp distribution plot for the rigid blade and leading-edge morphing blade (β_{max} = 5°), at point P1, is shown in Fig. 6.14. At point P1 in Fig. 6.13d, a peak positive vertical force is produced for both the rigid and morphing blade which results in significant suction at the leading-edge of the morphing section's lower surface. The high level of suction is visualised in the Cp scalar plots in Figs. 6.14a and 6.14c at blade B1 as well as the surface Cp distribution plot in Fig. 6.14e. In Fig. 6.14e, a large ridge is formed for the morphing blade, which signifies the initial formation and convection of a LEV. A ridge is also formed for the rigid blade however the strength of the LEV is less than for the morphing blade and initially lags in terms of convection. The difference in the LEV formation and convection characteristics between the rigid and morphing blades is due to the modification of the effects of blade-wake interference as illustrated in the non-dimensional vorticity plots in Figs. 6.14b and 6.14d. Both plots show the wake of the LEV produced by the proceeding blade interacting with both the succeeding rigid and morphing blade, however the effect of leading-edge morphing is shown to reduce the level of blade-wake interference experienced at the succeeding blade's lower surface.

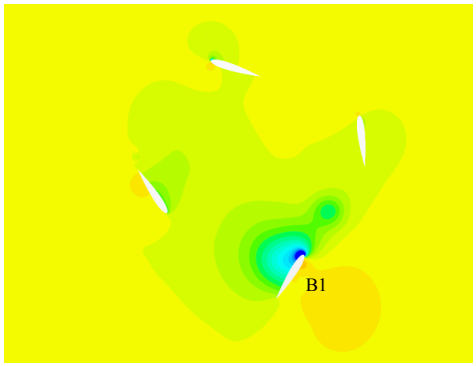

(a) Rigid

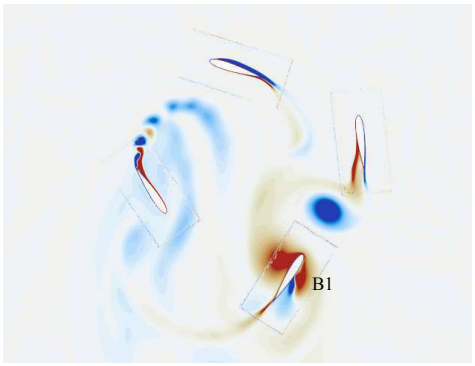

(b) Rigid

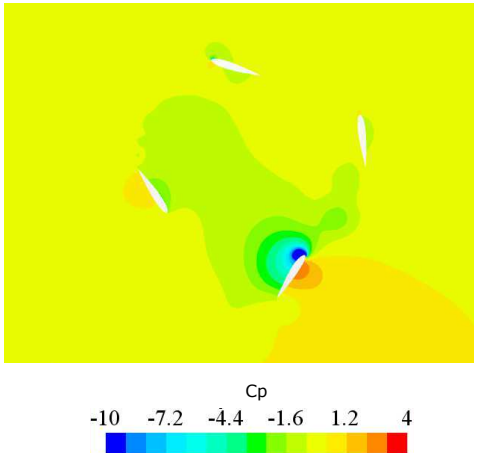

(c) $\beta_{max} = 5°$

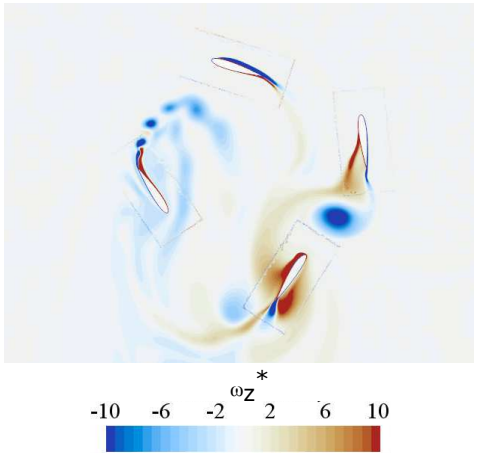

(d) $\beta_{max} = 5°$

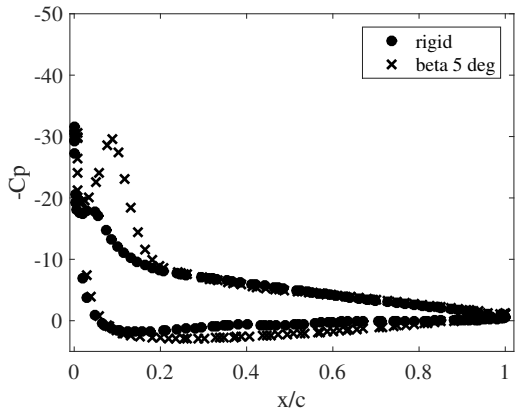

(e) Cp distribution

Figure 6.14: Visualisation of the flow-field characteristics for the cycloidal rotor under the operational conditions: Ω = 600rpm at point P1 from Fig. 6.13d. (a-c) - pressure coefficient scalar. (b-d) - Non-dimensional vorticity ($\omega_z^* = \frac{\omega_z c}{V_t}$). (e) - Surface pressure coefficient distribution.

At point P2 in the phase-averaged power plot in Fig. 6.13d, peak power absorption occurs for both the rigid and leading-edge morphing blade at approximately $\psi = 300°$. The Cp scalar plots in Figs. 6.15a and 6.15c visualise the convection of the LEV vortex across both the rigid and morphing blade B1's lower surface. The LEV convection is further illustrated in the surface Cp distribution plot in Fig. 6.15e, however the LEV

generated by the morphing blade lags behind the LEV generated by the rigid blade, indicating a reduction in the convection speed. The reduction in the LEV convection speed for the morphing blade is visualised in the non-dimensional vorticity plot in Fig. 6.15d. The effect of implementing leading-edge morphing is shown to produce a small counter-rotating vortex at the blade's lower surface where morphing is applied. This counter rotating vortex acts in the opposing direction to the LEV which results in the reduction of convection speed and strength of the LEV.

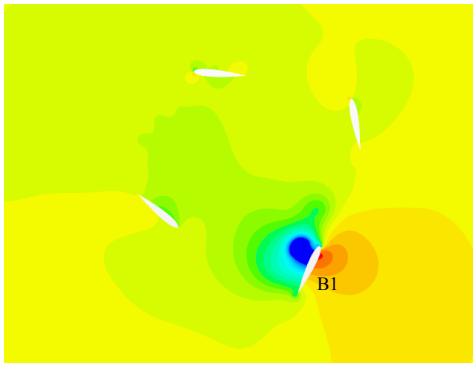

(a) Rigid

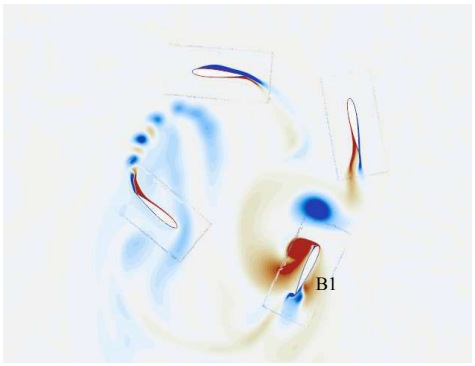

(b) Rigid

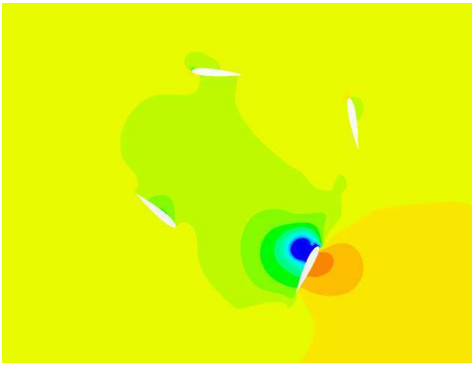

(c) $\beta_{max} = 5°$

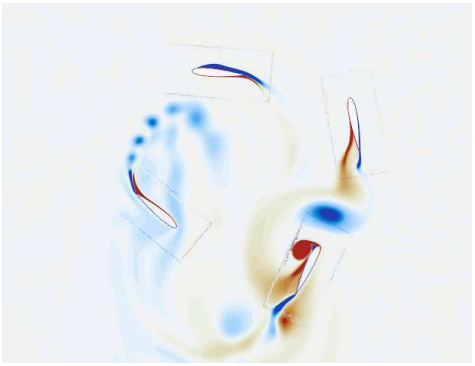

(d) $\beta_{max} = 5°$

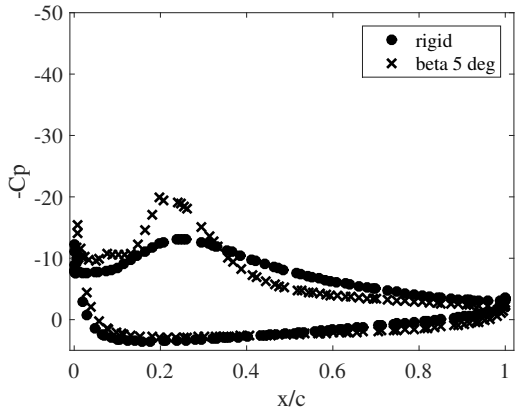

(e) Cp distribution

Figure 6.15: Visualisation of the flow-field characteristics for the cycloidal rotor under the operational conditions: Ω = 600rpm at point P2 from Fig. 6.13d. (a-c) - pressure coefficient scalar. (b-d) - Non-dimensional vorticity ($\omega_z^* = \frac{\omega_z c}{V_t}$). (e) - Surface pressure coefficient distribution.

Finally, point P3 in Fig. 6.13d is where peak suction at the trailing-edge for the rigid blade occurs. The Cp scalar plot in Fig. 6.16a visualises two discrete areas of low pressure across the lower surface of the rigid blade, B1. The large level of suction developed at the rigid blade's trailing-edge is due to the separation the LEV which results in the formation of a TEV. Previous research on dynamic stall of oscillating

aerofoils has shown that the TEV is responsible for the generation of significant negative peak pitching moments which are responsible for structural fatigue and excessive pitch link loading [71–73]. In terms of cycloidal rotor performance, the generation of large pitching moments due to the TEV also leads to an increase in power absorption. However the Cp scalar plot for the $\beta_{max} = 5^{\circ}$ morphing blade in Fig. 6.16c shows only one discrete area of low pressure over blade B1's lower surface which is the LEV. This is further confirmed in the surface Cp distribution plot in Fig. 6.16e which shows only the ridge at 0.4 x/c and no suction at the trailing-edge. This suggests that the LEV generated by the morphing blade has not convected far enough to develop the TEV which would confirm the reduction in the peak power absorption in comparison to the rigid blade.

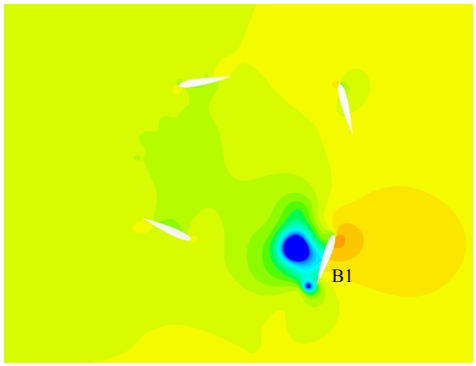

(a) Rigid

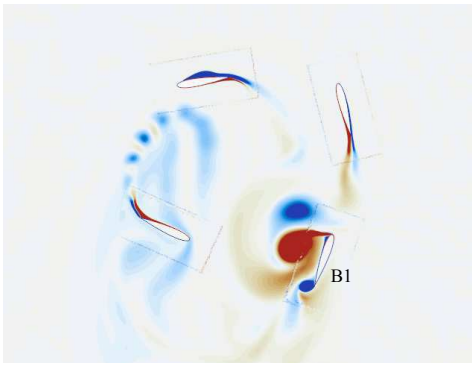

(b) Rigid

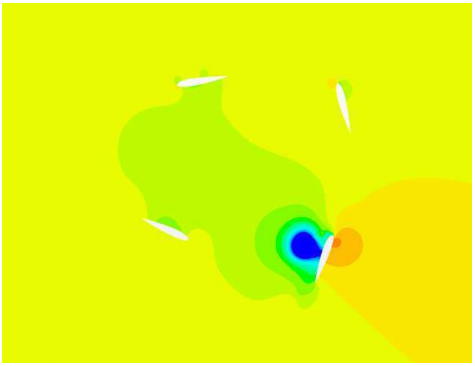

(c) $\beta_{max} = 5°$

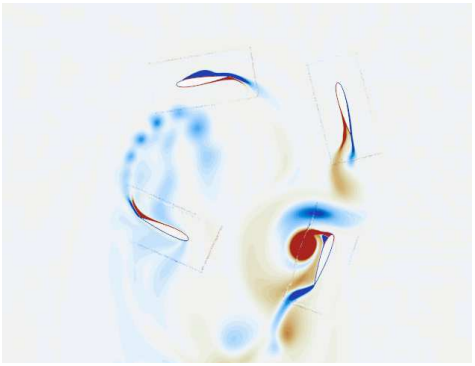

(d) $\beta_{max} = 5°$

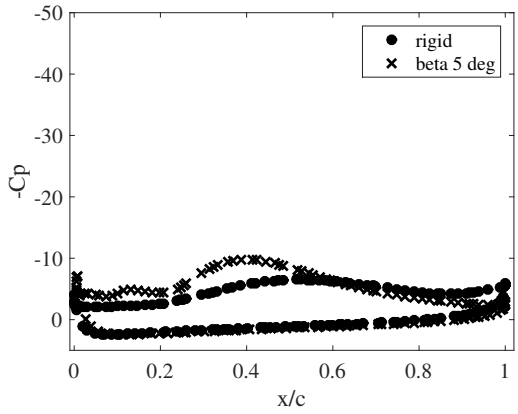

(e) Cp distribution

Figure 6.16: Visualisation of the flow-field characteristics for the cycloidal rotor under the operational conditions: Ω = 600rpm at point P3 from Fig. 6.13d. (a-c) - pressure coefficient scalar. (b-d) - Non-dimensional vorticity ($\omega_z^* = \frac{\omega_z c}{V_t}$). (e) - Surface pressure coefficient distribution..

6.5.3 Effect of leading-edge fixed droop

Next, the effect of variation of the blade leading-edge fixed droop on the rotor performance characteristics is assessed. The leading-edge fixed droop, FD_{amp}, is representative of the leading-edge morphing blade when at maximum deformation, and remains at the same deformation position for the entire simulation. The leading-

edge fixed droop deformation of the blades was set so that -ve FD_{amp} was achieved at $\psi = 270°$, which was previously shown to be effective in improving rotor performance with leading-edge morphing actuation. This results in +ve FD_{amp} occurring at $\psi = 90°$, which will lead to a nose-up of the leading-edge due to the orientation of the blade. Four different leading-edge fixed droop amplitudes are assessed which include: $FD_{amp} = 5°, 7.5°, 10°$, and $15°$. The leading-edge fixed droop amplitudes were selected based on the same settings used for the leading-edge morphing amplitude analysis. No other changes are applied to the operational conditions and rotor rotational velocity remains constant at $\Omega = 600rpm$.

The phase-averaged cycloidal rotor performance characteristics for both the rigid blade and the leading-edge fixed droop blade with varying FD_{amp} amplitudes is shown in Fig. 6.17. All leading-edge fixed droop amplitudes assessed are shown to have an effect on the rotor performance characteristics at both the rotor upper and lower regions, in comparison to the rigid blade.

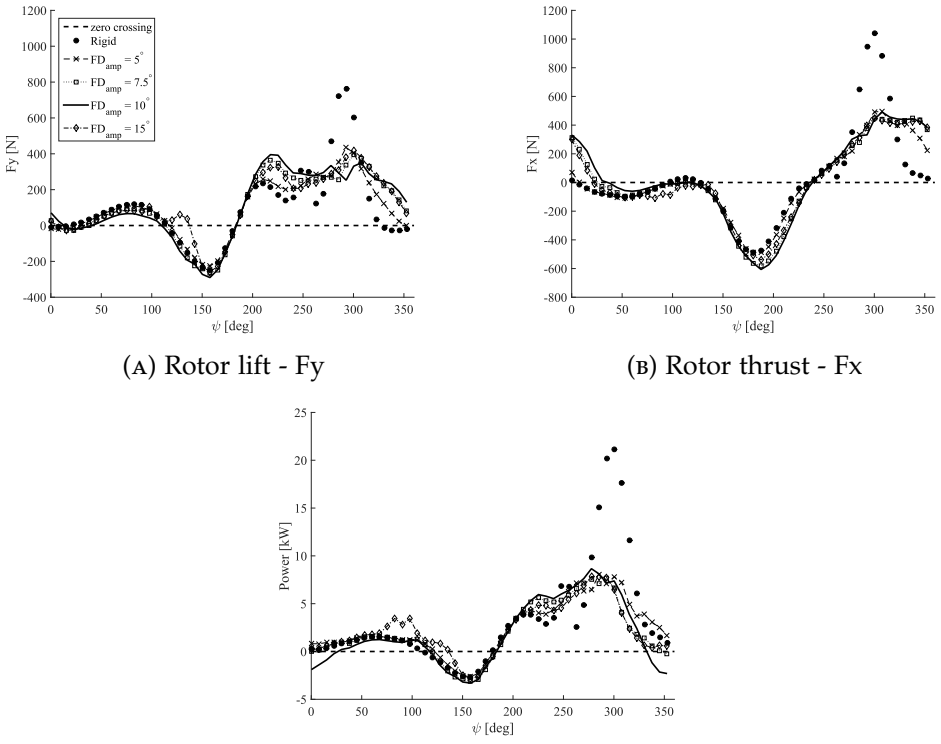

(a) Rotor lift - Fy

(b) Rotor thrust - Fx

(c) Rotor aerodynamic power

Figure 6.17: Phase-averaged cycloidal rotor aerodynamic performance results for a single blade at various FD_{amp} amplitudes. Operational conditions: Ω = 600 rpm, $\psi_{act} = 180°$(-ve). Results are phase-averaged over the last five of the 10 rotation cycles.

The phase-averaged rotor vertical force results in Fig. 6.17a shows that there is a change in the vertical force at both the rotor upper and lower regions when leading-edge fixed droop is applied. At the rotor upper region ($0^\circ \leq \psi \leq 180^\circ$), the peak vertical force reduces for an increase in FD_{amp} between $5^\circ \leq FD_{amp} \leq 10^\circ$ and follows the same vertical force trends as for the rigid blade. At $FD_{amp} = 15^\circ$ however, there is a modification of the vertical force trend as there is a direction reversal of the vertical force at $90^\circ \leq \psi \leq 180^\circ$, which indicates the formation of an LEV. This results in a larger rate reduction of vertical force in comparison to the other FD_{amp} settings. At the rotor lower region $180^\circ \leq \psi \leq 360^\circ$, the implementation of leading-edge fixed droop has a positive effect on the rotor vertical force distribution compared to the rigid blade. At $180^\circ \leq \psi \leq 270^\circ$, the level of increase in the vertical force increases for an increase in the leading-edge fixed droop amplitude for ($5^\circ \leq FD_{amp} \leq 10^\circ$). This means that attached flow is still maintained at the suction surface of the leading-edge fixed droop section, delaying the initiation of the LEV process. At $270^\circ \leq \psi \leq 360^\circ$, there is a significant reduction in the peak positive vertical force for all FD_{amp} amplitudes assessed in comparison to the rigid blade. This implies that the implementation of leading-edge negative fixed droop results in the mitigation of dynamic stall. $FD_{amp} = 10^\circ$ is the only leading-edge fixed droop amplitude to achieve a flat distribution for the vertical force, whereas the other FD_{amp} settings as well as the rigid blade produce an increase in the vertical force where the effects of dynamic stall are significant.

The phase-averaged results for the cycloidal rotor side force generated by both a rigid blade and a leading-edge fixed droop blade with a variation in FD_{amp} is shown in Fig. 6.17b. There is a significant improvement in the side force stability for all FD_{amp} amplitudes assessed in comparison to the rigid blade. This is due to the significant reduction in the peak positive side force generated by the leading-edge fixed droop blade at the right half of the rotor for all FD_{amp} amplitudes assessed. At the left half of the rotor region ($90^\circ \leq \psi \leq 270^\circ$), the side force trends are similar between the rigid and leading-edge fixed droop amplitude settings, however there is an increase in the peak negative side force for all FD_{amp} values assessed. The level of increase in the peak negative side force increases for an increase in FD_{amp} between the range $5^\circ \leq FD_{amp} \leq 10^\circ$.

The phase-averaged results for the cycloidal rotor aerodynamic power generated by both a rigid blade and a leading-edge fixed droop blade with a variation in FD_{amp} is shown in Fig. 6.17c. The effect of applying leading-edge fixed droop to the cycloidal rotor blades is highly effective at the rotor lower region ($180^\circ \leq \psi \leq 360^\circ$), where the effects of dynamic stall and blade-wake interference are significant. It is shown that the large levels of power absorption generated by the rigid blade as a result of the dynamic stall process, is removed for all FD_{amp} amplitudes considered. At the rotor upper region ($0^\circ \leq \psi \leq 180^\circ$), the majority of leading-edge fixed droop amplitudes assessed produce similar aerodynamic power trends compared to the rigid blade results (except at $FD_{amp} = 15^\circ$). At $FD_{amp} = 15^\circ$, there is an increase in the level of

power absorption at approximately $\psi = 90^\circ$ as a result of the physical leading-edge droop (nose-up) exciting the dynamic stall process at the rotor lower region. The remainder of the FD_{amp} cases assessed as well as the aerodynamic power results for the rigid blade do not excite the dynamic stall process at the rotor upper region.

The effect that leading-edge fixed droop has on the cycloidal rotor performance characteristics is further evaluated by assessing the time-averaged cycloidal rotor performance results for both the rigid blade and leading-edge fixed droop blade cases, as shown in Table 6.6. There are improvements in all of the cycloidal rotor performance characteristics assessed for all FD_{amp} amplitudes. The level of increase in PL, DL and C_T increases for an increase in FD_{amp} upto 10 degrees. The level of increase in PL, DL and C_T reduces slightly when increasing the leading-edge fixed droop amplitude from 10° to 15°. The largest performance gains is at the leading-edge fixed droop setting, $FD_{amp} = 10^\circ$, with an increase of 88.54%, 15.22% and 16.39% in PL, DL, and C_T respectively. There is an increase in the direction of the net rotor thrust vector for all FD_{amp} cases assessed against the rigid blade. Furthermore, all leading-edge fixed droop amplitude settings achieved reductions in C_P when compared to the rigid blade results. The level of reduction in C_P increases for an increase in FD_{amp} upto 10 degrees. The level of reduction in C_P decreases slightly when increasing FD_{amp} from 10 degrees to 15 degrees. $FD_{amp} = 10^\circ$ achieves the largest reduction in C_P, equating to 38.89% when compared to the rigid blade rotor.

Case	PL $[N/kW]$	DL $[N/m^2]$	ϕ $[deg]$	C_T [1]	C_P [1]
Rigid	31.82	366	84.25	0.61	0.61
$FD_{amp} = 5^\circ$	38.68	381.79	83.73	0.63	0.52
$FD_{amp} = 7.5^\circ$	54.27	417.34	85.50	0.69	0.41
$FD_{amp} = 10^\circ$	**61.67**	**426.27**	**83.77**	**0.71**	**0.36**
$FD_{amp} = 15^\circ$	51.03	415.27	86.53	0.69	0.43

Table 6.6: Time-averaged performance results for a 4-blade cycloidal rotor with rigid and leading-edge fixed droop blades with a variation in the leading-edge fixed droop amplitude. Results are time-averaged over the last five of the 10 rotation cycles and is at a rotor rotational velocity, Ω = 600 rpm.

Next, a comparison is made between the effects that leading-edge fixed droop and active leading-edge morphing have on the cycloidal rotor performance to highlight any differences in the rotor performance and flowfield characteristics. A comparison is made with the following conditions: $FD_{amp} = \beta_{max} = 15°$, as it was previously shown that the leading-edge fixed droop amplitude of 15 degrees had a detrimental effect on the cycloidal rotor performance at the rotor upper region.

The phase-averaged cycloidal rotor performance characteristics for a rigid blade, leading-edge fixed droop blade, and a leading-edge morphing blade at an amplitude of 15 degrees, is shown in Fig. 6.18. The vertical force results in Fig. 6.18a illustrate several key differences in the load distribution when comparing the results for the leading-edge fixed droop blade against the leading-edge morphing blade. At the rotor upper region ($0° \leq \psi \leq 180°$), the leading-edge morphing result achieves a similar trend in the vertical force distribution compared to the rigid blade result. The leading-edge fixed droop setting of 15 degrees however achieves a deviation of the vertical force distribution due to the excitation of dynamic stall as a result of the nose-up leading-edge droop deflection. At the rotor lower region ($180° \leq \psi \leq 360°$), both the leading-edge fixed droop and leading-edge morphing achieve similar vertical force results such as the removal of the dynamic overshoot and a flatter vertical force distribution.

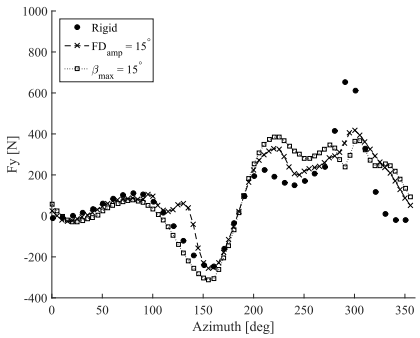

(a) Rotor lift - Fy

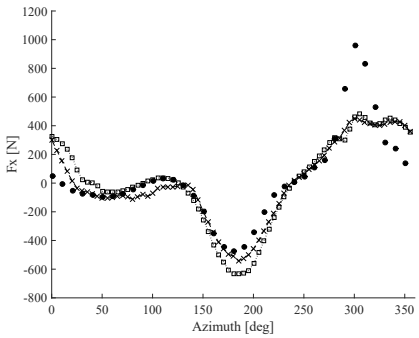

(b) Rotor thrust - Fx

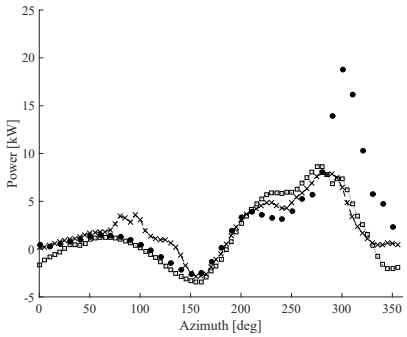

(c) Rotor aerodynamic power

Figure 6.18: Phase-averaged cycloidal rotor aerodynamic performance results comparison between a leading-edge fixed droop blade and a leading-edge morphing blade at a flap amplitude of 15 degrees. Operational conditions: Ω = 600 rpm, $\psi_{act} = 180°$(-ve). Results are phase-averaged over the last five of the 10 rotation cycles.

The phase-averaged cycloidal rotor side force results in Fig. 6.18b shows that the side force distribution trends are similar for the rigid blade, the leading-edge fixed droop blade, and the leading-edge morphing blade at the rotor upper region ($0^\circ \leq \psi \leq 180^\circ$). The morphing blade achieves the largest peak minimum side force result which is due to the reduction in the level of blade-wake interference within the rotor domain. At the rotor lower region ($180^\circ \leq \psi \leq 360^\circ$), both the leading-edge fixed droop and leading-edge morphing blade achieve similar peak positive side force results which are significantly lower than for the rigid blade result.

The phase-averaged rotor aerodynamic power results for the rigid blade, leading-edge fixed droop and leading-edge morphing blade is shown in Fig. 6.18c. The largest difference in rotor performance between the leading-edge fixed droop blade and leading-edge morphing blade is at the rotor upper region ($0^\circ \leq \psi \leq 180^\circ$). At the rotor upper region, it is shown that the leading-edge fixed droop blade generates power absorption as a result of exciting the formation of an LEV and dynamic stall. This does not occur for the leading-edge morphing blade, which follows the same power distribution trends as for the rigid blade. This is mainly due to the fact that there is no morphing actuation when the blade orbits through the rotor upper region. In the rotor lower region ($180^\circ \leq \psi \leq 360^\circ$), both the leading-edge fixed droop blade and leading-edge morphing blade achieve a similar power distribution and similar magnitudes in the peak power absorption. The leading-edge morphing blade achieves a larger level of power extraction near the end of the rotation cycle ($330^\circ \leq \psi \leq 360^\circ$) in comparison to the leading-edge fixed droop blade.

The differences in the rotor performance characteristics between the leading-edge fixed droop blade and the leading-edge morphing blade at a 15 degrees flap amplitude, are further investigated by analysing the flow-field characteristics at the rotor domain. Figure 6.19 illustrates the instantaneous non-dimensional vorticity and velocity scalar plots for both the leading-edge fixed droop and leading-edge morphing blades near the end of the last pitch cycle. Key variations in the flow-field characteristics between both blades are evident when analysing the non-dimensional vorticity plots in Figs. 6.19a and 6.19b. At the rotor upper region ($0^\circ \leq \psi \leq 180^\circ$), there is a formation of a LEV at blade, $B2$, which is due to the nose-up leading-edge fixed droop deflection. This leads to shedding of vortices at the proceeding blade, $B3$, as a result of exciting dynamic stall. This also results in an increase in the level of blade-wake interference at the rotor upper region for the leading-edge fixed droop blade in comparison to the leading-edge morphing blade. At the rotor lower region ($180^\circ \leq \psi \leq 360^\circ$), the level of blade-wake interference is greater for the leading-edge fixed droop blade in comparison to the leading-edge morphing blade. This is due to the shedding of the leading-edge fixed droop blade, $B2$ in Fig. 6.19a which is shown to convect towards the rotor lower region and interacting with blades, $B1$, and $B4$.

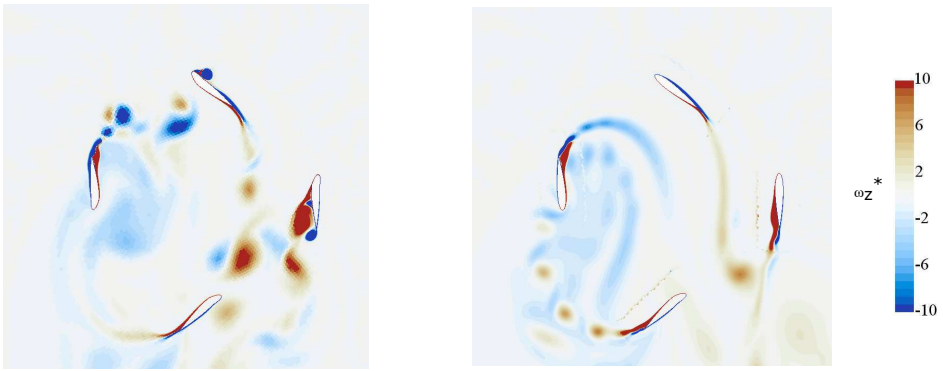

(a) $FD_{amp} = 15°$ (b) $\beta_{max} = 15°$

Figure 6.19: Visualisation of the flow-field characteristics for the cycloidal rotor, comparing FD_{amp} against β_{max} at 15 degrees flap amplitude. Operational conditions: Ω = 600rpm at t/T = 0.935 of 10th cycle. (a-c) - non-dimensional vorticity (($\omega_z^* = \frac{\omega_z c}{V_t}$)). (d-f) - Velocity magnitude (zoomed in). (g-h) - velocity magnitude (zoomed out).

It has been shown that there are key differences in the cycloidal rotor performance when implementing either the leading-edge fixed droop or leading-edge morphing method. The leading-edge fixed droop method offers a simpler solution in terms of manufacture, assembly, and operation while improving on the rotor performance characteristics in comparison to the rigid blade rotor. The leading-edge fixed droop method however, increases the level of blade-wake interference at the rotor upper region due to the physical camber applied which excites dynamic stall. The leading-morphing method is more advantageous as it significantly reduces the level of blade-wake interference at the rotor lower region and improves the rotor performance characteristics in comparison to the rigid blade rotor. The morphing blade also maintains a similar performance profile to the rigid blade at the rotor upper region as no actuation of leading-edge morphing is performed at this region. This results in the leading-edge morphing blade achieving a larger increase in the cycloidal rotor performance characteristics in comparison to the leading-edge fixed droop method. The disadvantage of implementing the leading-edge morphing method to a cycloidal rotor is the manufacturing and operational complexities of utilising a practical morphing system.

6.5.4 Effect of rotor solidity

The final part of this investigation assesses the effect of active leading-edge morphing on the cycloidal rotor performance for different rotor solidity values. The leading-edge morphing amplitude was set to $\beta_{max} = 10°$ as this was deemed to be most effective in terms of improving the rotor performance. Increasing the rotor solidity leads to an increase in the level of blade-wake interference, therefore an assessment will be made to determine the influence that blade-wake interference has on the rotor performance improvements gained by the implementation of leading-edge morphing. The rotor

solidity, σ is defined as:

$$\sigma = \frac{nc}{\pi D} \tag{6.16}$$

where n is the number of blades, c is the blade chord in metres, and D is the rotor diameter in metres.

The rotor solidity is altered by varying the total number of blades between: n = 2, 3, and 4. The rotor diameter and blade chord remain constant as well as the operational parameters such as the blade pitch amplitude and rotor rotational velocity. The blade's initial azimuthal position, ψ_i, is dependent on the rotor solidity, and is calculated using the following expression:

$$\psi_i(0) = \psi_1(0) + \frac{(i-1)2\pi}{n} \tag{6.17}$$

where i determines the position of the current blade relative to the blade azimuth angle of the first blade.

The time-averaged cycloidal rotor performance results for rigid and morphing blades with a variation in rotor solidity is shown in Fig. 6.20. For the majority of rotor solidity cases assessed, the implementation of leading-edge morphing is shown to increase the cycloidal rotor performance in contrast to rigid blades for an increase in rotor rotational velocity. The time-averaged rotor resultant thrust magnitude plot in Fig. 6.20a shows that the rate of increase in T_{res} improves with an increase in both rotor solidity and rotor rotational velocity for the rigid and leading-edge morphing blades. When operating at the larger rotor rotation velocity, Ω = 800 rpm, the largest level of resultant thrust produced is for the morphing 4-blade cycloidal rotor. Furthermore, the same level of resultant thrust is generated by the morphing 3-blade rotor in comparison to the rigid 4-blade rotor for the majority of rotor rotational velocities. This results in improvements in design areas such as the weight savings for the cycloidal rotor. The morphing 2-blade cycloidal rotor is shown to have a decrease in the level of resultant thrust produced when compared to the rigid rotor, implying that blade-wake interference contributes towards enhancing the rotor performance. Finally at the lower rotor rotation speed, Ω = 200 rpm, minimal improvements in the resultant thrust are achieved when leading-edge morphing is implemented for all rotor solidity cases assessed.

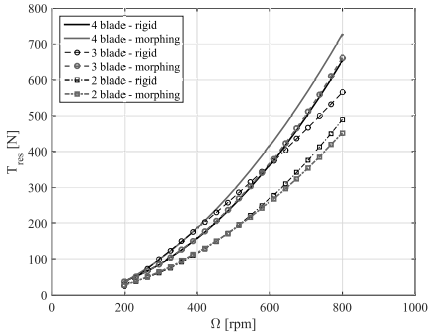

(a) Rotor resultant thrust

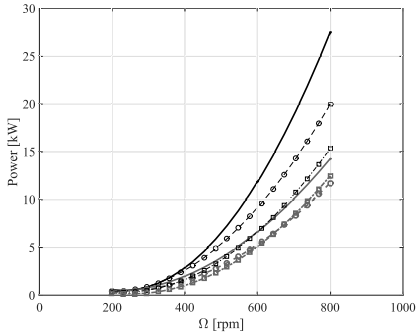

(b) Rotor aerodynamic power

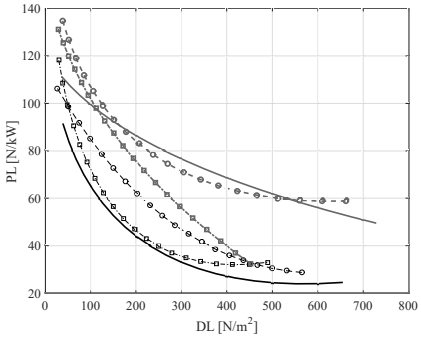

(c) Power-loading v. disk-loading

Figure 6.20: Time-averaged performance results for a 2-blade, 3-blade, & 4-blade cycloidal rotor with rigid and morphing blades. Operational conditions: Ω = 200, 400, 600, 800 rpm. $\beta_{max} = 10^{\circ}$. Results are time-averaged over the last five of the 10 rotation cycles.

The time-averaged aerodynamic power results in Fig. 6.20b illustrate that the level of power absorption increases for an increase in both the rotor rotational velocity and rotor solidity. At the larger rotor rotation velocity, Ω = 800 rpm, the implementation of leading-edge morphing decreases the power dissipated compared to the rigid rotor for all rotor solidity settings assessed. Furthermore, at Ω = 800 rpm, the morphing 4-blade rotor generates less power absorption in comparison to the rigid 2-blade rotor which highlights the significant effectiveness of leading-edge morphing on the cycloidal rotor performance. At the lower rotor rotation velocity, the level of improvements gained with the implementation of leading-edge morphing is minimal in comparison to the rigid rotor for all values of rotor solidity assessed.

Figure 6.20c shows the power-loading and disk-loading curves for both the rigid and morphing 2-blade, 3-blade, and 4-blade cycloidal rotor. For the majority of DL, leading-edge morphing improves on the power loading efficiency compared to the rigid rotors for all rotor solidities assessed. At the lower DL, the highest level of PL generated are for the morphing 2-blade and 3-blade cycloidal rotor. At a set disk-loading, DL = 400 N/m^2, the morphing 3-blade and 4-blade rotor generates a significant increase in the power-loading efficiency in contrast to all other cases assessed. The rigid 4-blade cycloidal rotor was the worst performing case as it

produced the lowest level of power-loading efficiency for the majority of the disk-loading range.

The time-averaged cycloidal rotor performance results for a variation in the rotor solidity and the rotor rotational velocity are presented in Table 6.7. The improvements gained in the power-loading efficiency for the morphing 3-blade and 4-blade rotor in comparison to their rigid counterparts increase for an increase in rotor rotational velocity. Table 6.7 also demonstrates that the effectiveness of leading-edge morphing on the cycloidal rotor performance increases with an increase in rotor solidity as positive improvements are gained in the disk-loading and thrust coefficient, C_T for all rotor rotational velocities assessed. Moreover, all morphing rotor solidity cases assessed are shown to achieve a reduction in C_P as the rotor rotational velocity increases in comparison to the rigid rotor solidity cases. At the higher rotor rotation speed, Ω = 800 rpm, there is a decrease in C_T for the morphing 2-blade rotor in comparison to the rigid 2-blade rotor. This result further confirms that blade-wake interference is a key parameter which contributes towards the cycloidal rotor performance improvements due to the implementation of leading-edge morphing [29].

Case	Ω $[rpm]$	PL $[N/kW]$	DL $[N/m^2]$	ϕ $[deg]$	C_T [1]	C_P [1]
4-blade - rigid	200	92.16	40.35	79.03	0.60	0.63
	400	48.26	155.25	79.04	0.58	0.57
	600	31.82	366.00	84.25	0.61	0.61
	800	23.64	652.74	77.36	0.61	0.61
4-blade - morphing	200	109.77	41.18	84.66	0.61	0.54
	400	91.31	176.83	79.18	0.66	0.35
	600	64.01	427.13	86.67	0.71	0.35
	800	50.79	724.04	81.83	0.67	0.32
3-blade - rigid	200	107.05	33.63	73.85	0.50	0.44
	400	63.02	164.52	84.58	0.61	0.46
	600	42.02	384.97	84.35	0.64	0.48
	800	28.00	558.40	74.92	0.52	0.44
3-blade - morphing	200	137.98	38.67	77.29	0.58	0.40
	400	81.69	158.72	75.58	0.59	0.35
	600	75.80	368.80	82.71	0.61	0.26
	800	55.66	661.23	80.12	0.62	0.26
2-blade - rigid	200	119.44	27.78	97.52	0.41	0.33
	400	62.49	121.88	85.40	0.45	0.35
	600	41.71	263.22	84.45	0.44	0.33
	800	31.84	491.51	86.44	0.46	0.34
2-blade - morphing	200	127.43	27.89	92.02	0.42	0.31
	400	107.62	120.20	82.11	0.45	0.20
	600	51.84	258.33	73.98	0.43	0.26
	800	36.23	453.15	78.30	0.42	0.28

Table 6.7: Time-averaged performance results for a 2-blade, 3-blade, & 4-blade cycloidal rotor with rigid and morphing blades for a variation in the rotor rotational velocity. Results are time-averaged over the last five of the 10 rotation cycles.

The 3-blade and 2-blade cycloidal rotor operating at Ω = 600 rpm is further analysed qualitatively to determine an explanation why the leading-edge morphing has a detrimental effect on the disk loading efficiency. The instantaneous non-dimensional vorticity, ω_z^*, and velocity magnitude scalar plots are visualised in Fig. 6.21. The non-dimensional vorticity plot in Fig. 6.21a illustrates the convection of an LEV and formation of a TEV by the rigid blade, B1. The LEV and TEV wake produced by the proceeding blade, B2 is also shown which interacts with the succeeding blade, B3. In contrast, the non-dimensional vorticity scalar of the morphing 3-blade rotor in Fig. 6.21b illustrates a delay in the formation and convection of a LEV from blade B1. This results in a production of a weaker LEV as shown by the wake of the proceeding blade, B2. Furthermore, the TEV has been prevented from fully forming which decreases the negative pitching moment and therefore improves on the power loading efficiency.

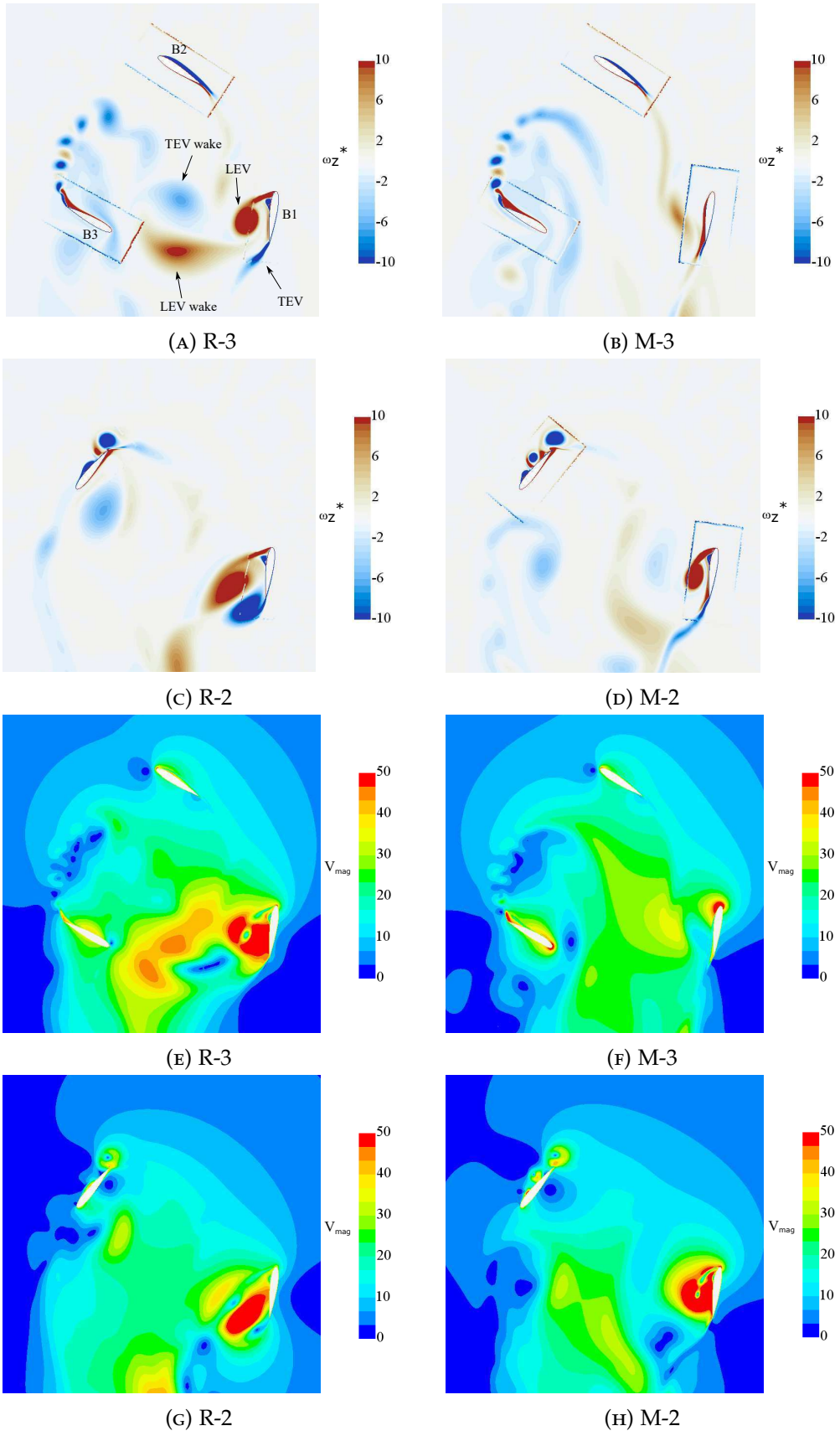

(a) R-3 (b) M-3

(c) R-2 (d) M-2

(e) R-3 (f) M-3

(g) R-2 (h) M-2

Figure 6.21: Visualisation of the flow-field characteristics for the cycloidal rotor with a variation in the rotor solidity and under the operational conditions: Ω = 600rpm at t/T = 0.935 of 10th cycle. (a-d) - non-dimensional vorticity ($\omega_z^* = \frac{\omega_z c}{V_t}$). (e-h) - Velocity magnitude (cycloidal rotor).

Evaluation of the instantaneous non-dimensional vorticity plot for the rigid 2-blade cycloidal rotor in Fig. 6.21c visualises the traditional features of dynamic stall due to the reduction in blade-wake interference. At blade B1, the LEV is fully formed and convects along the blade's lower surface, which leads to the formation of a strong TEV. In contrast, the ω_z^* scalar plot for the morphing 2-blade rotor in Fig. 6.21d demonstrates a delay in the dynamic stall process and a reduction in the size of the LEV due to the implementation of leading-edge morphing. This leads to a reduction in the size and strength of the TEV which is linked to the level of power absorption reduction. The modification of the blade-wake interference effects due to the implementation of leading-edge morphing is therefore the primary reason for the reduction in the disk-loading efficiency in comparison to the rigid 2-blade rotor. Therefore, it can be concluded that by increasing the level of blade-wake interference through increasing the total number of blades of a cycloidal rotor, the rotor's performance is significantly enhanced through the actuation of active, leading-edge morphing at the cycloidal rotor lower region which is dominated by dynamic stall effects.

6.6 CONCLUSIONS

A CFD investigation of a cycloidal rotor with active leading-edge morphing blades has been performed for a rotor operating under hover conditions. The main objective of this study was to evaluate the effect that active leading-edge morphing of the blades in the rotor lower half, where blade-wake interference effects are significant, has on the cycloidal rotor performance characteristics in comparison to a rigid blade rotor. A detailed parametric study was performed which evaluated different parameters relating to leading-edge morphing and cycloidal rotor configurations. A correlation was also made into the performance improvements leading-edge morphing achieves between a single cycloidal rotor orbiting blade and a single pitch-oscillating aerofoil, operating under deep dynamic stall conditions.

Overall, it has been demonstrated that applying active leading-edge morphing to the individual blades of a cycloidal rotor significantly improves the rotor performance characteristics. This is due to achieving dynamic stall alleviation which led to a reduction in the level of blade-wake interference. Determining the optimal blade azimuth angle to initialise leading-edge morphing as well as the direction of droop deflection was crucial in order to successfully achieve an improvement in cycloidal rotor performance. At the lower half of the cycloidal rotor where the effects of blade-wake interference and dynamic stall are more significant, large improvements in rotor performance are gained when leading-edge morphing is initialised at an blade azimuth angle of 180 degrees with negative droop deflection. This was primarily due to the delay and reduction in strength of the LEV which led to a reduction in the level of blade-wake interference acting on the succeeding blade. Applying leading-edge morphing to the upper half of the cycloidal rotor had little influence on the rotor performance characteristics.

When investigating the effect of the leading-edge morphing amplitude, it was shown that all leading-edge morphing amplitudes assessed (between 5 to 15 degrees) improved the cycloidal rotor performance characteristics by achieving reductions in the power coefficient as well as increasing the thrust coefficient. The most effective leading-edge morphing amplitude was 10 degrees, which was due to achieving the largest improvements in the thrust and power coefficient in comparison to the rigid blade rotor. The level of reduction in the power coefficient increased for an increase in the leading-edge morphing amplitude from 5 to 10 degrees. The level of reduction in the power coefficient decreased slightly when increasing the leading-edge morphing amplitude from 10 to 15 degrees. Moreover, all leading-edge morphing amplitudes assessed with the exception of 5 degrees was shown to improve the direction of the resultant thrust vector. A leading-edge morphing amplitude of 5 degrees was unsuccessful in removing the dynamic overshoot and was shown to increase the peak positive vertical force when compared against the rigid blade. This resulted in a small reduction in the thrust coefficient when compared against the rigid blade rotor.

The effect of leading-edge fixed droop was next investigated to assess its effect on the cycloidal rotor performance characteristics as well as to make a comparison between the leading-edge morphing method. All leading-edge fixed droop amplitudes assessed achieved similar levels of improvement (as for the leading-edge morphing method(in the thrust and power coefficient when compared against a rigid blade rotor. The leading-edge morphing method is the preferred option over the leading-edge fixed droop method due to reducing the level of blade-wake interference at the rotor lower half as well as achieving a larger improvement in the rotor performance characteristics. The leading-edge fixed droop method however offers a simpler solution in terms of manufacture, assembly, and operation while improving on the rotor performance characteristics in comparison to the rigid blade rotor. The disadvantage of the leading-edge morphing method is the manufacturing and operational complexities of implementing a practical cycloidal rotor morphing system.

Finally, it was demonstrated that leading-edge morphing was effective in improving the cycloidal rotor performance characteristics for all rotor solidity values assessed. The largest thrust coefficient was achieved by a 4-blade rotor with leading-edge morphing blades. Moreover the 3-blade cycloidal rotor with leading-edge morphing was able to achieve a slightly larger thrust coefficient in comparison to the rigid 4-blade rotor when operating at 800 rpm. All rotor solidity values with leading-edge morphing also achieved significant reductions in the power coefficient when compared against the rigid blade rotor.

The results from the correlation study between a single leading-edge morphing cycloidal rotor blade and a single pitch-oscillating leading-edge morphing aerofoil demonstrated similar key performance trends. The leading-edge morphing cycloidal blade achieved a significant reduction in the drag and moment coefficient during the pitch downstroke when compared against the rigid blade. There was also a

significant reduction in the negative pitch damping loop which has also been previously demonstrated in both the computational and experimental analysis of a single pitch-oscillating aerofoil operating in deep dynamic stall conditions.

Overall, this computational study demonstrated that both the leading-edge morphing and leading-edge fixed droop methods have a positive impact on the cycloidal rotor performance characteristics when compared to a rigid blade rotor. This is due to achieving dynamic stall alleviation at the rotor's lower half which resulted in a reduction in the level of blade-wake interference. This consequently led to an increase in the thrust coefficient and decrease in the power coefficient across the range of rotor rotational velocities and rotor solidity values assessed. The positive effects in aerodynamic performance that leading-edge morphing achieves are also similar for both a single cycloidal rotor blade and a single pitch-oscillating aerofoil.

There are key differences in the cycloidal rotor performance when implementing either the leading-edge fixed droop or leading-edge morphing method. The leading-edge fixed droop method offers a simpler solution in terms of manufacture, assembly, and operation while improving on the rotor performance characteristics in comparison to the rigid blade rotor. The leading-edge fixed droop method however, increases the level of blade-wake interference at the rotor upper region due to the physical camber applied which excites dynamic stall. The leading-morphing method is more advantageous as it significantly reduces the level of blade-wake interference at the rotor lower region and improves the rotor performance characteristics in comparison to the rigid blade rotor. The morphing blade also maintains a similar performance profile to the rigid blade at the rotor upper region as no actuation of leading-edge morphing is performed at this region. This results in the leading-edge morphing blade achieving a larger increase in the cycloidal rotor performance characteristics in comparison to the leading-edge fixed droop method. The disadvantage of implementing the leading-edge morphing method to a cycloidal rotor is the manufacturing and operational complexities of utilising a practical morphing system.

CHAPTER 7

CONCLUSIONS AND RECOMMENDATIONS FOR FUTURE WORK

This chapter summarises the key findings from this study in relation to investigating the effects of leading-edge morphing for both single pitch-oscillating aerofoils and multi-blade cycloidal rotor systems at the large Reynolds number range. Future work recommendations are then discussed in relation to further investigating the effects of active camber change on cycloidal rotor performance.

7.1 CONCLUSIONS

The initial phase of this study was to determine if applying leading-edge morphing to a single pitch oscillating aerofoil has a positive effect in achieving dynamic stall alleviation which leads to improvements in the aerodynamic characteristics. A computational URANS study of a single, pitch-oscillating NACA0015 aerofoil with active leading-edge morphing was performed under deep dynamic stall conditions at a large Reynolds number range $Re > 1{,}000{,}000$. A parametric study was performed to investigate different parameters associated with leading-edge morphing and comparisons were made against a rigid aerofoil.

When compared against the experimental results, the CFD model was shown to accurately predict key flow features of dynamic stall including the lift overshoot, the secondary vortex formation after the primary stall, the drag-rise and the moment stall. There were differences between the computational and experimental findings during the post stall and flow-reattachment stages of the pitch downstroke, which was due to the limitations of using RANS solvers and the choice of turbulence model used. Previous computational studies have shown that modelling transition effects or using a LES model approach can improve the CFD prediction in the post dynamic stall region.

It was shown from the CFD analysis that leading-edge morphing had a significant

effect on the aerodynamic characteristics due to achieving dynamic stall alleviation. There were significant reductions in the time-averaged peak drag and negative moment coefficients for the range of leading-edge morphing amplitudes assessed when compared against the rigid aerofoil. 10 degrees was the most effective leading-edge morphing amplitude setting as it achieved the largest increase in aerodynamic efficiency as well as achieving the largest reductions in Cd_{max} and Cm_{min}.

The leading-edge fixed droop method also achieved similar improvements in the aerodynamic characteristics in comparison to the leading-edge morphing method such as significant reductions in Cd_{max} and Cm_{min}. The rate of decrease in drag during the pitch downstroke was larger for the leading-edge fixed droop aerofoil in comparison to the leading-edge morphing aerofoil due to the lower local incidence at the leading-edge suction surface of the leading-edge fixed droop aerofoil. Moreover, the general aerodynamic characteristics of the leading-edge fixed droop blade are different when compared to the rigid NACA0015 aerofoil throughout the entire pitch cycle which was due to the implemented physical camber change; the leading-edge morphing aerofoil achieved similar aerodynamic characteristics as the rigid aerofoil for approximately half of the pitch cycle.

Variation of the proportion of aerofoil chord which had leading-edge morphing applied had a significant impact on the aerofoil's aerodynamic characteristics. The level of reduction in the time-averaged peak drag and negative moment coefficients increased for an increase in the proportion of aerofoil chord with leading-edge morphing applied.

The improvements in the aerodynamic characteristics achieved by leading-edge morphing was also effective when assessing a variation in the reduced frequency. The largest increase in the aerodynamic efficiency was achieved at the highest reduced frequency value of 0.153, which was due to achieving the largest decrease in the drag polar hysteresis loop. An increase in the reduced frequency also resulted in a delay of LEV formation. The delay in the lift stall lead to an increase in the peak drag and moment coefficients during the pitch downstroke.

The next phase of this study was to assess whether the effect of leading-edge morphing on the aerodynamic characteristics for a single pitch oscillating aerofoil can also be captured in an equivalent experimental leading-edge flap model. Dynamic stall wind tunnel testing of a NACA0015 aerofoil section with an active leading-edge flap was performed to validate the effects of leading-edge morphing from the CFD model developed in Chapter 3. A leading-edge flap section of 15 % chord was manufactured as it was shown from the computational results to mitigate the negative effects of dynamic stall while reducing the actuator forces required to maintain and control the flap with the available hardware.

The results from the static motion analysis showed that there was flow leakage within the volume of the leading-edge flap which had a significant effect on the

surface pressure measurements. This was primarily due to the leakage of negative pressure from the aerofoil's suction surface. The effect of flow leakage increased for an increase in incidence, which resulted in larger offsets in the measured stagnation pressure. The effect of flow leakage was mitigated by blocking the specific blocking transducer ports which generated the largest offsets. Wind tunnel blockage effects were shown to be more prominent at the larger incidence angles, however its effect on the measured aerodynamic force and moment coefficients are small when compared against the uncorrected results. There was also a delay in the static stall onset angle when comparing the experiment method against the CFD method. A possible reason for the delay in the static stall onset angle for the leading-edge flap model could be due to airflow passing through the recess section between the leading-edge flap and aerofoil section. It has been shown in previous experimental studies that airflow in leading-edge slots from the pressure side to the suction side can lead to a delay in the static and dynamic stall.

For the attached dynamic flow cases, there was a good agreement in the lift and moment coefficients when comparing the measured experimental results against the predicted computational results for both reduced frequency cases. There was a poorer agreement in the drag coefficient however due to the effect of flow leakage at the larger incidence angles from the experiment.

For the light dynamic stall cases, active leading-edge morphing was shown to reduce the level of aerodynamic hysteresis for all leading-edge morphing amplitudes assessed. The largest reduction in the peak negative moment coefficient was achieved at a leading-edge morphing amplitude of 10 degrees. The effect of leading-edge fixed droop was shown to reduce the aerodynamic hysteresis loops for all amplitudes assessed, however there was an overall change to the aerodynamic characteristics at the lower incidence angles. This was due to the implementation of the physical camber modification. An increase in the reduced frequency resulted in an increase in performance gains for both the leading-edge morphing and leading-edge fixed droop methods, with greater reductions achieved for Cd_{max} and Cm_{min}.

There was a poor agreement between the computational and experimental results for the dynamic light stall cases. The computational results predicted the full formation of the LEV which resulted in a significant loss of lift as well as a significant increase in the drag-rise and negative moment coefficient. These dynamic stall flow features were not captured from the experiment which could be due to the delay in stall from flow leakage through the leading-edge flap recess.

For the deep dynamic stall cases, leading-edge morphing demonstrated to have a significant effect in alleviating the negative effects of dynamic stall for all leading-edge morphing amplitudes assessed. It was also shown that activating leading-edge morphing within the first half of the pitch cycle reduced the level of hysteresis effects and the negative pitch damping loop, whilst achieving similar aerodynamic characteristics as the rigid NACA0015 aerofoil in the second half of the pitch cycle when leading-edge

morphing was deactivated. Leading-edge fixed droop also had a similar effect as leading-edge morphing on alleviating the negative effects of dynamic stall when compared against the rigid aerofoil. It was shown however that the leading-edge fixed droop method produced an overall change to the aerodynamic characteristics in comparison to the NACA0015 aerofoil, which was due to the implementation of a physical camber modification. An increase in the reduced frequency resulted in a larger decrease in Cd_{max} and Cm_{min} for both the leading-edge morphing and leading-edge fixed droop methods.

There was a good agreement in the average ΔCl, ΔCd, and ΔCm between the computational and experimental results for leading-edge morphing amplitudes $10 \leq \beta_{max} \leq 15$ degrees. There was also a good agreement between both the leading-edge morphing and leading-edge fixed droop methods when assessing the curve trend reductions in the maximum ΔCd. However, there was a poorer agreement between the experimental and computational results when comparing the maximum ΔCl and minimum ΔCm. This was primarily due to the computational results predicting the full formation of a primary LEV for the rigid aerofoil, and was mitigated by both the leading-edge morphing and leading-edge fixed droop methods. The experimental results for the rigid aerofoil did not capture the full formation of the primary LEV, and it was shown that both leading-edge flap methods maintained attached flow until the start of the pitch downstroke. This led to an increase in the maximum lift coefficient.

In summary, the experiment and CFD methods both capture similar effects of leading-edge morphing and leading-edge fixed droop for an aerofoil operating under deep dynamic stall conditions. Both leading-edge flap methods achieve significant reductions in the time-averaged and peak drag and negative moment coefficients in comparison to the rigid aerofoil. There is also a significant reduction in the negative pitch damping loop and the transition from negative to positive damping occurs earlier for both leading-edge flap methods. Moreover, both the experiment and CFD methods show that leading-edge morphing can maintain similar aerodynamic characteristics to the rigid aerofoil when morphing is inactive. Both methods also show that applying leading-edge fixed droop results in an overall change to the aerodynamic characteristics when compared to the rigid NACA0015 aerofoil.

The next phase of this study involved a correlation study between a single leading-edge morphing cycloidal rotor blade and a single pitch-oscillating leading-edge morphing aerofoil to assess whether there were similar performance trends associated to leading-edge morphing. The main findings from this study showed that there were similar performance trends in leading-edge morphing between both scenarios. The leading-edge morphing cycloidal blade achieved a significant reduction in the drag and moment coefficient during the pitch downstroke in comparison to the rigid blade. There was also a significant reduction in the negative pitch damping loop which has also been demonstrated previously in both the computation and experimental analysis of a single pitch-oscillating aerofoil operating in deep dynamic stall conditions.

The final phase of this study investigated whether applying active leading-edge morphing to a cycloidal rotor system has a significant impact on rotor performance at the region where blade-wake interference effects are significant. A computational URANS investigation of a multi-blade cycloidal rotor with active leading-edge morphing was performed to evaluate the effect of leading-edge morphing on the rotor performance under hover conditions. The main finding from this study confirmed that leading-edge morphing has a significant positive effect on the cycloidal rotor performance as a result of achieving dynamic stall alleviation which leads to an improvement in both the power-loading and disk-loading efficiency.

When assessing the rotor azimuth angle to initialise the pulsed leading-edge morphing motion, it was found that an azimuth angle of 180 degrees and with a negative droop deflection was the most effective setting. At this setting, there was a significant reduction in the rotor's peak vertical-force at the lower half of the rotor where blade-wake interference effects are significant, which resulted in a flatter lift distribution. There was also a reduction in the side-force instability as there was a significant reduction in the positive peak side-force generated at the right half of the rotor.

The effect of the leading-edge morphing amplitude was initialised at a blade azimuth angle of 180 degrees with negative droop deflection was also assessed. There were significant improvements in the power-loading efficiency and power dissipation reductions for all leading-edge morphing amplitudes assessed in comparison to the rigid blade rotor. All leading-edge morphing amplitudes assessed with the exception of 5 degrees were shown to improve the disk-loading characteristics as well as the direction of the resultant thrust vector. This was due to the fact that the 5 degree leading-edge morphing amplitude was unsuccessful in removing the dynamic vertical force overshoot feature in the rotor's lower half and was shown to increase the peak rotor positive vertical-force compared to the rigid blade. This also resulted in an increase in the side-force instability in comparison to the rigid blade.

Applying leading-edge fixed droop to the cycloidal rotor blades resulted in a modification of the rotor performance throughout the entire rotor azimuth domain. At the largest leading-edge fixed droop amplitude assessed (15 degrees), there was a fluctuation of the blade's vertical force distribution which resulted in the formation of a LEV at the cycloidal rotor's upper half. This was due to the orientation of the blade resulting in negative physical camber which caused an initiation of dynamic stall. This flow mechanism was not predicted by the other leading-edge fixed droop amplitudes as well as the leading-edge morphing amplitudes and the rigid aerofoil cases. The leading-edge morphing method is the preferred option over the leading-edge fixed droop method due to effectively reducing the level of blade-wake interference in the rotor's lower half, as well as maintaining similar performance as the rigid blade at the rotor's upper half.

A variation in the solidity of the cycloidal rotor showed that the largest amount

of resultant thrust generated at the highest rotor rotational speed assessed (800 rpm) was the 4-blade cycloidal rotor with leading-edge morphing. Moreover, the 3-blade cycloidal rotor with leading-edge morphing blades produced the same amount of resultant thrust in comparison to a rigid 4-blade cycloidal rotor over the range of rotor rotational velocities assessed. The 2-blade cycloidal rotor with leading-edge morphing blades was shown to reduce the level of resultant thrust generated in comparison to the rigid 2-blade cycloidal rotor which indicated that blade-wake interference can also contribute towards improving the performance characteristics of the cycloidal rotor. All rotor solidity values assessed demonstrated a reduction in the power coefficient across the rotor rotational velocity range when leading-edge morphing was applied to the blades.

Overall, this study demonstrated that both the leading-edge morphing and leading-edge fixed droop methods have a positive impact on both a single pitch oscillating aerofoil and a cycloidal rotor's performance characteristics. This is due to achieving dynamic stall alleviation which resulted in a significant reduction in the drag and negative moment coefficients generated by the blade. For the cycloidal rotor configuration, this consequently led to an increase in the thrust coefficient and decrease in the power coefficient across the range of rotor rotational velocities and rotor solidity values assessed. The positive effects in aerodynamic performance that leading-edge morphing achieves are also similar for both a single cycloidal rotor blade and a single pitch-oscillating aerofoil.

7.2 RECOMMENDATIONS FOR FUTURE WORK

With respect to the current study, the following areas are proposed for future work:

- Investigation of three-dimensional effects of cycloidal rotors with active leading-edge morphing blades. The current study was restricted to two-dimensional CFD modelling, which assessed the effects of active leading-edge morphing on the cycloidal rotor performance. The effects of the parallel blade vortex interaction can be predicted well using two-dimensional modelling, however the spanwise effects of dynamic stall as well the tip vortices are neglected, which have been shown in previous studies to affect the prediction of the cycloidal rotor's side-force.
- Design and develop a cycloidal rotor blade with a leading-edge compliant mechanism. This would require an optimisation method to optimally design the internal structure of the compliant mechanism which considers many factors such as: compliant mechanism boundary conditions/restrictions, the input force required to actively deform the compliant mechanism, location of the input force, the external force required to hold the shape of the compliant mechanism when it is not required to be deformed, and positioning of the beam element connections. Selecting actuators to supply the input force can prove to be difficult due to the restricted space available for the cycloidal blades, however potential, small-scale

smart actuators which could be implemented include shape memory alloys and piezo-electric actuators.

- Perform a fluid-structure interaction study of cycloidal rotor blades with active compliant leading-edge mechanism structures. This would follow on from the idea discussed previously. A co-simulation study can be performed using the commercial CFD package STAR-CCM+ and the commercial FEA package Abaqus. When performing a co-simulation study, at each time-step, the pressure forces acting on the surface of the cycloidal rotor blades would be transferred from the CFD solver to the FEA solver, which in return would determine the stress, strain, and displacements exerted on the blade's structure. The morphing schedule of the compliant mechanism would be modelled in Abaqus, with the active output displacements transferred over to the CFD solver.
- Wind-tunnel testing of a cycloidal rotor with active camber blades. This would be essential in validating the results from the computational study which modelled the cycloidal rotor performance characteristics with active leading-edge morphing. Force and moment measurements can be performed using a load balance and flowfield measurements can be performed using PIV to visualise the alterations to the blade-wake interference with active camber blades. As previously discussed, the difficulty will be designing the active camber blade system due to the restricted spacing within the cycloidal rotor blade's structure.

APPENDIX A

CAD MODEL DESIGN - BILL OF MATERIALS

This section provides details about the bill of materials associated to the CAD model design discussed in Section 4.3. The bill of materials is presented in Table A.1.

Item no.	Section	Part name	Quantity/Material
1	Aerofoil	Spar	1/Aluminium alloy
2	Aerofoil	Skin	2/Fibreglass
3&4	Aerofoil	Outer rib	4/Sika block M945
5	Aerofoil	Inner rib	4/Sika block M945
6	Leading-Edge flap	Skin	2/Fibreglass
7	Leading-Edge flap	Outer rib	4/Sika block M945
8	Leading-Edge flap	Inner rib	4/Sika block M945
9	External	Taper roller bearing	2/Stock
10	External	Linear actuator	1/Stock
11	External	Servo rod	1/Stock
12	Leading-Edge flap	Shaft	1/Stainless steel
13	External	Shaft collar	2/Stock
14	External	Moment arm	1/Aluminium alloy
15	External	Moment arm - slider connection	1/Aluminium alloy
16	External	Clevis end rod	1/Stock
17	External	Moment arm -dowel pin	1/Stock
18&19	External	End plate	4/Plywood
20	Aerofoil	Rectangular insert	2/Aluminium alloy
21	External	Actuator support - bottom	1/Aluminium alloy
22	External	Actuator support - top	1/Aluminium alloy
23	External	Actuator support - shaft connection	2/Aluminium alloy
24	External	End disk	2/Steel(En.32 or similar)
25	Wing model fabrication	Leading-edge flap mold	2/Sika block M330
26	Wing model fabrication	Aerofoil section mold	2/Sika block M330

Table A.1: Leading-edge flap model bill of materials.

APPENDIX B

PRESSURE MEASUREMENTS - FORCE AND MOMENT COEFFICIENT DERIVATION

This section provides the derivation process of the lift coefficient, C_l, drag coefficient, C_d, and moment coefficient, C_m, which is based on the pressure coefficient, Cp. This derivation process supports the analysis performed in Section 4.6.

The time-averaged pressure results produced by the pressure transducers can be transformed and integrated to calculate the normal and axial components of force produced by the aerofoil. The normal and axial force coefficients and be determined through integration over the aerofoil in the chord-wise coordinate system, as shown in Fig. B.1. The tangential force (shear) component is not considered as it's contribution towards the total force production is small in comparison to the pressure force component [34]. Consider element 1 on the aerofoil, ds_u, in Fig. B.1, which has a normal pressure acting on the panel, Cp_u. Note: $_u$, is defined at the upper surface and, $_l$, is defined at the lower surface.

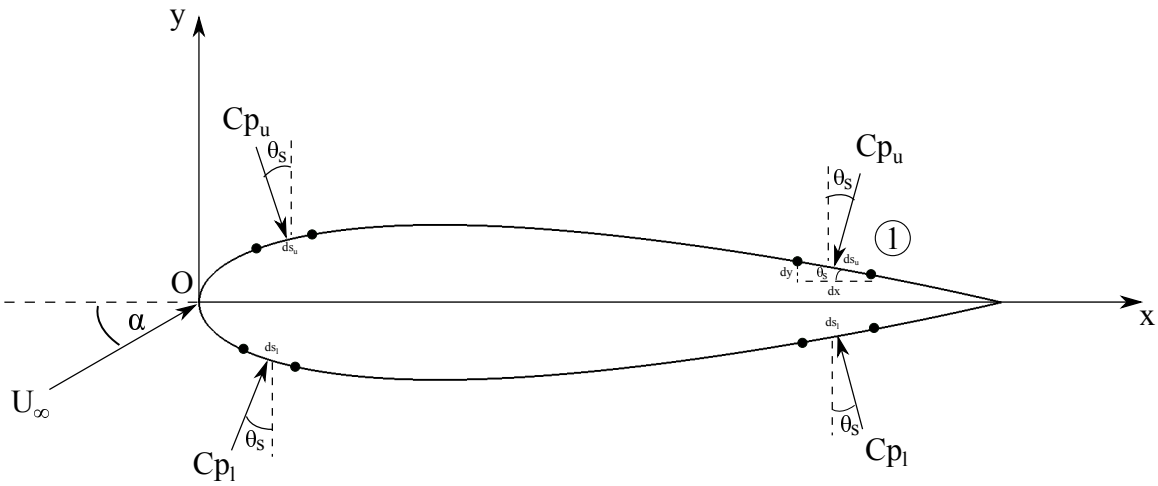

FIGURE B.1: Chord-wise pressure coefficient distribution coordinate system. Note: integration of the aerofoil panels are performed in the anti-clockwise direction, beginning at the trailing-edge's upper surface.

The normal force coefficient, Cn, and the axial force coefficient, Ca, acting on the panel can be determined as follows:

$$\begin{aligned} C_n &= -C_p \frac{ds}{c} cos(\theta_s) \\ C_a &= -C_p \frac{ds}{c} sin(\theta_s) \end{aligned} \tag{B.1}$$

where θ_s, is the angle of the panel on the aerofoil model, ds is the panel length in metres, and c is the aerofoil chord in metres.

The panel, ds_u, can be split into component form as follows:

$$\begin{aligned} dx &= cos(\theta_s) ds \\ dy &= sin(\theta_s) ds \end{aligned} \tag{B.2}$$

Note: the sign convention for dx in eq. (B.1) is negative on the aerofoil's upper surface and positive on the lower surface due to the sign convention. By substituting eq. (B.2) into eq. (B.1), the normal and axial force coefficients can be determined through chord-wise integration in the anti-clockwise direction as follows:

$$C_n = \oint_C C_{p_{av}} d\frac{x}{c} \tag{B.3}$$

$$C_a = -\oint_C C_{p_{av}} d\frac{y}{c} \tag{B.4}$$

where Cp_{av}, dx, and dy, are expressed as:

$$\begin{aligned} C_{p_{av}} &= 0.5(C_p(i) + C_p(i+1)) \\ dx &= x(i+1) - x(i) \\ dy &= y(i+1) - y(i) \end{aligned} \tag{B.5}$$

The lift coefficient, Cl, and drag coefficient, Cd, for the aerofoil can be determined through consideration of the incidence angle, α, as well as Cn and Ca:

$$C_l = C_n cos(\alpha) - C_a sin(\alpha) \tag{B.6}$$

$$C_d = C_n sin(\alpha) + C_a cos(\alpha) \tag{B.7}$$

The pitching moment coefficient, Cm, generated by the aerofoil can also be determined from the surface pressure distribution. Figure B.2 illustrates the coordinate

system defined for the moments acting on the aerofoil about the leading-edge and at the quarter chord respectively.

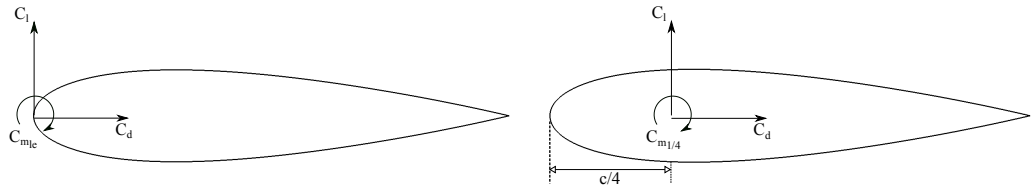

(a) Moment about the leading-edge (b) Moment about the quarter chord

Figure B.2: Moment coefficient coordinate system at specific aerofoil locations.

The moment coefficient acting about the aerofoil's leading-edge can be determined as follows:

$$C_{m_{LE}} = -\oint_C C_{p_{av}} (\frac{x}{c})_{av} d\frac{x}{c} \tag{B.8}$$

Once Cm_{LE} has been calculated, the moment about the quarter chord, $Cm_{1/4}$, can be easily obtained using:

$$C_{m_{c/4}} = C_{m_{LE}} + \frac{C_l}{4} \tag{B.9}$$

Equations (B.6 to B.9) are used to assess the accuracy of interpolation for the uniform, cosine, and the user-defined pressure transducer arrangement configurations in comparison to the computed CFD pressure distribution.

APPENDIX C

PRESSURE TRANSDUCER POSITIONING LIST

The positions of the pressure transducers which are installed in the leading-edge flap model is shown in Table C.1.

Transducer number	x/c	Surface	Part	Transducer number	x/c	Surface	Part
1	0.990	upper	aerofoil	28	0.004	lower	leading-edge flap
2	0.930	upper	aerofoil	29	0.018	lower	leading-edge flap
3	0.889	upper	aerofoil	30	0.035	lower	leading-edge flap
4	0.847	upper	aerofoil	31	0.050	lower	leading-edge flap
5	0.800	upper	aerofoil	32	0.076	lower	leading-edge flap
6	0.750	upper	aerofoil	33	0.125	lower	leading-edge flap
7	0.715	upper	aerofoil	34	0.400	lower	aerofoil
8	0.680	upper	aerofoil	35	0.500	lower	aerofoil
9	0.638	upper	aerofoil	36	0.600	lower	aerofoil
10	0.596	upper	aerofoil	37	0.705	lower	aerofoil
11	0.549	upper	aerofoil	38	0.800	lower	aerofoil
12	0.500	upper	aerofoil	39	0.889	lower	aerofoil
13	0.440	upper	aerofoil	40	0.971	lower	aerofoil
14	0.400	upper	aerofoil	/	/	/	/
15	0.380	upper	aerofoil	/	/	/	/
16	0.136	upper	leading-edge flap	/	/	/	/
17	0.121	upper	leading-edge flap	/	/	/	/
18	0.100	upper	leading-edge flap	/	/	/	/
19	0.083	upper	leading-edge flap	/	/	/	/
20	0.066	upper	leading-edge flap	/	/	/	/
21	0.051	upper	leading-edge flap	/	/	/	/
22	0.035	upper	leading-edge flap	/	/	/	/
23	0.018	upper	leading-edge flap	/	/	/	/
24	0.01	upper	leading-edge flap	/	/	/	/
25	0.006	upper	leading-edge flap	/	/	/	/
26	0.004	upper	leading-edge flap	/	/	/	/
27	0.002	upper	leading-edge flap	/	/	/	/

Table C.1: Chord-wise co-ordinates of pressure transducers.

APPENDIX D

EXPERIMENTAL METHODOLOGY SUPPLEMENT

D.1 MEASUREMENT UNCERTAINTY

This section presents the measurement uncertainty results for the instrumentation utilised in this study. The average relative measurement uncertainty, ϵ_{av} is defined as follows:

$$\epsilon_{av} = \frac{X_{sd}}{X_{mean}} \tag{D.1}$$

Where X_{sd} is the standard deviation of a general parameter and X_{mean} is the mean value of a general parameter. The average relative measurement uncertainty results are presented in Table D.1. Visualisations of the filtered data used to perform measurement uncertainty calculations for all instrumentation listed in Table D.1 are shown in Figs D.1 to D.8.

Instrumentation time (Wind tunnel/model)	Parameter	Motion (Static/Dynamic)	ϵ_{av} [%]
Wind tunnel	Thermostat (T_{static})	Static	0.0694
Wind tunnel	Pitot-tube (P_{total})	Static	0.0013
Wind tunnel	Micro-manometer (q)	Static	0.1748
Model	Hydraulic actuator (α)	Static	0.04696
Model	Linear servomotor (β_{max})	Dynamic	1.793
Model	Cp (Cn/Ca)	Static	[0.5290/2.9610]
Model	Cp (Cn/Ca)	Dynamic	[2.6089/74.5841]
Model	Cp $(Cl/Cd/Cm)$	Dynamic	[2.72/4.13/6.7]

TABLE D.1: Average relative measurement uncertainty results.

D.1.1 WIND TUNNEL INSTRUMENTATION

STATIC TEMPERATURE

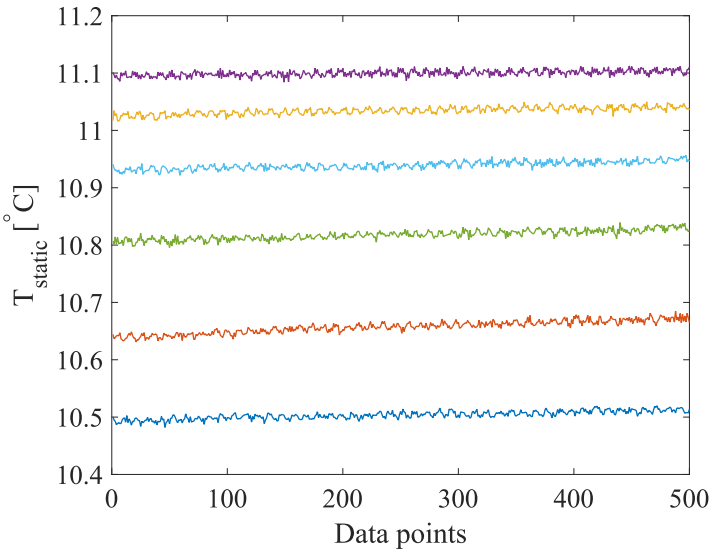

FIGURE D.1: Filtered static temperature measurement points.

TOTAL PRESSURE

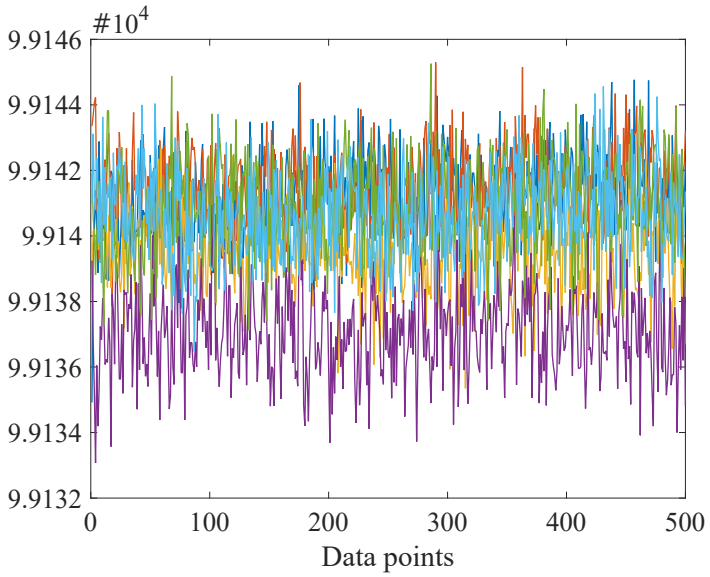

FIGURE D.2: Filtered total pressure measurement points.

DYNAMIC PRESSURE

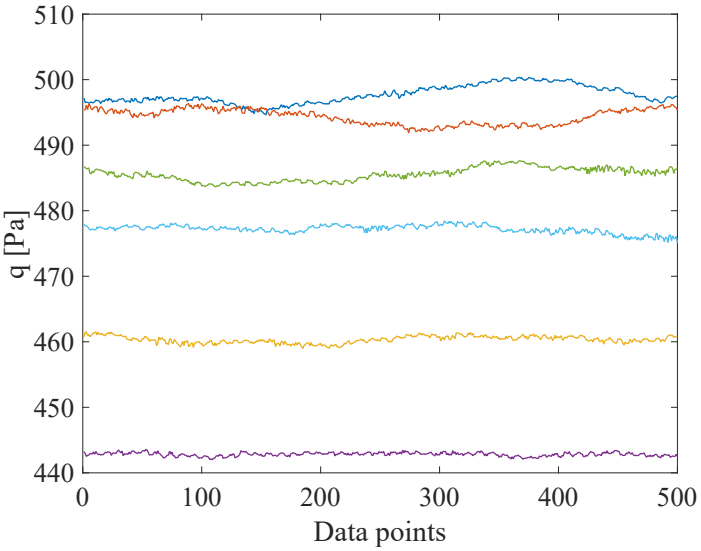

FIGURE D.3: Filtered dynamic pressure measurement points.

D.1.2 MODEL INSTRUMENTATION

INCIDENCE ANGLE

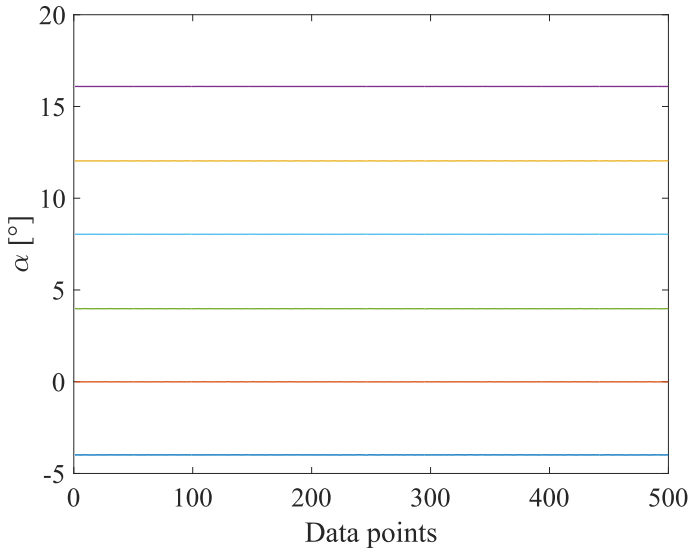

FIGURE D.4: Filtered static incidence angle measurement points.

LINEAR SERVOMOTOR ACTUATOR

Operational conditions:

- $\alpha_M = 16^\circ$, $\alpha_{amp} = 10^\circ$, k = 0.1021.
- $\beta_{max} = 10^\circ$

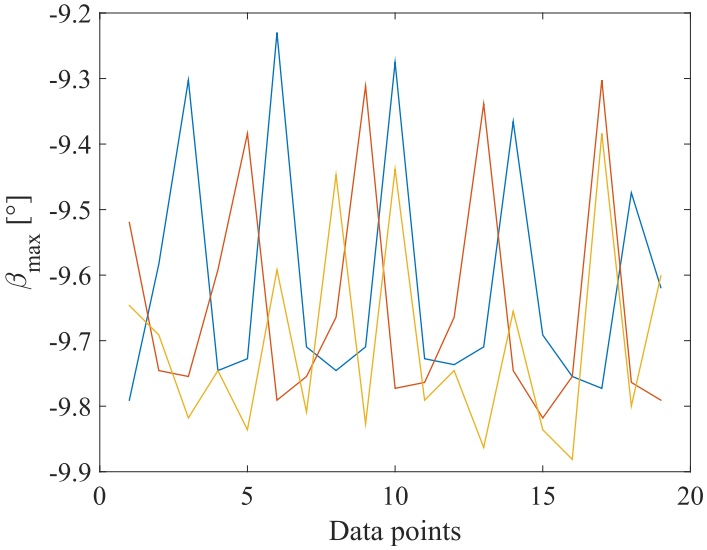

FIGURE D.5: Filtered static leading-edge morphing amplitude points.

SURFACE PRESSURE MEASUREMENTS - CN, CA

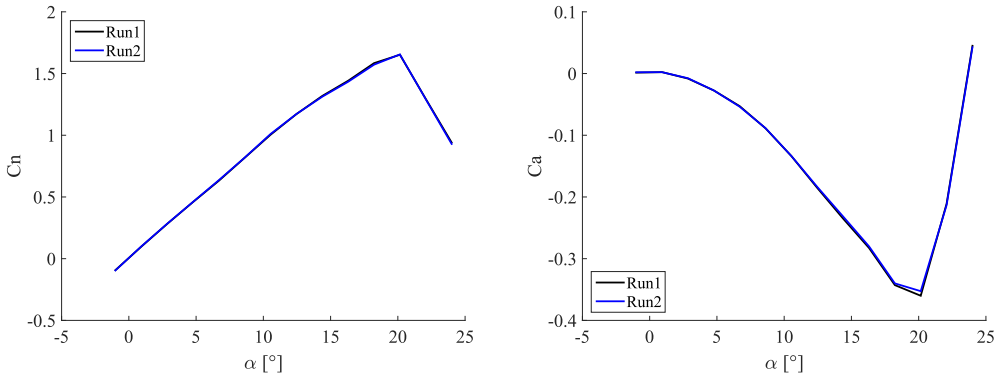

(A) Normal force coefficient (B) Axial force coefficient

FIGURE D.6: Filtered static normal and axial force measurement points.

Operational conditions:

- $\alpha_M = 16°$, $\alpha_{amp} = 10°$, k = 0.1021.
- $\beta_{max} = 0°$

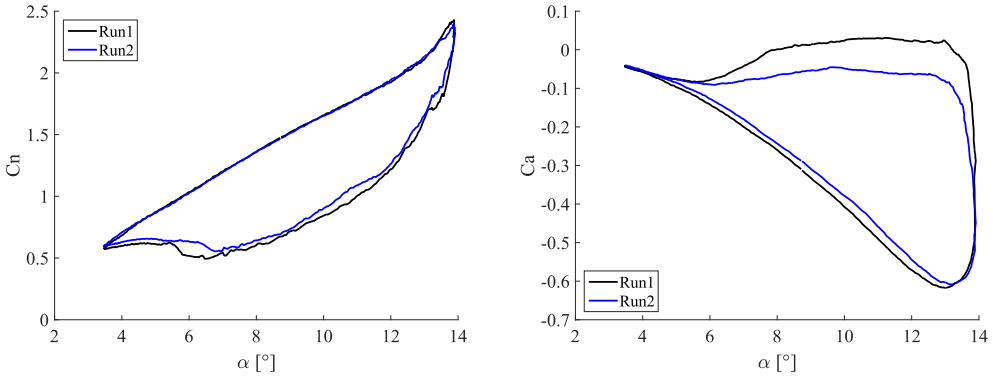

(A) Normal force coefficient (B) Axial force coefficient

FIGURE D.7: Filtered static normal and axial force measurement points.

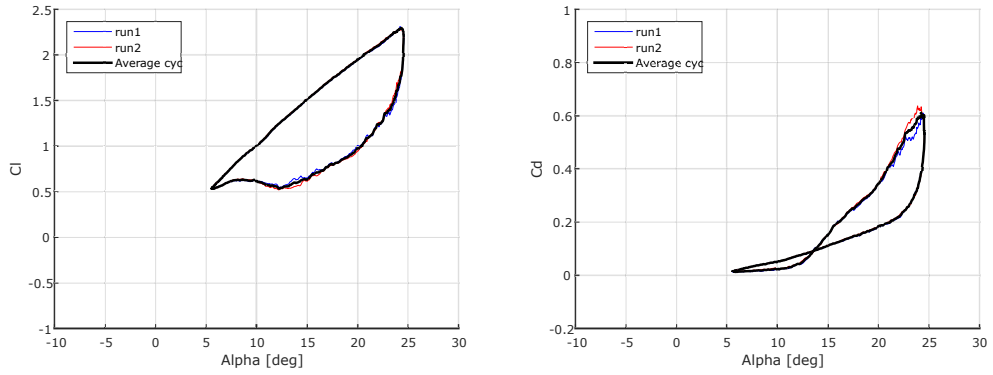

(A) Lift coefficient (B) Drag coefficient

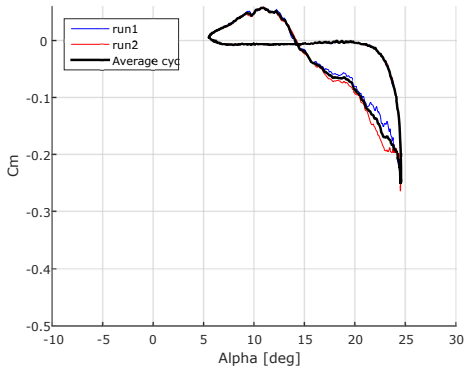

(C) Moment coefficient

FIGURE D.8: Filtered dynamic force and moment measurement points.

APPENDIX E

LIST OF PUBLICATIONS

The contents of this dissertation have been partially published, or in the process of being published, and presented in related conferences.

E.1 JOURNAL PUBLICATIONS

- Ferrier, L., Vezza, M., Zare-Behtash, H., Improving the aerodynamic performance of a cycloidal rotor through active compliant morphing, Aeronautical Journal, Vol 121, Issue 1241, 2017.
- Ferrier, L., Vezza, M., Zare-Behtash, H., Effect of Active Leading-Edge Morphing for a Single Pitch-Oscillating Cycloidal Rotor Blade, Under preparation for submission, Aeronautical Journal.
- Ferrier, L., Vezza, M., Zare-Behtash, H., Improving the Performance Characteristics of a Cycloidal Rotor in Hover through Active Leading-Edge Morphing, Under preparation for submission, Aeronautical Journal.

E.2 CONFERENCE PRESENTATIONS

- Ferrier, L., Vezza, M., Zare-Behtash, H., Improving the aerodynamic performance of a cycloidal rotor through active compliant morphing, Applied Aerodynamics RAeS conference, Bristol, UK, 2016.
- Ferrier, L., Vezza, M., Zare-Behtash, H., Compliant Mechanisms for Improved Aerodynamic Performance Characteristics of Cycloidal Rotors, 26th Scottish Fluid Mechanics Meeting, Edinburgh, UK, 2016.

BIBLIOGRAPHY

[1] M. Benedict, T. Jarugumilli, and I. Chopra, "Effects of Asymmetric Blade-Pitching Kinematics on Forward-Flight Performance of a Micro-Air-Vehicle-Scale Cycloidal-Rotor," *Journal of Aircraft*, vol. 53, no. 5, 2016.

[2] E. Shrestha, D. Yeo, M. Benedict, and I. Chopra, "Development of a meso-scale cycloidal-rotor aircraft for micro air vehicle application," *International Journal of Micro Air Vehicles*, vol. 9, no. 3, pp. 218–231, 2017.

[3] C. Y. Yun, I. K. Park, I. S. Hwang, and S. J. Kim, "Thrust Control Mechanism of VTOL UAV Cyclocopter with Cycloidal Blades System," *Journal of Intelligent Material Systems and Structures*, vol. 16, no. 11-12, pp. 937–943, 2005.

[4] M. Habibnia and J. Pascoa, "ANN assisted flow modeling and analysis for a cyclorotor in ground effect," *Aerospace Science and Technology*, vol. 95, pp. 105–495, 2019.

[5] Y. Hu, H. L. Zhang, and G. Wang, "Two-dimensional and three-dimensional numerical simulations of cycloidal propellers in hover," *Journal of Aerospace Engineering* vol. 232, no. 7, pp. 1223–1234, 2018.

[6] M. L. Mcnabb, *Development of a Cycloidal Propulsion Computer Model and Comparison with Experiment*. PhD thesis, Mississippi State University, 2001.

[7] C. M. Xisto, J. Leger, and J. C. Pascoa, "Parametric Analysis of a Large-scale Cycloidal Rotor in Hovering Conditions," *ASCEs Journal of Aerospace Engineering*, vol. 30, no. 1, pp. 1–14, 2016.

[8] H. Sachse, "Kirsten-Boeing Propeller," *Technical Memorandums, National Advisory Committee for Aeronautics*, vol. TM No.351, 1926.

[9] C. B. Strandgren, "The Theory of the Strandgren Cyclogiro," *Technical Memorandums, National Advisory Committee for Aeronautics*, vol. TM No. 727, 1933.

[10] J. Wheatley, "Simplified Aerodynamic Analysis of the Cyclogiro Rotating-Wing System," *Technical Notes, National Advisory Committee for Aeronautics*, vol. TN No. 467, 1933.

[11] J. Wheatley and R. Windler, "Wind-Tunnel Tests of a Cyclogiro Rotor," *Technical Notes, National Advisory Committee for Aeronautics*, vol. TN No. 528, 1935.

[12] W. F. Foshag and G. B. Beshler, "Review and Preliminary Evaluation of Lifting Horizontal-Axis Rotating-Wing Aeronautical Systems (HARWAS)," tech. rep., USAAVLABS, 1969.

[13] M. Benedict, M. Ramasamy, and I. Chopra, "Improving the Aerodynamic Performance of Micro-Air-Vehicle-Scale Cycloidal Rotor: An Experimental Approach," *Journal of Aircraft*, vol. 47, no. 4, pp. 1117–1125, 2010.

[14] I. S. Hwang, C. S. Hwang, S. Y. Min, I. O. Jeong, Y. H. Lee, and S. J. Kim, "Efficiency improvement of cycloidal wind turbine by active control of blade motion," *Sixteenth International Conference on Adaptive Structures and Technologies*, pp. 282–290, 2006.

[15] Y. B. Liang, L. X. Zhang, E. X. Li, F. Y. Zhang, "Blade pitch control of straight-bladed vertical axis wind turbine," *Springer*, vol. 23, pp. 1106–1114, 2016.

[16] Z. Mao, W. Tian, and S. Yan, "Influence analysis of blade chord length on the performance of a four-bladed Wollongong wind turbine," *Journal of Renewable and Sustainable Energy*, vol. 023303, no. 8, 2016.

[17] A. Dessoky, G. Bangga, T. Lutz, E. Kr, and R. Les, "Aerodynamic and aeroacoustic performance assessment of H-rotor darrieus VAWT equipped with wind-lens technology," *Energy*, vol. 175, pp. 76–97, 2019.

[18] A. Bianchini, F. Balduzzi, D. D. Rosa, and G. Ferrara, "On the use of Gurney Flaps for the aerodynamic performance augmentation of Darrieus wind turbines," *Energy Conversion and Management*, vol. 184, pp. 402–415, 2019.

[19] B. Zouzou, I. Dobrev, F. Massouh, and R. Dizene, "Experimental and numerical analysis of a novel Darrieus rotor with variable pitch mechanism at low TSR," *Energy*, vol. 186, p. 115832, 2019.

[20] S. Eriksson, H. Bernhoff, and M. Leijon, "Evaluation of different turbine concepts for wind power," *Renewable and Sustainable Energy Reviews*, vol. 12, pp. 1419–1434, 2008.

[21] M. M. Aslam Bhutta, N. Hayat, A. U. Farooq, Z. Ali, S. R. Jamil, and Z. Hussain, "Vertical axis wind turbine – A review of various configurations and design techniques," *Renewable and Sustainable Energy Reviews*, vol. 16, no. 4, pp. 1926–1939, 2012.

[22] B. Yang and C. Lawn, "Fluid dynamic performance of a vertical axis turbine for tidal currents," *Renewable Energy*, vol. 36, no. 12, pp. 3355–3366, 2011.

[23] U. K. Saha, S. Thotla, and D. Maity, "Journal of Wind Engineering Optimum design configuration of Savonius rotor through wind tunnel experiments," *Journal of Wind Engineering and Industrial Aerodynamics*, vol. 96, pp. 1359–1375, 2008.

[24] T. Brockett, "Hydrodynamic Analysis of Cycloidal Propulsors," in *The Society of Naval Architects and Marine Engineers*, Virginia Beach, VA, 1991.

[25] S. Hwang, Y. H. Lee, and S. J. Kim, "Optimization of cycloidal water turbine and the performance improvement by individual blade control," *Applied Energy*, vol. 86, pp. 1532–1540, 2009.

[26] J. J. Prabhu, V. Nagarajan, M. R. Sunny, and O. P. Sha, "On the fluid structure interaction of a marine cycloidal propeller," *Physics Procedia*, vol. 64, pp. 105–127, 2017.

[27] S. Nandy, V. Nagarajan, and O. P. Sha, "On the heuristic based electronic control of marine cycloidal propeller," *Applied Ocean Research*, vol. 78, no. October 2017, pp. 134–155, 2018.

[28] A. Halder, C. Walther, and M. Benedict, "Hydrodynamic modeling and experimental validation of a cycloidal propeller," *Ocean Engineering*, vol. 154, pp. 94–105, 2018.

[29] J. Boschma, "Cycloidal Propulsion for UAV VTOL Applications," tech. rep., BOSCH Aerospace Inc., 1998.

[30] C. Y. Yun, I. Park, and S. J. Kim, "A New VTOL UAV Cyclocopter with Cycloidal Blades System," *American Helicopter Society 64th Annual Forum*, 2004.

[31] H. Yu, L. Bin, and T. Beng, "The investigation of cyclogyro design and the performance," *25th International Congress of Aeronautical Sciences*, pp. 1–5, 2006.

[32] I. S. Hwang and S. J. Kim, "Aerodynamic Performance Enhancement of Cycloidal Rotor According to Blade Pivot Point Movement and Preset Angle Adjustment," *KSAS International Journal*, vol. 9, no. 2, pp. 58–63, 2008.

[33] I. S. Hwang, S. Y. Min, C. H. Lee, and S. J. Kim, "Development of a Four-Rotor Cyclocopter," *Journal of Aircraft*, vol. 45, no. 6, pp. 2151–2157, 2008.

[34] J. D. Anderson, *Fundamentals of Aerodynamics*. McGraw-Hill, third ed., 1991.

[35] A. Belloli, *Investigation of a Cycloidal Rotor for Micro Air Vehicles*. PhD thesis, University of Maryland, 2003.

[36] E. Parsons, *Investigation and Characterization of a Cycloidal Rotor for Application to a Micro-Air Vehicle*. Graduate report, University of Maryland, 2005.

[37] M. Benedict, *Fundamental Understanding of the Cycloidal-Rotor Concept for Micro Air Vehicle Applications*. Phd thesis, University of Maryland, 2010.

[38] M. Benedict, T. Jarugumilli, and I. Chopra, "Effect of Rotor Geometry and Blade Kinematics on Cycloidal Rotor Hover Performance," *Journal of Aircraft*, vol. 50, no. 5, pp. 1340–1352, 2013.

[39] M. Benedict, T. Jarugumilli, V. Lakshminarayan, and I. Chopra, "Effect of Flow Curvature on Forward Flight Performance of a Micro-Air-Vehicle-Scale Cycloidal-Rotor," *AIAA Journal*, vol. 52, no. 6, pp. 1159–1169, 2014.

[40] M. Benedict, J. Mullins, V. Hrishikeshavan, and I. Chopra, "Development of a Quad Cycloidal-Rotor Unmanned Aerial Vehicle," *Journal of the American Helicopter Society*, vol. 61, no. 2, pp. 1–12, 2016.

[41] C. C. Runco, B. Himmelberg, and M. Benedict, "Experimental Studies on a Mesoscale Cycloidal Rotor in Hover," *Journal of Aircraft*, vol. 56, no. 2, 2019.

[42] C. M. Walther, F. Saemi, M. Benedict, and V. Lakshminarayan, "Symmetric Versus Asymmetric Pitching of a Cycloidal Rotor Blade at Ultra-Low Reynolds Numbers," *Journal of Aircraft*, vol. 56, no. 3, 2019.

[43] C. M. Reed, D. A. Coleman, and M. Benedict, "Force and flowfield measurements to understand unsteady aerodynamics of cycloidal rotors in hover at ultra-low Reynolds numbers," *International Journal of Micro Air Vehicles*, vol. 11, 2019.

[44] C. Xisto, J. Páscoa, J. Leger, P. Masarati, G. Quaranta, M. Morandini, L. Gagnon, D. Wills, and M. Schwaiger, "Numerical modelling of geometrical effects in the performance of a cycloidal rotor," *11th World Congress on Computational Mechanics*, pp. 1–12, 2014.

[45] D. Wills and M. Schwaiger, "D-dalus," in *US EUCOM Science Technology Conference*, (Stuttgart), 2012.

[46] C. M. Xisto, J. C. Páscoa, M. Abdollahzadeh, J. A. Leger, M. Schwaiger, D. Wills, P. Masarati, and L. Gagon, "PECyT - Plasma Enhanced Cycloidal Thruster," *50th AIAA/ASME/SAE/ASEE Joint Propulsion Conference*, no. July 2014, 2014.

[47] J. Pascoa, "Cycloidal Rotor Optimised for Propulsion," tech. rep., European Union Seventh Framework Programme, 2015.

[48] M. Schwaiger and D. Wills, "D-Dalus VTOL – efficiency increase in forward flight," *Aircraft Engineering and Aerospace Technology*, vol. 88, no. 5, pp. 594–604, 2016.

[49] P. G. Migliore and W. P. Wolfe, "The Effects of Flow Curvature on the Aerodynamics of Darrieus Wind Turbines," tech. rep., Department of Aerospace Engineering, West Virginia University, 1980.

[50] P. Jain and A. Abhishek, "Modelling and Simulation of Virtual Camber in Cycloidal Rotors," *AIAA Journal*, vol. 55, no. 4, pp. 4–7, 2017.

[51] J. M. Rainbird, A. Bianchini, F. Balduzzi, J. Peiró, J. M. R. Graham, G. Ferrara, and L. Ferrari, "On the influence of virtual camber effect on airfoil polars for use in simulations of Darrieus wind turbines," *Energy Conversion and Management*, vol. 106, pp. 373–384, 2015.

[52] H. Zhang, Y. Hu, and G. Wang, "The effect of aerofoil camber on cycloidal propellers," *Aircraft Engineering and Aerospace Technology*, vol. 8, no. August 2017, pp. 1156–1167, 2018.

[53] J. Tang, Y. Hu, B. Song, and H. Yang, "Unsteady Aerodynamic Optimization of Airfoil for Cycloidal Propellers Based on Surrogate Model," *Journal of Aircraft*, vol. 54, no. 4, 2017.

[54] A. J. Wadcock, L. A. Ewing, E. Solis, M. Potsdam, and G. Rajagopalan, "Rotorcraft Downwash Flow Field Study to Understand the Aerodynamics of Helicopter Brownout," in *American Helicopter Society Southwest Region Technical Specialists Meeting*, (Dallas Texas), 2008.

[55] K. Singh, "Numerical Modeling of Stall and Poststall Events of a Single Pitching Blade of a Cycloidal Rotor," vol. 141, no. January, pp. 1–16, 2019.

[56] Y. Hu, H. Zhang, and C. Tan, "The effect of the aerofoil thickness on the performance of the MAV scale cycloidal rotor," *The Aeronautical Journal*, vol. 119, no. 1213, pp. 343–364, 2015.

[57] D. A. Dekterev, and Y. N. Goryunov, "Investigation of the effects of end faces design on parameters of cycloidal rotor ," *Thermophysics*, vol. 1105, 2018.

[58] S. Siegel, J. Seidel, K. Cohen, and T. McLaughlin, "A Cycloidal Propeller Using Dynamic Lift," *37th AIAA Fluid Dynamics Conference and Exhibit*, vol. 4232, no. June, pp. 1–14, 2007.

[59] A. Choudhry, R. Leknys, M. Arjomandi, and R. Kelso, "An insight into the dynamic stall lift characteristics," *Experimental Thermal and Fluid Science*, vol. 58, pp. 188–208, 2014.

[60] L. W. Carr and M. S. Chandrasekhara, "Compressibility Effects on Dynamic Stall," *Aerospace Science*, vol. 32, no. 6, pp. 523–573, 1996.

[61] J. A. Ekaterinaris and M. F. Platzer, "Computational prediction of airfoil dynamic stall," *Progress in Aerospace Sciences*, vol. 33, no. 11-12, pp. 759–846, 1998.

[62] F. O. Carta, "An Analysis of the Stall Flutter Instability of Helicopter Rotor Blades," *Journal of the American Helicopter Society*, vol. 12, no. 4, pp. 1–18, 1967.

[63] M. Ramasamy, J. S. Wilson, W. J. McCroskey, and P. B. Martin, "Measured Characteristics of Cycle-To-Cycle Variations in Dynamic Stall," *Proc. AHS Technical Meeting on Aeromechanics Design for Vertical Lift*, 2016.

[64] J. Niu, J. Lei, and T. Lu, "Numerical research on the effect of variable droop leading-edge on oscillating NACA 0012 airfoil dynamic stall," *Aerospace Science and Technology*, vol. 72, pp. 476–485, 2018.

[65] K. Kaufmann, C. B. Merz, and A. D. Gardner, "Dynamic Stall Simulations on a Pitching Finite Wing," *Journal of Aircraft*, vol. 54, no. 4, pp. 1303–1316, 2017.

[66] G. Leishman, *Principles of Helicopter Aerodynamics*. Cambridge University Press, 2002 ed.

[67] A. Choudhry, M. Arjomandi, and R. Kelso, "Methods to control dynamic stall for wind turbine applications," *Renewable Energy*, vol. 86, pp. 26–37, 2016.

[68] S. Opitz, A. D. Gardner, and K. Kaufmann, "Aerodynamic and structural investigation of an active back-flow flap for dynamic stall control," *CEAS Aeronautical Journal*, vol. 5, no. 3, pp. 279–291, 2014.

[69] A. D. Gardner, T. Knopp, K. Richter, and H. Rosemann, "Numerical investigation of pulsed air jets for dynamic stall control on the OA209 airfoil," *Notes on Numerical Fluid Mechanics and Multidisciplinary Design*, vol. 121, pp. 287–295, 2011.

[70] M. L. Post and T. C. Corke, "Separation Control Using Plasma Actuators: Dynamic Stall Vortex Control on Oscillating Airfoil," *AIAA Journal*, vol. 44, no. 12, pp. 3125–3135, 2006.

[71] D. Feszty, E. A. Gillies, and M. Vezza, "Alleviation of Airfoil Dynamic Stall Moments via Trailing-Edge-Flap Flow Control," *AIAA Journal*, vol. 42, no. 1, pp. 17–25, 2004.

[72] R. Green, E. Gillies, and Y. Wang, "Trailing edge flap flow control for dynamic stall," *Aeronautical Journal*, vol. 115, no. 1170, pp. 493–503, 2011.

[73] P. Gerontakos and T. Lee, "PIV study of flow around unsteady airfoil with dynamic trailing-edge flap deflection," *Experiments in Fluids*, vol. 45, no. 6, pp. 955–972, 2008.

[74] M. S. Chandrasekhara, P. B. Martin, and C. Tung, "Compressible Dynamic Stall Control Using a Variable Droop Leading Edge Airfoil," *Journal of Aircraft*, vol. 41, no. 4, pp. 862 – 869, 2004.

[75] P. Martin, K. McAlister, M. Chandrasekhara, and W. Geissler, "Dynamic Stall Measurements and Computations for a VR-12 airfoil with a Variable Droop Leading edge," in *American Helicopter Society 59th Annual Forum*, pp. 472–489, 2003.

[76] J. J. Bain, L. N. Sankar, J. V. R. Prasad, O. A. Bauchau, D. A. Peters, and C. J. He, "Computational Modeling of Variable-Droop Leading Edge in Forward Flight," *Journal of Aircraft*, vol. 46, no. 2, pp. 617–626, 2009.

[77] S. Kota, G. Ervin, R. Osborn, and R. A. Ormiston, "Design and Fabrication of an Adaptive Leading Edge Rotor Blade," *American Helicopter Society 64th Annual Forum*, no. October, 2008.

[78] S. Kota, K. Lu, Z. Kreiner, B. Trease, and J. Geiger, "Design and Application of Compliant Mechanisms for Morphing Aircraft Structures," *Smart Structures and Materials 2003: Industrial and Commercial Applications of Smart Structures Technologies*, vol. 5054, pp. 24–33, 2003.

[79] S. Kota, J. A. Hetrick, and R. Osborn, "Adaptive structures: Moving into the mainstream," *Aerospace America*,. September, pp. 16–18, 2006.

[80] T. Xinxing, G. Wenjie, S. Chao, and L. Xiaoyong, "Topology optimization of compliant adaptive wing leading edge with composite materials," *Chinese Journal of Aeronautics*, vol. 27, no. 6, pp. 1488–1494, 2014.

[81] S. Vasista, J. Riemenschneider, B. van de Kamp, H. P. Monner, R. C. M. Cheung, C. Wales, and J. E. Cooper, "Evaluation of a Compliant Droop-Nose Morphing Wing Tip via Experimental Tests," *Journal of Aircraft*, vol. 54, no. 2, pp. 1–16, 2016.

[82] H. Lomax, T. Pulliam, and D. Zingg, *Fundamentals of Computational Fluid Dynamics*. Berlin: Springer, 2001.

[83] "CD-Adapco STAR-CCM+ documentation," version 12.04.010-R8, 2015.

[84] S. Wang, D. B. Ingham, L. Ma, M. Pourkashanian, and Z. Tao, "Turbulence modeling of deep dynamic stall at relatively low Reynolds number," *Journal of Fluids and Structures*, vol. 33, pp. 191–209, 2012.

[85] Y. Kim and Z.-T. Xie, "Modelling the effect of freestream turbulence on dynamic stall of wind turbine blades," *Computers and Fluids*, vol. 129, pp. 53–66, 2016.

[86] B. Hand, G. Kelly, and A. Cashman, "Numerical simulation of a vertical axis wind turbine airfoil experiencing dynamic stall at high Reynolds numbers," *Computers and Fluids*, vol. 149, pp. 12–30, 2017.

[87] M. Ghasemian, Z. N. Ashrafi, and A. Sedaghat, "A review on computational fluid dynamic simulation techniques for Darrieus vertical axis wind turbines," *Energy Conversion and Management*, vol. 149, pp. 87–100, 2017.

[88] G. Bangga, G. Hutomo, R. Wiranegara, and H. Sasongko, "Numerical study on a single bladed vertical axis wind turbine under dynamic stall," *Journal of Mechanical Science and Technology*, vol. 31, no. 1, pp. 261–267, 2017.

[89] J. Sangwan, T. K. Sengupta, and P. Suchandra, "Investigation of compressibility effects on dynamic stall of pitching airfoil," *Physics of Fluids*, vol. 29, no. 7, 2017.

[90] R. H. Barnard and D. R. Philpott, *Aircraft Flight, A Description of the Physical Principles of Aircraft Flight*. Pearson, 4th edition, 2010.

[91] D. Munday, J. Jacob, and G. Huang, "Active flow control of separation on a wing with oscillatory camber," *40th AIAA Aerospace Sciences Meeting and Exhibit*, vol. 39, no. 1, pp. 187–189, 2002.

[92] O. Bilgen and M. I. Friswell, "Piezoceramic composite actuators for a solid-state variable-camber wing," *Journal of Intelligent Material Systems and Structures*, vol. 25, no. 7, pp. 806–817, 2014.

[93] K. Richter, A. Le Pape, T. Knopp, M. Costes, V. Gleize, and A. D. Gardner, "Improved Two-Dimensional Dynamic Stall Prediction with Structured and Hybrid Numerical Methods," *Journal of the American Helicopter Society*, vol. 56, no. 4, pp. 1–12, 2011.

[94] V. Motta, A. Guardone, and G. Quaranta, "Influence of airfoil thickness on unsteady aerodynamic loads on pitching airfoils," *Journal of Fluid Mechanics*, vol. 774, pp. 460–487, 2015.

[95] M. Chandrasekhara, M. C. Wilder, and L. W. Carr, "Competing Mechanisms of Compressible Dynamic Stall," *AIAA Journal*, vol. 36, no. 3, pp. 387–393, 1998.

[96] M. S. Chandrasekhara, M. C. Wilder, and L. W. Carr, "Compressible Dynamic Stall Control Using Dynamic Shape Adaptation," *AIAA Journal*, vol. 39, no. 10, pp. 2021–2024, 2001.

[97] J. A. Ekaterinaris, "Numerical Investigations of Dynamic Stall Active Control for Incompressible and Compressible Flows," *Journal of Aircraft*, vol. 39, no. 1, 2002.

[98] P. Spalart and S. Allmaras, "A one-equation turbulence model for aerodynamic flows," *AIAA-92-0439*, 1992.

[99] D. Wilcox, *Turbulence Modeling for CFD*. DCW Industries, Inc., 2nd edition, 1998.

[100] F. Menter, "Two-equation eddy-viscosity turbulence modelling for engineering applications," *AIAA Journal*, vol. 32, pp. 1598–1605, 1994.

[101] P. Spalart, "Effective Inflow Conditions for Turbulence Models in Aerodynamic Calculations," *AIAA Journal*, vol. 45, pp. 2544–2553, 2007.

[102] R. Green, R. Galbraith, and A. Niven, "The Convection Speed of the Dynamic Stall Vortex," tech. rep., University of Glasgow, Department of Aerospace Engineering, Report No 9202, Glasgow, 1992.

[103] T. Jarugumilli, A. H. Lind, M. Benedict, V. K. Lakshminarayan, A. R. Jones, and I. Chopra, "Experimental and computational flow field studies of a MAV-scale cycloidal rotor in forward flight," *69th American Helicopter Society International Annual Forum 2013*, vol. 4, pp. 2354–2371, 2013.

[104] A. Jirásek, T. L. Jeans, M. Martenson, R. M. Cummings, and K. Bergeron, "Improved methodologies for the design of maneuver for stability and control simulations," *Aerospace Science and Technology*, vol. 25, no. 1, pp. 203–223, 2013.

[105] A. J. Buchner, M. W. Lohry, L. Martinelli, J. Soria, and A. J. Smits, "Dynamic stall in vertical axis wind turbines: Comparing experiments and computations," *Journal of Wind Engineering and Industrial Aerodynamics*, vol. 146, pp. 163–171, 2015.

[106] M. Sahin, L. N. Sankar, M. S. Chandrasekhara, and C. Tung, "Dynamic stall alleviation using a deformable leading edge concept - A numerical study," *Journal of Aircraft*, vol. 40, no. 1, pp. 77–85, 2003.

[107] Igus, "iglidur Tribo-Tape B160.", *Technical Specification Sheet*

[108] Copley Controls Corp, "Models STA 2504-2510 Servotube Actuator.", *Technical Specification Sheet*, 2018

[109] P. Gerontakos, *An Experimental Investigation of Flow Over an Oscillating Airfoil*. PhD thesis, University of McGill, 2004.

[110] D-tacq Solutions, "http://www.d-tacq.com/modproducts.shtml,", Date accessed: February 2020.

[111] D-tacq Solutions, "A0420FMC Product Specification.", *Technical Specification Sheet*

[112] First Sensor, "HDI Series Amplified pressure sensors.", *Technical Specification Sheet*

[113] General Electric, "Druck DPI 610/615 Portable Pressure Calibrator Series - K0415.", *Technical Specification Sheet*

[114] Copley Controls Corp, "Xenus Plus User Guide," 2015.

[115] Copley Controls Corp,"CME 2 User Guide."

[116] S. Beyhaghi and R. S. Amano, "Journal of Wind Engineering Industrial Aerodynamics A parametric study on leading-edge slots used on wind turbine airfoils at various angles of attack," *Journal of Wind Engineering Industrial Aerodynamics*, vol. 175, no. December 2017, pp. 43–52, 2018.

[117] Z. Ni, M. Dhanak, and T.C. Su, "Performance Characteristics of Airfoils with Leading-Edge Tubercles and an Internal Slot," AIAA Journal, vol. 57, no. 6, 2019.

[118] J. B. Barlow William H Rae, J. Alan Pope, and J. Wiley, "Low-Speed Wind Tunnel Testing", 3rd Edition, *John Wiley and Sons, Inc*, 1999.

[119] M. Costes, F. Richez, A. Le Pape, and R. Gavériaux, "Numerical investigation of three-dimensional effects during dynamic stall," *Aerospace Science and Technology*, vol. 47, pp. 216–237, 2015.

[120] A. H. Lind and A. R. Jones, "Unsteady aerodynamics of reverse flow dynamic stall on an oscillating blade section," *Physics of Fluids*, vol. 28, no. 7, 2016.

[121] S. Wang, D. B. Ingham, L. Ma, M. Pourkashanian, and Z. Tao, "Numerical investigations on dynamic stall of low Reynolds number flow around oscillating airfoils," *Computers and Fluids*, vol. 39, no. 9, pp. 1529–1541, 2010.

[122] A. H. Lind, T. Jarugumilli, M. Benedict, V. K. Lakshminarayan, A. R. Jones, and I. Chopra, "Flow field studies on a micro-air-vehicle-scale cycloidal rotor in forward flight," *Experiments in Fluids*, vol. 55, no. 12, pp. 1–17, 2014.